Technische Universität Kaiserslautern

Fachbereich Chemie

CRYO TAGGING INFRARED SPECTROSCOPY AND TEMPERATURE CONTROLLED KINETIC STUDIES IN A TANDEM TRAP MASS SPECTROMETER

Am Fachbereich Chemie der Technischen Universität Kaiserslautern zur Erlangung
des akademischen Grades "Doktor der Naturwissenschaften" genehmigte

Dissertation
(D386)

vorgelegt von
Dipl.-Chem. Jennifer Mohrbach

Tag der wissenschaftlichen Aussprache: 03.03.2017

Betreuer: Prof. Dr. G. Niedner-Schatteburg

Technische Universität Kaiserslautern

Der experimentelle Teil der vorliegenden Arbeit wurde in der Zeit von Oktober 2013 bis Dezember 2016 im Fachbereich Chemie der Technischen Universität Kaiserslautern unter der Betreuung von Prof. Dr. G. Niedner-Schatteburg angefertigt.

Datum des Antrags der Eröffnung des Promotionsverfahrens: 30.11.2016

Promotionskommission:

Vorsitzender	Prof. Dr. H. Sitzmann
1. Berichterstatter	Prof. Dr. G. Niedner-Schatteburg
2. Berichterstatter	Prof. Dr. M. Gerhards

meiner Familie

„Man merkt nie, was schon getan wurde,

man sieht immer nur, was noch zu tun bleibt.“

Marie Curie

CONTENT

1. Introduction 1

2. Experimental Methods and Setup 9

2.1 Fourier Transform Ion Cyclotron Resonance Mass Spectrometry 9

2.2 The FRITZ Setup 11

Electrospray Ionization (ESI) Source 14

Laser Vaporization (LVAP) Cluster Ion Source 15

2.3 Isothermal Cryo Kinetics of Cationic Transition Metal Clusters 17

Relative Rate Constants 17

Absolute Rate Constants 18

2.4 Infrared Multiple Photon Dissociation 19

Optical Parametric Oscillator / Amplifier (OPO/OPA) 20

2.5 Computational Methods 22

2.6 References 23

3. Vibrational Fingerprints of Ligated Tetranuclear Cobalt Clusters 27

3.1 Publication: "Vibrational fingerprints of a tetranuclear cobalt carbonyl cluster within an ion trap" 29

3.1.1 Abstract 31

3.1.2 Introduction 32

3.1.3 Experimental and Computational Methods 35

3.1.4 Results and Discussion 39

3.1.5 Conclusions and Outlook 43

3.1.6 References 44

3.1.7 Supplementary Information 48

3.2 Vibrational fingerprints of mixed tetranuclear cobalt carbonyl / dinitrogen clusters $[Co_4(CO)_n(dppa\text{-}H^+)N_2]^-$ within an ion trap 51

4. Cryo Kinetics and Spectroscopy of Cationic Transition Metal Clusters 55

4.1 Publication: "Infrared spectroscopy of N_2 adsorption on size selected cobalt cluster cations in isolation" 57

4.1.1 Abstract 59
4.1.2 Introduction 60
4.1.3 Experimental Methods 61
4.1.4 Results and Discussion 62
4.1.5 Conclusions 68
4.1.6 Acknowledgements 68
4.1.7 Notes and References 69

4.2 Publication: “Cryo Kinetics and Spectroscopy of Cationic Nickel Clusters: Rough and Smooth Surfaces” 73
4.2.1. Abstract 75
4.2.2 Introduction 76
4.2.3 Experimental and Computational Methods 79
4.2.5 Conclusions 98
4.2.6 Acknowledgements 99
4.2.7 References 99
4.2.8 Supplementary Information 107

4.3 Paper draft: “Isothermal Cryo Kinetics of Cationic Nickel Clusters” 131
4.3.1 Abstract 133
4.3.2 Introduction 134
4.3.3 Experimental and Computational Methods 136
4.3.4 Results and Discussion 138
4.3.5 Conclusions 150
4.3.6 Acknowledgements 151
4.3.7 References 151
4.3.8 Supplementary Information 155

4.4 Paper draft: “Isothermal Cryo Kinetics of Cationic Iron Clusters” 167
4.4.1 Abstract 169
4.4.2 Introduction 170
4.4.3 Experimental and Computational Methods 172
4.4.4 Results and Discussion 174
4.4.5 Conclusions and Outlook 182
4.4.6 Acknowledgements 182

4.4.7 References 183
4.4.8 Supplementary Information 187

5. Summary and Outlook 197

References 199
5.1 Zusammenfassung und Ausblick 201
Referenzen 204

6. Appendix 207

6.1 Publication: “Vibrational Blue Shift of coordinated N_2 in $[Fe_3O(OAc)_6(N_2)_n]^+$: “Non Classical” Dinitrogen Complexes” 207

1. INTRODUCTION

Transition metals (TMs) are of indisputable importance for many catalytic processes and have been studied extensively in the past decades.[1-9] The partially filled d and f shells of TMs dominate their properties as free atoms, clusters or in bulk phase. Clusters bridge the gap between atoms and bulk[10] and serve as model systems for the investigation of chemical[11-19] and physical[4,20-24] behavior. They help to unravel the complex reactivity of heterogeneous catalysts by studying the effect of e.g. particle size, shape or even charge state. Gas phase reactivity studies of early TM oxide clusters are largely motivated by their relevance for industrial oxidation catalysis.[25-37] Such studies have provided insight into actual catalytic mechanisms. The adsorption of diatomic molecules like hydrogen (H_2), nitrogen (N_2), or carbon monoxide (CO) on TM clusters and the co-adsorption of such molecules are of significant interest due to their relevance for industrial processes, e.g. the Fischer-Tropsch or the Haber-Bosch process.[38-39] Early cluster studies revealed remarkable size- and structure-dependent properties of clusters,[40-44] and provided insights into the repetitively stated cluster-surface analogy.[17, 39, 45-48] In this so-called "non-scalable cluster size regime"[23, 49-50] the found atom-by-atom dependent variation superimpose to the gradual, scalable change of cluster properties by size.[23, 51]

Therefore, knowledge about the exact geometric structure of small and intermediate sized clusters would allow fundamental insights into TM cluster properties. The reactivity toward small molecules provides an indirect way to determine the cluster structure. Based on the number of molecules adsorbed on the cluster surface, information on available adsorption sites and consequently on the shape of the cluster is received. A molecule can be adsorbed in different sites on a cluster surface (Fig. 1), which can vary with coverage, temperature, pressure, and from one crystallographic plane to another. In general, molecularly adsorbed species can be bound in atop or bridging sites. For instance, CO has been observed in atop, bridge, face, and hollow sites, while N_2 clearly prefers atop adsorption sites. In the context of CO adsorption to metal clusters and of related carbonyl complexes it was shown that adsorbates may be used to titrate available surface sites up to saturation for the elucidation of underlying structural motifs.[52-53] The chemical probe technique uses the adsorption of small molecules to saturate cluster surface sites and to identify adsorption plateaus.[54-55]

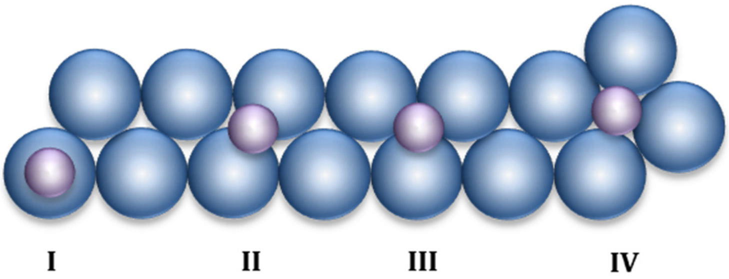

Figure 1. Schematic representation (top view) of different adsorbate binding sites for head-on adsorption. There exist several nomenclatures for the description of the same adsorbate binding site: (I) atop, μ_1-coordinated, linearly or terminal bound, (II) twofold coordinated, μ_2-coordinated, or bridge bound, (III) threefold coordinated, μ_3-coordinated, or face bound and (IV) fourfold coordinated or μ_4-coordinated.

The degree of weakening of an adsorbates' bond strength can be used as a characteristic fingerprint for the respective binding site. Vibrational modes of adsorbates on TM clusters and in TM coordination complexes as isolated ions can be studied by Infrared Multiple Photon Dissociation (IR-MPD).[56-58] Shifts in adsorbate frequencies are often used for the study of binding sites on TM surfaces, thus the CO molecule may be viewed as a classic probe molecule in surface science.[59-60] In general, a weakening of the CO bond results in a lowering or redshifting of the carbonyl stretch frequency. Most TM carbonyls follow this behavior.[61-69] The CO stretching vibration probes the metal-ligand bonding in a sensitive way: its frequency indicates subtle details of the hosts' electronic structure, and it helps to elucidate its binding site and the geometric binding arrangement.[70-73]

The aim of the research described in this thesis was to obtain fundamental knowledge on the interaction of diatomic molecules with charged TM clusters. With the help of gas phase infrared (multiple) photon dissociation (IR-(M)PD) experiments in combination with density functional theory (DFT) it has been shown that this approach can provide cluster size and adsorbate coverage dependent information on cluster surface morphologies.

The experimental setup and the applied methods used to produce and detect the TM clusters are introduced in chapter 2. Chapter 3 addresses the impact of the stepwise decrease of CO coverage on a tetranuclear cobalt complex when isolated at low temperatures (26 K). A comprehensive characterization of CO adsorption types and their specific coverage dependent influence on the transition metal core and spin states will be given. The second research part (chapter 4) represents the main component of this thesis. A considerable number of N_2 adsorption studies on naked cationic TM clusters and IR spectroscopic studies on their respective cluster adsorbate complexes have been performed. The combination of these studies has provided information on metal-adsorbate bonding and has unraveled structure-reactivity relationships. We compare our results to experimental and theoretical studies, which aim to gain insight into TM cluster structures and adsorption behavior. The thesis will be concluded by a summary of the presented results and an outlook on future experiments.

References

1. Buchwalter, P.; Rose, J.; Braunstein, P., Multimetallic Catalysis Based on Heterometallic Complexes and Clusters. *Chem. Rev.* **2015**, *115*, 28-126.
2. Musaev, D. G.; Morokuma, K., Transition Metal Catalyzed σ-Bond Activation and Formation Reactions. In *Theoretical Aspects of Transition Metal Catalysis*, Frenking, G., Ed. Springer Berlin Heidelberg: Berlin, Heidelberg, 2005; pp 1-30.
3. Niedner-Schatteburg, G., Cooperative Effects in Clusters and Oligonuclear Complexes of Transition Metals in Isolation. In *Clusters – Contemporary Insight in Structure and Bonding*, Springer Berlin Heidelberg, **2017**, pp 1-40.
4. Baletto, F.; Ferrando, R., Structural Properties of Nanoclusters: Energetic, Thermodynamic, and Kinetic Effects. *Reviews of modern physics,* **2005**, *77*, 371.
5. Bond, G. C.; Thompson, D. T., Catalysis by Gold. *Catal. Rev.-Sci. Eng.* **1999**, *41*, 319-388.
6. Kubas, G. J., Fundamentals of H-2 Binding and Reactivity on Transition Metals Underlying Hydrogenase Function and H-2 Production and Storage. *Chem. Rev.* **2007**, *107*, 4152-4205.
7. Bohme, D. K.; Schwarz, H., Gas-Phase Catalysis by Atomic and Cluster Metal Ions: The Ultimate Single-Site Catalysts. *Angewandte Chemie-International Edition,* **2005**, *44*, 2336-2354.
8. O'Hair, R. A. J.; Khairallah, G. N., Gas Phase Ion Chemistry of Transition Metal Clusters: Production, Reactivity, and Catalysis. *Journal of Cluster Science* **2004**, *15*, 331-363.
9. Böhme, D. K.; Schwarz, H., Gas-Phase Catalysis by Atomic and Cluster Metal Ions: The Ultimate Single-Site Catalysts. *Angewandte Chemie International Edition* **2005**, *44*, 2336-2354.
10. Haberland, H.; Buck, U.; Scoles, G., Experimental Methods. In *Clusters of Atoms and Molecules*, Springer: 1994; pp 207-252.

11. Simoes, J. M.; Beauchamp, J., Transition Metal-Hydrogen and Metal-Carbon Bond Strengths: The Keys to Catalysis. *Chem. Rev.* **1990**, *90*, 629-688.
12. Berg, C.; Schindler, T.; Niedner-Schatteburg, G.; Bondybey, V. E., Reactions of Simple Hydrocarbons with Nb+ N: Chemisorption and Physisorption on Ionized Niobium Clusters. *The Journal of chemical physics* **1995**, *102*, 4870-4884.
13. Heinemann, C.; Wesendrup, R.; Schwarz, H., Pt+-Mediated Activation of Methane: Theory and Experiment. *Chemical physics letters* **1995**, *239*, 75-83.
14. Wesendrup, R.; Schwarz, H., Tantalum-Mediated Coupling of Methane and Carbon Dioxide in the Gas Phase. *Angewandte Chemie International Edition in English* **1995**, *34*, 2033-2035.
15. Achatz, U.; Berg, C.; Joos, S.; Fox, B. S.; Beyer, M. K.; Niedner-Schatteburg, G.; Bondybey, V. E., Methane Activation by Platinum Cluster Ions in the Gas Phase: Effects of Cluster Charge on the Pt 4 Tetramer. *Chemical Physics Letters* **2000**, *320*, 53-58.
16. Böhme, D. K.; Schwarz, H., Gas-Phase Catalysis by Atomic and Cluster Metal Ions: The Ultimate Single-Site Catalysts. *Angewandte Chemie International Edition* **2005**, *44*, 2336-2354.
17. Pfeffer, B.; Jaberg, S.; Niedner-Schatteburg, G., Reactions of Simple Aromatic Heterocycles with Niobium Cluster Ions (N < 30). *J. Chem. Phys.* **2009**, *131*, 194305.
18. Barzen, L.; Tombers, M.; Merkert, C.; Hewer, J.; Niedner-Schatteburg, G., Benzene Activation and H/D Isotope Effects in Reactions of Mixed Cobalt Platinum Clusters: The Influence of Charge and of Composition. *International Journal of Mass Spectrometry* **2012**, *330*, 271-276.
19. Tombers, M.; Barzen, L.; Niedner-Schatteburg, G., Inverse H/D Isotope Effects in Benzene Activation by Cationic and Anionic Cobalt Clusters. *The Journal of Physical Chemistry A* **2013**, *117*, 1197-1203.
20. Wang, L.-S.; Li, X.; Zhang, H.-F., Probing the Electronic Structure of Iron Clusters Using Photoelectron Spectroscopy. *Chemical Physics* **2000**, *262*, 53-63.
21. Knickelbein, M. B., Electric Dipole Polarizabilities of Ni 12–58. *The Journal of Chemical Physics* **2001**, *115*, 5957-5964.
22. Wrigge, G.; Astruc Hoffmann, M.; Issendorff, B. v.; Haberland, H., Ultraviolet Photoelectron Spectroscopy of to To. *The European Physical Journal D-Atomic, Molecular, Optical and Plasma Physics* **2003**, *24*, 23-26.
23. Haberland, H.; Kleinermanns, K.; Träger, F., Cluster. In *Lehrbuch Der Experimentalphysik Band 5 - Gase, Nanosysteme, Flüssigkeiten*, 2nd ed.; Walter de Gruyter: 2006; p 819.
24. Song, W.; Lu, W.-C.; Wang, C.; Ho, K., Magnetic and Electronic Properties of the Nickel Clusters Nin (N⩽ 30). *Computational and Theoretical Chemistry* **2011**, *978*, 41-46.
25. Asmis, K. R., Structure Characterization of Metal Oxide Clusters by Vibrational Spectroscopy: Possibilities and Prospects. *Physical Chemistry Chemical Physics* **2012**, *14*, 9270-9281.
26. Asmis, K. R.; Wende, T.; Bruemmer, M.; Gause, O.; Santambrogio, G.; Stanca-Kaposta, E. C.; Doebler, J.; Niedziela, A.; Sauer, J., Structural Variability in Transition Metal Oxide Clusters: Gas Phase Vibrational Spectroscopy of V3o6-8+. *Physical Chemistry Chemical Physics* **2012**, *14*, 9377-9388.
27. Bhunia, A.; Gamer, M. T.; Ungur, L.; Chibotaru, L. F.; Powell, A. K.; Lan, Y.; Roesky, P. W.; Menges, F.; Riehn, C.; Niedner-Schatteburg, G., From a Dy(III) Single

Molecule Magnet (SMM) to a Ferromagnetic (Mn(II)Dy(III)Mn(II) Trinuclear Complex. *Inorganic Chemistry* **2012**, *51*, 9589-9597.

28. Dietl, N.; Schlangen, M.; Schwarz, H., Thermal Hydrogen-Atom Transfer from Methane: The Role of Radicals and Spin States in Oxo-Cluster Chemistry. *Angewandte Chemie-International Edition* **2012**, *51*, 5544-5555.
29. Feyel, S.; Scharfenberg, L.; Daniel, C.; Hartl, H.; Schroeder, D.; Schwarz, H., Dehydrogenation of Methanol by Vanadium Oxide and Hydroxide Cluster Cations in the Gas Phase. *Journal of Physical Chemistry A* **2007**, *111*, 3278-3286.
30. Feyel, S.; Schroder, D.; Schwarz, H., Gas-Phase Oxidation of Isomeric Butenes and Small Alkanes by Vanadium-Oxide and -Hydroxide Cluster Cations. *Journal of Physical Chemistry A* **2006**, *110*, 2647-2654.
31. Hirabayashi, S.; Ichihashi, M.; Kondow, T., Enhancement of Ammonia Dehydrogenation by Introduction of Oxygen onto Cobalt and Iron Cluster Cations. *Journal of Physical Chemistry A* **2010**, *114*, 13040-13044.
32. Lang, S. M.; Bernhardt, T. M., Gas Phase Metal Cluster Model Systems for Heterogeneous Catalysis. *Physical Chemistry Chemical Physics* **2012**, *14*, 9255-9269.
33. Nagata, T.; Miyajima, K.; Hardy, R. A.; Metha, G. F.; Mafune, F., Reactivity of Oxygen Deficient Cerium Oxide Clusters with Small Gaseous Molecules. *Journal of Physical Chemistry A* **2015**, *119*, 5545-5552.
34. Nagata, T.; Miyajima, K.; Mafune, F., Oxidation of Nitric Oxide on Gas-Phase Cerium Oxide Clusters Via Reactant Adsorption and Product Desorption Processes. *Journal of Physical Chemistry A* **2015**, *119*, 10255-10263.
35. Nagata, T.; Miyajima, K.; Mafune, F., Stable Stoichiometry of Gas-Phase Cerium Oxide Cluster Ions and Their Reactions with Co. *Journal of Physical Chemistry A* **2015**, *119*, 1813-1819.
36. Wang, B.; Chen, W.-J.; Zhao, B.-C.; Zhang, Y.-F.; Huang, X., Tetratungsten Oxide Clusters W4On-/0 (N=10-13): Structural Evolution and Chemical Bonding. *Journal of Physical Chemistry A* **2010**, *114*, 1964-1972.
37. Xue, W.; Wang, Z.-C.; He, S.-G.; Xie, Y.; Bernstein, E. R., Experimental and Theoretical Study of the Reactions between Small Neutral Iron Oxide Clusters and Carbon Monoxide. *Journal of the American Chemical Society* **2008**, *130*, 15879-15888.
38. Dry, M. E., Present and Future Applications of the Fischer–Tropsch Process. *Applied Catalysis A: General* **2004**, *276*, 1-3.
39. Ertl, G., Reactions at Surfaces: From Atoms to Complexity (Nobel Lecture). *Angew. Chem. Int. Ed.* **2008**, *47*, 3524-3535.
40. Morse, M. D.; Geusic, M.; Heath, J.; Smalley, R., Surface Reactions of Metal Clusters. II. Reactivity Surveys with D2, N2, and Co. *The Journal of chemical physics* **1985**, *83*, 2293-2304.
41. Kaldor, A.; Cox, D.; Trevor, D.; Zakin, M., Atoms, Molecules and Clusters. *Z. Phys. D* **1986**, *3*, 195-204.
42. Suslick, K. S., High-Energy Processes in Organometallic Chemistry. **1987**.
43. Knickelbein, M. B., Reactions of Transition Metal Clusters with Small Molecules 1. *Annu. Rev. Phys. Chem.* **1999**, *50*, 79-115.
44. Alonso, J. A., Electronic and Atomic Structure, and Magnetism of Transition-Metal Clusters. *Chem. Rev.* **2000**, *100*, 637-678.
45. Muetterties, E. L., Metal Clusters in Catalysis 3. Clusters as Models for Chemisorption Processes and Heterogeneous Catalysis. *Bull. Soc. Chim. Belg.* **1975**, *84*, 959-986.

46. Muetterties, E. L., Molecular Metal Clusters. *Science* **1977**, *196*, 839-848.
47. Muetterties, E. L.; Rhodin, T. N.; Band, E.; Brucker, C. F.; Pretzer, W. R., Clusters and Surfaces. *Chem. Rev.* **1979**, *79*, 91-137.
48. Shustorovich, E., Cluster-Surface Analogy: New Developments. In *Quantum Chemistry: The Challenge of Transition Metals and Coordination Chemistry*, Veillard, A., Ed. Springer Netherlands: **1986**; Vol. 176, pp 445-464.
49. Heiz, U.; Landman, U., *Nanocatalysis*. Springer: Berlin, **2007**.
50. Landman, U.; Yoon, B.; Zhang, C.; Heiz, U.; Arenz, M., Factors in Gold Nanocatalysis: Oxidation of Co in the Non-Scalable Size Regime. *Top. Catal.* **2007**, *44*, 145-158.
51. Rips, I.; Jortner, J., Ion Solvation in Clusters. *J. Chem. Phys.* **1992**, *97*, 536-546.
52. Ganteför, G.; Icking-Konert, G. S.; Handschuh, H.; Eberhardt, W., Co Chemisorption on Ni N, Pd N and Pt N Clusters. *Int. J. Mass Spectrom. Ion Processes* **1996**, *159*, 81-109.
53. Ervin, K. M., Metal-Ligand Interactions: Gas-Phase Transition Metal Cluster Carbonyls. *Int. Rev. Phys. Chem.* **2001**, *20*, 127-164.
54. Parks, E.; Nieman, G.; Pobo, L.; Riley, S., The Uptake of Ammonia by Iron Clusters: A New Procedure for the Study of Metal Cluster Chemistry. *The Journal of chemical physics* **1987**, *86*, 1066-1067.
55. Parks, E.; Weiller, B.; Bechthold, P.; Hoffman, W.; Nieman, G.; Pobo, L.; Riley, S., Chemical Probes of Metal Cluster Structure: Reactions of Iron Clusters with Hydrogen, Ammonia, and Water. *The Journal of Chemical Physics* **1988**, *88*, 1622-1632.
56. Duncan, M. A., Spectroscopy of Metal Ion Complexes: Gas-Phase Models for Solvation. *Annu. Rev. Phys. Chem.* **1997**, *48*, 69-93.
57. Duncan, M. A., Infrared Spectroscopy to Probe Structure and Dynamics in Metal Ion-Molecule Complexes. *Int. Rev. Phys. Chem.* **2003**, *22*, 407-435.
58. Walker, N. R.; Walters, R. S.; Duncan, M. A., Frontiers in the Infrared Spectroscopy of Gas Phase Metal Ion Complexes. *New J. Chem.* **2005**, *29*, 1495-1503.
59. Somorjai, G., Introduction to Surface Science and Catalysis. *See for example Wiley, New York* **1994**.
60. Ertl, G., *Reactions at Solid Surfaces*; John Wiley & Sons, **2010**; Vol. 14.
61. Goldman, A. S.; Krogh-Jespersen, K., Why Do Cationic Carbon Monoxide Complexes Have High Co Stretching Force Constants and Short Co Bonds? Electrostatic Effects, Not σ-Bonding. *Journal of the American Chemical Society* **1996**, *118*, 12159-12166.
62. Lupinetti, A. J.; Fau, S.; Frenking, G.; Strauss, S. H., Theoretical Analysis of the Bonding between Co and Positively Charged Atoms. *The Journal of Physical Chemistry A* **1997**, *101*, 9551-9559.
63. Frenking, G.; Pidun, U., Ab Initio Studies of Transition-Metal Compounds: The Nature of the Chemical Bond to a Transition Metal. *Journal of the Chemical Society, Dalton Transactions* **1997**, 1653-1662.
64. Moore, D. T.; Oomens, J.; Eyler, J. R.; Meijer, G.; von Helden, G.; Ridge, D. P., Gas-Phase IR Spectroscopy of Anionic Iron Carbonyl Clusters. *Journal of the American Chemical Society* **2004**, *126*, 14726-14727.
65. Fielicke, A.; von Helden, G.; Meijer, G.; Simard, B.; Rayner, D. M., Gold Cluster Carbonyls: Vibrational Spectroscopy of the Anions and the Effects of Cluster Size, Charge, and Coverage on the Co Stretching Frequency. *The Journal of Physical Chemistry B* **2005**, *109*, 23935-23940.

66. Velasquez, J.; Njegic, B.; Gordon, M. S.; Duncan, M. A., Ir Photodissociation Spectroscopy and Theory of Au+(Co)n Complexes: Nonclassical Carbonyls in the Gas Phase. *The Journal of Physical Chemistry A* **2008**, *112*, 1907-1913.
67. Reed, Z. D.; Duncan, M. A., Infrared Spectroscopy and Structures of Manganese Carbonyl Cations, Mn(Co)N+ (N = 1–9). *Journal of the American Society for Mass Spectrometry* **2010**, *21*, 739-749.
68. Ricks, A. M.; Reed, Z. E.; Duncan, M. A., Infrared Spectroscopy of Mass-Selected Metal Carbonyl Cations. *Journal of Molecular Spectroscopy* **2011**, *266*, 63-74.
69. Bistoni, G.; Rampino, S.; Scafuri, N.; Ciancaleoni, G.; Zuccaccia, D.; Belpassi, L.; Tarantelli, F., How Π Back-Donation Quantitatively Controls the Co Stretching Response in Classical and Non-Classical Metal Carbonyl Complexes. *Chemical Science* **2016**, *7*, 1174-1184.
70. Wrighton, M., Photochemistry of Metal Carbonyls. *Chem. Rev.* **1974**, *74*, 401-430.
71. Nakamoto, K., *Infrared and Raman Spectra of Inorganic and Coordination Compounds*; Wiley Online Library, **1986**.
72. Huheey, J. E.; Keitler, E.; Keitler, R., Inorganic Chemistry, Principles of Structure and Bonding. Harper Collins College Publishers, New York: **1993**.
73. Frenking, G.; Fröhlich, N., The Nature of the Bonding in Transition-Metal Compounds. *Chem. Rev.* **2000**, *100*, 717-774.

2. EXPERIMENTAL METHODS AND SETUP

2.1 Fourier Transform Ion Cyclotron Resonance Mass Spectrometry

The functional principle of the cyclotron was first described in the 1930's by Lawrence.[1-3] It has been the basis for the development of modern ion cyclotron resonance (ICR) mass spectrometers since 1949.[4] An enormous performance increase became possible by the introduction of Fourier Transform Mass Spectrometry (FT-MS) in 1974 by Comisarow and Marshall[5-6] and the combination of FT-ICR devices with superconducting magnets.[7-9]

The most important component of an ICR mass spectrometer is the ion trap (ICR cell, or Penning trap), which is located in a strong homogeneous magnetic field. This field is used to trap the ions on circular paths in the ion trap. They undergo two opposing forces, the Lorentz and the Centrifugal force:

$$F_L = qv_{xy}B \qquad \text{(Eq. 2.1)}$$

$$F_{cf} = \frac{mv_{xy}^2}{r} \qquad \text{(Eq. 2.2)}$$

F_L	*Lorentz force*
F_{cf}	*Centrifugal force*
q	*charge of the ion ($q = z \cdot e$)*
z	*number of charges*
e	*elementary charge*
v_{xy}	*velocity of the ion in the xy plane*
B	*magnetic field*
m	*ion mass*
r	*radius of the ion's orbit*

If the ions are in balance on these trajectories, they experience an angular velocity ω_c. The cyclotron frequency f_c is proportional to the mass to charge (m/z) ratio but independent of the initial ion velocity in the xy-plane.

$$\omega_c = 2\pi f_c = \frac{v_{xy}}{r} = \frac{q}{m}B \qquad \text{(Eq. 2.3)}$$

$$f_c = \frac{qB}{2\pi m} \qquad \text{(Eq. 2.4)}$$

An ICR cell typically consists of at least six plates (Fig. 2.1). The two excitation plates are facing each other and provide the radio frequency for the alternating electric field. A frequency sweep is applied to the excitation plates to accelerate the ions. As a result, their orbits increase while they retain their specific cyclotron frequency. The spectrum is recorded by measuring an image current induced in the two detection plates when the ions pass by the plates. The cell also has a front and a back plate for trapping. The ions enter the cell through the front plate and are trapped along the z-axis by an electrostatic field.

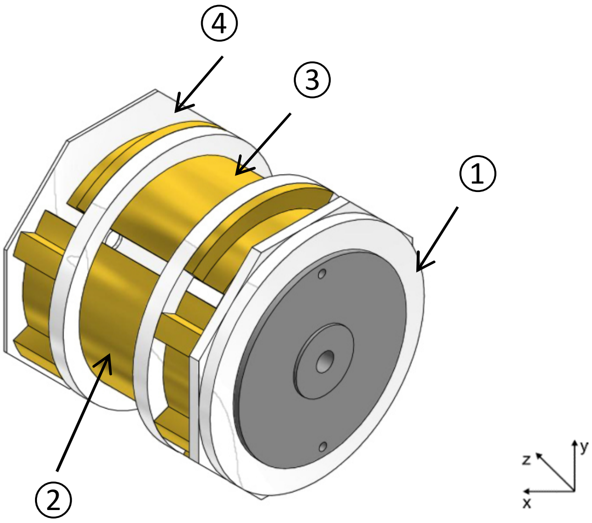

Figure 2.1.[10] Sketch of an ICR cell (design: Bruker Infinity Cell™): (1) front trapping plate, (2) excitation plate, (3) detection plate, (4) back trapping plate.

The movement of the ions in the trap is composed of several components: the axial movement, which is called trapping motion with the frequency ω_z, the radial movement (superposition of the modified cyclotron movement) with the frequency ω_+ and the mass independent magnetron motion with the frequency ω_- (Fig. 2.2). The frequencies of the ionic movements are determined by the trapping parameters, i.e the magnetic field strength B, the trapping potential U_{dc} and the dimension d of the trap, as follows:

$$\omega_z = \sqrt{\frac{qU_{dc}}{md^2}} \qquad \text{(Eq. 2.5)}$$

$$\omega_- \approx \frac{\omega_z^2}{2\omega_c} = \frac{U_{dc}}{2d^2B} \qquad \text{(Eq. 2.6)}$$

$$\omega_+ \approx \omega_c - \frac{\omega_z^2}{2\omega_c} = \omega_c - \frac{U_{dc}}{2d^2 B} \qquad \text{(Eq. 2.7)}$$

$$\omega_- < \omega_z < \omega_+ \qquad \text{(Eq. 2.8)}$$

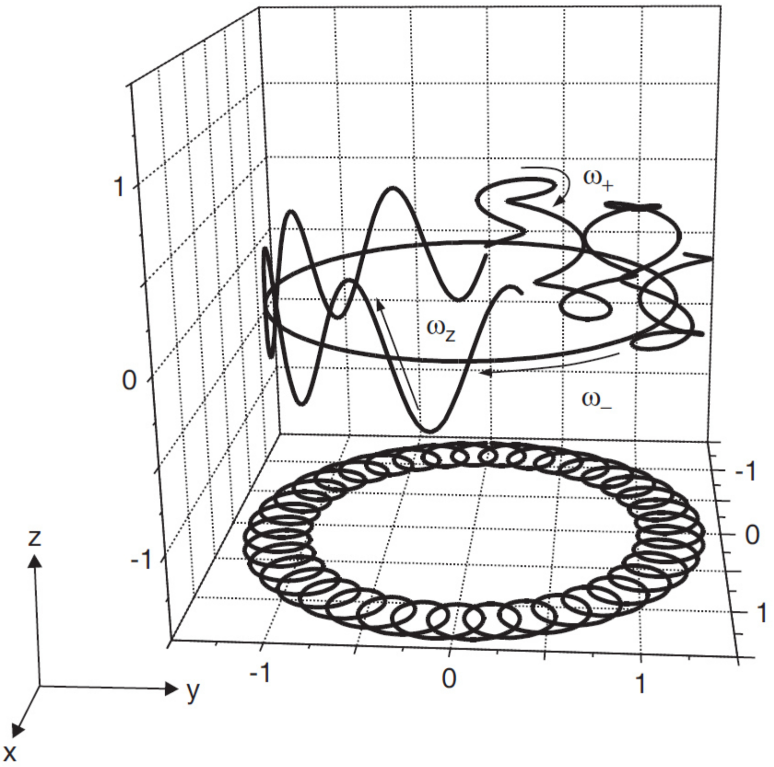

Figure 2.2.[11] Representation of the ion motions within an ICR cell, the resulting form of the trajectory during the capture process and its projection on the xy-plane.

2.2 The FRITZ Setup

The “FRITZ” setup is a modified Fourier Transform Ion Cyclotron Resonance mass spectrometer. It is based on a commercially purchased Bruker *Apex Ultra* FT-ICR. Modifications present as an electrostatic quadrupole ion beam bender for multiple source attachments, in this setup the Laser VAPorization (LVAP) cluster ion source and the ElectroSpray Ionization (ESI) source. The FRITZ setup also contains two cryogenically cooled ion traps, the hexapole collision cell and the ICR cell (Fig. 2.3). In our experiments the hexapole serves as ion trap for kinetic investigations and the ICR cell serves as ion trap, mass separator and mass analyzer at once.

In order to carry out measurements in the low-temperature range, the mass spectrometer was equipped with two cryostats. The hexapole collision cell is located in the high vacuum region on the axis of the magnetic field. The trap is connected to the second stage of a 4 K two-stage closed cycle He cryostat (Sumitomo SRDK-101E, compressing unit HC4E). The temperature is monitored by two temperature sensors (LakeShore, Cernox™ CX-1050-CO-HT-P-1.4M, calibrated from 1.4 – 420 K), one on each cooling stage. Temperature adjustment is achieved by heating resistors (Catridge Heater, Janis Research, R = 50 Ω), controlled and monitored by a temperature controller (LakeShore, Model 336).

The ICR cell is located in the high field region (B = 7 T) of a superconducting solenoid. The trap is connected to a 10 K two-stage closed cycle He cryostat (Sumitomo SRDK-408S2, compressing unit W-71D). Shielding for radiative heating of the trap is achieved by two actively cooled and three passive shielding tubes.[12] Three temperature sensors (LakeShore, Cernox™, calibrated from 4 – 325 K) distributed over the cryogenic setup monitor the temperature within the ultra-high vacuum region.

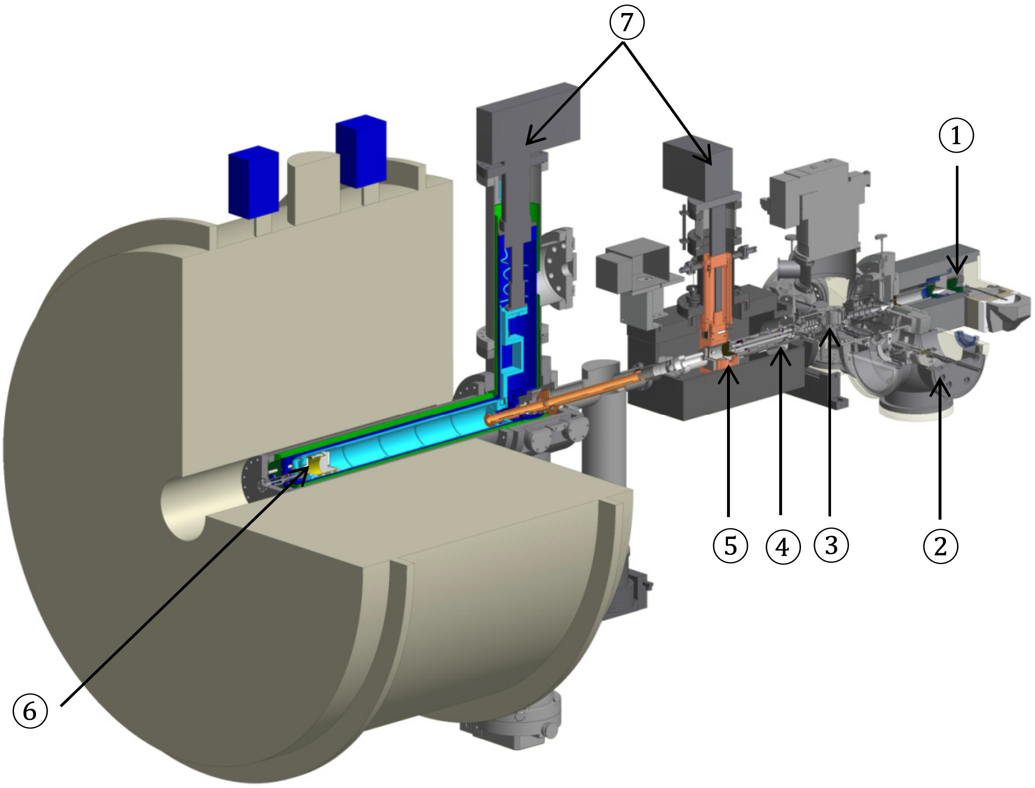

Figure 2.3.[10] Schematic drawing of the FRITZ setup, a modified FT-ICR mass spectrometer. Here, the ESI source (1) is shown on the magnetic field axis. In the actual setup the ESI source is located at a 90 ° angle to the magnetic field axis, opposing the LVAP cluster ion source (2). The ions are bend on the magnetic field axis by the quadrupole ion beam bender (3), mass selected in a quadrupole mass filter (4), stored in the hexapole collision cell (5) and transferred to the ICR cell (6). Both ion traps are cryogenically cooled by two stage-closed cycle He cryostats (7).

Two ion sources are attached for the investigation of a wide range of transition metal containing ions (*cf.* Fig. 2.4). In addition to a commercially available ESI source (Bruker Daltonics, Apollo II), a homebuilt LVAP source serves for the generation of bare metal clusters. Both ion sources are connected by a homebuilt gate valve which allows for the independent operation of the individual vacuum systems, respectively. The ions are guided into a homebuilt electrostatic quadrupole ion beam bender by several ion optics, attached to the gate valves. The ion beam produced by either one of the ion sources is bent by 90 ° onto the magnetic field axis and transferred into the first ion trap, the hexapole collision cell. A linear quadrupole mass filter prior to this trap serves for mass selection. Reaction and/or collision gas is injected into the ion trap by either a pulsed or a leak valve. After a variable storage time (usually 0 – 30 s), the accumulated ions are transferred to the ICR cell.

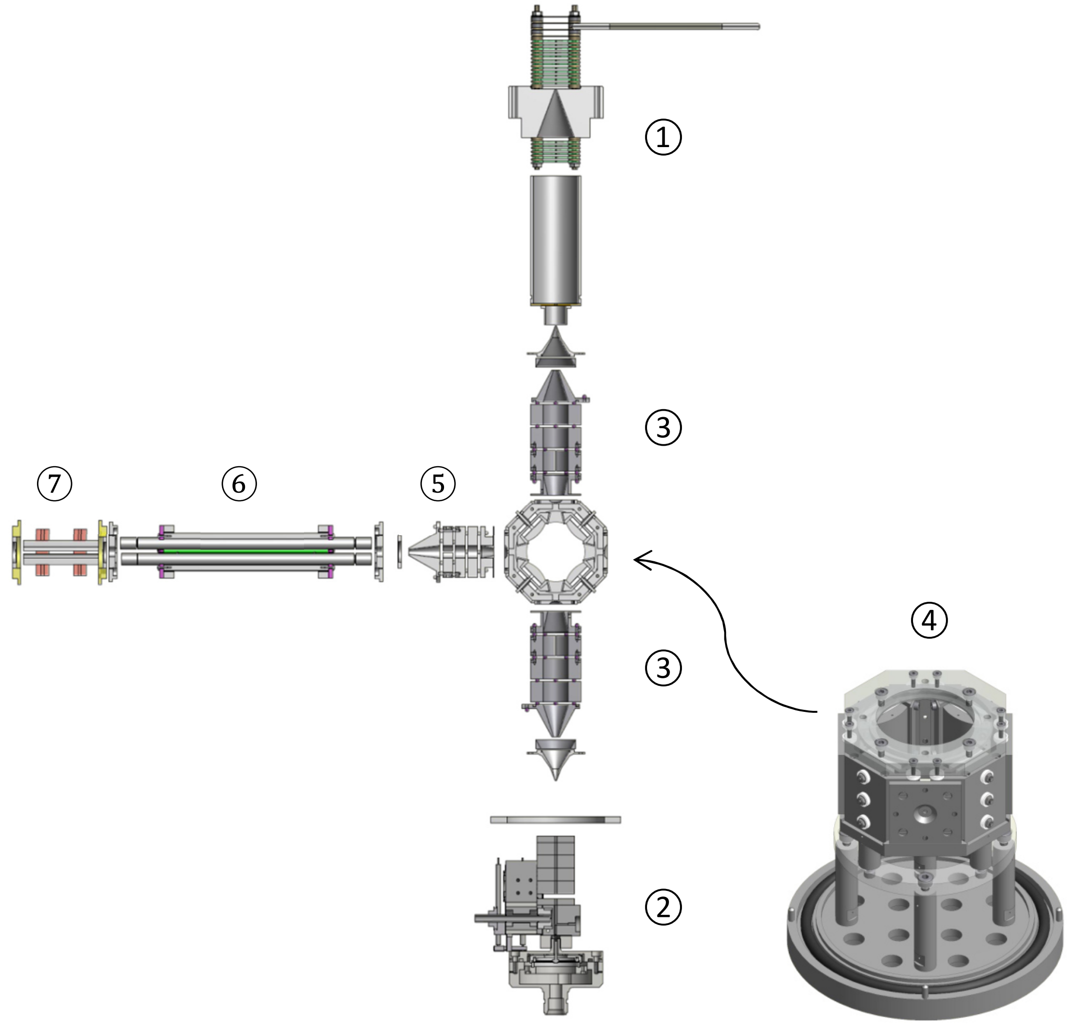

Figure 2.4. Sketch of the ion sources and respective ion optics up to the cryogenically cooled hexapole collision cell: (1) ESI source, (2) LVAP cluster ion source, (3) and (5) ion optics, (4) ion beam bender, (6) quadrupole mass filter, (7) hexapole collision cell.

Electrospray Ionization (ESI) Source

Electrospray ionization mass spectrometry has become one of the most important techniques in modern mass spectrometry.[13-15] The electrospray ionization is a gentle process to transfer ions from solution into the gas phase. Electrospray as a method to nebulize a liquid sample by means of an electric field is a known technique. The underlying physical effect was first described in 1964 by Taylor.[16] Only a few years later Dole speculated on the generation of molecular beams of large molecules using this technique.[17] In the 1980s Fenn and his group succeeded in transferring large molecules as ions into the gas phase without destroying them[18-20] and the importance of this achievement was underlined by the bestowal of the Nobel-Prize to John Fenn in 2002.[21] The fundamentals of ESI ion formation can be found in the literature.[20, 22-24] Next to proteins with a very high mass to charge ratio,[25-27] ESI is also very efficient in creating ionic species of smaller transition metal adsorbate complexes,[28-30] which will be investigated in the course of this study.

We use a commercially available ESI source (Bruker Daltonics, Apollo II, *cf.* Fig. 2.5). The dissolved sample is introduced through the nebulizer assembly into the spray chamber, where it is subject to the ESI process by means of an electrical field between the inner chamber wall and the spray shield.

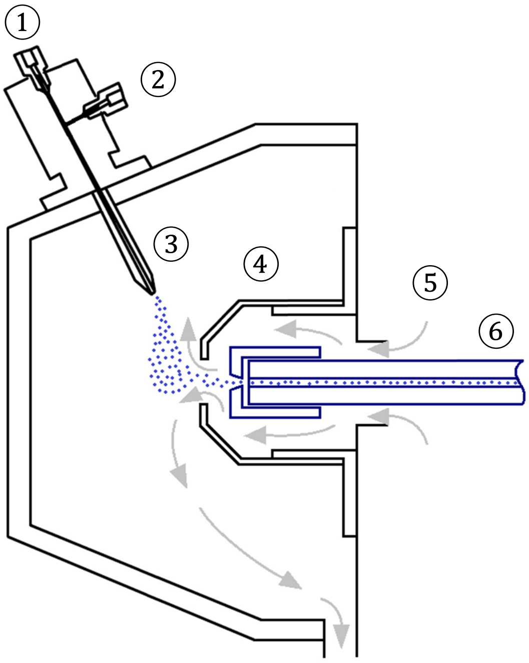

Figure 2.5.[31] Schematic drawing of the *Bruker Apollo II* ESI source chamber and transfer. (1) sample inlet, (2) nebulizer gas inlet, (3) spray needle, (4) spray shield, (5) dry gas flow, (6) glass capillary.

Hamilton™ gas tight syringes (0.5 ml) placed in an automated syringe pump serve to inject the sample solution (~ 1 x 10^{-4} mol/l) into the spray needle through a peak capillary. Heated drying gas (N_2, 220 °C) facilitates the evaporation of solvent molecules. The ions enter the vacuum chamber through a dielectric glass capillary (Ø 0.5 mm, length 160 mm). The capillary is coated with platinum at both ends to apply an additional transfer gradient. From the capillary exit the ions are deflected into the first of two ion funnels, with the assistance of a deflector. The entrance of the first ion funnel is biased with 150 V. Along the length of this first funnel the voltage is dropped from 150 V down to its last element - skimmer 1 – at 30 V forming an electric field, which pushes the ions in forward direction. At the same time the RF field applied to the first funnel together with collisions helps focusing the ions to pass through the aperture of skimmer 1. By increasing the skimmer 1 voltage, so-called in source collision induced dissociation (in source CID) can be achieved. After passing skimmer 1 the ions enter a second funnel leading to skimmer 2. Passing through the second skimmer, the ions enter the source hexapole, which can be used to accumulate ions between skimmer 2 and the extract electrode of the hexapole.

Laser Vaporization (LVAP) Cluster Ion Source

Within the FRITZ setup, the investigated cationic transition metal clusters are produced by a homebuilt LVAP cluster ion source.[32-33] The major components of this source are a homebuilt piezo electric valve,[34] an expansion/ interaction region and an expansion channel (Fig 2.6).

Within the interaction region, the second harmonic (532 nm) of a Nd:YAG laser (Innolas, Spitlight300, 20 Hz) is focused on a rotating foil comprising of the metal of interest. The thickness of this foil varies between 0.1 and 0.5 mm. The laser pulse creates a plasma at the surface of the rotating metal foil. This plasma contains neutral atoms as well as cationic and anionic species. A homebuilt piezo electric valve creates a transverse He gas pulse, which captures the hot plasma. The valve operates with a backing pressure of 15 – 20 bar, a repetition rate of 20 Hz and an opening time of approximately 40 µs. The gas pulse expands into a vacuum chamber with a pressure of about 3 x 10^{-7} mbar raising this pressure up to 2 x 10^{-4} mbar. The expanding gas cools down the atoms and ions created in the plasma and cluster formation starts. Cluster formation completes within the expansion channel. Clusters in the size range of 2 to 40 atoms per cluster are created. Variation of backing pressure, valve opening time and laser-valve-delay serves to influence the intensity maximum in the created cluster size distribution. The cluster charge state of choice is selected by applying according voltages to extract the ionic clusters from the source region.

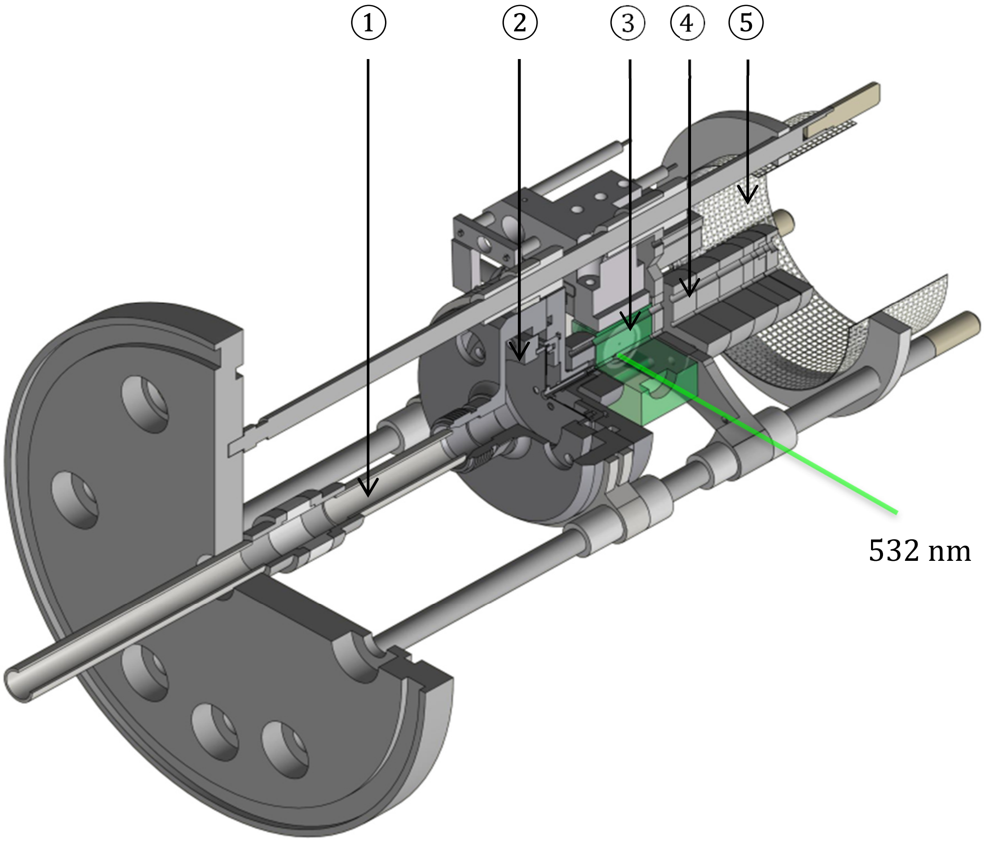

Figure 2.6.[10] Schematic drawing of the LVAP source: (1) gas inlet, (2) piezoelectric valve, (3) expansion/interaction region, (4) expansion channel, (5) mesh.

The cobalt foil was purchased form Alfa Aesar (purity 99.95 %). Iron and nickel foils were purchased as mono isotopic materials from Oak Ridge National Lab (Fe-56, purity 99.93 %; Ni-58, purity 99.61 %).

2.3 Isothermal Cryo Kinetics of Cationic Transition Metal Clusters

We investigate the stepwise N_2 adsorption on size selected transition metal clusters at cryogenic temperatures (30 K and below). The ions are generated within the LVAP source and transferred into the cryogenically cooled hexapole collision cell (Fig. 2.8). Buffer and reaction gas are introduced continuously. Sufficient nitrogen attachment is achieved by increasing the pressure in the ion trap up to 5.0×10^{-7} mbar. Additional He is introduced to accomplish an efficient trapping and cooling of the ions.

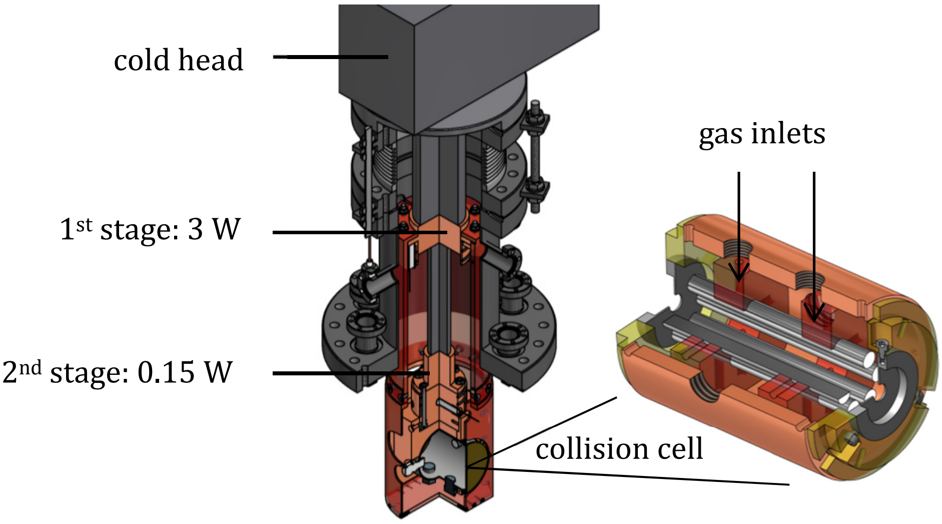

Figure 2.8. Sketch of the modified hexapole collision cell. Separate gas inlets ensure the connection of pre-cooled and warm gas lines.

After storing the mass-selected ions for a variable time (0 – 30 s), the manipulated ions of the form $[M_n(N_2)_m]^+$ are guided by electrostatic lenses into the FT-ICR cell. A reaction can be proven by the appearance of additional masses in the mass spectrum and simultaneous decrease of the intensity of the former parent ion.

Relative Rate Constants

Multiple mass spectra are recorded while varying the reaction delay (ion storage time in the hexapole collision cell). For kinetic investigations the ICR cell serves for the detection of the formed $[M_n(N_2)_m]^+$ cluster adsorbate complexes. The ICR cell is held at temperatures below 10 K to prevent heating of the clusters by black body radiation prior to ion detection. The kinetic curves of cationic TM clusters and their nitrogen adducts originate from reaction delay scans and subsequent evaluation of the recorded mass spectra. Fits to pseudo-first-order-kinetics occur through the “evofit” program.[35] Fitting the experimental kinetics implies the quantitative determination of relative rate constants for N_2 adsorption for each step m → m+1, and for N_2 desorption for each step m+1 → m alike:

$$[M_n(N_2)_m]^+ + N_2 \underset{k_{-(n,m+1)}}{\overset{k_{(n,m)}}{\rightleftarrows}} [M_n(N_2)_{m+1}]^+ \qquad \text{(Eq. 2.9)}$$

Absolute Rate Constants

The classical Langevin collision rate of ions with neutrals[36] is conveniently extended towards polar molecules by the average dipole orientation theory (ADO).[37-38] The ADO theory gives the theoretical limit of the absolute rate constants, the collision rate k_{ADO}, based on a classical trajectory of a linear dipole in the field of a point charge:

$$k_{ADO} = \frac{q}{2\varepsilon_0\sqrt{\mu}}\left(\sqrt{\alpha} + c\mu_D\sqrt{\frac{2}{\pi k_B T}}\right) \qquad \text{(Eq. 2.10)}$$

μ is the reduced mass (of the cluster adsorbate complex), α is the polarizability and μ_D is the dipole moment (in Debye). The parameter c lies between 0 and 1, and can be expressed by the polarizability volume α'and μ_D.[39]

This ADO theory is frequently used to calculate the reaction rates of charged clusters with small molecules, knowingly underestimating the reaction rates for charged metal clusters significantly.[33, 40-41] Kummerlöwe and Beyer introduced two models for calculating the collision rates of ionic clusters with neutral molecules, the hard sphere average dipole orientation model (HSA) and the surface charge capture (SCC) model.[42] In both models, the cluster and the neutral reaction partner are treated as hard spheres, and the charge is treated as point charge. For the HSA collision rate k_{HSA}, the charge is located in the center of the cluster, while in the SCC model (k_{SCC}), the charge is drawn to the cluster surface by the attractive interaction with the neutral collision partner.

The relative rate constants $k_{(n,m)}$ determine the absolute rate constants $k_{(n,m)}^{abs}$, the absolute collision gas number densities $\rho_{N2}(T)$ serving as the conversion factor:

$$k_{(n,m)}^{abs} = k_{(n,m)}/\rho_{N2}(T) \qquad \text{(Eq. 2.11)}$$

We obtain approximate values for $\rho_{N2}(T)$ indirectly from the pressure in the surrounding chamber $p_c^{(300\,K)}$ and an effective geometry factor c_{app}:

$$\rho_{N2}(26\,K) = \frac{c_{app}p_c^{300\,K}}{k_B T_{300\,K}} \qquad \text{(Eq. 2.12)}$$

The geometry factor c_{app} shows to bear a significant dependence on the temperature of the hexapole ion trap. By numerous kinetic studies of transition metal cluster cations with neutral reactants at cryogenic temperatures we evaluated this factor c_{app} to 1.8 ± 0.4 at 26 K with a net uncertainty of ± 50%. The quotient of the absolute rate constants and the collision rate enables us to calculate the absolute reaction efficiency γ for the adsorption of N_2 by transition metal clusters. This absolute reaction efficiency indicates the probability of a reaction occurring after a collision between a transition metal cluster ion and its reaction partner.

$$\gamma = \frac{k_{abs}}{k_{coll}} \qquad \text{(Eq. 2.13)}$$

Note that the case of N_2 adsorption makes reaction efficiencies equivalent to sticking probabilities as defined in conjunction with surface science.

2.4 Infrared Multiple Photon Dissociation

Direct absorption measurements on transition metal (TM) cluster complexes in the gas-phase are difficult due to the low number densities of typical ion experiments which do not provide for sufficient optical density. More elaborate schemes of indirect detection of photonic absorptions have been developed, such as so-called consequence or action spectroscopy.[43-45] The InfraRed Multiple Photon Dissociation (IR-MPD) is one of these advanced techniques.[46-47] The IR absorption spectrum can be reconstructed by recording the photo induced fragmentation yield as a function of photon frequency. IR-MPD experiments on gas-phase species were initially performed in a limited spectral range (~ 900 – 1100 cm^{-1}) using line-tunable CO_2 lasers.[48-50] It has proven helpful to study the vibrational modes of adsorbates on transition metal clusters and in TM coordination complexes as isolated ions by IR-MPD.[51-54] This method has further gained by the introduction of tunable free electron lasers (FEL).[55-57] Cryo IR-action spectroscopy achieves significant advances by so called tagging or messenger techniques where weakly bound species serve to provide for a preferred fragmentation channel, sometimes driven by single photon absorption.[58-59] IR-MPD bears the intrinsic risk of power broadening, either by the use of free electron lasers or of table top Optical Parametric Oscillator/Amplifier (OPO/OPA) systems.[53, 55, 60-62]

Optical Parametric Oscillator / Amplifier (OPO/OPA)

An optical parametric oscillator (OPO) is a coherent light source consisting of an optical resonator and a nonlinear optical crystal. It is based on the optical gain from parametric amplification in this crystal, rather than from stimulated emission.[63-64] Nonlinear optical crystals provide for the generation of second-harmonic frequencies (or higher).[65] The crystal allows for the conversion of an intense laser wave of one frequency into two output waves (signal and idler waves) by means of second order nonlinear optical interaction. The wave with the higher frequency is called signal. The outgoing waves are influenced by the heat and refraction index of the crystal. A tunable laser output is achieved by changing the angle of the crystal according to the axis of the incident light.[66] An optical parametric amplifier (OPA) allows for the amplification of the idler wave from the output of the OPO.

Within this work, a *Dean Guyer* OPO/OPA (LaserVision) laser systems has been used to convert the fundamental (1064 nm) of a pulsed injection seeded Nd^{3+}:YAG laser (Continuum-PL8000; 10 Hz) into tunable IR radiation (Fig. 2.9). A beam splitter separates the incoming pump beam into two beam lines. One third of the original intensity is frequency doubled (532 nm), and the resulting wave serves as input for the OPO resonator. The resonator contains two potassium titanyl phosphate (KTP) crystals, which convert the 532 nm wave into a signal 1 and an idler 1 wave. A silicon filter separates the higher energetic signal 1 wave, while the remaining idler 1 wave serves as input for the amplifier. Within the OPA the idler 1 wave is recombined with the residual two thirds of the original 1064 nm pump wave.

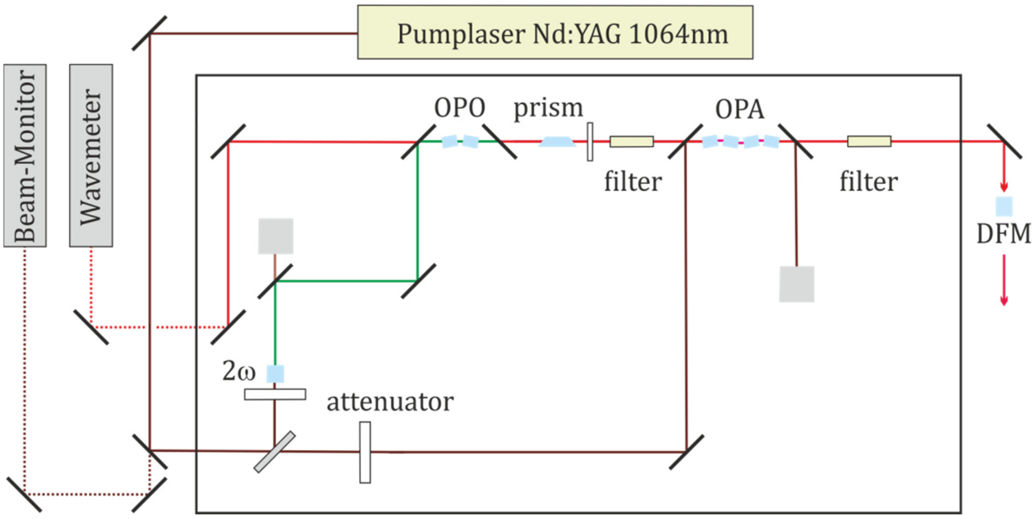

Figure 2.9. Scheme of the LaserVision broadband OPO/OPA laser system. Lines indicate the pathway of the incoming and arrows of the outcoming laser beam.

The OPA consists of four potassium titanyl arsenate (KTA) crystals. During the amplification process, the original pump wave is converted into a signal 2 and an idler 2 wave. The idler wave of the OPO output (idler 1) determines the wavelength of the signal 2 wave (Fig. 2.10).

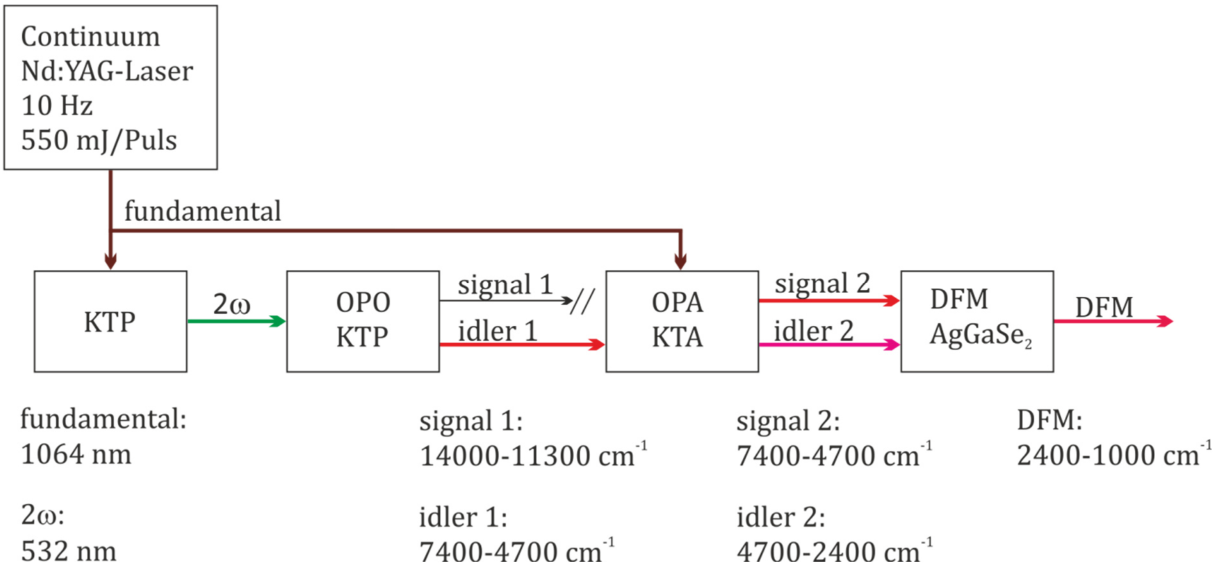
Continuum
Nd:YAG-Laser
10 Hz
550 mJ/Puls
fundamental
KTP
2ω
OPO
KTP
signal 1
idler 1
OPA
KTA
signal 2
idler 2
DFM
AgGaSe$_2$
DFM
fundamental:
1064 nm
2ω:
532 nm
signal 1:
14000-11300 cm^{-1}
idler 1:
7400-4700 cm^{-1}
signal 2:
7400-4700 cm^{-1}
idler 2:
4700-2400 cm^{-1}
DFM:
2400-1000 cm^{-1}

Figure 2.10. Schematic representation of the stepwise frequency conversion process of the LaserVision OPO/OPA laser system. A potassium titanyl phosphate (KTP) crystal serves for second harmonic generation (2ω). Two additional KTP crystals serve for the optical parametric oscillator (OPO) process. Four potassium titanyl arsenate (KTA) crystals serve for the optical parametrical amplification (OPA) process. Difference frequency mixing (DFM) is achieved by the $AgGaSe_2$ crystal.

The spectral range of the resulting idler 2 is between 2400 and 4700 cm^{-1}, the resulting signal 2 exhibits a range from 4700 – 7400 cm^{-1}. Since these two waves exhibit different polarizations, a suitable filter can be used to separate them. If those two waves are recombined within a difference frequency mixing (DFM) crystal ($AgGaSe_2$) a spectral range from 1000 – 2400 cm^{-1} is accessible. The OPO/OPA output provides energy up to 15 mJ/pulse. Using the DFM, the power is much lower (approximately 1 - 2.5 mJ/pulse). The intensity of the OPO/OPA output is controlled by a variable attenuator (λ/2-plates) in the light path of the linear polarized 1064 nm beam, respectively.

The LaserVision KTP/KTA optical parametric oscillator/amplifier system pumped by a 10 Hz injection seeded Nd^{3+}:YAG laser provides tunable IR radiation in the range of 1000 and 7400 cm^{-1}.

2.5 Computational Methods

The comparison of experimental data with quantum chemical calculations has become inevitable. Much effort has been spent in the computational prediction of molecular properties. One approach for modeling the electronic ground state properties of many-body systems is the density functional theory (DFT),[67-69] which is based on the electron density in the ground state. During the calculations the geometry of the molecule is energy optimized. Not only characteristic atom-atom bond lengths or angles can be extracted out of the geometry, also vibrational spectra can be predicted.

The idea of using the electron density as the basic variable for the description of a molecules' energy goes back to the approximations of Thomas[70] and Fermi[71] in the 1920's. DFT was first placed on a solid theoretical basis with the introduction of two theorems by Hohenberg and Kohn.[72] In 1964, they argued that the ground state properties of a many-body system with N electrons are uniquely determined by the position-dependent electron density. Through the use of functionals of the electron density, the many-body problem of N electrons with $3N$ spatial coordinates reduces to 3 spatial coordinates. Only one year later, Kohn and Sham demonstrated that the electron density of an interacting system could be obtained from simple one-electron theory.[73] Instead of solving the Schrödinger equation for the whole N particle system, N one-electron Schrödinger equations are solved, the Kohn-Sham equations. The exchange-correlation (XC) term can e.g. be approached by the local density approximation (LDA), in which the density at a local point is assumed to be uniform. The generalized gradient approximation (GGA) on the other hand incorporates the local change in density. The use of hybrid functionals – combining GGA methods with partially calculating exchange energy according to the Hartree-Fock-formalism – has become very popular. Despite the longer calculation effort the results are more precise.

Within this work, all energetic and structural calculations were performed using the ECCE (Extensible Computational Chemistry Environment) interface[74] to submit and monitor calculations running with the Gaussian 09 program package.[75] The specific use of basis sets and functionals will be indicated within the according chapters. The calculations were gratefully performed on the computing clusters of the TU Kaiserslautern, which are under the supervision of the group of Prof. Ch. vanWüllen.

2.6 References

1. Lawrence, E. O.; Edlefsen, N. E., On the Production of High Speed Protons. *Science* **1930**, *72*, 376-377.
2. Lawrence, E. O.; Livingston, M. S., The Production of High Speed Light Ions without the Use of High Voltages. *Physical Review* **1932**, *40*, 19-35.
3. Lawrence, E. O.; Cooksey, D., On the Apparatus for the Multiple Acceleration of Light Ions to High Speeds. *Physical Review* **1936**, *50*, 1131-1140.
4. Sommer, H.; Thomas, H. A.; Hipple, J. A., The Measurement of E/M by Cyclotron Resonance. *Physical Review* **1951**, *82*, 697-702.
5. Comisarow, M. B.; Marshall, A. G., Frequency-Sweep Fourier Transform Ion Cyclotron Resonance Spectroscopy. *Chemical Physics Letters* **1974**, *26*, 489-490.
6. Comisarow, M. B.; Marshall, A. G., Fourier-Transform Ion-Cyclotron Resonance Spectroscopy. *Chemical Physics Letters* **1974**, *25*, 282-283.
7. Amster, I. J., Fourier Transform Mass Spectrometry. *Journal of Mass Spectrometry* **1996**, *31*, 1325-1337.
8. Marshall, A. G., Milestones in Fourier Transform Ion Cyclotron Resonance Mass Spectrometry Technique Development. *International Journal of Mass Spectrometry* **2000**, *200*, 331-356.
9. Smith, R. D., Evolution of Esi–Mass Spectrometry and Fourier Transform Ion Cyclotron Resonance for Proteomics and Other Biological Applications. *International Journal of Mass Spectrometry* **2000**, *200*, 509-544.
10. Kolling, T.; Kampschulte, H., T. K. Autodesc Inventor(R)
11. Blaum, K., High-Accuracy Mass Spectrometry with Stored Ions. *Physics Reports* **2006**, *425*, 1-78.
12. Kampschulte, H., Entwicklung Einer Tieftemperatur FT-ICR Zelle Und Ihre Charakterisierung Mittels Reaktionskinetiken Und Synchrotron-Spektroskopie. *Doctoral Thesis*, **2010**.
13. Rossi, D. T.; Sinz, M., *Mass Spectrometry in Drug Discovery*; CRC Press, 2001.
14. Ardrey, R. E., *Liquid Chromatography-Mass Spectrometry: An Introduction*; John Wiley & Sons, **2003**.
15. Schalley, C. A., The Expanding Role of Mass Spectrometry in Biotechnology Gary Siuzdak. *Journal of the American Society for Mass Spectrometry* **2004**, *15*, 625-625.
16. Taylor, G., Disintegration of Water Drops in an Electric Field. *Proceedings of the Royal Society of London. Series A. Mathematical and Physical Sciences* **1964**, *280*, 383-397.
17. Dole, M.; Mack, L. L.; Hines, R. L.; Mobley, R. C.; Ferguson, L. D.; Alice, M. B., Molecular Beams of Macroions. *The Journal of Chemical Physics* **1968**, *49*, 2240-2249.
18. Yamashita, M.; Fenn, J. B., Electrospray Ion Source. Another Variation on the Free-Jet Theme. *The Journal of Physical Chemistry* **1984**, *88*, 4451-4459.
19. Yamashita, M.; Fenn, J. B., Negative Ion Production with the Electrospray Ion Source. *The Journal of Physical Chemistry* **1984**, *88*, 4671-4675.
20. Fenn, J. B.; Mann, M.; Meng, C. K.; Wong, S. F.; Whitehouse, C. M., Electrospray Ionization for Mass Spectrometry of Large Biomolecules. *Science (New York, N.Y.)* **1989**, *246*, 64-71.
21. Fenn, J. B., Electrospray Wings for Molecular Elephants (Nobel Lecture). *Angewandte Chemie International Edition* **2003**, *42*, 3871-3894.
22. Fenn, J. B.; Mann, M.; Meng, C. K.; Wong, S. F.; Whitehouse, C. M., Electrospray Ionization–Principles and Practice. *Mass Spectrometry Reviews* **1990**, *9*, 37-70.

23. Schalley, C. A.; Armentrout, P. B., *Modern Mass Spectrometry*; Springer Science & Business Media, **2003**; Vol. 225.
24. Gross, J. H., *Mass Spectrometry: A Textbook*; Springer Science & Business Media, **2004**.
25. Schalley, C. A., Supramolecular Chemistry Goes Gas Phase: The Mass Spectrometric Examination of Noncovalent Interactions in Host–Guest Chemistry and Molecular Recognition. *International Journal of Mass Spectrometry* **2000**, *194*, 11-39.
26. Cristoni, S.; Bernardi, L. R., Development of New Methodologies for the Mass Spectrometry Study of Bioorganic Macromolecules. *Mass spectrometry reviews* **2003**, *22*, 369-406.
27. Heck, A. J.; van den Heuvel, R. H., Investigation of Intact Protein Complexes by Mass Spectrometry. *Mass spectrometry reviews* **2004**, *23*, 368-389.
28. Colton, R.; D'Agostino, A.; Traeger, J. C., Electrospray Mass Spectrometry Applied to Inorganic and Organometallic Chemistry. *Mass Spectrometry Reviews* **1995**, *14*, 79-106.
29. Traeger, J. C., Electrospray Mass Spectrometry of Organometallic Compounds. *International Journal of Mass Spectrometry* **2000**, *200*, 387-401.
30. Menges, F. Structure and Reactivity of Isolated Mononuclear and Oligonuclear Metal Complexes. *Doctoral Thesis*, **2013**.
31. Apollo II – Mtp Users Manual. Bruker Daltonics GmbH: **2006**; p 11.
32. Maruyama, S.; Anderson, L. R.; Smalley, R. E., Direct Injection Supersonic Cluster Beam Source for FT-ICR Studies of Clusters. *Review of scientific instruments* **1990**, *61*, 3686-3693.
33. Berg, C.; Schindler, T.; Niedner-Schatteburg, G.; Bondybey, V. E., Reactions of Simple Hydrocarbons with Nb+ N: Chemisorption and Physisorption on Ionized Niobium Clusters. *The Journal of Chemical Physics* **1995**, *102*, 4870-4884.
34. Proch, D.; Trickl, T., A High-Intensity Multi-Purpose Piezoelectric Pulsed Molecular Beam Source. *Review of Scientific Instruments* **1989**, *60*, 713-716.
35. Graf, M., *Diploma Thesis, TU Kaiserslautern* **2006**, *(unpublished)*.
36. Langevin, M. In *Une Formule Fondamentale De Théorie Cinétique*, Annales de chimie et de physique, Series, **1905**; pp 245-288.
37. Su, T.; Bowers, M. T., Theory of Ion-Polar Molecule Collisions. Comparison with Experimental Charge Transfer Reactions of Rare Gas Ions to Geometric Isomers of Difluorobenzene and Dichloroethylene. *The Journal of Chemical Physics* **1973**, *58*, 3027-3037.
38. Su, T.; Bowers, M. T., Ion-Polar Molecule Collisions. Proton Transfer Reactions of H3+ and CH5+ to the Geometric Isomers of Difluoroethylene, Dichloroethylene, and Difluorobenzene. *Journal of the American Chemical Society* **1973**, *95*, 1370-1373.
39. Su, T.; Bowers, M. T., Ion-Polar Molecule Collisions: The Effect of Ion Size on Ion-Polar Molecule Rate Constants; the Parameterization of the Average-Dipole-Orientation Theory. *International Journal of Mass Spectrometry and Ion Physics* **1973**, *12*, 347-356.
40. Balteanu, I.; Balaj, O. P.; Fox-Beyer, B. S.; Rodrigues, P.; Barros, M. T.; Moutinho, A. M. C.; Costa, M. L.; Beyer, M. K.; Bondybey, V. E., Size- and Charge-State-Dependent Reactivity of Azidoacetonitrile with Anionic and Cationic Rhodium Clusters Rhn±. *Organometallics* **2004**, *23*, 1978-1985.

41. Anderson, M. L.; Ford, M. S.; Derrick, P. J.; Drewello, T.; Woodruff, D. P.; Mackenzie, S. R., Nitric Oxide Decomposition on Small Rhodium Clusters, Rh N+. *The Journal of Physical Chemistry A* **2006**, *110*, 10992-11000.
42. Kummerlöwe, G.; Beyer, M. K., Rate Estimates for Collisions of Ionic Clusters with Neutral Reactant Molecules. *International Journal of Mass Spectrometry* **2005**, *244*, 84-90.
43. Woodin, R. L.; Bomse, D. S.; Beauchamp, J. L., Multiphoton Dissociation of Molecules with Low Power Continuous Wave Infrared Laser Radiation. *Journal of the American Chemical Society* **1978**, *100*, 3248-3250.
44. Bomse, D. S.; Woodin, R. L.; Beauchamp, J. L., Molecular Activation with Low-Intensity Cw Infrared Laser Radiation. Multiphoton Dissociation of Ions Derived from Diethyl Ether. *Journal of the American Chemical Society* **1979**, *101*, 5503-5512.
45. Okumura, M.; Yeh, L. I.; Lee, Y. T., The Vibrational Predissociation Spectroscopy of Hydrogen Cluster Ions. *The Journal of Chemical Physics* **1985**, *83*, 3705-3706.
46. MacAleese, L.; Maître, P., Infrared Spectroscopy of Organometallic Ions in the Gas Phase: From Model to Real World Complexes. *Mass Spectrometry Reviews* **2007**, *26*, 583-605.
47. Polfer, N. C., Infrared Multiple Photon Dissociation Spectroscopy of Trapped Ions. *Chemical Society Reviews* **2011**, *40*, 2211-2221.
48. Selegue, T. J.; Moe, N.; Draves, J. A.; Lisy, J. M., Gas Phase Solvation of Na+ with Methanol. *The Journal of chemical physics* **1992**, *96*, 7268-7278.
49. Buck, U., Structure and Dynamics of Small Size Selected Molecular Clusters. *The Journal of Physical Chemistry* **1994**, *98*, 5190-5200.
50. Rayner, D.; Lian, L.; Athanassenas, K.; Collings, B.; Fournier, R.; Mitchell, S.; Hackett, P., Ir Studies of Chemisorption on Molecular Surfaces: Ammonia on Silver Clusters. *Surface Review and Letters* **1996**, *3*, 649-654.
51. Duncan, M. A., Spectroscopy of Metal Ion Complexes: Gas-Phase Models for Solvation. *Annu. Rev. Phys. Chem.* **1997**, *48*, 69-93.
52. Duncan, M. A., Infrared Spectroscopy to Probe Structure and Dynamics in Metal Ion-Molecule Complexes. *Int. Rev. Phys. Chem.* **2003**, *22*, 407-435.
53. Walker, N. R.; Walters, R. S.; Duncan, M. A., Frontiers in the Infrared Spectroscopy of Gas Phase Metal Ion Complexes. *New Journal of Chemistry* **2005**, *29*, 1495-1503.
54. Roithova, J., Characterization of Reaction Intermediates by Ion Spectroscopy. *Chem. Soc. Rev.* **2012**, *41*, 547-559.
55. Oomens, J.; Sartakov, B. G.; Meijer, G.; von Helden, G., Gas-Phase Infrared Multiple Photon Dissociation Spectroscopy of Mass-Selected Molecular Ions. *International Journal of Mass Spectrometry* **2006**, *254*, 1-19.
56. MacAleese, L.; Maitre, P., Infrared Spectroscopy of Organometallic Ions in the Gas Phase: From Model to Real World Complexes. *Mass Spectrom. Rev.* **2007**, *26*, 583-605.
57. Schöllkopf, W.; Gewinner, S.; Junkes, H.; Paarmann, A.; von Helden, G.; Bluem, H.; Todd, A. M. M. In *The New IR and THz FEL Facility at the Fritz Haber Institute in Berlin*, **2015**; pp 95121L-95121L-13.
58. Kamrath, M. Z.; Garand, E.; Jordan, P. A.; Leavitt, C. M.; Wolk, A. B.; Van Stipdonk, M. J.; Miller, S. J.; Johnson, M. A., Vibrational Characterization of Simple Peptides Using Cryogenic Infrared Photodissociation of H-2-Tagged, Mass-Selected Ions. *J. Am. Chem. Soc.* **2011**, *133*, 6440-6448.

59. Wolk, A. B.; Leavitt, C. M.; Garand, E.; Johnson, M. A., Cryogenic Ion Chemistry and Spectroscopy. *Accounts of Chemical Research* **2014**, *47*, 202-210.
60. Valle, J. J.; Eyler, J. R.; Oomens, J.; Moore, D. T.; van der Meer, A. F. G.; von Helden, G.; Meijer, G.; Hendrickson, C. L.; Marshall, A. G.; Blakney, G. T., Free Electron Laser-Fourier Transform Ion Cyclotron Resonance Mass Spectrometry Facility for Obtaining Infrared Multiphoton Dissociation Spectra of Gaseous Ions. *Review of Scientific Instruments* **2005**, *76*, 023103.
61. Lang, J.; Gaffga, M.; Menges, F.; Niedner-Schatteburg, G., Two-Color Delay Dependent Ir Probing of Torsional Isomerization in a [AgL1L2]+ Complex. *Physical Chemistry Chemical Physics* **2014**, *16*, 17417-17421.
62. Gaffga, M.; Munstein, I.; Müller, P.; Lang, J.; Thiel, W. R.; Niedner-Schatteburg, G., Multistate-Mediated Rearrangements and FeCl2 Elimination in Dinuclear Fepd Complexes. *The Journal of Physical Chemistry A* **2015**, *119*, 12587-12598.
63. Giordmaine, J.; Miller, R. C., Tunable Coherent Parametric Oscillation in Linb O 3 at Optical Frequencies. *Physical Review Letters* **1965**, *14*, 973.
64. Byer, R. L.; Herbst, R. L., Parametric Oscillation and Mixing. In *Nonlinear Infrared Generation*, Shen, Y. R., Ed. Springer Berlin Heidelberg: Berlin, Heidelberg, **1977**; pp 81-137.
65. Franken, P.; Hill, A. E.; Peters, C.; Weinreich, G., Generation of Optical Harmonics. *Physical Review Letters* **1961**, *7*, 118.
66. Eckardt, R. C.; Nabors, C.; Kozlovsky, W. J.; Byer, R. L., Optical Parametric Oscillator Frequency Tuning and Control. *JOSA B* **1991**, *8*, 646-667.
67. Parr, R. G. and Weitao, R. G. Y., Density-Functional Theory of Atoms and Molecules, *Oxford University Press*, **1987**.
68. Levine, I. N., *Quantum Chemistry*, Upper Saddle River, N.J.: Prentice Hall, **2000**.
69. Sholl, D. S. and Steckel, J. A., Density functional theory: a practical introduction, **2009**.
70. Thomas, L. H., The calculation of atomic fields, *Proc. Camb. Phil. Soc*. **1926**, *23*, 542-548.
71. Fermi, E., Eine statistische Methode zur Bestimmung einiger Eigenschaften des Atoms und ihre Anwendung auf die Theorie des periodischen Systems der Elemente, *Z. Phys.*, **1928**, *48*, 73-79.
72. Hohenberg, P.; Kohn, W., Inhomogeneous Electron Gas. *Physical Review* **1964**, *136*, B864-B871.
73. Kohn, W. and Sham, L. J., Self-consistent equations including exchange and correlation effects, *Phys. Rev.*, **1965**, 140, A1133-A1138.
74. Schuchardt, K.; Didier, B.; Black, G., Ecce—a Problem-Solving Environment's Evolution toward Grid Services and a Web Architecture. *Concurrency and computation: practice and experience* **2002**, *14*, 1221-1239.
75. Frisch, M. J.; Trucks, G.; Schlegel, H.; Scuseria, G.; Robb, M.; Cheeseman, J.; Scalmani, G.; Barone, V.; Mennucci, B.; Petersson, G., Gaussian 09, Revision A. 1. *Gaussian Inc., Wallingford, CT* **2009**.

3. VIBRATIONAL FINGERPRINTS OF LIGATED TETRANUCLEAR COBALT CLUSTERS

In this chapter I present the results on gas phase IR-(M)PD investigations on isolated tetranuclear cobalt carbonyl and mixed cobalt carbonyl/dinitrogen clusters in the respective vibrational stretching ranges when isolating these clusters at low temperatures (26 K and below). The results on the influence of the CO ligands on the structure and the spin multiplicity of the Co_4 core are introduced, discussed and concluded in a published paper manuscript. My contributions to the presented manuscript are stated prior to the manuscript. The results on the mixed CO/N_2 clusters were not part of the publication and are presented in chapter 3.2.

3.1 Publication: "Vibrational fingerprints of a tetranuclear cobalt carbonyl cluster within an ion trap"

The following work has been published at the Journal of Molecular Spectroscopy with the title: "Vibrational fingerprints of a tetranuclear cobalt carbonyl cluster within an ion trap".

The experiments were performed by Sebastian Dillinger and myself. The data evaluation was done by myself. The computations were performed by Johannes Lang and Marc Prosenc. The initial paper draft was put together by myself. P. Braunstein and G. Niedner-Schatteburg were involved in the revision of the manuscript.

Full reference to the publication:

JENNIFER MOHRBACH, JOHANNES LANG, SEBASTIAN DILLINGER, MARC H PROSENC, PIERRE BRAUNSTEIN, AND GEREON NIEDNER-SCHATTEBURG, *Vibrational fingerprints of a tetranuclear cobalt carbonyl cluster within an ion trap,* Journal of Molecular Spectroscopy, **2017**, *332*, 103-108.

http://dx.doi.org/10.1016/j.jms.2016.11.008

Vibrational Fingerprints of a Tetranuclear Cobalt Carbonyl Cluster within an Ion Trap

Jennifer Mohrbach[a], Johannes Lang[a], Sebastian Dillinger[a], Marc Prosenc[a],
Pierre Braunstein[b], and Gereon Niedner-Schatteburg[a]

[a]Fachbereich Chemie and Forschungszentrum OPTIMAS,
Technische Universität Kaiserslautern, 67663 Kaiserslautern, Germany
[b]Laboratoire de Chimie de Coordination, Institut de Chimie, UMR 7177 CNRS,
Université de Strasbourg, 67081 Strasbourg, France

3.1.1 Abstract

We present well resolved ($\Delta\tilde{\nu}$ = 3 cm^{-1}) Infrared Multiple Photon Dissociation (IR-MPD) spectra of $[Co_4(CO)_n(dppa-H^+)]^-$ (n = 3 - 10, dppa = $NH(PPh_2)_2$) in the carbonyl stretching range when isolating these species at low temperatures (26 K and below). We utilize IR-MPD in conjunction with DFT calculations to investigate the influence of CO ligands on structure and spin multiplicity of the Co_4 core. The recorded spectra reveal multiple bands of CO stretching vibrations which shift by reduction of CO coverage. This indicates an according change of coordination motifs, and we find a conclusive interpretation of all recorded IR features in the case of the saturated n = 10 compound, likely in a singlet state as in solution. We tentatively postulate a singlet/triplet to quintet spin-flip upon removal of the first one or two CO ligands (from n = 10 to n = 9, 8) as well as a conceivable isomerization at a particular CO coverage (n = 6).

3.1.2 Introduction

High resolution mass spectrometry is currently known mostly for its favourable application in analytics, often associated with key words like genomics, proteomics, metabolomics or petroleomics.[1-3] Other than that, high resolution MS is convenient for the spectroscopic investigation of small to medium sized species (m/z < 5000 amu/e and/or up to 200 atoms) when these form individual ions in vacuum. Direct absorption spectroscopy would fail at the number densities of typical ion experiments which do not provide for sufficient optical density. It is of help to invoke instead more elaborate schemes of indirect detection of photonic absorptions, such as so-called consequence or action spectroscopy.[4-6] IR-MPD is one of these advanced techniques.[7-8] It bears the intrinsic risk of power broadening, either by the use of free electron lasers or of table top Optical Parametric Oscillator/Amplifier (OPO/OPA) systems.[9-13] Contemporary IR-action spectroscopy achieves significant advances by so called tagging or messenger techniques where weakly bound, largely inert species (small rare gases and/or H_2) serve to provide for a preferred fragmentation channel, sometimes driven by single photon absorption.[14-16] Somewhat stronger bound messengers (Ar, Kr, Xe, CO, N_2) often preserve structures of the hosting species, while their influence onto spectral features allows for additional insights.

Notably, most of the current IR-MPD and messenger/tagging spectroscopic studies take place through single pulse illumination of mass selected ion packages “on the fly” prior to or within Reflectron-Time-Of-Flight (ReTOF) mass spectrometer setups. Only recently, experiments started to combine the advantages of ion trapping and IR-MPD/tagging experiments.

Carbon monoxide is one of the most widely studied ligands in surface and cluster science. Transition Metal (TM) carbonyls are of major significance in organometallic and inorganic chemistry, and they provide classic examples of metal–ligand bonding.[17-21] TM cluster carbonyls act as versatile catalysts,[18, 22] they serve as model systems for the study of chemisorption on highly curved surfaces,[23] and as precursors for the production of nanoparticles.[24]

The CO stretching vibration probes the metal-ligand bonding in a sensitive way: its frequency indicates subtle details of the hosts electronic structure, and it helps to elucidate its binding site and the geometric binding arrangement.[25-2627-28] Shifts in CO frequencies are often used for the study of binding sites on TM surfaces, and the CO molecule may be viewed as a classic probe molecule in surface science.[23, 29] Vibrational

CO shifts are usually discussed in terms of the Dewar-Chatt-Duncanson model, that explains coordinative complexation to single TM centers,[30-31] or in terms of the Blyholder model, when interpreting surface coordination.[32] Both models describe CO coordination in terms of a donor-acceptor-synergism as follows: The carbonyls C-atom donates electron density from the doubly occupied carbon lone pair σ-orbital along the M–C–O axis into empty TM d orbitals; the coordinating TM center(s) donate(s) back electron density from its (their) occupied d-levels (or d-bands) into one of the antibonding π* orbitals of the CO. Combined effects of σ donation and π back-bonding most often lead to a weakening of the CO bond and consequently to a lowering or red-shifting of the carbonyl stretch frequency. Most TM carbonyls follow this "classical" behavior, although examples are known for "non-classical" metal carbonyl complexes, their main feature being a blueshift in CO stretch which is now understood in terms of an interplay between π-back donation and electrostatic effects.[33-41] The study of in situ generated TM clusters helped to elucidate the influence of net charge and oxidation state (+/0/-) onto the single molecule CO adsorption in terms of a charge dilution model.[42] Thermochemical insights – such as Co-CO binding enthalpies and more - arose from a sophisticated combination of ionization and dissociation experiments of atomic cobalt ion carbonyl complexes with *ab initio* calculations.[4344] The IR-MPD studies of such complexes revealed an induced spin quenching (triplet to singlet) upon an increase of CO coordination (n = 4 to 5).[36]

The obvious progress in the elucidation of carbonyl complex structure and bonding has brought with it several nomenclatures for the description of the prevailing coordination motifs: Bonding/coordination of a single CO molecule via its C-terminus to a single metal or TM center – irrespective of the metal coordination to its neighbours if any – has been termed as: terminal, end on, on top, atop, s1, μ_1, μ^1, and η_1 – this listing not claiming completeness. For reason of simplicity, we will exclusively utilize the term "terminal" CO and the label CO_{term} in the following. Bonding/coordination of a single CO molecule via its C-terminus to two metal or TM centers has been addressed by: bridging, s2, μ_2, μ^2, "in between". We will exclusively utilize the term μ_2-CO. The third likely coordination motif of CO involves three metal or TM centers in bonding/coordination. This motif has been labeled as: capping, on hollow, s3, μ_3, and μ^3. We likely do not see this motif in our present study. When appropriate we will discuss it in terms of μ_3-CO.

In our current ion trapping spectroscopic study, we investigate the tetranuclear cobalt carbonyl complex $[Co_4(CO)_{10}dppa]$[45] which is stabilized by the well-established diphosphine short-bite bridging ligand μ_2-dppa (cf. Scheme 1, dppa = $NH(PPh_2)_2$).[46] IR spectra of the complex (from KBr plates and in solution) reveal seven bands in the 1930–2070 cm^{-1} range and three bands in 1770–1860cm^{-1} range, arising from terminal and μ_2-CO ligands. This is consistent with a C_s molecular symmetry.

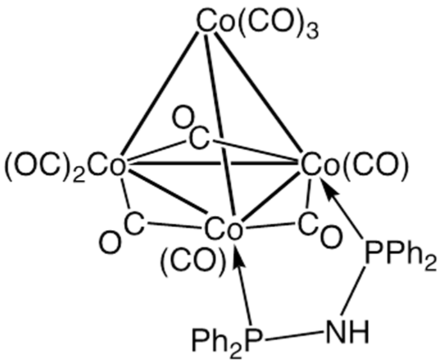

Scheme 1: Molecular structure of the neutral tetranuclear cluster $[Co_4(CO)_{10}dppa]$ (dppa = $NH(PPh_2)_2$). The complex consists of a Co_4 core, three μ_2-CO and seven terminal CO ligands. The dppa ligand bridges two basal cobalt atoms.

The complex finds application in the preparation of TM phosphides, which is generally not easy and otherwise requires the direct combination of elements at high temperature, the reaction of toxic phosphide with metal or metal hydride, or metal organic chemical vapour deposition techniques. Instead, pure cobalt phosphide nanoparticles can be obtained from $[Co_4(CO)_{10}dppa]$ by anchoring and thermal treatment.[47-49] The $[Co_4(CO)_{10}dppa]$ complex moreover may serve as a model system for the stepwise regioselective elimination of CO ligands from a metal cluster. The dppa ligand in $[Co_4(CO)_{10}dppa]$ stabilizes the Co_4 core and orients further cluster functionalization by selective CO substitution. A second dppa ligand or a N-functionalized dppa ligand would bridge that metal–metal bond which is opposite to that spanned by the first dppa ligand.[47-49] The regioselective CO elimination would allow e.g. for the specific anchoring of this metal complex within a nanoporous membrane.[50]

In this study, we strive for fundamental insight in its own right from the stepwise CO elimination off anionic derivatives of the $[Co_4(CO)_{10}dppa]$ complex by Collision Induced Dissociation (CID) and by IR-MPD investigations, in conjunction with Density Functional Theory (DFT) modelling of the anions geometries, spin couplings and force constants. The Co_4 core within these anions might be viewed as a highly curved nano-sized metal surface. Upon adoption of this analogy, it seems appropriate to view the stepwise detachment of CO ligands from the complex as a change in CO surface coverage.

3.1.3 Experimental and computational methods

We utilized a customized Fourier Transform Ion Cyclotron Resonance (FT-ICR) mass spectrometer (Apex Ultra, Bruker Daltonics) equipped with an Electrospray Ionization (ESI) source (Apollo 2, Bruker) and a home-built laser vaporization cluster ion source [51] [52] (Fig.1).

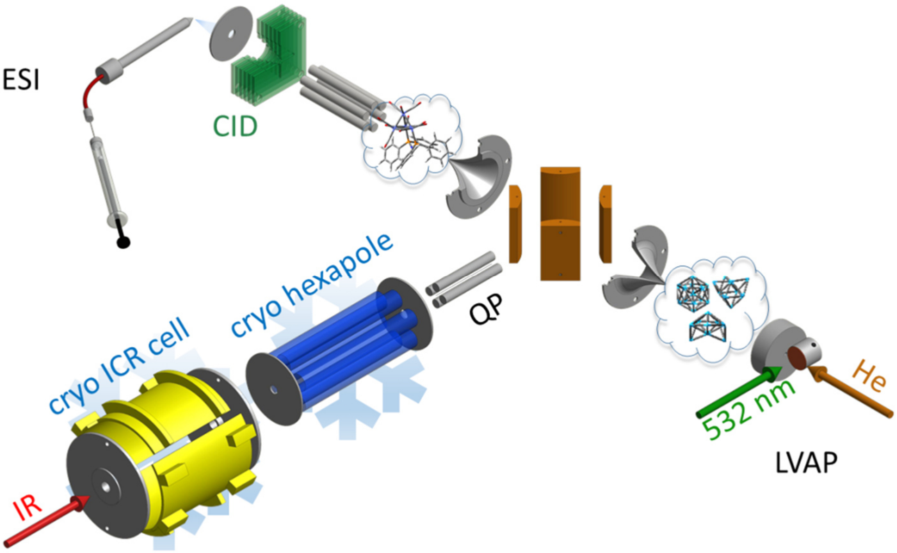

Figure 1: Schematic drawing of our dual source tandem cryo trap FT-ICR MS setup. Ions are generated either in a Laser VAPorization (LVAP) source or in an Electro Spray Ionization (ESI) source. Either type of ions are injected into the first ion trap (cryo hexapole) via a switchable 90° ion bender and a quadrupole mass filter (QP). Buffer and reaction gases are introduced either pulsed or continuously. The cryo cooled ions and their reaction products are guided into the cryo ICR-cell, where they are isolated, irradiated by IR laser pulses and detected.

The molecular precursor complex [$Co_4(CO)_{10}$dppa] was synthesized from [$Co_4(CO)_{12}$] and characterized by its IR (from KBr plates and in solution) and $^1H/^{31}P$ NMR spectra.[45] Sample solutions of the [$Co_4(CO)_{10}$dppa] complex in acetonitrile at the concentration of 1×10^{-4} mol/l were used without further purification and continuously infused into the ESI source by a syringe pump at a flow rate of 2 μL min^{-1}. The ion source was set to negative electrospray ionization mode. Nitrogen was used as drying gas with a flow rate of 3.0 L min^{-1} at 200°C. The solutions were electro-sprayed at a nebulizer flow of 1.5 L min^{-1} and the spray shield was held at 3.6 kV. We obtained the deprotonated complex $[Co_4(CO)_{10}(dppa\text{-}H^+)]^-$, abbreviated $[Co_4(CO)_{10}L]^-$ in the following. In the ESI source, the ions may undergo Collision Induced Dissociation (CID) on demand. The successive elimination of up to seven CO ligands is achieved by stepwise increase of the skimmer voltage (at the first ion funnel) from -25 to -95 V (in source CID). Further increase of the funnel voltage did not enhance the elimination beyond seven CO ligands. We mass selected individual members from the resulting series of fragments $[Co_4(CO)_nL]^-$ (n = 3 - 9) and guided those into a 26 K hexapole ion trap. The ion trap is cooled by a closed cycle helium cryostat and held at 26 K for the measurements. Buffer (He) gas was introduced continuously. The pressure is increased from 1.7×10^{-7} mbar up to 3.0×10^{-6} mbar to accomplish efficient trapping and cooling of the ions. The cryo cooled ions are guided by electrostatic lenses into the FT-ICR cell of the so-called ‘‘infinity’’ type.[53] This cell is cooled to a temperature of about 10 K with a closed cycle helium cryostat to prevent heating of the clusters by black body radiation. The ICR cell is used for trapping, isolation and detection of the ions. It is coupled to a tuneable pulsed IR laser ($\Delta\tilde{\nu} = 0.9$ cm^{-1}, $\Delta t = 7$ ns) to record IR-MPD spectra of isolated $[Co_4(CO)_nL]^-$ (n = 3 - 10) complexes. Fragmentation of the isolated species (CO elimination) indicates the absorption by a resonant vibrational frequency (Fig. 2, a). The laser power was attenuated for n = 6 - 10 in the range from 1850 cm^{-1} to 2050 cm^{-1} to prevent excessive fragmentation. In the case of $[Co_4(CO)_nL]^-$ (n = 4-10) the only observed fragmentation channel was the loss of CO. In the case of $[Co_4(CO)_3L]^-$ the only observed fragment (395 m/z) may be assigned to $[Co_4(CO)_3NP_2]^-$ due to the loss of all four phenyl groups from the dppa ligand. Addition of N_2 gas in the cryo hexapole results in N_2 adsorption to coordinatively unsaturated $[Co_4(CO)_nL]^-$ (n = 6, 8) complexes. These N_2 complexes are isolated in the ICR cell and illuminated by infrared laser pulses. Here, the photo induced loss of N_2 indicates a resonant excitation of the complex (Fig. 2, b). Note, that the modest mass difference between CO and N_2 of about 0.01 amu can be accurately resolved with our experimental setup.

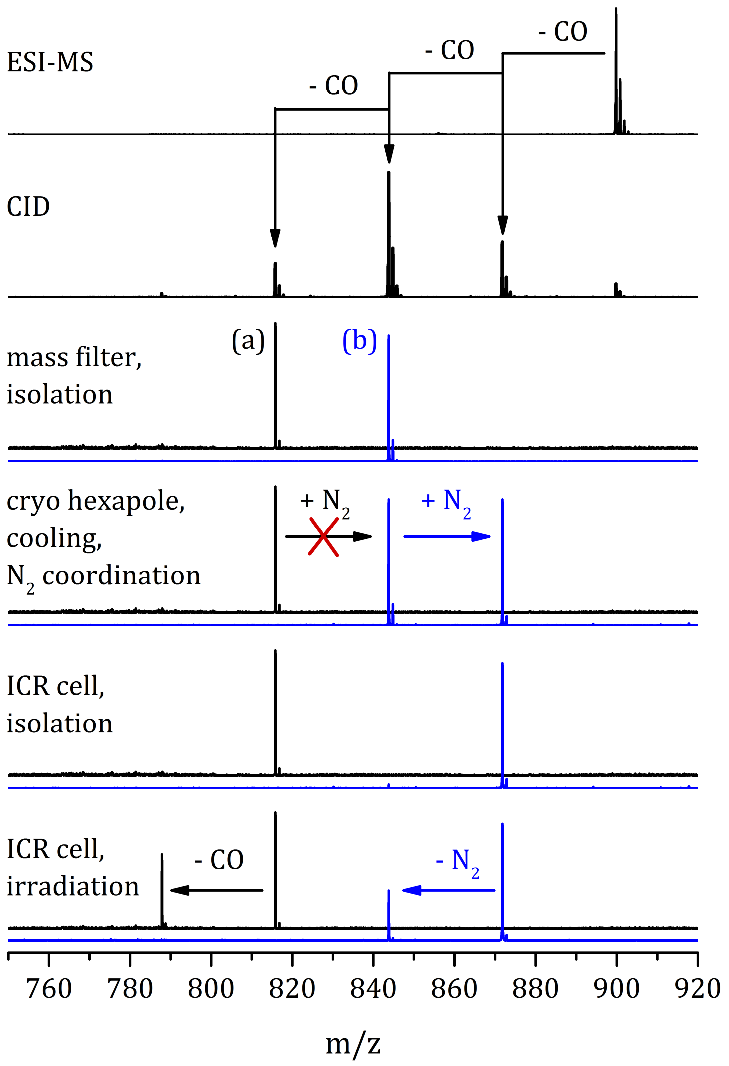

Figure 2: Mass spectra illustrating the experimental methods. The ESI source delivers $[Co_4(CO)_{10}L]^-$ (899 m/z). Subsequent CID yields a series of under-coordinated $[Co_4(CO)_nL]^-$ (n = 3-9) complexes via successive decarbonylation. After isolation one of these, the ions of choice are trapped and cryo cooled within the RF hexapole ion trap (a,b). Optional N_2 gas intake may result in the adsorption of one N_2 molecule to distinct complexes, n = 6, 8 only (blue spectra, b). Either type of ions (with or without N_2 attached) are guided into a 10 K ICR cell, isolated, irradiated by IR laser pulses, and analyzed for their fragments.

The IR laser is a KTP/KTA optical parametric oscillator/amplifier (OPO/A, LaserVision) system pumped by a pulsed 10 Hz injection seeded Nd^{3+}:YAG laser (Continuum, Powerlite DLS 8000). In this work we used the difference frequency (DF) between the OPA signal and idler waves generated in a $AgGaSe_2$ crystal (0.1 – 1.2 mJ per pulse). We recorded IR-MPD spectra in the range of 1500–2300 cm^{-1}. Each trapped and isolated package of ions is irradiated by 15 laser pulses to yield a sufficient amount of fragment ions. The IR spectra were recorded as mass chromatograms while continuously scanning the IR frequency (typically < 0.2 cm^{-1}/s). The IR-MPD signal was evaluated as $\Sigma_i F_i/(\Sigma_i F_i + \Sigma_i P_i)$, where F_i and P_i indicate the fragment and the parent ion signals, respectively. An experimental IR-MPD spectrum arises from a plot of the fragmentation efficiency as a function of laser frequency.

Optimized minimum energy structures and linear IR absorption spectra were calculated at the B3LYP[54-55] and PBE0[56] level of theory using 6-31++G** basis sets (C, H, N, O, P), and Stuttgart RSC 1997[57] effective core potential (Co) basis sets, respectively, as implemented in the Gaussian 09 program package.[58] Standard convergence criteria were applied. Full geometry optimization of all nuclear coordinates yields multiple local minimum structures. The lowest energy structure is assumed to represent the most stable isomer. We present singlet as well as quintet spin states. We scaled the calculated harmonic vibrational frequencies by a factor of 0.954 in order to match the calculated highest frequency CO vibration band in $[Co_4(CO)_{10}L]^-$ (unscaled at 2143 cm^{-1}) to our experimental value of 2044 cm^{-1}.

3.1.4 Results and discussion

IR-MPD Spectra

The IR-MPD spectra of the investigated $[Co_4(CO)_nL]^-$ (n = 3-10) complexes (Fig. 3) exhibit several strong bands in the range 1880–2050 cm^{-1}, which we assign to the stretching vibrational modes of terminal CO ligands, and weaker bands around 1810 cm^{-1} which we assign to the stretching vibration modes of μ_2-CO ligands.

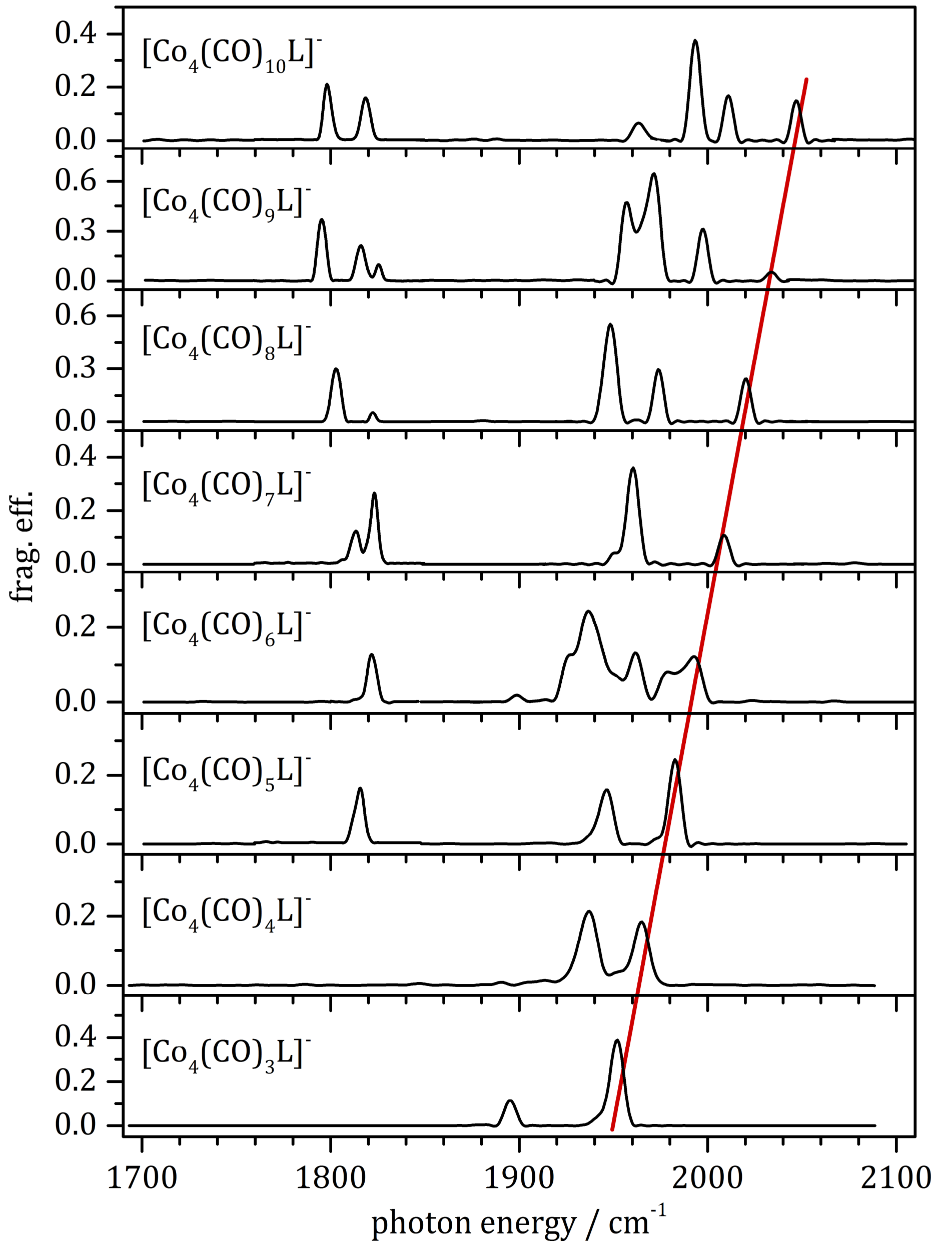

Figure 3: IR-MPD spectra of $[Co_4(CO)_nL]^-$ (n = 3 – 10) complexes at 26 K. The red line serves to guide the eye, emphasizing the redshift of the terminal carbonyl stretches with decarbonylation.

There are multiple bands for the terminal CO ligands for all n = 3 - 10 investigated. All bands are significantly redshifted by 97–247 cm^{-1} with respect to the free CO vibration at 2143 cm^{-1}. Judging by the band with highest frequency (indicated by the red line in Fig. 2), all redshifts increase by ~ 90 cm^{-1} upon decarbonylation (seven fold CO-elimination). The observed redshifts are indicative for a reduction of force constants and weakening of the CO bonds. The likely associated bond lengthening arises through electron density transfer from the tetranuclear cobalt core into antibonding 2π* CO acceptor orbitals. As seen before[59] the extent of such electron density shift/charge transfer/electronic transfer does depend on CO coverage. The stepwise decrease of CO coverage reduces the total electron back donation from the Co_4 core to the antibonding CO π* orbitals, or it enables a higher donation per CO ligand. We assume a combination of both. If so, these arguments fall in line with the observed redshifts of CO_{term} vibrations which increase by decarbonylation/CO elimination.

A conclusive interpretation of all observed CO_{term} bands is not possible at current stage of investigation. DFT modelling helps in the case of n = 10 (see subsequent section), and not beyond. Some obvious findings deserve attention: The spectra of $[Co_4(CO)_nL]^-$ (n = 10, 9, 8, 7, 5, 4, 3) reveal 4, 4, 3, 2, 2, 2 and 2 distinct CO_{term} bands. The level of distinct absorption motifs reduces in parallel to a reduction of the CO coverage. The n = 6 case is unique: We find up to 6 partially resolved CO_{term} features. This indicates either a highly specific Co-CO coordination per each CO, or it hints towards an isomeric variation that does not occur in any of the other cases. Isomeric variance may originate from Co_4 core isomers, from variation of CO coordination, or even from a coexistence of complexes in different spin multiplets (singlet/triplet/quintet/…). Naked cobalt clusters are known for their very high spin states[60] [61], and an adsorbate induced partial quenching is likely.[62] Further elucidation of such effects remains to thorough DFT modelling in the future.

The low energy part of the spectra reveals features typical of μ_2-CO coordination. Such fingerprints prevail at n = 5 - 10 and vanish at n = 3, 4. Other than in the CO_{term} bands, there is no systematic redshift variation as a function of coverage for the μ_2-CO bands. The magnitude of the μ_2-CO redshift is large (~ 340 cm^{-1}) and in line with numerous previous observations.[63] [26] [19] In remarkable contrast to the up to six distinct CO_{term} bands, there are just two distinct μ_2-CO bands at 1790–1810 and 1810–1830 cm^{-1}, respectively. These two bands likely correspond to two species, μ_2^a (< 1810 cm^{-1}) and μ_2^b (> 1810 cm^{-1}). The μ_2^a species occurs only at highest coverages n = 8 - 10, and the μ_2^b

species occurs only at high coverages n = 5 - 10. At this point the successful DFT modelling of the n = 10 case enables a convincing assignment of these two species (see below).

Our investigation did not find evidence for any IR-MPD bands in the range of 1500-1700 cm^{-1} (n = 6 - 10), which allow us to rule out μ_3-CO coordination in $[Co_4(CO)_nL]^-$.

An interpretation solely in terms of electrostatics and electron density shifts falls short of all prevailing effects. Surely there are coverage dependent steric effects which reflect surface “crowding” by CO adsorbates, and which likely cause concomitant terminal - μ_2 - μ_3 - rearrangements. In parallel, there will be a change in the order of individual $\Delta_{surface}H(\mu_x\text{-CO})$ values. Small coverages may go with $\Delta_{surface}H(CO_{term}) > \Delta_{surface}H(\mu_2\text{-CO}) \sim \Delta_{surface}H(\mu_3\text{-CO})$ in preference of terminal CO; high coverages may go with $\Delta_{surface}H(\mu_2\text{-CO}) \sim \Delta_{surface}H(\mu_3\text{-CO}) > \Delta_{surface}H(CO_{term})$ in preference of $\mu_{2,3}$-CO. Indeed, our spectra show that CO_{term} prevails at all levels of “coverage” while μ_2-CO fingerprints diminish upon reduction of CO coverage.

DFT modelling

We have conducted DFT modelling of the $[Co_4(CO)_{10}L]^-$ complex, and we obtained its linear IR absorption spectra in singlet and quintet (+ 6 kJ/mol) spin states. The calculation of force constants in triplet state did not converge, irrespective of the chosen exchange-correlation functional (B3LYP and PBE0). Geometry optimized calculations of the singlet and triplet state at the somewhat more approximate BP86 level have identified a singlet ground state and a high energy (+46 kJ/mol) triplet state. While we take this finding with a grain of caution, it shall suffice to rule out triplet contributions at the current stage of investigation.

In the following we compare two computed IR spectra (in singlet and quintet state by PBE0) to the experimental IR-MPD spectrum in the CO stretching frequency range (Figure 4). A B3LYP singlet spectrum is virtually identical to that one by PBE0 (cf. supplement Fig. S1). The DFT computations reveal seven CO_{term} bands and three μ_2-CO bands, some of which are almost degenerate. Upon folding in the experimental resolution of 3 cm^{-1}, the DFT modelling predicts four observable CO_{term} bands and three observable μ_2-CO bands in the case of a singlet spin state – in agreement with the experimental IR-MPD findings. We provide an illustrative visualization of the calculated displacement vectors of these modes in Fig. S2 of the supplement. The two μ_2-CO species mentioned above can be assigned either to the one CO ligand bridging the same Co atoms as the dppa ligand (μ_2^a), or to the two CO ligands bridging one dppa bridged Co atom and the third basal Co atom (μ_2^b). We clearly rule out contributions from the calculated quintet state, which would predict six CO_{term} bands across a wider range of frequencies in undisputable disagreement with the experiment.

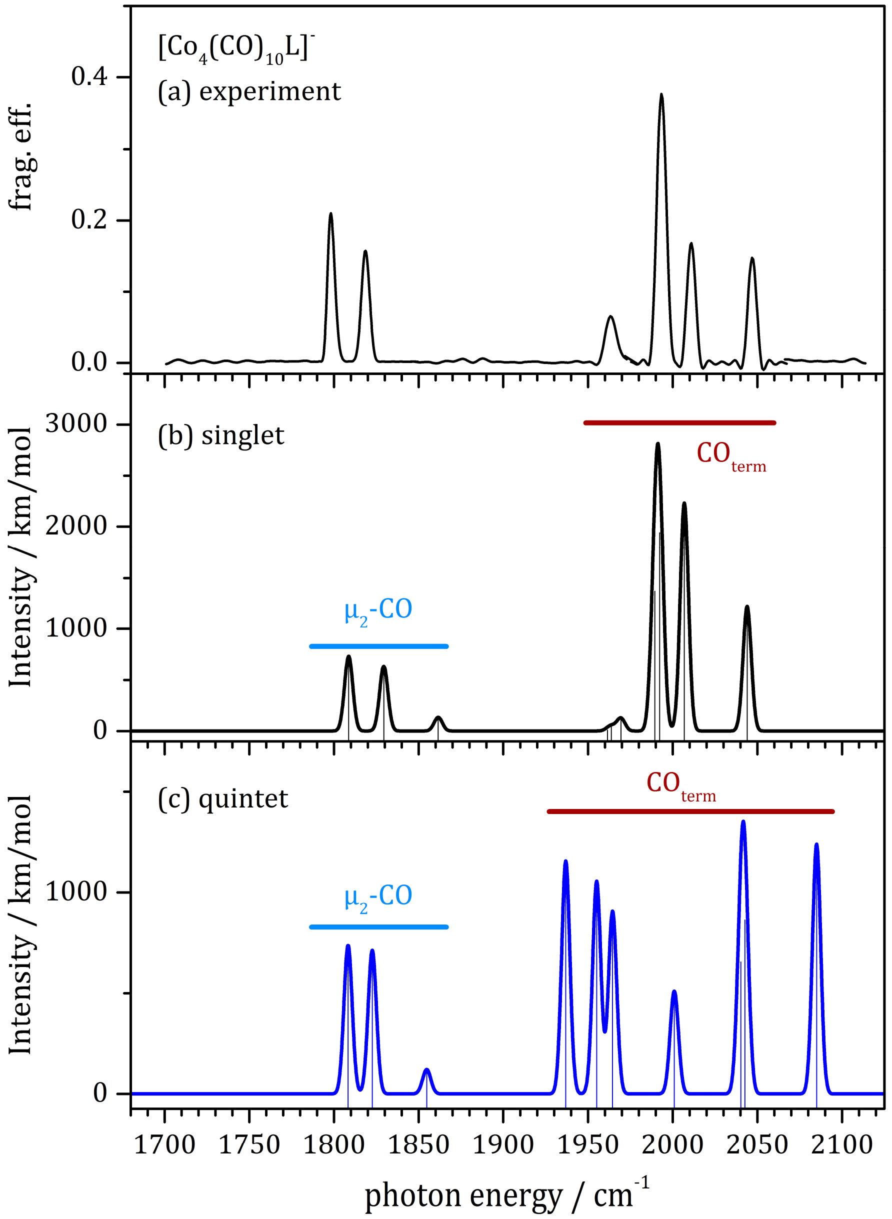

Figure 4: IR-MPD spectrum of $[Co_4(CO)_{10}L]^-$ at 26 K (a) and calculated IR absorption spectra of geometry optimized singlet (b) and quintet (+6kJ/mol) (c) spin state. The calculations were performed at the Stuttgart 1997 ECP (Co) and PBE0/6-31++G** (H, C, N, O, P) level of theory. The frequencies are scaled with 0.954, and calculated lines were broadened with Gaussians (FWHM = 3 cm^{-1}). The lowest triplet state (+46 kJ/mol) is discussed in the text. For the vector characters of all 10 singlet vibrations refer to Fig. S2 in the supplement.

Unfortunately, our current attempts of further DFT modelling ($n < 10$) have not yet lead to converged data and verifiable conclusions. We are tentatively assuming, that decarbonylation will allow for higher spin states, partially co-existing.

3.1.5 Conclusions and Outlook

It became possible to record well resolved IR spectra of $[Co_4(CO)_{10}L]^-$ ($n = 3 - 10$) in the range of CO_{term} and μ_2-CO vibrations when isolating these species at low temperatures (26 K and below). We find several bands which shift upon reduction of CO coverage, indicating a variation of coordination motifs. In conjunction with DFT modelling, we find a conclusive interpretation of all recorded IR features in the case of the saturated $n = 10$ compound, likely in a singlet state similar to solution. We currently fail to achieve such conclusive interpretation in all other cases. We currently speculate about spin switching into higher multiplet states (from singlet into triplet/quintet or even higher) upon stepwise decarbonylation, and about a conceivable isomerization at a particular CO coverage ($n = 6$). The CO coverage dependent redshift of the highest CO_{term} is indicative of the charge dependent $2\pi^*(CO)$ back donation and of its concomitant bond weakening. In contrast, the μ_2-CO bands modulate in appearance and intensity upon change of the CO coverage – without shifting significantly.

We are in the process of recording further spectra of Co_4 species with a mixed N_2 – CO coverage, and we are enforcing further DFT analysis by all means. Once achieved, the then calculated $\Delta_{surface}H(CO)$ and $\Delta_{surface}H(N_2)$ values will allow for an elucidation of additional steric effects ("crowding"). We anticipate these effects to modulate the electronics in the known acceptor-donor type Co-CO and Co-N_2 bindings. Such steric effects most likely cause CO_{term} to μ_2–CO to μ_3–CO rearrangements, and it will be fascinating to compare such findings to the data of CO and N_2 adsorption on flat surfaces.

3.1.6 References

1. Patti, G. J.; Yanes, O.; Siuzdak, G., Innovation: Metabolomics: the apogee of the omics trilogy. *Nat Rev Mol Cell Biol* **2012,** *13* (4), 263-269.
2. Tyers, M.; Mann, M., From genomics to proteomics. *Nature* **2003,** *422* (6928), 193-197.
3. Marshall, A. G.; Rodgers, R. P., Petroleomics: Chemistry of the underworld. *Proceedings of the National Academy of Sciences* **2008,** *105* (47), 18090-18095.
4. Okumura, M.; Yeh, L. I.; Lee, Y. T., The vibrational predissociation spectroscopy of hydrogen cluster ions. *The Journal of Chemical Physics* **1985,** *83* (7), 3705-3706.
5. Woodin, R. L.; Bomse, D. S.; Beauchamp, J. L., Multiphoton dissociation of molecules with low power continuous wave infrared laser radiation. *Journal of the American Chemical Society* **1978,** *100* (10), 3248-3250.
6. Bomse, D. S.; Woodin, R. L.; Beauchamp, J. L., Molecular activation with low-intensity CW infrared laser radiation. Multiphoton dissociation of ions derived from diethyl ether. *Journal of the American Chemical Society* **1979,** *101* (19), 5503-5512.
7. Polfer, N. C., Infrared multiple photon dissociation spectroscopy of trapped ions. *Chemical Society Reviews* **2011,** *40* (5), 2211-2221.
8. MacAleese, L.; Maître, P., Infrared spectroscopy of organometallic ions in the gas phase: From model to real world complexes. *Mass Spectrometry Reviews* **2007,** *26* (4), 583-605.
9. Oomens, J.; Sartakov, B. G.; Meijer, G.; von Helden, G., Gas-phase infrared multiple photon dissociation spectroscopy of mass-selected molecular ions. *International Journal of Mass Spectrometry* **2006,** *254* (1–2), 1-19.
10. Valle, J. J.; Eyler, J. R.; Oomens, J.; Moore, D. T.; van der Meer, A. F. G.; von Helden, G.; Meijer, G.; Hendrickson, C. L.; Marshall, A. G.; Blakney, G. T., Free electron laser-Fourier transform ion cyclotron resonance mass spectrometry facility for obtaining infrared multiphoton dissociation spectra of gaseous ions. *Review of Scientific Instruments* **2005,** *76* (2), 023103.
11. Walker, N. R.; Walters, R. S.; Duncan, M. A., Frontiers in the infrared spectroscopy of gas phase metal ion complexes. *New Journal of Chemistry* **2005,** *29* (12), 1495-1503.
12. Lang, J.; Gaffga, M.; Menges, F.; Niedner-Schatteburg, G., Two-color delay dependent IR probing of torsional isomerization in a [AgL1L2]+ complex. *Physical Chemistry Chemical Physics* **2014,** *16* (33), 17417-17421.
13. Gaffga, M.; Munstein, I.; Müller, P.; Lang, J.; Thiel, W. R.; Niedner-Schatteburg, G., Multistate-Mediated Rearrangements and FeCl2 Elimination in Dinuclear FePd Complexes. *The Journal of Physical Chemistry A* **2015,** *119* (51), 12587-12598.
14. Wolk, A. B.; Leavitt, C. M.; Garand, E.; Johnson, M. A., Cryogenic Ion Chemistry and Spectroscopy. *Accounts of Chemical Research* **2014,** *47* (1), 202-210.
15. Headrick, J. M.; Bopp, J. C.; Johnson, M. A., Predissociation spectroscopy of the argon-solvated H5O2+ "zundel" cation in the 1000–1900 cm−1 region. *The Journal of Chemical Physics* **2004,** *121* (23), 11523-11526.
16. Asvany, O.; Brünken, S.; Kluge, L.; Schlemmer, S., COLTRAP: a 22-pole ion trapping machine for spectroscopy at 4 K. *Applied Physics B* **2014,** *114* (1-2), 203-211.
17. Braunstein, P.; Raithby, P. R.; Oro, L. A., *Metal clusters in chemistry*. Wiley-vch Weinheim, Germany: Wiley-VCH, **1999**; Vol. 1-3, 1798.
18. Cotton, A. F.; Wilkinson, G.; Bochmann, M.; Murillo, C. A., *Advanced inorganic chemistry*. Wiley: **1999**.

19. Huheey, J. E.; Keiter, E. A.; Keiter, R. L.; Medhi, O. K., *Inorganic chemistry: principles of structure and reactivity*. Pearson Education India: **2006**.
20. Aubke, F.; Wang, C., Carbon monoxide as a σ-donor ligand in coordination chemistry. *Coordination Chemistry Reviews* **1994,** *137*, 483-524.
21. Hartwig, J. F., *Organotransition metal chemistry: from bonding to catalysis*. Univ Science Books: **2010**.
22. Heck, R., *Organotransition Metal Chemistry A Mechanistic Approach*. Academic Press: **1974**.
23. Somorjai, G., Introduction to Surface Science and Catalysis. *See for example Wiley, New York* **1994**.
24. Buchwalter, P.; Rosé, J.; Braunstein, P., Multimetallic Catalysis Based on Heterometallic Complexes and Clusters. *Chemical Reviews* **2015,** *115* (1), 28-126.
25. Huheey, J. E.; Keitler, E.; Keitler, R., Inorganic Chemistry, Principles of Structure and Bonding. Harper Collins College Publishers, New York: **1993**.
26. Wrighton, M., Photochemistry of metal carbonyls. *Chemical Reviews* **1974,** *74* (4), 401-430.
27. Frenking, G.; Fröhlich, N., The nature of the bonding in transition-metal compounds. *Chemical Reviews* **2000,** *100* (2), 717-774.
28. Nakamoto, K., *Infrared and Raman spectra of inorganic and coordination compounds*. Wiley Online Library: **1986**.
29. Ertl, G., *Reactions at solid surfaces*. John Wiley & Sons: **2010**; Vol. 14.
30. Chatt, J.; Duncanson, L., 586. Olefin co-ordination compounds. Part III. Infra-red spectra and structure: attempted preparation of acetylene complexes. *Journal of the Chemical Society (Resumed)* **1953**, 2939-2947.
31. Dewar, J., A review of the pi-complex theory. *Bulletin de la Societe Chimique de France* **1951,** *18* (3-4), C71-C79.
32. Blyholder, G., Molecular orbital view of chemisorbed carbon monoxide. *The Journal of Physical Chemistry* **1964,** *68* (10), 2772-2777.
33. Fielicke, A.; von Helden, G.; Meijer, G.; Simard, B.; Rayner, D. M., Gold Cluster Carbonyls: Vibrational Spectroscopy of the Anions and the Effects of Cluster Size, Charge, and Coverage on the CO Stretching Frequency. *The Journal of Physical Chemistry B* **2005,** *109* (50), 23935-23940.
34. Moore, D. T.; Oomens, J.; Eyler, J. R.; Meijer, G.; von Helden, G.; Ridge, D. P., Gas-phase IR spectroscopy of anionic iron carbonyl clusters. *Journal of the American Chemical Society* **2004,** *126* (45), 14726-14727.
35. Reed, Z. D.; Duncan, M. A., Infrared Spectroscopy and Structures of Manganese Carbonyl Cations, Mn(CO)n+ (n = 1–9). *Journal of the American Society for Mass Spectrometry* **2010,** *21* (5), 739-749.
36. Ricks, A. M.; Reed, Z. E.; Duncan, M. A., Infrared spectroscopy of mass-selected metal carbonyl cations. *Journal of Molecular Spectroscopy* **2011,** *266* (2), 63-74.
37. Velasquez, J.; Njegic, B.; Gordon, M. S.; Duncan, M. A., IR Photodissociation Spectroscopy and Theory of Au+(CO)n Complexes: Nonclassical Carbonyls in the Gas Phase. *The Journal of Physical Chemistry A* **2008,** *112* (9), 1907-1913.
38. Goldman, A. S.; Krogh-Jespersen, K., Why Do Cationic Carbon Monoxide Complexes Have High CO Stretching Force Constants and Short CO Bonds? Electrostatic Effects, Not σ-Bonding. *Journal of the American Chemical Society* **1996,** *118* (48), 12159-12166.
39. Lupinetti, A. J.; Fau, S.; Frenking, G.; Strauss, S. H., Theoretical analysis of the bonding between CO and positively charged atoms. *The Journal of Physical Chemistry A* **1997,** *101* (49), 9551-9559.

40. Frenking, G.; Pidun, U., Ab initio studies of transition-metal compounds: the nature of the chemical bond to a transition metal. *Journal of the Chemical Society, Dalton Transactions* **1997,** (10), 1653-1662.
41. Bistoni, G.; Rampino, S.; Scafuri, N.; Ciancaleoni, G.; Zuccaccia, D.; Belpassi, L.; Tarantelli, F., How π back-donation quantitatively controls the CO stretching response in classical and non-classical metal carbonyl complexes. *Chemical Science* **2016,** *7* (2), 1174-1184.
42. Fielicke, A.; von Helden, G.; Meijer, G.; Pedersen, D. B.; Simard, B.; Rayner, D. M., Size and charge effects on the binding of CO to late transition metal clusters. *Journal of Chemical Physics* **2006,** *124* (19), 194305-194305.
43. Gengeliczki, Z.; Sztáray, B.; Baer, T.; Iceman, C.; Armentrout, P. B., Heats of formation of Co (CO) 2NOPR3, R= CH3 and C2H5, and its ionic fragments. *Journal of the American Chemical Society* **2005,** *127* (26), 9393-9402.
44. Goebel, S.; Haynes, C. L.; Khan, F. A.; Armentrout, P. B., Collision-Induced Dissociation Studies of Co (CO) x+, x= 1-5: Sequential Bond Energies and the Heat of Formation of Co (CO) 4. *Journal of the American Chemical Society* **1995,** *117* (26), 6994-7002.
45. Moreno, C.; Macazaga, M. J.; Marcos, M. L.; González-Velasco, J.; Delgado, S., [CO4(CO)12] derivatives with bis(diphenylphosphino) amine, an electrochemical study. *Journal of Organometallic Chemistry* **1993,** *452* (1), 185-192.
46. Fliedel, C.; Ghisolfi, A.; Braunstein, P., Functional Short-Bite Ligands: Synthesis, Coordination Chemistry, and Applications of N-Functionalized Bis (diaryl/dialkylphosphino) amine-type Ligands. *Chemical Reviews* **2016,** *116* (16), 9237-9304.
47. Buchwalter, P.; Rosé, J.; Lebeau, B.; Ersen, O.; Girleanu, M.; Rabu, P.; Braunstein, P.; Paillaud, J.-L., Characterization of cobalt phosphide nanoparticles derived from molecular clusters in mesoporous silica. *Journal of nanoparticle research* **2013,** *15* (12), 1-21.
48. Buchwalter, P.; Rosé, J.; Lebeau, B.; Rabu, P.; Braunstein, P.; Paillaud, J.-L., Stoichiometric molecular single source precursors to cobalt phosphides. *Inorganica Chimica Acta* **2014,** *409*, 330-341.
49. Schweyer-Tihay, F.; Braunstein, P.; Estournes, C.; Guille, J.; Lebeau, B.; Paillaud, J.-L.; Richard-Plouet, M.; Rosé, J., Synthesis and Characterization of Supported Co2P Nanoparticles by Grafting of Molecular Clusters into Mesoporous Silica Matrixes. *Chemistry of materials* **2003,** *15* (1), 57-62.
50. Braunstein, P.; Kormann, H.-P.; Meyer-Zaika, W.; Pugin, R.; Schmid, G., Strategies for the anchoring of metal complexes, clusters, and colloids inside nanoporous alumina membranes. *Chemistry* **2000,** *6* (24), 4637-4646.
51. Maruyama, S.; Anderson, L. R.; Smalley, R. E., Direct injection supersonic cluster beam source for FT-ICR studies of clusters. *Review of scientific instruments* **1990,** *61* (12), 3686-3693.
52. Berg, C.; Schindler, T.; Niedner-Schatteburg, G.; Bondybey, V. E., Reactions of simple hydrocarbons with Nb+ n: chemisorption and physisorption on ionized niobium clusters. *The Journal of chemical physics* **1995,** *102* (12), 4870-4884.
53. Caravatti, P.; Allemann, M., The 'infinity cell': A new trapped-ion cell with radiofrequency covered trapping electrodes for Fourier transform ion cyclotron resonance mass spectrometry. *Organic Mass Spectrometry* **1991,** *26* (5), 514-518.
54. Dunning Jr, T. H., Gaussian basis sets for use in correlated molecular calculations. I. The atoms boron through neon and hydrogen. *The Journal of chemical physics* **1989,** *90* (2), 1007-1023.

55. Woon, D. E.; Dunning Jr, T. H., Gaussian basis sets for use in correlated molecular calculations. III. The atoms aluminum through argon. *The Journal of chemical physics* **1993,** *98* (2), 1358-1371.
56. Adamo, C.; Barone, V., Toward reliable density functional methods without adjustable parameters: The PBE0 model. *The Journal of chemical physics* **1999,** *110* (13), 6158-6170.
57. Dolg, M.; Stoll, H.; Preuss, H.; Pitzer, R. M., Relativistic and correlation effects for element 105 (hahnium, Ha): a comparative study of M and MO (M= Nb, Ta, Ha) using energy-adjusted ab initio pseudopotentials. *The Journal of Physical Chemistry* **1993,** *97* (22), 5852-5859.
58. Frisch, M. J.; Trucks, G.; Schlegel, H.; Scuseria, G.; Robb, M.; Cheeseman, J.; Scalmani, G.; Barone, V.; Mennucci, B.; Petersson, G., Gaussian 09, revision A. 1. *Gaussian Inc., Wallingford, CT* **2009**.
59. Reboredo, F. A.; Galli, G., Size and structure dependence of carbon monoxide chemisorption on cobalt clusters. *The Journal of Physical Chemistry B* **2006,** *110* (15), 7979-7984.
60. Dillinger, S.; Mohrbach, J.; Hewer, J.; Gaffga, M.; Niedner-Schatteburg, G., Infrared spectroscopy of N 2 adsorption on size selected cobalt cluster cations in isolation. *Physical Chemistry Chemical Physics* **2015,** *17* (16), 10358-10362.
61. Meyer, J.; Tombers, M.; van Wüllen, C.; Niedner-Schatteburg, G.; Peredkov, S.; Eberhardt, W.; Neeb, M.; Palutke, S.; Martins, M.; Wurth, W., The spin and orbital contributions to the total magnetic moments of free Fe, Co, and Ni clusters. *The Journal of Chemical Physics* **2015,** *143* (10), 104302.
62. Akin, S. T.; Zamudio-Bayer, V.; Duanmu, K.; Leistner, G.; Hirsch, K.; Bülow, C.; Ławicki, A.; Terasaki, A.; Issendorff, B. v.; Truhlar, D. G.; Lau, J. T.; Duncan, M. A., Size-Dependent Ligand Quenching of Ferromagnetism in $Co_3(benzene)_n^+$ Clusters Studied with X-ray Magnetic Circular Dichroism Spectroscopy, *J. Phys. Chem. Lett.,* **2016**, *7 (22)*, 4568-4575.
63. Janiak, C.; Meyer, H.-J.; Gudat, D.; Alsfasser, R., *Moderne Anorganische Chemie*. Walter de Gruyter: **2012**.

3.1.7 Supplementary Information

Vibrational Fingerprints of a Tetranuclear Cobalt Carbonyl Cluster within an Ion Trap

Jennifer Mohrbach[a], Johannes Lang[a], Sebastian Dillinger[a], Marc Prosenc[a],
Pierre Braunstein[b], and Gereon Niedner-Schatteburg[a]

[a]Fachbereich Chemie and Forschungszentrum OPTIMAS,
Technische Universität Kaiserslautern, 67663 Kaiserslautern, Germany
[b]Laboratoire de Chimie de Coordination, Institut de Chimie, UMR 7177 CNRS,
Université de Strasbourg, 67081 Strasbourg, France

Content

Figure S1: IR-MPD spectrum of $[Co_4(CO)_{10}L]^-$ at 26 K (a) and calculated IR absorption spectra of the geometry optimized singlet spin state. The calculations were performed at the Stuttgart 1997 ECP, PBE0/6-31++G** (b) and B3LYP/6-31++G** (c) level of theory. The frequencies are scaled with 0.954 (PBE0) and 0.973 (B3LYP). Calculated lines were broadened with Gaussian envelope curves (FWHM = 3 cm^{-1}).

Figure S2: IR-MPD spectrum of $[Co_4(CO)_{10}L]^-$ at 26 K, calculated IR absorption spectra for the singlet spin state performed at the Stuttgart 1997 ECP and, PBE0/6-31++G** level of theory (top) and the illustrative visualization of the calculated displacement vectors of the carbonyl modes (bottom).

1. Comparison: PBE0 and B3LYP singlet spectra

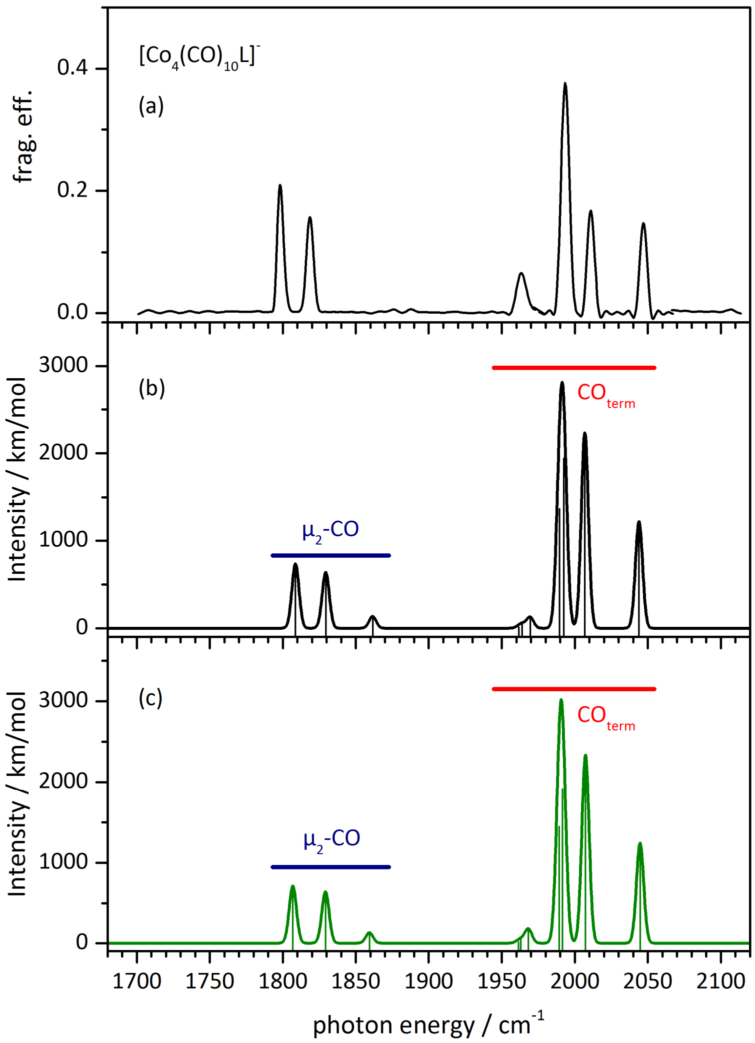

Figure S1: IR-MPD spectrum of $[Co_4(CO)_{10}L]^-$ at 26 K (a) and calculated IR absorption spectra of the geometry optimized singlet spin state. The calculations were performed at the Stuttgart 1997 ECP, PBE0/6-31++G** (b) and B3LYP/6-31++G** (c) level of theory. The frequencies are scaled with 0.954 (PBE0) and 0.973 (B3LYP). Calculated lines were broadened with Gaussian envelope curves (FWHM = 3 cm^{-1}).

2. Visualization of the calculated displacement vectors

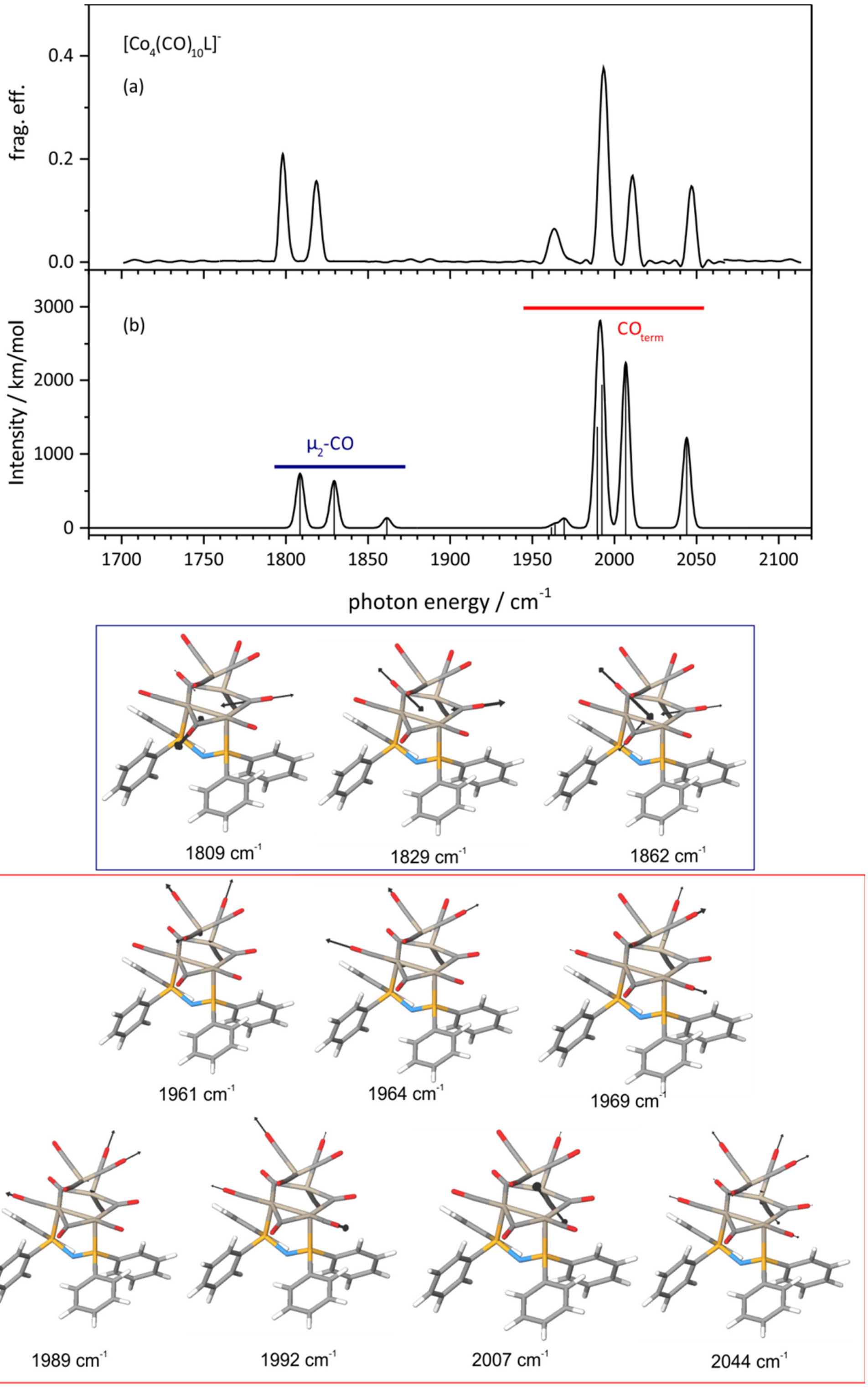

Figure S2: IR-MPD spectrum of $[Co_4(CO)_{10}L]^-$ at 26 K, calculated IR absorption spectra for the singlet spin state performed at the Stuttgart 1997 ECP and, PBE0/6-31++G** level of theory (top) and the illustrative visualization of the calculated displacement vectors of the carbonyl modes (bottom).

3.2 Vibrational fingerprints of mixed tetranuclear cobalt carbonyl/ dinitrogen clusters $[Co_4(CO)_n(dppa\text{-}H^+)N_2]^-$ within an ion trap

In the following, results on the Infrared Multiple Photon Dissociation (IR-MPD) investigation on mixed tetranuclear cobalt carbonyl/dinitrogen $[Co_4(CO)_n(dppa\text{-}H^+)N_2]^-$ ($n = 6, 8$; dppa = $NH(PPh_2)_2$) clusters are presented. The carbonyl and dinitrogen stretching vibrational frequencies of these clusters are probed and compared to the IR-MPD spectra of the previously discussed cobalt carbonyl complexes. The influence of the adsorbed N_2 on the CO stretching modes is presented and discussed. The recorded spectra reveal head-on binding of the N_2 molecules, respectively. We find strong evidence for the isomerization at a particular CO coverage ($n = 6$).

As described in the previous chapter (*cf.* 3.1.3), we obtained the deprotonated complex $[Co_4(CO)_{10}(dppa\text{-}H^+)]^-$ (abbreviated $[Co_4(CO)_{10}L]^-$) from electrospray ionization. The successive elimination of CO ligands may serve for open coordination sites on the Co cluster core. The mass selected complexes $[Co_4(CO)_{10}L]^-$ ($n = 3\text{-}10$) are guided into a 26 K hexapole ion trap. The ion trap is held at 26 K and N_2 is introduced continuously. Additional He buffer gas is introduced to accomplish efficient trapping and cooling of the ions. The cryo cooled ions are guided by electrostatic lenses into the FT-ICR cell. The N_2 gas intake results in the adsorption of one N_2 molecule to distinct complexes, $n = 6, 8$, only. The ions are isolated, irradiated by IR laser pulses, and analyzed for their fragments. The only observed fragmentation channel for the mixed carbonyl/dinitrogen comples was the loss of N_2. The laser power was attenuated to prevent excessive fragmentation. The mixed $[Co_4(CO)_8(N_2)_1L]^-$ complex could be obtained by sufficient N_2 adsorption to the $[Co_4(CO)_8L]^-$ complex (> 50 %). The N_2 adsorption to the $[Co_4(CO)_6L]^-$ complex only yielded ~ 10 % of the mixed $[Co_4(CO)_6(N_2)_1L]^-$ complex. Note, that neither an increase of N_2 pressure nor of storage times up to 5 s would drive the N_2 adsorption beyond this limit.

$[Co_4(CO)_8(N_2)_1L]^-$

We measured the IR-MPD spectra of the $[Co_4(CO)_8L]^-$, $[Co_4(CO)_9L]^-$ and $[Co_4(CO)_8(N_2)_1L]^-$ complexes (Fig. 1). All spectra exhibit several strong bands in the range from 1880 cm^{-1} to 2050 cm^{-1}, which can be assigned to the stretching vibrational modes of terminal CO ligands, and bands around 1800 cm^{-1} which can be assigned to the stretching vibration modes of μ_2-CO ligands. The mixed $[Co_4(CO)_8(N_2)_1L]^-$ complex reveals an additional band at 2197 cm^{-1} which is in line with the N2 stretching frequency of head-on bound N_2 when adsorbed on cobalt clusters (*cf.* chapter 4.1).

The direct comparison of the spectra shows a significant influence of the adsorbed N_2 on the vibrational modes of the terminal CO ligands (*cf.* Fig. 1, right). Whereas the $[Co_4(CO)_8L]^-$ complex reveals three intense terminal CO bands, the $[Co_4(CO)_9L]^-$ and $[Co_4(CO)_8(N_2)_1L]^-$ complexes exhibit four bands. The head-on adsorption of a N_2 molecule to the $[Co_4(CO)_8L]^-$ complex most likely forces a μ_2-CO ligand into a terminal bound position, similar to the arrangement in the $[Co_4(CO)_9L]^-$ complex.

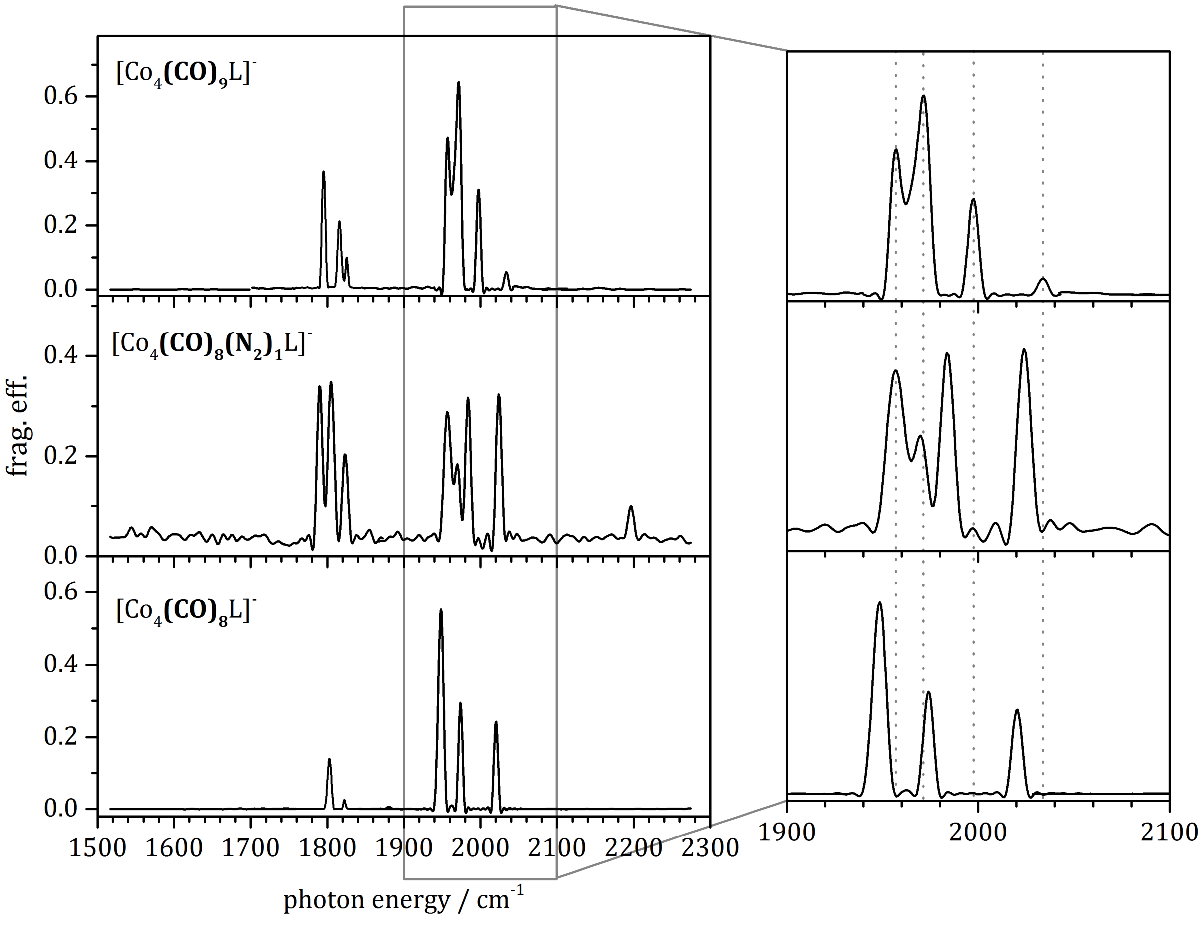

Figure 1: Left: IR-MPD spectra of the cobalt carbonyl complexes $[Co_4(CO)_nL]^-$ (n = 9, 8) in comparison with the spectrum of the mixed carbonyl/ dinitrogen complex $[Co_4(CO)_8N_2L]^-$ at 26 K. Right: A zoom into the CO_{term} stretching vibration region.

$[Co_4(CO)_6(N_2)_1L]^-$

The IR-MPD spectra of the $[Co_4(CO)_6L]^-$, $[Co_4(CO)_7L]^-$ and $[Co_4(CO)_6(N_2)_1L]^-$ complexes (Fig. 2) exhibit strong terminal CO bands and weaker vibrational modes of the μ_2-CO ligands. In the case of $[Co_4(CO)_6L]^-$ we find up to six partially resolved CO_{term} features. The mixed $[Co_4(CO)_6(N_2)_1L]^-$ complex reveals three partially resolved CO_{term} features, three μ_2-CO stretching frequencies and two N_2 stretching frequencies around 2180 cm^{-1}. The IR-MPD spectrum also shows two additional bands around 1700 cm^{-1} which might originate from μ_3-CO coordination. These findings strongly corroborate the presence of isomers. Isomeric variance may originate from Co_4 core isomers, from variation of CO coordination, or even from a coexistence of complexes in different spin multiplets (singlet/triplet/quintet/…).

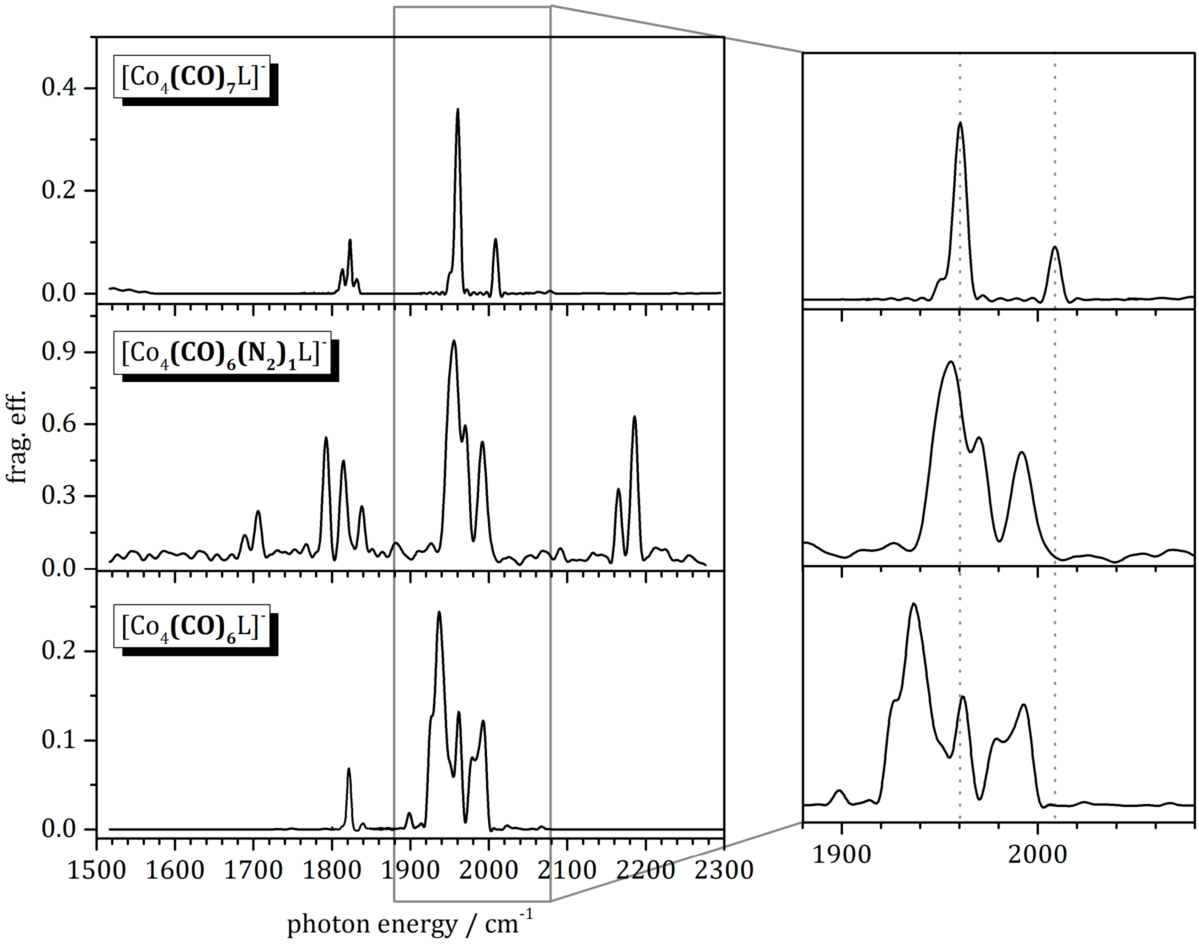

Figure 2: Left: IR-MPD spectra of the cobalt carbonyl complexes $[Co_4(CO)_nL]^-$ (n = 7, 6) in comparison with the spectrum of the mixed carbonyl/ dinitrogen complex $[Co_4(CO)_6N_2L]^-$ at 26 K. Right: A zoom into the CO_{term} stretching vibration region.

The fact that the N_2 adsorption to the $[Co_4(CO)_6L]^-$ complex is limited to ~ 10 % and the occurrence of two N_2 stretching frequencies in the IR-MPD spectra of the $[Co_4(CO)_6(N_2)_1L]^-$ complex indicate the existence of at least three isomers. Further elucidation of the origin of all observed vibrational features remains to persistent density functional theory (DFT) computations of the stepwise decarbonylation and distinct N_2 adsorption.

4. CRYO KINETICS AND SPECTROSCOPY OF CATIONIC TRANSITION METAL CLUSTERS

In this chapter I present the results on N_2 adsorption studies on cationic iron, cobalt and nickel clusters under cryo conditions and in isolation. The results on isothermal gas phase cryo kinetics and infrared photon dissociation spectroscopy are given, discussed, introduced and concluded in two published paper manuscripts and two paper drafts. The contributions of myself to the presented manuscripts are stated prior to the respective manuscripts.

4.1 Publication: “Infrared spectroscopy of N_2 adsorption on size selected cobalt cluster cations in isolation”

The following work has been published at Physical Chemistry Chemical Physics with the title: “Infrared spectroscopy of N_2 adsorption on size selected cobalt cluster cations in isolation”.

The experiments were performed by the experimental team consisting of S. Dillinger, J. Hewer, M. Gaffga and myself. The data evaluation was done by S. Dillinger and myself. G. Niedner-Schatteburg performed the computations and was involved in the revision of the manuscript. The initial paper draft was put together by S. Dillinger.

The contributions of myself to the presented manuscript consist in being part of the experimental team which acquired the presented data, being involved in the data evaluation and revision of the manuscript.

Full reference to the publication:

SEBASTIAN DILLINGER, JENNIFER MOHRBACH, JOACHIM HEWER, MAXIMILAN GAFFGA, AND GEREON NIEDNER-SCHATTEBURG, *Infrared spectroscopy of N_2 adsorption on size selected cobalt cluster cations in isolation,* Phys. Chem. Chem. Phys., **2015**, *17,* 10358.

DOI: 10.1039/c5cp00047e

Infrared Spectroscopy of N_2 Adsorption on Size Selected Cobalt Cluster Cations in Isolation

Sebastian Dillinger, Jennifer Mohrbach, Joachim Hewer, Maximilian Gaffga,
and Gereon Niedner-Schatteburg

Fachbereich Chemie and Forschungszentrum OPTIMAS,
Technische Universität Kaiserslautern, 67663 Kaiserslautern, Germany

4.1.1 Abstract

We report IR active N_2 stretching frequencies in isolated and size selected cobalt cluster nitrogen adsorbate complexes, $[Co_n(N_2)_1]^+$ as recorded by virtue of InfraRed Photon Dissociation (IRPD) spectroscopy. The observed frequencies of the $[Co_n(N_2)_1]^+$ complexes ($n = 8 – 17$) are significantly redshifted (2180 to 2290 cm^{-1}) with respect to the IR inactive vibrations of free N_2 (2359 cm^{-1}). These bands are assigned to a μ_1 head-on type of coordination of the N_2 to the cobalt cluster surface, revealing remarkable cluster size dependent features to interpret.

4.1.2 Introduction

It is often difficult to investigate heterogeneously catalyzed reactions due to their complexity. Reactions of isolated transition metal clusters may serve to elucidate elementary processes in such reactions. The initial adsorption event is often the rate limiting step in multistep bond activation that precedes any further activation and the phenomenon of gas adsorption in layers became early subject of research.[1-2] Historically adsorption is classified into chemisorption and physisorption by phenomenological persistence of the adsorbate. Physisorbed species often serve as precursors for activation. The initial adsorption and activation of N_2 is the rate limiting step in the Haber-Bosch process. Therefore the characterization of the precursor state is of great importance for the mechanistic understanding of this catalytic conversion.[3]

CO adsorption on metal surfaces has been characterized by numerous kinetic[4-7] and spectroscopic studies.[8-10] The observed redshift of the CO stretching vibration is understood to indicate the CO coordination site – on top (μ_1), on bridge (μ_2) or on hollow (μ_3). It moreover reflects interaction strength and of course charge effects. Complementary insights arise from the IR based characterization of CO adsorbates on the surfaces of isolated metal clusters.[11-13]

There is equally great interest in the kinetics of the N_2 adsorption on metal surfaces.[14-16] Spectroscopic and kinetic studies of N_2 adsorbed on Fe(111) revealed that there are three characteristic α-, δ- and γ-states, which refer to side-on, and head-on adsorption to highly and to less coordinated metal surface atoms.[17-19] Many reaction studies have been performed for a better understanding of the N_2 adsorption kinetics with metal clusters.[20-25] Two of these studies[24-25] have drawn far reaching structural conclusions from so called uptake plots of average association numbers of multiple N_2 molecules under flow reactor conditions. They discuss icosahedral, hexagonal (hcp) and face centered cubic (fcc) packing speculating about pressure dependent inter conversion. Despite obvious need merely a single spectroscopic study elucidated the N_2 adsorption on isolated metal clusters, namely those of Ruthenium,[26] with no unambiguous assignment of the recorded spectral features.

Common interpretation of the head-on adsorption of CO and N_2 to surfaces of extended bulk metal samples and of size selected clusters arises in terms of a σ-donor π-acceptor synergistic bonding scheme according to the so called Blyholder model.[27] *Ab initio* DFT modelling reaches its limits when it comes to the appropriate choice of exchange correlation functionals.[7]

The present study probes the N-N stretching frequency of N_2 when adsorbed on size selected cobalt cluster cations at cryogenic temperatures. We aim to gain insight into the binding motifs of the adsorbates and towards the structure of the cobalt clusters themselves. Preliminary *ab initio* DFT calculations augment the current experiments, failing to provide unambiguous structural conclusions as of now.

4.1.3 Experimental Methods

A customized Fourier Transform - Ion Cyclotron Resonance (FT-ICR) – mass spectrometer (Apex Ultra Bruker Daltonics) served to perform the cluster production, isolation, N_2 condensation, InfraRed Photon Dissociation (IRPD) and mass analysis. The metal clusters were generated using a home-built laser vaporization cluster ion source as described before.[28-29] In brief, cobalt atoms are evaporated from a rotating 1 mm thick cobalt foil by the second harmonic of a pulsed Nd:YAG laser. The hot plasma is captured by a He gas pulse (40 µs, 10 – 15 bar) created by a home-built piezoelectric valve.[30] The atoms and ions are cooled and aggregate to clusters in the subsequent jet expansion through a 60 mm long channel (2 mm diameter) into vacuum (10^{-6} mbar). The clusters are skimmed and injected into a cryogenic hexapole ion trap passing different ion lenses, a 90 degrees ion beam bender and a quadrupole mass filter. The ion trap is cooled to 26 K by a closed cycle He cryostat. Buffer or reaction gas can be introduced both pulsed and continuously. In this work we used the continuous gas inlet. He or Ar (He: $[Co_{8-10}(N_2)_1]^+$, Ar: $[Co_{11-17}(N_2)_1]^+$) is used to increase the pressure in the ion trap from 1.7×10^{-7} mbar up to 1.0×10^{-6} mbar to accomplish the efficient trapping and cooling of the ions. The attachment of nitrogen is achieved due to impurities in the buffer gas and can only be observed at temperatures below 28 K. After storage of the ions for a variable time (0 – 10 s), the manipulated ions are guided by electrostatic lenses into the FT-ICR cell of the so-called “infinity” type.[31] This cell is held at a temperature of 10 K with a closed cycle He cryostat to prevent heating of the clusters by black body radiation. The cell is also used for isolation and detection of the ions.

For the acquisition of the (IRPD) spectra the FT-ICR cell is coupled to a tunable IR laser ($\delta n = 0.9$ cm^{-1}, $\delta t = 7$ ns). This laser is a KTP/KTA optical parametric oscillator/amplifier (OPO/A, LaserVision) system pumped by a pulsed 10 Hz injection seeded Nd:YAG laser (PL8000, Continuum). The difference frequency (DF) between the OPA signal and idler waves is generated in a $AgGaSe_2$ crystal. This generates IR radiation in the range of 1400 – 2400 cm^{-1}. Each trapped and isolated package of ions is irradiated by 10 – 15 laser pulses (0.1 – 1.2 mJ/pulse) to yield a sufficient amount of fragment ions. The IR spectra were recorded as ion chromatograms while continuously scanning the IR wavelength. The IRPD signal was evaluated as $\Sigma_i F_i/(\Sigma_i F_i+\Sigma_i P_i)$, where F_i and P_i indicate fragment and the parent ion signals, respectively. An experimental IRPD spectrum arises from a plot of the fragmentation efficiency as a function of laser frequency. We employed the IRPD spectroscopy in the 2100 – 2350 cm^{-1} range on the $[Co_n(N_2)_1]^+$ species (n = 8 – 17). In this range we expected the N_2 stretching frequencies of the species. For all complexes the loss of the N_2 was the only observed fragmentation channel.

4.1.4 Results and Discussion

The cold IRPD spectra of the cryo cooled $[Co_n(N_2)_1]^+$ cluster adsorbate complexes reveal well resolved bands (*cf.* Fig. 1). All complexes show a single or multiple IR active bands within the range of 2180 to 2290 cm^{-1} (2110 – 2350 cm^{-1} probed). These bands are significantly redshifted with respect to the IR inactive stretching mode of free N_2 (at 2359 cm^{-1} [32]). Some clusters show multiple bands (n = 14 – 17), other clusters reveal single bands (n = 8 – 13). Dissociative $[N\text{-}Co_n\text{-}N]^+$ adsorption would inevitably lead to much lower Co-N stretching frequencies which may become as low as 600 cm^{-1} when interstitial nitrides form. Therefore we confirm molecular (intact) adsorption (physisorption) of N_2 on naked cobalt cluster surfaces. While we cannot exclude some (at present invisible) dissociation of N_2 we do not find forcing evidence. Such an activation would, if any, occur in competition to intact adsorption

The observed cluster size dependence reveals continuous variations and "jumps"/discontinuities alike. The dotted red line serves to guide the eye. It is slightly tilted towards the red with cluster size. A plain charge dilution effect would lead to an opposite effect namely to a blue shifting by increasing cluster size. Instead one might recall the (likely) metallic nature of the cobalt cluster allowing for electron density shifts in response to external perturbation. Such polarization may couple back to the perturbing adsorbate – the more the larger the cluster. Hence this would lead to a weakening of the N-N binding strength and an increasing redshift of the stretching frequency with cluster size.

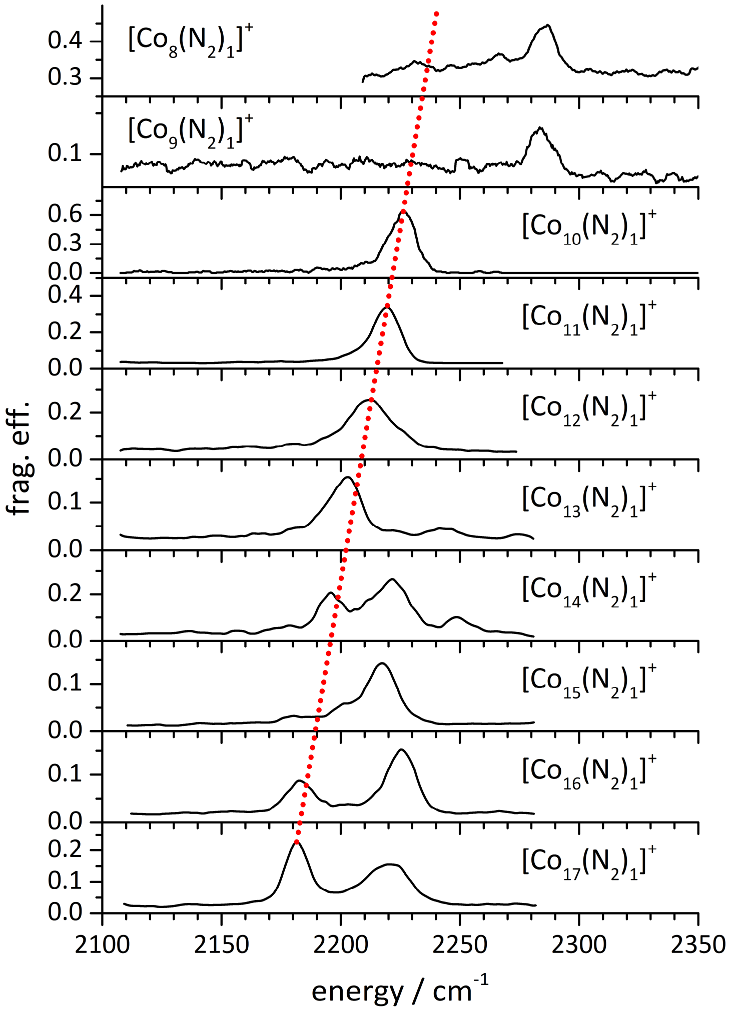

Fig. 1: IRPD spectra of $[Co_n(N_2)_1]^+$ for n = 8 – 17. The dotted red line serves to guide the eye. Its slight tilt with cluster size indicates a conceivable cooperative polarization effect. Note the variation in the observed peak positions and splittings. Multiple major peaks likely indicate cluster core isomers, spin isomers or N_2 bonding isomers while weak sidebands to the blue may arise from combination bands (N_2 stretching and wagging modes, *cf.* Table 1). Note the "jump" of the major peak from n = 9 to n = 10.

Looking at the bands in detail it is obvious that $[Co_8(N_2)_1]^+$ and $[Co_9(N_2)_1]^+$ do not follow the trend illustrated by the red line. The absorption of $[Co_8(N_2)_1]^+$ and $[Co_9(N_2)_1]^+$ (both at 2285 cm^{-1}) are significantly less redshifted than those of all other cluster complexes studied. The clusters with n = 10 – 13 show merely one strong band that aligns well to the mentioned polarization effect (2226, 2219, 2212, 2203 cm^{-1}). In the case of $[Co_{13}(N_2)_1]^+$ this main absorption band is accompanied by weak sidebands to the blue. These may arise from combination bands (N_2 stretching and wagging modes, *cf.* Table 1, as supported by calculations). Besides these sidebands of $[Co_{13}(N_2)_1]^+$, the main band is in line with a possible icosahedral structure (I_h). A major difference arises for even larger clusters, which reveal multiple bands. These are possibly due to cobalt cluster isomers, to spin state isomers or to N_2 bonding isomers or to combinations of all three effects. $[Co_{14}(N_2)_1]^+$ is most prominent in revealing three major bands (at 2195, 2222, 2248 cm^{-1}). A possible explanation is the presence of spin isomers. The Co_{14}^+ cluster core structure is conceivable, yet speculative. Our preliminary calculations reveal a possible adatom to a icosahedral core (little overall relaxation), alternatively: significant reorganization (from Co_{13}^+ to Co_{14}^+) through incorporation of the extra Co atom into prior Co_{13}^+ cluster surface, e.g. by opening the prior five membered rings to a six membered ring. This would provide for a higher (sixfold) coordinated Co surface atom in the center of the six membered ring. This working hypothesis might serve to explain the new band at 2222 cm^{-1} in $[Co_{14}(N_2)_1]^+$.

A similar picture can be found in $[Co_{15}(N_2)_1]^+$, except for the vanishing “red” peak (which was strong for $[Co_{10\text{-}14}(N_2)_1]^+$), indicative of a major change in structural binding motif. Possibly explained by a change from icosahedral to hexagonal close-packed (hcp) as found in larger cobalt clusters by Trapped Ion Electron Diffraction (TIED) experiments (Co bulk: hcp; Co cluster: icosahedral).[33]

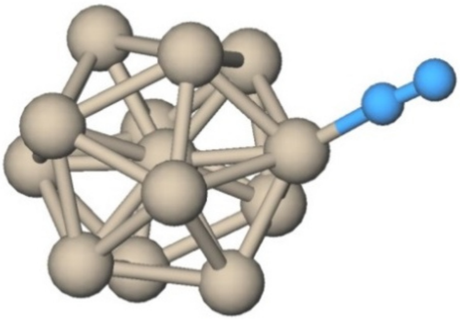

Fig. 2: Computed geometry of $[Co_{13}(N_2)_1]^+$. The assumed icosahedral Co_{13}^+ core is a low lying stable geometry, and it only physisorbs N_2 in μ_1 head-on coordination. Note, that all cobalt surface atoms are equivalent, thus giving rise to a single IR active N-N stretching vibration at about 2230 cm^{-1} (scaled by 0.95) with variations by spin multiplicity of the cobalt cluster core (likely 2 S + 1 = 25, 27, 29, 31) (See text for discussion).

DFT calculations of $[Co_{13}(N_2)_1]^+$ (at PBE0/ECP(Co); cc-pVTZ(N) level of theory) reveal full icosahedral I_h geometry of the Co_{13}^+ core with little relaxation by the N_2 attachment. SCF convergence is tedious and can be achieved only by tolerating relaxed SCF convergence criteria of 10^{-5} (as compared to 10^{-8} in "standard" DFT calculations). Choice of an appropriate spin multiplicity is crucial. Our previous XMCD investigations yielded a spin magnetic moment of 2.30(15) μ_B/atom for the Co_{14}^+ cluster.[34] That implies 32(2) unpaired electrons and a multiplicity of $\mathbf{2S+1=33(2)}$. Our present DFT calculations have revealed stable high spin state structures of a $[Co_{14}(N_2)_1]^+$ complex with multiplicities 30 (+47), 32(0) and 34(+29), relative stabilities in kJ/mol indicated in parentheses. Both findings are in good agreement - assuming that N_2 adsorption does not alter spin states in Co_{14}^+.

On the basis of this agreement we utilized our DFT approach to undertake an extended search of minimum structures of $[Co_8(N_2)_1]^+$, $[Co_9(N_2)_1]^+$, $[Co_{10}(N_2)_1]^+$ (*cf.* Fig. 3), $[Co_{13}(N_2)_1]^+$, $[Co_{14}(N_2)_1]^+$ and $[Co_{17}(N_2)_1]^+$. The calculations reveal head-on N_2 binding in μ_1 N-Co coordination, irrespective of chosen cobalt cluster geometry – allowing for full relaxation without constraints – and irrespective of chosen N_2 coordination site, and irrespective of particular spin multiplicity. Other assumed coordinations (μ_2 or μ_3) relax towards μ_1 coordination. Any activation towards dinitride species was found vastly endothermic.

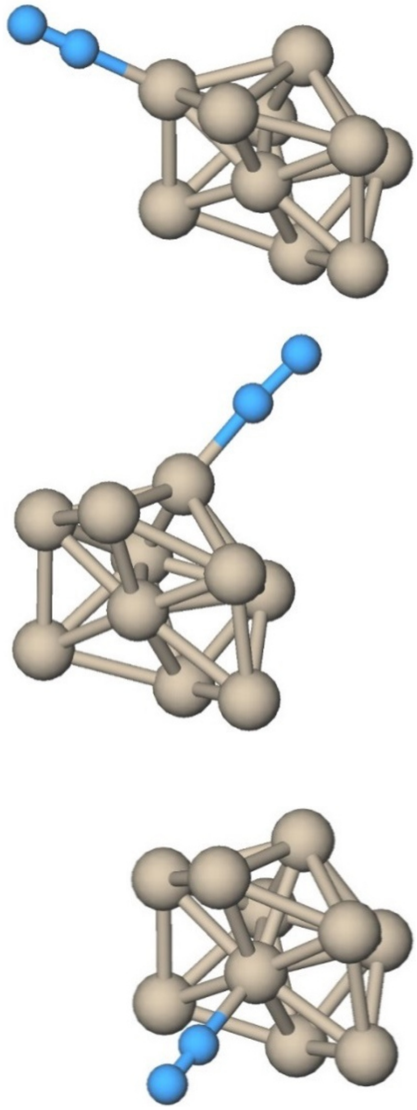

Fig. 3: Three computed geometries of $[Co_{10}(N_2)_1]^+$. The calculated species show the different binding sites of N_2 to the Co_{10}^+ core. N_2 only coordinates μ_1 head-on. The structures differ in the binding motif of the coordination site (Co atom). The structures illustrate an adsorption of N_2 on a Co atom which in turn coordinates to four -(top), five -(middle) or six-(bottom) membered cobalt atom rings. It comes somewhat as a surprise that the present DFT calculations find little variation of N_2 stretching frequencies in response to this change of coordination (e.g. shifts by less than 10 cm^{-1}).

Table 1: Computed vibrations in $[Co_{13}(N_2)_1]^+$ (I_h, $2S + 1 = 15$). Explicitly listed values document all those modes that involve significant motion of either of the two N-atoms.

Mode	Type	Freq. cm^{-1}	Scaled freq. cm^{-1}	IR intensity km mole^{-1}
ν_1	N_2 wagging	33.8	32.1	0.04
ν_2	N_2 wagging	46.7	44.4	0.08
ν_3	N↑-N-Co↓ bending	78	74	0.17
ν_3 … ν_{37}	Co_{13}^+ skeleton modes	78 … 306		< 2.7
ν_{38}	N↑-N↓-Co↑ bending	354	336	37
ν_{39}	N-N stretching	2338	2221	605

Standard *ab initio* calculations reveal force constants and subsequent normal mode analysis reveal harmonic vibrational frequencies. After appropriate lump sum scaling for anharmonicities (empirical factor 0.95) the thus obtained values compare to experimental data. We chose to document the case of $[Co_{13}(N_2)_1]^+$ in more detail (*cf.* Table 1) assuming an icosahedral I_h geometry of Co_{13}^+ (*cf.* Fig. 2) The IR inactive N-N stretching mode of free N_2 at 2359 cm^{-1} redshifts through coordination with Co_{13}^+ to 2203 cm^{-1} (expt.) and 2221 cm^{-1} (calc. ν_{39}) in $[Co_{13}(N_2)_1]^+$. The concomitant N-N-Co bending mode within $[Co_{13}(N_2)_1]^+$ is predicted to occur at 336 cm^{-1} which is outside of our experimental probing range. However, the experimental spectrum reveals weak sidebands to the N_2 stretching mode which locate at $\nu_s(N_2)$ + 15 cm^{-1}, 35 cm^{-1} and (maybe) 68 cm^{-1}. We assign these sidebands to combination modes ($\nu_{39} + \nu_1$), ($\nu_{39} + \nu_2$) and ($\nu_{39} + \nu_3$), which is in qualitative agreement with the DFT computed ν_1, ν_2 and ν_3 values of + 32 cm^{-1}, + 44 cm^{-1} and + 78 cm^{-1}.

Despite all current effort the accordingly computed vibrational spectra of other clusters (as listed above) do not recover the subtle changes in the recorded experimental spectra. Obtained N_2 stretching frequencies do indeed fall into the range of experimental values. There is, however, no further insight from calculations into the origin of the three experimental observations: general and steady increase of N_2 redshift, sudden increase of N_2 redshift when going from $[Co_{8,9}(N_2)_1]^+$ to $[Co_{10}(N_2)_1]^+$, and multiple strong vibrational peaks in the spectra of cluster $[Co_{14}(N_2)_1]^+$ and beyond.

It remains to be seen whether further calculations achieve more insight. Four improvements come to our minds. Broken symmetry DFT would allow to check for conceivable antiferromagnetic coupling.[35-38] Variation of the DFT functional is mandatory and tedious. Dispersion interaction needs to be considered. Dynamic basin hopping/annealing calculations might retrieve otherwise overlooked geometries.

4.1.5 Conclusions

The N_2 adsorption on cationic Co_n^+ clusters in the size range of n = 8 – 17 has been investigated via IRPD spectroscopy. The recorded spectra revealed remarkable cluster size dependent features. All species show bands within the range of 2180 to 2290 cm^{-1}, suggesting a head-on μ_1 coordination of the N_2 on the cluster surface. Current DFT calculations reveal a possible icosahedral Co_{13}^+ core. Nevertheless the calculations do not allow for a final assignment of the observed spectral features (e.g. the "jump" from n = 9 to n = 10 or the presence of multiple bands). It is mandatory to spend further effort in *ab initio* calculations to gain invaluable insight into the binding motifs of the nitrogen and of conceivable activation routes.

4.1.6 Acknowledgements

This work was supported by the DFG founded transregional collaborative research center SFB/TRR 88 "3MET.de" and by the state research center OPTIMAS.

4.1.7 Notes and references

1. Langmuir, I., THE ADSORPTION OF GASES ON PLANE SURFACES OF GLASS, MICA AND PLATINUM. *J. Am. Chem. Soc.* **1918,** *40*, 1361-1403.
2. Brunauer, S.; Emmett, P. H.; Teller, E., Adsorption of gases in multimolecular layers. *J. Am. Chem. Soc.* **1938,** *60*, 309-319.
3. Ertl, G., Surface Science and Catalysis—Studies on the Mechanism of Ammonia Synthesis: The P. H. Emmett Award Address. *Catalysis Reviews* **1980,** *21* (2), 201-223.
4. Cox, D. M.; Reichmann, K. C.; Trevor, D. J.; Kaldor, A., CO CHEMISORPTION ON FREE GAS-PHASE METAL-CLUSTERS. *J. Chem. Phys.* **1988,** *88* (1), 111-119.
5. Somorjai, G. A., *Introduction to Surface Chemistry and Catalysis*. John Wiley & Sons: **1994**.
6. Ertl, G.; Neumann, M.; Streit, K. M., Chemisorption of CO on the Pt(111) surface. *Surf. Sci.* **1977,** *64* (2), 393-410.
7. Nilsson, A.; Pettersson, L. G. M., Chapter 2 - Adsorbate Electronic Structure and Bonding on Metal Surfaces. In *Chemical Bonding at Surfaces and Interfaces*, Nørskov, A. N. G. M. P. K., Ed. Elsevier: Amsterdam, **2008**; pp 57-142.
8. Crossley, A.; King, D. A., INFRARED-SPECTRA FOR CO ISOTOPES CHEMISORBED ON PT 111 - EVIDENCE FOR STRONG ABSORBATE COUPLING INTERACTIONS. *Surf. Sci.* **1977,** *68* (1), 528-538.
9. Hammaker, R. M.; Francis, S. A.; Eischens, R. P., INFRARED STUDY OF INTERMOLECULAR INTERACTIONS FOR CARBON MONOXIDE CHEMISORBED ON PLATINUM. *Spectrochimica Acta* **1965,** *21* (7), 1295-&.
10. Hoffmann, F. M., Infrared reflection-absorption spectroscopy of adsorbed molecules. *Surf. Sci. Rep.* **1983,** *3* (2-3), 107-192.
11. Fielicke, A.; Gruene, P.; Meijer, G.; Rayner, D. M., The adsorption of CO on transition metal clusters: A case study of cluster surface chemistry. *Surf. Sci.* **2009,** *603* (10-12), 1427-1433.
12. Fielicke, A.; von Helden, G.; Meijer, G.; Pedersen, D. B.; Simard, B.; Rayner, D. M., Size and charge effects on the binding of CO to late transition metal clusters. *J. Chem. Phys.* **2006,** *124* (19).
13. Lyon, J. T.; Gruene, P.; Fielicke, A.; Meijer, G.; Rayner, D. M., Probing C-O bond activation on gas-phase transition metal clusters: Infrared multiple photon dissociation spectroscopy of Fe, Ru, Re, and W cluster CO complexes. *J. Chem. Phys.* **2009,** *131* (18).
14. King, D. A.; Wells, M. G., REACTION-MECHANISM IN CHEMISORPTION KINETICS - NITROGEN ON (100) PLANE OF TUNGSTEN. *Proceedings of the Royal Society of London Series a-Mathematical and Physical Sciences* **1974,** *339* (1617), 245-269.
15. King, D. A.; Wells, M. G., MOLECULAR-BEAM INVESTIGATION OF ADSORPTION KINETICS ON BULK METAL TARGETS - NITROGEN ON TUNGSTEN. *Surf. Sci.* **1972,** *29* (2), 454-&.
16. Ertl, G.; Lee, S. B.; Weiss, M., Kinetics of nitrogen adsorption on Fe(111). *Surf. Sci.* **1982,** *114* (2–3), 515-526.

17. Rao, C. N. R.; Rao, G. R., NATURE OF NITROGEN ADSORBED ON TRANSITION-METAL SURFACES AS REVEALED BY ELECTRON-SPECTROSCOPY AND COGNATE TECHNIQUES. *Surf. Sci. Rep.* **1991,** *13* (7), 221-263.
18. Tsai, M. C.; Ship, U.; Bassignana, I. C.; Küppers, J.; Ertl, G., A vibrational spectroscopy study on the interaction of N2 with clean and K-promoted Fe(111) surfaces: π-bonded dinitrogen as precursor for dissociation. *Surf. Sci.* **1985,** *155* (2–3), 387-399.
19. Mortensen, J. J.; Hansen, L. B.; Hammer, B.; Nørskov, J. K., Nitrogen Adsorption and Dissociation on Fe(111). *J. Catal.* **1999,** *182* (2), 479-488.
20. Knickelbein, M. B., Reactions of transition metal clusters with small molecules. *Annu. Rev. Phys. Chem.* **1999,** *50*, 79-115.
21. Morse, M. D.; Geusic, M. E.; Heath, J. R.; Smalley, R. E., SURFACE-REACTIONS OF METAL-CLUSTERS .2. REACTIVITY SURVEYS WITH D-2,N-2, AND CO. *J. Chem. Phys.* **1985,** *83* (5), 2293-2304.
22. Berces, A.; Hackett, P. A.; Lian, L.; Mitchell, S. A.; Rayner, D. M., Reactivity of niobium clusters with nitrogen and deuterium. *J. Chem. Phys.* **1998,** *108* (13), 5476-5490.
23. Fuyi, L.; Ming, L.; Lin, T.; Armentrout, P. B., Guided ion beam studies of the reactions of Co n+ (n=1-18) with N 2: cobalt cluster mononitride and dinitride bond energies. *J. Chem. Phys.* **2008,** *128* (19), 194313-1-194313-194313-12.
24. Ho, J.; Parks, E. K.; Zhu, L.; Riley, S. J., REACTIONS OF SMALL COBALT CLUSTERS WITH N-2 - IMPLICATIONS FOR CLUSTER STRUCTURE. *Chem. Phys.* **1995,** *201* (1), 245-261.
25. Riley, S. J., The atomic structure of transition metal clusters. *J. Non-Cryst. Solids* **1996,** *205–207, Part 2* (0), 781-787.
26. Kerpal, C.; Harding, D. J.; Lyon, J. T.; Meijer, G.; Fielicke, A., N-2 Activation by Neutral Ruthenium Clusters. *J. Phys. Chem. C* **2013,** *117* (23), 12153-12158.
27. Blyholder, G., MOLECULAR ORBITAL VIEW OF CHEMISORBED CARBON MONOXIDE. *J. Phys. Chem.* **1964,** *68* (10), 2772-&.
28. Maruyama, S.; Anderson, L. R.; Smalley, R. E., DIRECT INJECTION SUPERSONIC CLUSTER BEAM SOURCE FOR FT-ICR STUDIES OF CLUSTERS. *Rev. Sci. Instrum.* **1990,** *61* (12), 3686-3693.
29. Berg, C.; Schindler, T.; Niednerschatteburg, G.; Bondybey, V. E., REACTIONS OF SIMPLE HYDROCARBONS WITH NB-N(+) - CHEMISORPTION AND PHYSISORPTION ON IONIZED NIOBIUM CLUSTERS. *J. Chem. Phys.* **1995,** *102* (12), 4870-4884.
30. Proch, D.; Trickl, T., A HIGH-INTENSITY MULTI-PURPOSE PIEZOELECTRIC PULSED MOLECULAR-BEAM SOURCE. *Rev. Sci. Instrum.* **1989,** *60* (4), 713-716.
31. Caravatti, P.; Allemann, M., The ‘infinity cell’: A new trapped-ion cell with radiofrequency covered trapping electrodes for fourier transform ion cyclotron resonance mass spectrometry. *Org. Mass Spectrom.* **1991,** *26* (5), 514-518.
32. Haynes, W. M., *CRC Handbook of Chemistry and Physics, 93rd Edition*. Taylor & Francis: **2012**.

33. Rapps, T.; Ahlrichs, R.; Waldt, E.; Kappes, M. M.; Schooss, D., On the Structures of 55-Atom Transition-Metal Clusters and Their Relationship to the Crystalline Bulk. *Angewandte Chemie-International Edition* **2013,** *52* (23), 6102-6105.
34. Peredkov, S.; Neeb, M.; Eberhardt, W.; Meyer, J.; Tombers, M.; Kampschulte, H.; Niedner-Schatteburg, G., Spin and Orbital Magnetic Moments of Free Nanoparticles. *Phys. Rev. Lett.* **2011,** *107* (23).
35. Kessler, E. M. V.; Schmitt, S.; van Wullen, C., Broken symmetry approach to density functional calculation of zero field splittings including anisotropic exchange interactions. *J. Chem. Phys.* **2013,** *139* (18).
36. van Wullen, C., Broken Symmetry Approach to Density Functional Calculation of Magnetic Anisotropy or Zero Field Splittings for Multinuclear Complexes with Antiferromagnetic Coupling. *J. Phys. Chem. A* **2009,** *113* (43), 11535-11540.
37. Neese, F., Definition of corresponding orbitals and the diradical character in broken symmetry DFT calculations on spin coupled systems. *J. Phys. Chem. Solids* **2004,** *65* (4), 781-785.
38. Neese, F., Prediction of molecular properties and molecular spectroscopy with density functional theory: From fundamental theory to exchange-coupling. *Coord. Chem. Rev.* **2009,** *253* (5-6), 526-563.

4.2 Publication: "Cryo Kinetics and Spectroscopy of Cationic Nickel Clusters: Rough and Smooth Surfaces"

The following work has been published in a slightly shorter version at the Journal of Physical Chemistry C with the title: "Cryo Kinetics and Spectroscopy of Cationic Nickel Clusters: Rough and Smooth Surfaces".

The experiments were performed by S. Dillinger and myself. The computations were performed by S. Dillinger. The data evaluation was done by myself. The initial paper draft was put together by myself. G. Niedner-Schatteburg was involved in the revision of the manuscript.

Full reference to the publication:

JENNIFER MOHRBACH, SEBASTIAN DILLINGER, AND GEREON NIEDNER-SCHATTEBURG, *Cryo Kinetics and Spectroscopy of Cationic Nickel Clusters: Rough and Smooth Surfaces,* J. Phys. Chem. C, **2017**, *121* (20), 10907–10918.

DOI: 10.1021/acs.jpcc.6b12167

Cryo Kinetics and Spectroscopy of Cationic Nickel Clusters: Rough and Smooth Surfaces

Jennifer Mohrbach, Sebastian Dillinger, and Gereon Niedner-Schatteburg

Fachbereich Chemie and Forschungszentrum OPTIMAS,
Technische Universität Kaiserslautern,
67663 Kaiserslautern, Germany

4.2.1. Abstract

The stepwise N_2 adsorption on size selected Ni_9^+ and Ni_{13}^+ clusters at 26 K is studied in a hybrid tandem ion trap instrument. Adsorption kinetics of these clusters in conjunction with Infrared Photon Dissociation (IR-PD) spectroscopy of their cluster adsorbate complexes allow for the elucidation of various N_2 coverage and cluster size dependent effects, which are related to the rough Ni_9^+ and smooth Ni_{13}^+ cluster surface morphologies. Pseudo-first-order kinetic fits confirm consecutive adsorption steps by single exponentially decays exclusively. The recorded IR-PD spectra of all observed cluster adsorbate complexes reveal IR active vibrational bands at frequencies of 2170 cm^{-1} to 2260 cm^{-1}, which coincides with the range of metal head-on coordinated N-N stretching modes. Density Functional Theory (DFT) calculations confirm the experiments and reinforce a possible isomerization with low N_2 coverage in the case of Ni_9^+.

4.2.2 Introduction

Reactivity studies of naked metal clusters are an ongoing endeavor, providing new perspectives on the repetitively stated cluster-surface analogy.[1-6] In the “non-scalable cluster size regime”[7-9] atom-by-atom dependent variation superimpose to the gradual, scalable change of cluster properties by size.[7, 10] Non-scalable jumps in molecular adsorption to size selected clusters have been interpreted in terms of structural changes at local binding sites on the cluster surfaces.[11-15] In the context of CO adsorption to metal clusters and of related carbonyl complexes it showed that adsorbates may well serve to titrate available surface sites up to saturation for the elucidation of underlying structural motifs.[16-17] Beyond mere adsorption it warrants to study and understand the activation of this and other diatomic molecules such as e.g. NO, N_2, and H_2, driven by perspectives and challenges in heterogeneous catalysis.[18-20]

It has proven helpful to study the vibrational modes of adsorbates on transition metal (TM) clusters and in TM coordination complexes as isolated ions by Infrared Multiple Photon Dissociation (IR-MPD).[21-24] This method has further gained by the introduction of tunable free electron lasers (FEL).[25-27] Cryo IR-action spectroscopy achieves significant advances by so called tagging or messenger techniques where weakly bound species serve to provide for a preferred fragmentation channel, sometimes driven by single photon absorption.[28-29] The study of in situ generated TM clusters helped to elucidate the influence of net charge and oxidation state onto the single molecule CO adsorption in terms of a charge dilution model.[30-32]

N_2 coordination. Isoelectronic to CO, the N_2 molecule - nonpolar when isolated – polarizes upon surface adsorption through a σ donor π acceptor synergism in analogy to that of CO – some differences in size and shape of participating MOs notwithstanding. The resulting red shifts of CO vibrations are usually discussed in terms of the Dewar-Chatt-Duncanson model, which explains coordinative complexation to single TM centers,[33-34] or in terms of the Blyholder model, when interpreting surface coordination.[35] The concept of both models applies to N_2 adsorption as well. The discovery of Dinitrogen-pent-amine Ru(II) complexes in 1965[36] has initiated a fertile field of N_2 coordination chemistry[37-40] in quest for its activation.

Early DFT revealed strong preference of N_2 for end-on coordination to single Fe centers with some evidence for rather exceptional side-on η^2 coordination of at most two N_2 to otherwise naked Fe atoms.[41-42] Other than in a Zr-N_2-Zr arrangement[39, 43] and to the best of our knowledge there is no spectroscopic evidence for such side-on coordination to a transition metal center in a molecular coordination complex. In this respect, it pays to recognize a most recent study of N_2 adsorption to Ta clusters, which interprets their experimental findings in terms of a DFT computed N_2 side-on (η^2) coordination.[44] Recent IR-MPD studies of N_2 adsorption to Ru clusters have concluded in exclusive end-on (η^1) coordination.[45]

Prior studies of nickel clusters. Experiments on magnetism of neutral and cationic Ni clusters were recently reviewed in the context of XMCD gas phase studies.[46] In parallel to the experiments an increasing interest arose to model the electronic and magnetic properties of these nickel clusters,[47-49] and of nickel alloys.[48, 50-52] The particularly narrow PES spectrum of Ni_{13} was interpreted in terms of a highly symmetric structure, likely of icosahedral T_d symmetry.[53-54] CO adsorption up to saturation to small nickel clusters Ni_n ($n = 2$-20) revealed the limits of electron counting rules and the stability of larger clusters with internal metal atoms, while small clusters ($n \leq 13$) undergo adsorption induced structural changes in favor of enhanced adsorption to achieve coverages close to the electron counting rule predictions for the bare cluster geometries.[55] D_2 was found to adsorb readily to Ni_n^+ ($n = 2$-16) while the formation of Ni_nD^+ exhibits thresholds.[56] A simulation of Ni_n ($n = 2$-150) by a dedicated *Aufbau/Abbau* method predicted structures, symmetries and stabilities of most stable isomers and found particular high stability of Ni_{13}.[57] Studies of activated CH_4 reactions with Ni_n^+ ($n = 2$-16) found a rich chemistry that is consistent with simple bond order considerations.[58] IR-MPD studies of H_2 adsorbed onto Ni_{4-6}^+ revealed propensities for activation and hydride formation.[59-60] IR-MPD spectroscopy helped to characterize vibrational patterns of hydrated and comlexed Ni^+.[61-62] First adsorption studies of N_2 on nickel were carried out in the 1950s on evaporated nickel films[63] and on nickel powders.[64] N_2 uptake studies with nickel clusters Ni_n ($n = 3$-28) were interpreted in terms of head-on N_2 coordination.[65-66]

Kinetic models. The classical Langevin collision rate of ions with neutrals[67] is conveniently extended towards polar molecules by the average dipole orientation theory (ADO).[68-69] This ADO theory is frequently used to calculate the reaction rates of charged clusters with small molecules, knowingly underestimating the reaction rates for charged metal clusters significantly.[70-72] Another model to estimate the collision rates of ionic clusters with neutral molecules is the surface charge capture model (SCC), which leads to significantly increased collision rate constants, in comparison with Langevin or ADO rates.[73]

Prior Nickel - N_2 spectroscopy. IR spectra of nitrogen adsorbed on silica-supported Ni films[74] revealed a strong infrared absorption band at 2202 cm^{-1}, attributed to the N-N stretching vibration of head-on bound N_2. A combined IR spectroscopy and electron-microscopic study of N_2 adsorbed on silica supported nickel samples (at -80 to - 20 °C) revealed that this IR active N_2 only occurs on nickel particles with diameters between 15 and 70 Å.[75] Matrix infrared spectra of e. g. $Ni(N_2)_n$ (n = 1-4) in argon[76] reinforce interpretation in terms of an end-on coordination. Several strong dinitrogen frequencies in the range of 2100 - 2230 cm^{-1} were identified in these matrix infrared spectra. More recently, there was a report on N_2 stretching frequencies at 2223/2234 cm^{-1} by an end-on coordinated N_2 in cationic Ni(II) complexes,[77] well in line with those observed for N_2 adducts of molecular Ni(II) halides.[78] The N_2 interaction with an open coordination site on a Ni(I) macrocycle revealed head-on coordination with a dinitrogen frequency at 2170 cm^{-1}.[79]

Our approach: We have been preparing ionic TM clusters within ion traps e.g. for kinetic studies of hydrocarbon activation,[6] and we have introduced X-ray studies by cryo ion trapping for the investigation of spin and orbital contributions to the magnetic moments of TM clusters.[46, 80] In parallel we have utilized table top IR lasers for the identification of dark IR-MPD bands in oligonuclear TM complexes,[81] and of torsional isomerizations,[82] and of multistate-mediated rearrangements.[83] Recently we have upgraded our instrumentation towards tandem cryo ion trapping,[84] and we have started a long term quest for the vibrational spectroscopy of N_2 adsorbates on size selected TM clusters under isothermal cryo conditions, first results on $[Co_n(N_2)_1]^+$ clusters and on Fe based "non-classical" dinitrogen complexes being published.[85-86] This study aims to elucidate N_2 adsorption onto cationic nickel clusters, $[Ni_n(N_2)_m]^+$, by a combination of kinetic investigations, IR-PD spectroscopy, and DFT based modelling of structures and vibrations. We aim to gain insight into the metal-adsorbate bonding and to unravel structure-reactivity relationships. Within this work we have chosen to discuss the archetypical cases of Ni_9^+ and Ni_{13}^+ in more detail and up to the prevailing adsorption limits of saturation.

4.2.3 Experimental and computational methods

A customized Fourier Transform Ion Cyclotron Resonance (FT-ICR) mass spectrometer (Apex Ultra Bruker Daltonics) served to perform the cluster production, isolation, N_2 condensation, InfraRed Photon Dissociation (IR-PD) and mass analysis. The nickel clusters were generated using a home-built laser vaporization cluster ion source as described before.[70, 87] In brief, nickel atoms are evaporated from a rotating 0.4 mm thick isotopically enriched ^{58}Ni foil (99,61 %, Oak Ridge National Laboratories) by the second harmonic of a pulsed Nd:YAG laser (Innolas *Spitlight 300*, 20 Hz). The hot plasma is captured by a He gas pulse (40 µs, 15 bar) created by a homebuilt piezoelectric valve.[88] The atoms and ions are cooled and aggregate to clusters in the subsequent jet expansion through a 50 mm long channel (Ø 2 mm) into vacuum (10^{-7} mbar). The clusters are skimmed and injected into a cryogenic hexapole ion trap passing a 90 degrees ion beam bender and a quadrupole mass filter. The ion trap is cooled to 26 K by a closed cycle He cryostat. Buffer and reaction gas are introduced continuously. Sufficient nitrogen attachment is achieved by increasing the pressure in the ion trap from 1.1×10^{-7} mbar up to 3.0×10^{-7} mbar. Additional He is introduced to increase the pressure up to 3.0×10^{-6} mbar to accomplish an efficient trapping and cooling of the ions. After storing the mass-selected ions for a variable time (0-5 s), the manipulated ions of the form $[Ni_n(N_2)_m]^+ = (n,m)$ are guided by electrostatic lenses into the FT-ICR cell of the so-called "infinity" type.[89] The ICR cell is held at temperatures below 10 K with a closed cycle He cryostat to prevent heating of the clusters by black body radiation prior to ion detection.

For kinetic investigations the ICR cell serves for the detection of the formed $[Ni_n(N_2)_m]^+ = (n,m)$ cluster adsorbate complexes. The kinetic curves of cationic nickel clusters and their nitrogen adducts originate from reaction delay scans and subsequent evaluation of the recorded mass spectra. Fits to pseudo-first-order-kinetics occur through the "evofit" program.[90] Our thus determined rate constants for the (9,m) species (recorded at $p(N_2) = 3.0 \times 10^{-7}$ mbar) are normalized to the experimental conditions for the (13,m) species (recorded at $p(N_2) = 1.3 \times 10^{-7}$ mbar). The relative rate constants $k_{(n,m)}$ determine the absolute rate constants $k_{(n,m)}^{abs}$, the absolute collision gas number densities $\rho_{N2}(T)$ serving as the conversion factor:

$$k_{(n,m)}^{abs} = k_{(n,m)}/\rho_{N2}(T)$$

We obtain approximate values for $\rho_{N2}(T)$ indirectly from the pressure in the surrounding chamber $p_c^{(300\,K)}$ and an effective geometry factor c_{app}:

$$\rho_{N2}(26\;K) = \frac{c_{app}p_c^{300\;K}}{k_B T_{300\;K}}$$

The geometry factor c_{app} shows to bear a significant dependence on the temperature of the hexapole ion trap. By numerous kinetic studies of transition metal cluster cations with neutral reactants at cryogenic temperatures we evaluated this factor c_{app} to 1.8 ± 0.4 at 26 K with a net uncertainty of ± 50%. The quotient of the absolute rate constants and the collision rate enables us to calculate the absolute reaction efficiency γ for the adsorption of N_2 by cationic Ni clusters. This absolute reaction efficiency indicates the probability of a reaction occurring after a collision between a metal cluster ion and its reaction partner.

To record IR-PD spectra, the ICR cell is used for the isolation of each observed (n,m) species, subsequent storage for ion irradiation and for the detection of the resulting ions. It is coupled to a tunable IR laser (dn= 0.9 cm^{-1}, dt = 7 ns). The laser comprises of a KTP/KTA optical parametric oscillator/amplifier (OPO/A, LaserVision) system pumped by a pulsed 10 Hz injection seeded Nd:YAG laser (PL8000, Continuum). In this work we used the difference frequency (DF) between the OPA signal and idler waves generated in a $AgGaSe_2$ crystal. This generates IR radiation in the range of 1000 – 2400 cm^{-1}. Each trapped and isolated package of ions is irradiated by 5 – 10 laser pulses (0.1 – 1.2 mJ per pulse) to yield a sufficient amount of fragment ions. The IR spectra were recorded as mass chromatograms while continuously scanning the IR wavelength. The IR-PD signal was evaluated as $\Sigma F_i/(\Sigma_i F_i + \Sigma P_i)$, where F_i and P_i indicate the fragment and the parent ion signals, respectively. An experimental IR-PD spectrum arises from a plot of the fragmentation efficiency as a function of laser frequency. We employed the IR-PD spectroscopy in the 2140 - 2300 cm^{-1} range on the isolated (n,m) species. In this range we expected the N_2 stretching frequencies of these species. For all complexes the loss of N_2 was the only observed fragmentation channel.

Linear IR absorption spectra were calculated at the PBE0[91] level of theory using the cc-pVTZ basis sets[92] (N), and the Stuttgart RSC 1997[93] effective core potential (Ni), respectively, as implemented in the Gaussian 09 program package.[94] All calculated spectra were scaled to account for prevailant anharmonicities (empirical factor 0.93). Full geometry optimization yielded multiple local minimum structures for spin multiplicities $2S + 1 = 6 – 18$ (e.g. Table S4 in the SI). The lowest energy structure is assumed to represent the most stable isomer. All local minimum structures were confirmed by the absence of imaginary frequencies. SCF convergence is tedious and can be achieved only at the expense of relaxed SCF convergence criteria of 10^{-5} (as compared to 10^{-8} in DFT calculations on light main group elemnts). Zero point energy effects are small if any (see Table S1).

4.2.4 Results and Discussion

Molecular nitrogen adsorption on nickel cluster cations: Trends and limits of adsorption

We stored the generated $[Ni_n(N_2)_m]^+$ = (n,m) cluster adsorbate complexes in the cryogenic hexapole under isothermal conditions at 26 K. In all investigated cases (n = 5,..,20) stepwise N_2 uptake reaches a strict adsorption limit m_{max}. Here (Fig. 1) and in the following we elucidate the two cases of (n,m) = (9,m) and (13,m).

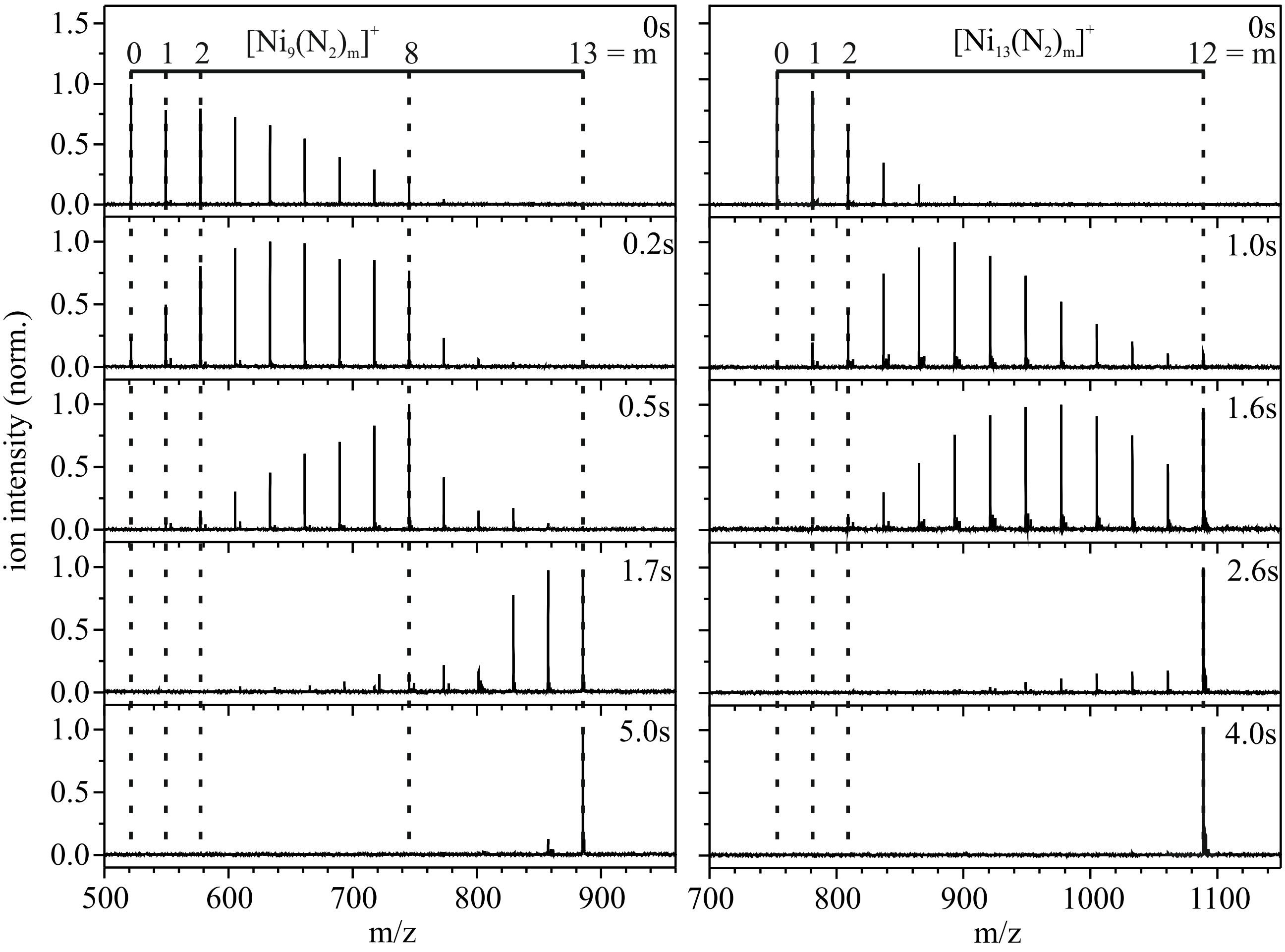

Figure 1. Temporal evolution of the mass spectra of mass-selected Ni_9^+ = (9,0) clusters exposed to 3.0 x 10^{-7} mbar of N_2 in 3.0 x 10^{-6} mbar of He at 26 K for up to 5 s (left) and of mass-selected Ni_{13}^+ = (13,0) clusters exposed to 1.3 x 10^{-7} mbar of N_2 in 3.0 x 10^{-6} mbar of He at 26 K for up to 4 s (right).

Starting from the bare nickel clusters, the temporal evolution of the detected species reveals a successive gain of 28 m/z, which does indicate the adsorption of molecular nitrogen. This temporal evolution indicates subtle details: In the case of (9,m) we observe the N_2 adsorption limit at (9,13) preceded by an additional intermittent adsorption limit at (9,8), which does not suppress further adsorption but causes some retardation. In the case of (13,m) we observe a sole N_2 adsorption limit at (13,12) without any intermittent adsorption limit or retardation. Note that neither an increase of N_2 pressure nor of storage times up to 30 s would drive the N_2 adsorption beyond these limits at (9,13) and (13,12).

Isothermal kinetics under cryogenic conditions

We further investigated the stepwise N_2 adsorption on Ni_9^+ and Ni_{13}^+ clusters at 26 K by recording their reaction kinetics in more detail, and we performed pseudo-first-order kinetic fits by our genetic algorithm routine, which confirms consecutive adsorption steps (Fig. 2). Both Ni_9^+ and Ni_{13}^+ clusters decay mono exponentially without any indication of a second component. This, and the overall superior quality of all fits, entitles us to fit each consecutive step by a single rate constant throughout. The fit of the very last adsorption step of (9,12) → (9,13) requires a significant backward reaction in parallel, which indicates swift N_2 desorption (9,13) → (9,12). It is noteworthy at this point to emphasize the obvious and manifest differences in the reaction kinetics of Ni_9^+ and Ni_{13}^+: N_2 adsorption to Ni_9^+ takes place step by step at individual rates: Each step is different. N_2 adsorption to Ni_{13}^+ takes place step by step at equal rates: Each step is the same.

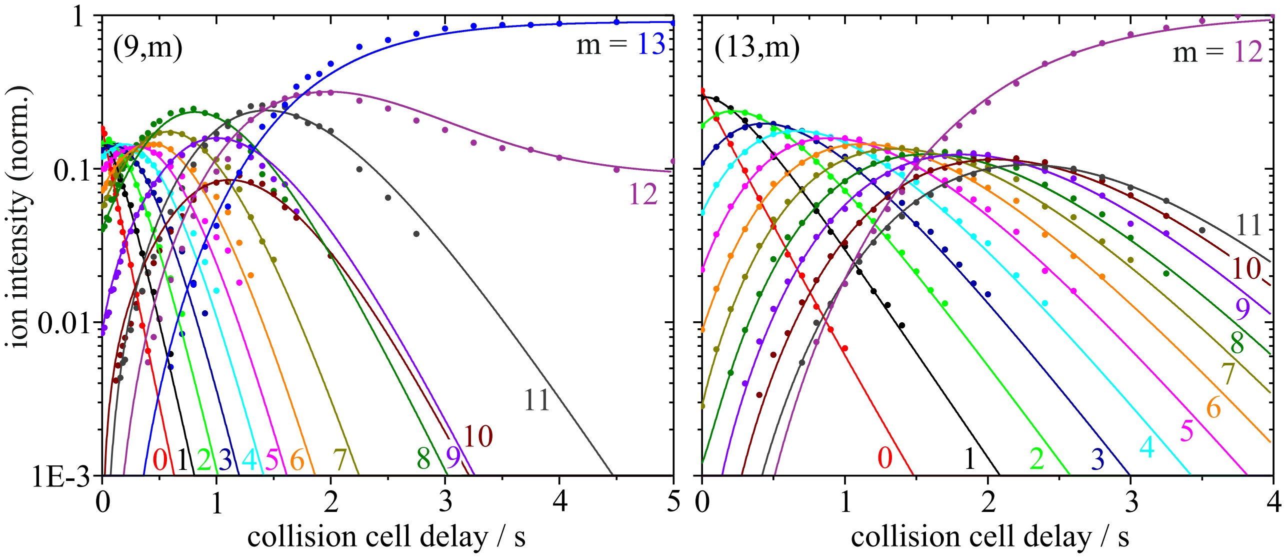

Figure 2. Isothermal kinetics of the stepwise N_2 adsorption by isolated Ni_9^+ clusters (left) and Ni_{13}^+ clusters (right) at 26 K. The fits (shown as lines) assume pseudo-first-order kinetics in a reaction chain of up to 13 consecutive steps for Ni_9^+ clusters and up to 12 for Ni_{13}^+ clusters.

Fitting the experimental kinetics implies the quantitative determination of relative rate constants for N_2 adsorption $k_{(9,m)}$ and $k_{(13,m)}$ for each step m → m+1, and for N_2 desorption $k_{-(9,m+1)}$ and $k_{-(13,m+1)}$ for each step m+1 → m alike:

$$[Ni_n(N_2)_m]^+ + N_2 \underset{k_{-(n,m+1)}}{\overset{k_{(n,m)}}{\rightleftarrows}} [Ni_n(N_2)_{m+1}]^+$$

The consecutive relative rate constants of the (9,m) species (*cf.* Fig. 3, Tab. 1) $k_{(9,m)}$ are constant up to $k_{(9,4)}$ within the uncertainties of the fits. Relative rate constants start to decline at $k_{(9,5)}$ and reach a minimum at $k_{(9,8)} = 1.5\ s^{-1}$. The rate constants of the two subsequent adsorption steps $k_{(9,9)}$ and $k_{(9,10)}$ increase with further adsorption declining to a total minimum of $k_{(9,12)} = 0.7\ s^{-1}$ (Tab. 2). Please note the sole significant backward reaction of N_2 desorption from (9,13) of $k_{-(9,13)} = 0.07$. In all other cases any desorption/back reaction is insignificant up to our experimental detection limits. The determined relative rate constants of the (13,m) species are constant without variation within uncertainties of the fits up to the adsorption limit ($k_{(13,m)} \sim 4.4\ s^{-1}$; *cf.* Fig. 3, Tab. 2).

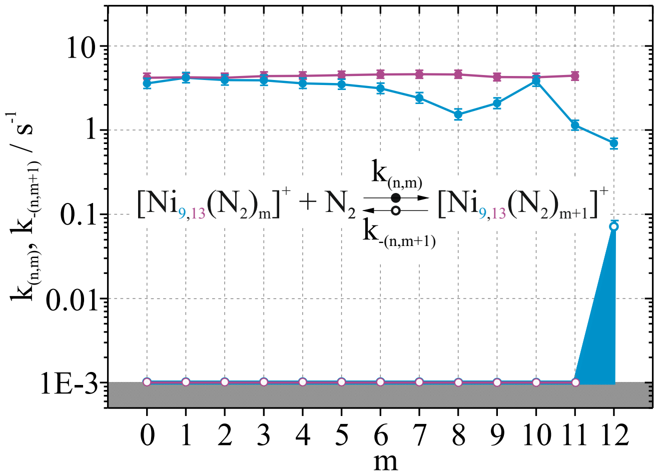

Figure 3. Observed rate constants of the (9,m) species (blue) and the (13,m) species (red) as a function of N_2 coverage. Filled circles show the rate of adsorption and open circles indicate single N_2 desorption.

Collision rate constants are calculated as Langevin rates and on the basis of the SCC model. The ratios of the determined absolute rate constants $k^{abs}_{(n,m)}$ and either of the two collision rates k_L or k_{SCC} provide for absolute reaction efficiencies $\gamma_{L(n,m)}$ or $\gamma_{SCC(n,m)}$, respectively (see Tab.s S2and S3 for all values). Note that the current case of N_2 adsorption makes reaction efficiencies equivalent to sticking probabilities as defined in conjunction with surface science.

We obtain absolute rate constants in the range of 10^{-10} cm^3 s^{-1} for all adsorption steps. In the case of (9,m) the absolute rate constants for the N_2 adsorption attain their minimum of 1.24 x 10^{-10} cm^3 s^{-1} when reaching the adsorption limit. The absolute reaction efficiency for this last adsorption step is as low as 21 % ($\gamma_{L(9,12)}$) or 9 % ($\gamma_{SCC(9,12)}$), respectively (*cf.* Tab. 1). In contrast, the absolute rate constant for the observed N_2 desorption from (9,13) is an order of magnitude smaller (*cf.* Tab. S2).

Table 1. Pseudo-first-order rate constants for the N_2 adsorption on Ni_9^+ clusters $k_{(9,m)}$ for each step m → m+1, related absolute rate constants $k^{abs}_{(9,m)}$ and calculated absolute reaction efficiencies $\gamma_{L(9,m)}$ and $\gamma_{SCC(9,m)}$.

m	$k_{(9,m)}$ s^{-1}	$k^{abs}_{(9,m)}$ 10^{-10} cm^3 s^{-1}	$\gamma_{L(9,m)}$	$\gamma_{SCC9,m)}$
0	3.6(3)	6.37	1.05	0.50
1	4.2(3)	7.43	1.23	0.58
2	3.9(3)	6.90	1.14	0.53
3	3.9(3)	6.90	1.15	0.53
4	3.6(3)	6.37	1.06	0.49
5	3.5(3)	6.19	1.03	0.47
6	3.1(3)	5.48	0.91	0.41
7	2.4(2)	4.25	0.71	0.32
8	1.5(2)	2.65	0.44	0.20
9	2.1(2)	3.72	0.62	0.27
10	3.8(4)	6.72	1.12	0.49
11	1.1(1)	1.94	0.33	0.14
12	0.7(1)	1.24	0.21	0.09

The absolute rate constants for the N_2 adsorption on Ni_{13}^+ clusters $k^{abs}_{(13,m)}$ stay constant up the N_2 adsorption limit. They exceed the predicted Langevin rates (~ 6.0 x 10^{-10} cm^3 s^{-1}) by 30 %, and they are 40 % below the collision rates (~ 13.5 x 10^{-10} cm^3 s^{-1}) by the SCC model. (*cf.* Tab. 2).

Table 2. Pseudo-first-order rate constants for the N_2 adsorption on Ni_{13}^+ clusters $k_{(13,m)}$ for each step $m \rightarrow m+1$, related absolute rate constants $k_{(13,m)}^{abs}$ and calculated absolute reaction efficiencies $\gamma_{L(13,m)}$ and $\gamma_{SCC(13,m)}$.

m	$k_{(13,m)}$ s^{-1}	$k_{(13,m)}^{abs}$ 10^{-10} cm^3 s^{-1}	$\gamma_{L(13,m)}$	$\gamma_{SCC(13,m)}$
0	4.2(2)	7.38	1.23	0.54
1	4.2(2)	7.38	1.23	0.54
2	4.2(2)	7.38	1.23	0.53
3	4.4(2)	7.74	1.29	0.56
4	4.4(2)	7.74	1.29	0.55
5	4.5(2)	7.91	1.32	0.56
6	4.6(3)	8.09	1.35	0.57
7	4.6(3)	8.09	1.35	0.57
8	4.6(3)	8.09	1.36	0.56
9	4.3(2)	7.56	1.27	0.52
10	4.2(2)	7.38	1.24	0.51
11	4.4(2)	7.74	1.30	0.53

There is a significant change in the reaction rates for $m \geq 9$ in (9,m), and there is an undisputable absence of $m \geq 13$ species in (13,m). These two eminent findings may indicate various N_2 coverage and cluster size dependent effects: A change in the adsorption type (e.g. end-on, side-on, head-on/atop (μ_1), bridging (μ_2) or face bound (μ_3) etc.), a change in the N_2 adsorption number per site (vicinal vs. geminal binding motifs), a change of the cluster geometry (reorganization/ isomerization), N_2 adsorption shell closing, first monolayer formation, saturation of all coordination sites, differences in the morphology of the respective cluster surfaces.

A change in the N_2 adsorption type with coverage is rather unlikely on Ni compounds. Investigations of N_2 adsorbed on Ni(100) and Ni(110) surfaces have suggest end-on coordination.[95-96] N_2 adsorption studies on neutral Ni clusters[65-66] reinforce head-on coordination.

A change in the N_2 adsorption number per site on neutral Ni clusters has been suggested from so called uptake plots of average association numbers of multiple N_2 molecules under flow reactor conditions.[65-66] It is found that atoms that are four or less coordinate can bind two nitrogen molecules. In some cases nitrogen adsorption causes a change in the cluster structure, usually to one that can accommodate more N_2 molecules.

It is an ongoing issue whether the prevalence of conceiving cluster isomers would have consequences on kinetic studies and how they would emerge. Two cases may prevail. If isomers undergo reactive processes at comparable rates it would show as kinetics of a single species. It would not make a difference. If isomers react with different rates it would show in the form of bi- or multi-exponential kinetics. In the present cases of N_2 adsorption on nickel clusters we have found no evidence for multi-exponential kinetics. All fits are by single exponentials, and we conclude that there is no evidence for distinctly different isomers. If prevailing they do need to take very similar structures and react with equal rates.

The closing of a first adsorption shell would imply occupation of all available adsorption sites, which is first monolayer formation in surface science language. Once achieved, a change in kinetic efficiency of subsequent adsorption steps would be inevitable.

Any discussion in terms of cluster surfaces requires prior knowledge – or at less sincere estimates – of cluster geometries. Icosahedral shapes and according trigonal binding motifs seem likely, given the ground breaking electron diffraction experiments of Schooß, Kappes et al.,[97] which unambiguously unraveled a double closed shell icosahedral shape of Ni_{55}^- ions when trapped in an ion trap. From this and other work it is known that icosahedral motifs minimize surface energy in disfavor of bulk cohesion. It seems justified to assume such icosahedral motifs prevailing in smaller clusters as well – as confirmed by our DFT calculations (*cf.* in passage 3.4). A perfect icosahedron of Ni_{13}^+ provides for a single bulk atom and for 12 surface atoms of equal coordination to six nearest neighbors. It shows a smooth surface.

The Ni_9^+ cluster arranges its atoms in remarkable contrast, likely in the form of a tricapped octahedron or in the form of a bicapped pentagonal bipyramid– which upon further cluster growth would easily isomerize into pure icosahedral shape. These cluster geometries provide various coordinated Ni atoms ranging from threefold coordination up to eightfold coordination to nearest neighbors. Both types show a rough surface.

The origin of the found variation in relative rate constants in Ni_9^+ and its absence in Ni_{13}^+ seem to relate to the cluster surface morphologies. However, we address this issue by recording IR-PD spectra of the (n,m) species of interest.

Experimental IR-PD spectra of the (n,m) species (n = 9, 13; m = 1,..,13)

We have recorded IR-PD spectra of a large range of $[Ni_n(N_2)_m]^+$ cluster adsorbate complexes. Here we want to present and discuss the two cases (n,m) = (9,m) and (13,m) up to $m = m_{max}$. The IR-PD spectra reveal several vibrational bands at frequencies of 2170 cm^{-1} to 2260 cm^{-1} (Fig. 4). The range of these bands coincides with the range of metal head-on coordinated N-N stretching modes in $[Co_n(N_2)_1]^+$ cluster adsorbate complexes of our previous study.[85] All bands are significantly redshifted with respect to the IR inactive stretching mode of free N_2 at 2330 cm^{-1}.

The recorded IR-PD spectra of (9,m) show remarkable shifts of peak positions and onset of splittings by increase of the N_2 coverage (*cf.* Fig. 4, left). This is indicative of a rough surface – as suggested by our kinetic results. In more detail: The IR-PD spectrum of the singly adsorbed species (9,1) shows a single band at 2238 cm^{-1}. The (9,2) species shows a second blueshifted band at 2250 cm^{-1}. Going to higher N_2 coverages for the (9,m) clusters ($m > 2$) an additional readshifted weaker band occurs in the IR-PD spectra. The spectra in the range from m = 3 - 8 stand out by successive shifting of the stretching frequencies from 2220 - 2260 cm^{-1} to 2200 - 2240 cm^{-1} resulting in a major band at 2230 cm^{-1} and a minor band at 2210 cm^{-1} for the (9,8) species. The spectrum of the (9,9) species shows three resolved bands induced by a 10 cm^{-1} splitting of the major band. Further adsorption up to m = 13 leads to complicated vibrational patterns comprising multiple bands within a range of 70 cm^{-1}. The spectrum of the (9,13) species shows two strong bands at 2181 cm^{-1} and 2252 cm^{-1} and several less intense bands in between. Note the overall asymmetrical broadening of the vibrational pattern to the red with N_2 coverage.

We also recorded the IR-PD spectrum of the (9,13) species in an extended frequency range of 1010 - 2340 cm^{-1} (*cf.* Fig. S1 of the supplementary information) – with no further recordable features arising. Thus, there is no evidence for the presence of adsorption types other than the head-on bound N_2 as evident in the presented spectra.

Each (13,m) IR-PD spectrum (Fig. 4, right) shows a single dominant band around 2222 cm^{-1} which does not shift upon increasing N_2 adsorption up to saturation. This encourages the proposition of a smooth Ni_{13}^+ clusters surface, where all 12 surface atoms are equivalent. Note the minor peak at 2230 cm^{-1} for (13,3) that progressively shifts to the blue and decreases with further N_2 adsorption (black dotted line in Fig. 4). We tentatively attribut this feature to combination bands with N_2 wagging modes. Interestingly, this would imply a gradual stiffening of the wagging coordinate with increasing N_2 coverage of the adsorbing, curved cluster surface. This allows us to deduce a self organized proximity of as little as three to four N_2 adsorbates on the Ni_{13}^+ cluster surface, and in consequence, an attraction amongst these adsorbates – albeit a weak one. Note that a coupling between the adsorbed N_2 molecules could cause symetric and antisymetric N_2 stretching modes. These modes would accur in the IR-PD spectra with about equal intensities.

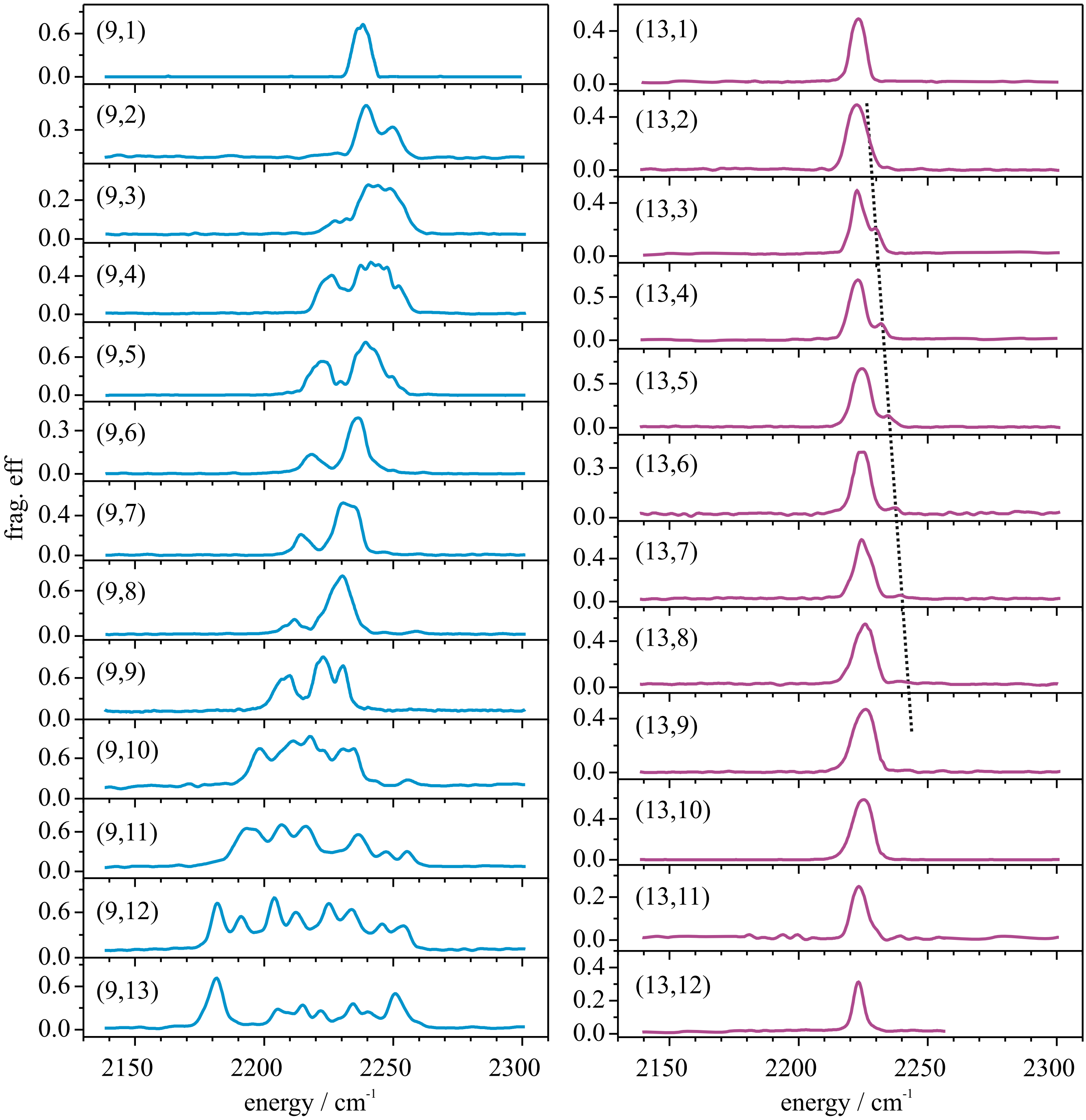

Figure 4: IR-PD spectra of the (9,m) species (blue curves/left) and (13,m) species (red curves/right) at 26 K. Note the variation in the observed band positions and splittings with further adsorption for the (9,m) species in contrast to the single dominant band for all (13,m) species. The black dotted line highlights the minor peak, that progressively shifts to the blue and decreases with further N_2 adsorption. See text for details.

Comparison of the experimental IR-PD spectra with simulations

Geometry optimizations yielded multiple local minimum structures for the naked Ni_9^+ cluster, likely in an octet or decet spin state. A bicapped pentagonal bipyramidal cluster core is favoured. The found three most stable structures (0 – 21 kJ/mol) are of this motif and differ in positions of the capping two atoms. There is another stable structure (+ 30 kJ/mol) that consist of a tricapped octahedral geometry. Both structural motifs, the pentagonal and octahedral ones, prefer neighboring caping atoms in order to reach high coordination of their Ni atoms (computed geometries and their relative stabilities are shown in Fig. S2 of the supplementary information). We treated the Ni_{13}^+ cluster core in an assumed icosahedral structure only. Geometry optimization for multiple spin multiplicities resulted in a clearly preferred 2S + 1 = 16 spin state (relative stabilities for 2S + 1 = 10-18 are listed in Tab. S4 of the supplementary information).

In the case of Ni_9^+ the observed N_2 adsorption limit at (9,13) is consistent with a tricapped octahedral as well as a bicapped pentagonal bipyramidal structure (both with neighboring capping atoms). In the case of Ni_{13}^+ the observed N_2 adsorption limit at (13,12) is consistent with the icosahedral structure (*cf.* Fig. 5).

The tricapped octahedron of Ni_9^+ provides for three atoms of threefold coordination to nearest neighbors, one atom of fourfold coordination, two atoms of fivefold coordination, two atoms of sixfold coordination, and one atom with sevenfold coordination. The bicapped pentagonal bipyramid provides for four atoms of fourfold coordination, two atoms of fivefold coordination, two atoms of sixfold coordination, and one atom with eightfold coordination. These geometries corroborate the observed adsorption limit (9,13) as well as the intermittent adsorption limit (9,8). The (9,8) case would result from all but the seven- or eightfold coordinated Ni atoms binding one N_2 molecule, and (9,13) from geminal binding of N_2 to the three- and fourfold coordinated Ni atoms and single N_2 binding to the seven- or eightfold coordinated Ni atoms.

The icosahedral Ni_{13}^+ provides for a single bulk atom and for 12 Ni surface atoms of equal coordination to six nearest Ni neighbors. This geometry corroborates the observed adsorption limit (13,12), which results from binding of a single N_2 to each of the 12 Ni surface atoms – a motif that may be called a mono layer or a first solvation shell at will.

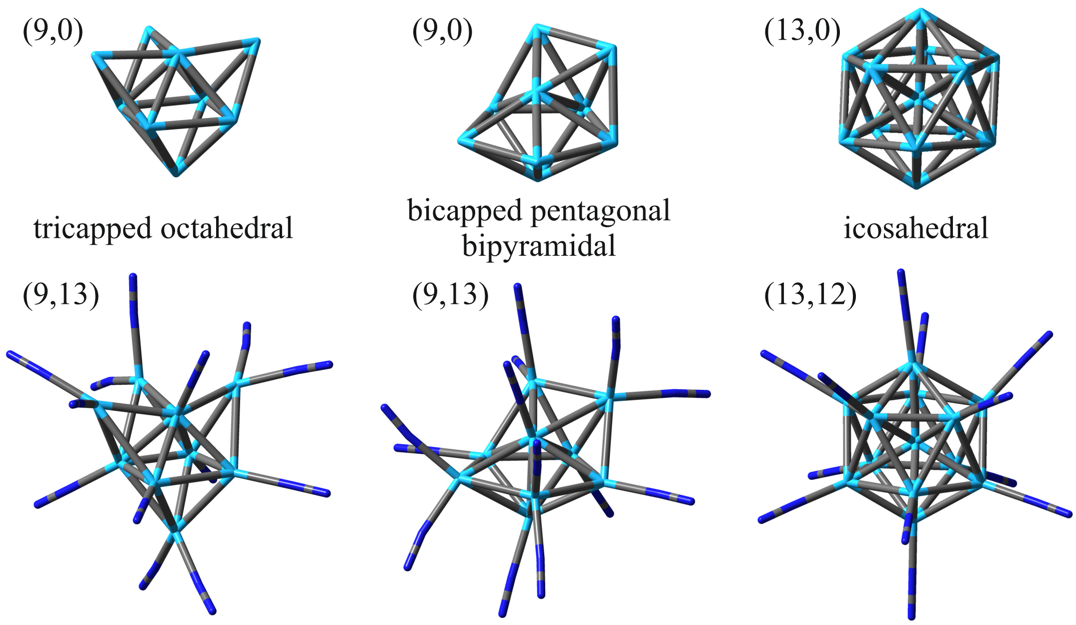

Figure 5. Computed geometries of different possible (n,m) (m = 0, m_{max}) species. The displayed tricapped octahedral and bicapped pentagonal bipyramidal Ni_9^+ clusters and the icosahedral Ni_{13}^+ cluster are low lying stable geometries. Sole head-on coordination results in (9,13) from geminal N_2 binding to the three- and four-coordinate atoms and single N_2 binding to the five, six, seven and eight-coordinate atoms. (13,12) results from single N_2 binding to all 12 surface atoms.

We have conducted further DFT simulations to obtain linear IR absorption spectra for numerous relevant complex structures, and with variation of the spin multiplicity of the Ni cluster cores. The obtained IR spectra for the (n,m) species are sensitive to the binding position of the adsorbed N_2, to its adsorption angle and to geminal N_2 adsorption (two N_2 adsorbate to one Ni atom). We have considered a variation of spin multiplicities in the range of $2S + 1 = 6\text{-}18$. Note, that the spin contamination is insignificantly small (e.g. in case of decets: $S^2\text{-}24.75 < 10^{-2}$). In the case of the Ni_9^+ cluster we find highest stability in octet and decet spin states, and this persists upon N_2 adsortion up to the adsortion limit (9,13). In the case of the Ni_{13}^+ cluster we find a clear preference of high spin states in the naked cluster ($2S+1 = 16$), that diminishes gradually upon stepwise N_2 adsorption up to the adsorption limit (13,12) which is preferentially a decet. In the following, we restrict ourselves to the elucidation of the cases (n,m) = (9,2), (9,5), (9,8), (9,9) and (13,12).

The best fit of the experimental IR-PD spectrum of $[Ni_9(N_2)_2]^+$ is obtained by a DFT simulation of the tricapped octahedron (9,2) species, where the two N_2 adsorbates locate at two (out of three) capping atoms (c.f Fig. 6). The calculated two N – N stretching frequencies split by 10 cm^{-1}, the N_2 adsorbates locating on the inner and one of the two outer Ni capping atoms, which make for two similar, but inequivalent adsorption sites. The N_2 adsorbate at the outer capping Ni atom reveals a Ni-N bond distance (1.92 Å) which is 0.02 Å greater than that at the inner capping Ni atom (1.90 Å). The former case corresponds to a weaker π back-bonding, resulting in a blueshift of the N_2 stretching frequency.[98] Note, that the second band cannot be explained by the assumption of a bicapped pentagonal bipyramial cluster core, where a double N_2 adsorption to the lowest coordinated Ni atoms would lead to degenerate vibrational bands with a vanishing splitting – other than observed.

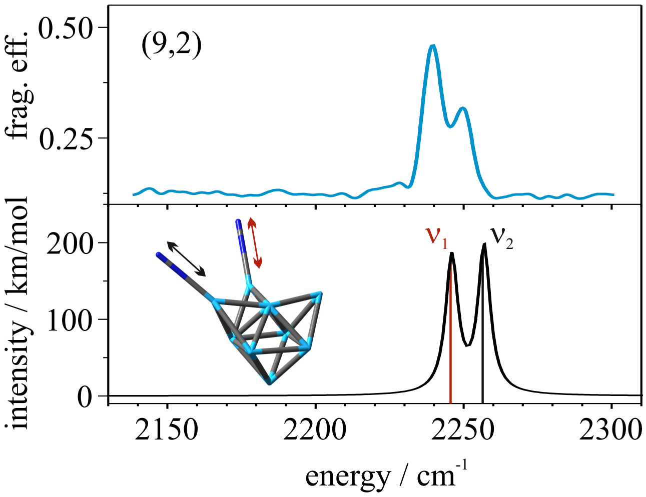

Figure 6. IR-PD spectrum of (9,2) (blue) and the calculated IR absorption spectrum for the tricapped octahedral motif where the N_2 molecules are adsorbed by different Ni capping atoms (black; PBE0/ECP(Ni), cc-pVTZ(N), $2S + 1 = 10$). The calculated spectrum is scaled by 0.93 and simulated using the gaussian profile of fwhm = 5 cm^{-1}.

When further increasing the N_2 coverage ($m = 3$) the simulated spectra are in line with the experimental spectra when sticking with the assumption of a tricapped octahedral structure. Note, that it is not feasible to achieve a definite assignment of the experimental spectrum, which is not fully resolved. It is conceivable, that there are multiple N_2 adsorption isomers. For even higher adsoption numbers ($m \geq 4$) we find best agreement of calculated and measured IR spectra when assuming a bicapped pentagonal bipyramidal motif. However, there may be a bicapped pentagonal bipyramid and a tricapped octahedron in coexistence.

In particular when reckoning the $m = 5$ case the adsorption angles of the N_2 molecules appear to influence the absorption spectra significantly (Fig. 7). This comes in parallel to the theoretical prediction of an isomerization of the Ni_9^+ cluster by the increased N_2

coverage: Naked and m ≤ 4 tricapped octahedra seem to become a bicapped pentagonal bipyramid, and the dectet spin state persists. It would be a valid point of further investigation to check for the N_2 bending coordinate by parametric variation in a series of explicit DFT calculations, and to check for possible fingerprints by even colder high resolution IR spectra.

The N_2 uptake studies of small neutral Ni clusters[65] emphasize two cases, Ni_8 and Ni_9, with evidence for two (or more) bare cluster structures at very low N_2 coverages. The mass spectra show clear bimodal distributions which hint for an isomerization at low N_2 coverages. They suggest that these two clusters, each, have two isomers of comparable energy. We are in line with these early findings.[99]

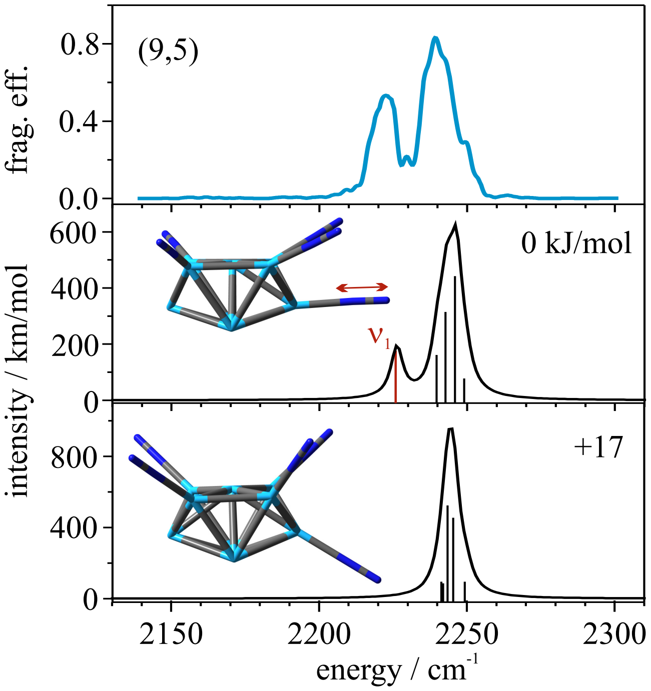

Figure 7. IR-PD spectrum of **(9,5)** (blue) and calculated IR absorption spectra for the bicapped pentagonal bipyramidal motif with different N_2 adsorption angles (black; PBE0/ECP(Ni), cc-pVTZ(N), 2S + 1 = 10) scaled by 0.93 and simulated using the gaussian profile of fwhm = 5 cm^{-1}. Note that the viewpoint of the Ni_9^+ cluster is rotated with respect to that of Fig. 5.

Another issue of great interest is the onset of major splittings of the main N_2 stretching band for m > 8 (Fig. 8). We interpret these splittings in terms of a geminal N_2 adsorption – two N_2 adsorbates to a single Ni atom – in the (9,9) case. The resulting symmetric and antisymmetric N_2 stretching frequencies would split by ~10 cm^{-1}. DFT modelling reveals: The higher an adsorbing Ni atom is coordinated within the cluster the more redshifted is the stretching frequency of the adsorbed N_2. It is unlikely that the origin of the observed vibrational splittings of (9,9) originates from an N_2 coordination to the highest coordinated Ni atom – which stays vacant in favor of the geminal N_2 adsorption at a low coordinated Ni atom.

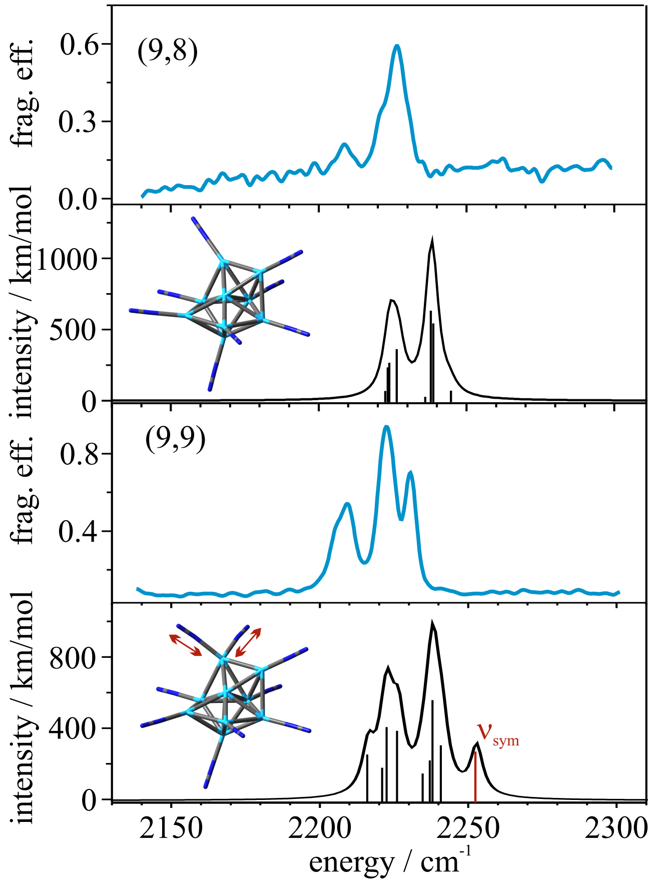

Figure 8. IR-PD spectra of (9,8) and (9,9) (blue) and calculated IR absorption spectra for the bicapped pentagonal bipyramidal motif with and without geminal binding (black; PBE0/ECP(Ni),cc-pVTZ(N), 2S + 1 = 10) scaled by 0.93 and simulated using the gaussian profile of fwhm = 5 cm^{-1}.

Trends in the calculated N_2 binding energies of Ni_9^+ are in line with the kinetic and spectroscopic findings of this study (Tab. 3). The first N_2 binds stronger, $\Delta_{ads}H^{0\ K}(9,1) = 76$ kJ/mol (0.79 eV), than all subsequent adsorbates, namely all other (9,m) cases. Further N_2 adsorption up to the (9,8) species takes place with $\Delta_{ads}H^{0\ K}(9,m \leq 8) \sim 50$ kJ/mol. It is the 9th N_2 molecule which binds significantly weaker, $\Delta_{ads}H^{0\ K}(9,9) \sim 20$ kJ/mol - a finding which nicely matches the occurrence of an observed intermittent limit at (9,8). Notice, that the case of (9,9) favors by ~5 kJ/mol one instance of geminal N_2 adsorption over one N_2 adsorption to the highest (eightfold) coordinated Ni site.

Table 3. Calculated N_2 binding energies of the last adsorbed N_2 (highlighted in magenta) to various (9,m) species in decet spin states.

(n.m)	calculated N_2 binding energy / kJ/mol	
(9,1)	-75.9	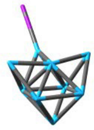
(9,2)	-53.6	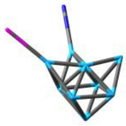
(9,8)	-46.5	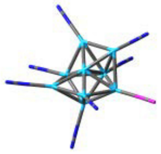
(9,9)	-20.4	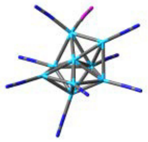
(9,9)	-15.8	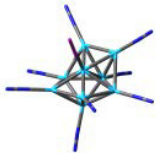

Further N_2 adsorption up to the adsorption limit at (9,13) leads to complicated vibrational patterns comprising multiple bands, most likely by further splittings as a result of geminal N_2 adsorption on the remaining three lowest coordinated Ni atoms and by adsorption on the highest coordinated Ni atom. The observed vibrational bands spread out over more than 70 cm^{-1} for m > 9, and this finding is well reproduced by our calculated IR spectra, but they fail in reflecting the absolut vibrational patterns (*cf.* Fig. S5-12 in the supplemaentary information for more details on the (9.m) species).

In the case of $[Ni_{13}(N_2)_{12}]^+$, which is the (13,12) species, we find good agreement of the experimental IR-PD spectra and the calculated IR absorption spectra, when assuming a spin quenching from $2S + 1 = 16 \rightarrow 10$ when $m = 0 \rightarrow 12$. Each experimental (13,m) IR-PD spectrum shows a single dominant band around 2222 cm^{-1} which does not shift upon increasing N_2 adsorption up to its limit. Assuming a perfect icosahedral Ni_{13}^+ core, all 12 surface atoms would be equivalent and the N_2 stretching frequencies would degenerate – as observed. Note, that such degeneracy is indeed predicted from DFT calculations of (13,m) when assuming the gradual spin quenching discussed above. Otherwise, there would be clearly discernible band splittings (*cf.* Fig. 9) – other than observed.

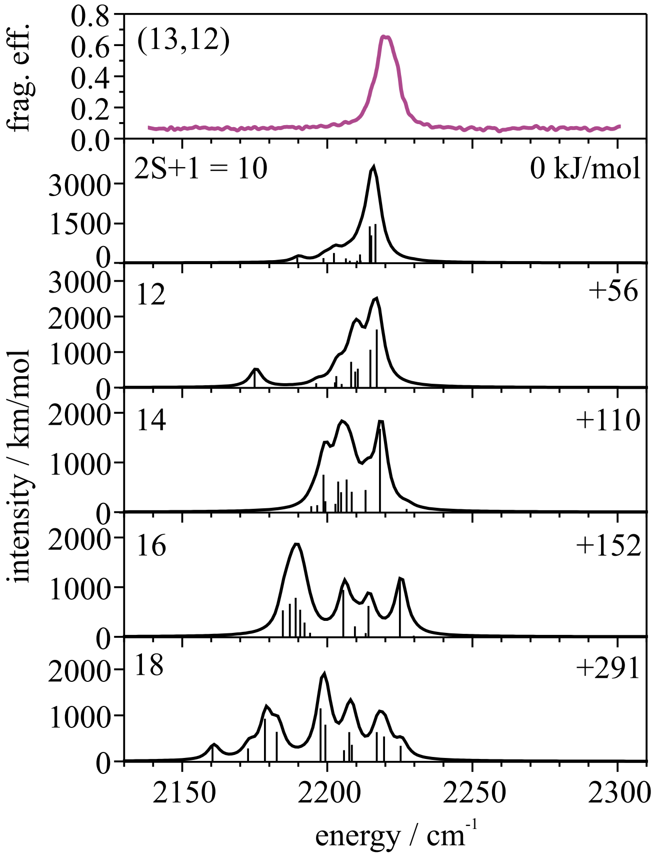

Figure 9. IR-PD spectrum of (13,12) (red) and calculated IR absorption spectra (black; PBE0/ECP(Ni),cc-pVTZ(N)) scaled by 0.93 with variation by the spin multiplicity of the icosahedral nickel cluster core (likely 2S + 1 = 10, 12, 14, 16, 18) and simulated using the gaussian profile of fwhm = 5 cm^{-1}.

Linear IR absorption spectra of several (9,m) species were calculated including the Grimme correction for dispersion with the original D3 damping function (GD3).[100] There is no significant change in band positions or intensities (*cf.* Fig. S13-14 in the supplementary information for the comparison of calculated spectra for (9,8) and (9,9) including GD3).

There is no clear correlation between N_2 vibrational frequencies and individual adsorption enthalpies, in particular when multiple N_2s adsorb. Their vibrational modes are coupled, and the adsorption/desorption likely implies reorganization of the adsorbate layer.

Our DFT level of theory would not cover antiferromagnetic coupling within the Ni cluster core. As of now we conclude that there is no evidence by our IR-PD spectra of either ferro- or antiferromagnetic coupling in Ni_{13}^+. Other than in the case of Fe_{13}^+,[46, 101] the XMCD investigation of Ni_{13}^+ did not reveal any evidence for a reduction of magnetic moments by antiferromagnetic coupling.[46]

Finally, our non relativistic DFT level of theory does not cover relativistic effects such as – most notably – spin orbit couplings. These, however, likely alter the orbital occupations within the Ni cluster core, which in turn might influence the coupling to and force constants with N_2 adsorbates. Thus, the calculated adsorbate vibrations may depend significantly on the spin multiplicity and in case of otherwise equivalent adsorbate motifs.

4.2.5 Conclusions

We have investigated the stepwise N_2 adsorption on size selected Ni_n^+ (n = 5-20) clusters by recording their reaction kinetics at 26 K in a hexapole ion trap. We performed pseudo-first-order kinetic fits, which confirm consecutive adsorption steps by single exponentially decays exclusively, and we have chosen to discuss the archetypical cases of Ni_9^+ and Ni_{13}^+ in more detail. These two clusters show remarkable differences in the N_2 adsorption trends and in the adsorption limits of saturation: N_2 adsorption on Ni_9^+ takes place at individual rates up to the adsorption limit at $[Ni_9(N_2)_{13}]^+$ and retards at an additional intermittent adsorption limit at $[Ni_9(N_2)_8]^+$. The fit of the very last adsorption step reveals a significant backward reaction, which indicates swift N_2 desorption. N_2 adsorption on Ni_{13}^+ takes place at equal rates up to the adsorption limit at $[Ni_{13}(N_2)_{12}]^+$. Ourt findings indicative a rough cluster surface of Ni_9^+ with inequivalent adsorption sites and a smooth cluster surface of Ni_{13}^+ with equivalent adsorption sites.

We have further investigated the origin of the found variation in relative rate constants in Ni_9^+ and its absence in Ni_{13}^+ *via* IR-PD spectroscopy. The recorded spectra of all observed cluster adsorbate complexes reveal IR active vibrational bands at frequencies of 2170 cm^{-1} to 2260 cm^{-1}. The recorded range of these bands is compatible with the range of published head-on coordinated N-N stretching modes on TM metals. The IR-PD spectra of $[Ni_9(N_2)_m]^+$ show significant shifts of peak positions and onset of splittings by increase of the N_2 coverage, as suggested by our kinetic results. In contrast, all IR-PD spectra of $[Ni_{13}(N_2)_m]^+$ shows a single dominant band around 2222 cm^{-1} which does not shift upon increasing N_2 adsorption up to saturation. This further encourages the proposition of a smooth Ni_{13}^+ clusters surface, where all surface atoms are equivalent.

Current DFT calculations reinforce a possible isomerization with low N_2 coverage in the case of Ni_9^+, most likely from a tricapped octahedron to a bicapped pentagonal bipyramid, and geminal binding of N_2 setting in at m = 9. In the case of Ni_{13}^+ we assume an icosahedral structure which coincides with all experimental findings and theory.

Our present study unravels subtle details of N_2 adsorption to individual sites on cluster surfaces of high (Ni_9^+) and low curvatures (Ni_{13}^+). High curvature enables low coordinated sites and surface roughness. Low curvature implies a higher regularity, equal coordinated sites and surface smoothness. The rough surface of Ni_9^+ provides for a large variation of N_2 adsorption in terms of enthalpy and N_2 bond softening, while the smooth surface of Ni_{13}^+ merely provides one such case at all levels of N_2 coverage. It seems likely that a variation of adsorption conditions is more efficient for catalytic needs than a single situation. Rough likely beats smooth. The current study paves the way for subsequent N_2 activation studies with more active transition metals and their alloys. Such studies are underway.

4.2.6 Acknowledgements

The ^{58}Ni isotopic sample used in this research was supplied by the United States Department of Energy Office of Science by the Isotope Program in the Office of Nuclear Physics. This work was supported by the German research foundation DFG within the transregional collaborative research center SFB/TRR 88 "Cooperative effects in homo and heterometallic complexes" (3MET.de) and by the state research center OPTIMAS.

4.2.7 References

1. Muetterties, E. L., Metal Clusters in Catalysis .3. Clusters as Models for Chemisorption Processes and Heterogeneous Catalysis. *Bull. Soc. Chim. Belg.* **1975**, *84*, 959-986.
2. Muetterties, E. L., Molecular Metal Clusters. *Science* **1977**, *196*, 839-848.
3. Muetterties, E. L.; Rhodin, T. N.; Band, E.; Brucker, C. F.; Pretzer, W. R., Clusters and Surfaces. *Chem. Rev.* **1979**, *79*, 91-137.
4. Shustorovich, E., Cluster-Surface Analogy: New Developments. In *Quantum Chemistry: The Challenge of Transition Metals and Coordination Chemistry*, Veillard, A., Ed. Springer Netherlands: **1986**, *176*, 445-464.
5. Ertl, G., Reactions at Surfaces: From Atoms to Complexity (Nobel Lecture). *Angew. Chem. Int. Ed.* **2008**, *47*, 3524-3535.
6. Pfeffer, B.; Jaberg, S.; Niedner-Schatteburg, G., Reactions of Simple Aromatic Heterocycles with Niobium Cluster Ions (n < 30). *J. Chem. Phys.* **2009**, *131*, 194305.
7. Haberland, H.; Kleinermanns, K.; Träger, F., Cluster. In *Lehrbuch Der Experimentalphysik Band 5 - Gase, Nanosysteme, Flüssigkeiten*, 2nd ed.; Walter de Gruyter: **2006**.
8. Heiz, U.; Landman, U., *Nanocatalysis*. Springer: Berlin, **2007**.
9. Landman, U.; Yoon, B.; Zhang, C.; Heiz, U.; Arenz, M., Factors in Gold Nanocatalysis: Oxidation of Co in the non-Scalable Size Regime. *Top. Catal.* **2007**, *44*, 145-158.
10. Rips, I.; Jortner, J., Ion Solvation in Clusters. *J. Chem. Phys.* **1992**, *97*, 536-546.
11. Knickelbein, M. B.; Menezes, W. J., Metal Cluster-Rare Gas Van Der Waals Complexes: Physisorption on a Microscopic Scale. *J. Phys. Chem.* **1992**, *96*, 6611-6616.

12. De Heer, W. A., The Physics of Simple Metal Clusters: Experimental Aspects and Simple Models. *Reviews of Modern Physics* **1993**, *65*, 611.
13. Ho, J.; Zhu, L.; Parks, E.; Riley, S., Temperature Dependence of the Reactions of Small Cobalt Clusters with Deuterium. *J. Chem. Phys.* **1993**, *99*, 140-147.
14. Knickelbein, M. B., Reactions of Transition Metal Clusters with Small Molecules 1. *Annu. Rev. Phys. Chem.* **1999**, *50*, 79-115.
15. Häkkinen, H.; Abbet, S.; Sanchez, A.; Heiz, U.; Landman, U., Structural, Electronic, and Impurity-Doping Effects in Nanoscale Chemistry: Supported Gold Nanoclusters. *Angew. Chem. Int. Ed.* **2003**, *42*, 1297-1300.
16. Ervin, K. M., Metal-Ligand Interactions: Gas-Phase Transition Metal Cluster Carbonyls. *Int. Rev. Phys. Chem.* **2001**, *20*, 127-164.
17. Ganteför, G.; Icking-Konert, G. S.; Handschuh, H.; Eberhardt, W., CO Chemisorption on Ni_n, Pd_n and Pt_n Clusters. *Int. J. Mass Spectrom. Ion Processes* **1996**, *159*, 81-109.
18. Zambelli, T.; Wintterlin, J.; Trost, J.; Ertl, G., Identification of the" Active Sites" of a Surface-Catalyzed Reaction. *Science* **1996**, *273*, 1688.
19. Nørskov, J. K.; Bligaard, T.; Logadottir, A.; Bahn, S.; Hansen, L. B.; Bollinger, M.; Bengaard, H.; Hammer, B.; Sljivancanin, Z.; Mavrikakis, M., Universality in Heterogeneous Catalysis. *J. Catal.* **2002**, *209*, 275-278.
20. Honkala, K.; Hellman, A.; Remediakis, I.; Logadottir, A.; Carlsson, A.; Dahl, S.; Christensen, C. H.; Nørskov, J. K., Ammonia Synthesis from First-Principles Calculations. *Science* **2005**, *307*, 555-558.
21. Duncan, M. A., Spectroscopy of Metal Ion Complexes: Gas-Phase Models for Solvation. *Annu. Rev. Phys. Chem.* **1997**, *48*, 69-93.
22. Duncan, M. A., Infrared Spectroscopy to Probe Structure and Dynamics in Metal Ion-Molecule Complexes. *Int. Rev. Phys. Chem.* **2003**, *22*, 407-435.
23. Walker, N. R.; Walters, R. S.; Duncan, M. A., Frontiers in the Infrared Spectroscopy of Gas Phase Metal Ion Complexes. *New J. Chem.* **2005**, *29*, 1495-1503.
24. Roithova, J., Characterization of Reaction Intermediates by Ion Spectroscopy. *Chem. Soc. Rev.* **2012**, *41*, 547-559.
25. Oomens, J.; Sartakov, B. G.; Meijer, G.; von Helden, G., Gas-Phase Infrared Multiple Photon Dissociation Spectroscopy of Mass-Selected Molecular Ions. *Int. J. Mass spectrom.* **2006**, *254*, 1-19.
26. MacAleese, L.; Maitre, P., Infrared Spectroscopy of Organometallic Ions in the Gas Phase: From Model to Real World Complexes. *Mass Spectrom. Rev.* **2007**, *26*, 583-605.
27. Schöllkopf, W.; Gewinner, S.; Junkes, H.; Paarmann, A.; von Helden, G.; Bluem, H.; Todd, A. M. M. In *The New Ir and Thz Fel Facility at the Fritz Haber Institute in Berlin*, **2015**; 95121L-95121L-13.
28. Kamrath, M. Z.; Garand, E.; Jordan, P. A.; Leavitt, C. M.; Wolk, A. B.; Van Stipdonk, M. J.; Miller, S. J.; Johnson, M. A., Vibrational Characterization of Simple Peptides Using Cryogenic Infrared Photodissociation of H_2-Tagged, Mass-Selected Ions. *J. Am. Chem. Soc.* **2011**, *133*, 6440-6448.

29. Wolk, A. B.; Leavitt, C. M.; Garand, E.; Johnson, M. A., Cryogenic Ion Chemistry and Spectroscopy. *Acc. Chem. Res.* **2014**, *47*, 202-210.
30. Gruene, P.; Fielicke, A.; Meijer, G.; Rayner, D. M., The Adsorption of Co on Group 10 (Ni, Pd, Pt) Transition-Metal Clusters. *PCCP* **2008**, *10*, 6144-6149.
31. Fielicke, A.; von Helden, G.; Meijer, G.; Pedersen, D. B.; Simard, B.; Rayner, D. M., Size and Charge Effects on the Binding of CO to Late Transition Metal Clusters. *J. Chem. Phys.* **2006**, *124*, 194305-194305.
32. Harding, D. J.; Fielicke, A., Platinum Group Metal Clusters: From Gas-Phase Structures and Reactivities Towards Model Catalysts. *Chemistry* **2014**, *20*, 3258-3267.
33. Chatt, J.; Duncanson, L., 586. Olefin Co-Ordination Compounds. Part Iii. Infra-Red Spectra and Structure: Attempted Preparation of Acetylene Complexes. *J. Chem. Soc.* **1953**, 2939-2947.
34. Dewar, J., A Review of the Pi-Complex Theory. *Bull. Soc. Chim. Fr.* **1951**, *18*, C71-C79.
35. Blyholder, G., Molecular Orbital View of Chemisorbed Carbon Monoxide. *J. Phys. Chem.* **1964**, *68*, 2772-2777.
36. Allen, A.; Senoff, C., Nitrogenopentammineruthenium (Ii) Complexes. *Chem. Commun.* **1965**, 621-622.
37. Corfield, P. W.; Doedens, R. J.; Ibers, J. A., Studies of Metal-Nitrogen Multiple Bonds .I. Crystal and Molecular Structure of Nitridodichlorotris(Diethylphenyl-phosphine)Rhenium(V) Rencl2 P(C2h5)2c6h5 3. *Inorg. Chem.* **1967**, *6*, 197.
38. Collman, J. P., Patterns of Organometallic Reactions Related to Homogeneous Catalysis. *Acc. Chem. Res.* **1968**, *1*, 136-143.
39. Cohen, J. D.; Mylvaganam, M.; Fryzuk, M. D.; Loehr, T. M., Resonance Raman Studies of Dinuclear Zirconium Complexes with a Bridging Dinitrogen Ligand - Possible N_2-Coordination Models for Nitrogenase. *J. Am. Chem. Soc.* **1994**, *116*, 9529-9534.
40. MacKay, B. A.; Fryzuk, M. D., Dinitrogen Coordination Chemistry: On the Biomimetic Borderlands. *Chem. Rev.* **2004**, *104*, 385-401.
41. Duarte, H. A.; Salahub, D. R.; Haslett, T.; Moskovits, M., $Fe(N_2)_n$ (n= 1-5): Structure, Bonding, and Vibrations from Density Functional Theory. *Inorg. Chem.* **1999**, *38*, 3895-3903.
42. Haslett, T.; Fedrigo, S.; Bosnick, K.; Moskovits, M.; Duarte, H.; Salahub, D., Binary Iron-Dinitrogen Compounds Synthesized by Co-Deposition of Mass-Selected Fe, Fe_2, and Fe_3 with N_2. *J. Am. Chem. Soc.* **2000**, *122*, 6039-6044.
43. Cohen, J. D.; Fryzuk, M. D.; Loehr, T. M.; Mylvaganam, M.; Rettig, S. J., Synthesis and Structure of a Zirconium Dinitrogen Complex with a Side-on Bridging N_2 Unit. *Inorg. Chem.* **1998**, *37*, 112-119.
44. Mafuné, F.; Tawaraya, Y.; Kudoh, S., Nitrogen Molecule Adsorption on Cationic Tantalum Clusters and Rhodium Clusters and Desorption from Their Nitride Clusters Studied by Thermal Desorption Spectrometry. *J. Phys. Chem. A* **2016**, *120*, 4089-4095.

45. Kerpal, C.; Harding, D. J.; Lyon, J. T.; Meijer, G.; Fielicke, A., N_2 Activation by Neutral Ruthenium Clusters. *Journal of Physical Chemistry C* **2013**, *117*, 12153-12158.
46. Meyer, J.; Tombers, M.; van Wüllen, C.; Niedner-Schatteburg, G.; Peredkov, S.; Eberhardt, W.; Neeb, M.; Palutke, S.; Martins, M.; Wurth, W., The Spin and Orbital Contributions to the Total Magnetic Moments of Free Fe, Co, and Ni Clusters. *J. Chem. Phys.* **2015**, *143*, 104302/1-104302/12.
47. Petkov, P. S.; Vayssilov, G. N.; Krueger, S.; Roesch, N., Density Functional Study of Ni_6 Clusters Containing Impurity Atoms. *Chem. Phys.* **2008**, *348*, 61-68.
48. Guzman-Ramirez, G.; Robles, J.; Vega, A.; Aguilera-Granja, F., Stability, Structural, and Magnetic Phase Diagrams of Ternary Ferromagnetic 3d-Transition-Metal Clusters with Five and Six Atoms. *J. Chem. Phys.* **2011**, *134*, 054101/1-054101/9.
49. Song, W.; Lu, W.-C.; Wang, C. Z.; Ho, K. M., Magnetic and Electronic Properties of the Nickel Clusters Ni_n ($n \leq 30$). *Comput. Theor. Chem.* **2011**, *978*, 41-46.
50. Sahoo, S.; Rollmann, G.; Entel, P., First-Principles Calculation of Cluster Geometries and Magnetization of Pure Ni and Fe-Ni Clusters. *Phase Transitions* **2005**, *78*, 723-731.
51. Gao, C.; Zhang, X., Geometries and Physical Properties of W_nNi_m ($n + m \leq 7$) Clusters. *J. Comput. Theor. Nanosci.* **2010**, *7*, 612-618.
52. Das, N. K.; Shoji, T., Geometry, Orbital Interaction, and Oxygen Chemisorption Properties of Chromium-Doped Nickel Clusters. *J. Phys. Chem. C* **2012**, *116*, 13353-13367.
53. Wang, L. S.; Wu, H., Photoelectron Spectroscopy of Transition Metal Clusters. *Z. Phys. Chem. (Munich)* **1998**, *203*, 45-55.
54. Morenzin, J.; Kietzmann, H.; Bechthold, P. S.; Gantefor, G.; Eberhardt, W., Localization and Bandwidth of the 3d-Orbitals in Magnetic Ni and Co Clusters. *Pure Appl. Chem.* **2000**, *72*, 2149-2157.
55. Kerns, K. P.; Parks, E. K.; Riley, S. J., The Binding of CO to Nickel Clusters. II. Structural Implications and Comparisons with Electron Counting Rules. *J. Chem. Phys.* **2000**, *112*, 3394-3407.
56. Liu, F.; Liyanage, R.; Armentrout, P. B., Guided Ion Beam Studies of the Reaction of Ni_n^+ (n=2-16) with D_2: Nickel Cluster-Deuteride Bond Energies. *J. Chem. Phys.* **2002**, *117*, 132-141.
57. Grigoryan, V. G.; Springborg, M., Structural and Energetic Properties of Nickel Clusters: $2 \leq n \leq 150$. *Phys. Rev. B: Condens. Matter Mater. Phys.* **2004**, *70*, 205415/1-205415/15.
58. Liu, F.; Zhang, X.-G.; Liyanage, R.; Armentrout, P. B., Methane Activation by Nickel Cluster Cations, Ni_n^+ (n=2-16): Reaction Mechanisms and Thermochemistry of Cluster-CH_x (x=0-3) Complexes. *J. Chem. Phys.* **2004**, *121*, 10976-10990.
59. Swart, I.; de Groot, F. M. F.; Weckhuysen, B. M.; Gruene, P.; Meijer, G.; Fielicke, A., H_2 Adsorption on 3d Transition Metal Clusters: A Combined Infrared Spectroscopy and Density Functional Study. *J. Phys. Chem. A* **2008**, *112*, 1139-1149.

60. Swart, I.; Gruene, P.; Fielicke, A.; Meijer, G.; Weckhuysen, B. M.; de Groot, F. M. F., Molecular Adsorption of H_2 on Small Cationic Nickel Clusters. *PCCP* **2008**, *10*, 5743-5745.
61. Walters, R. S.; Jaeger, T. D.; Duncan, M. A., Infrared Spectroscopy of $Ni^+(C_2H_2)_n$ Complexes: Evidence for Intracluster Cyclization Reactions. *J. Phys. Chem. A* **2002**, *106*, 10482-10487.
62. Walters, R. S.; Pillai, E. D.; Duncan, M. A., Solvation Dynamics in $Ni^+(H_2O)_n$ Clusters Probed with Infrared Spectroscopy. *J. Am. Chem. Soc.* **2005**, *127*, 16599-16610.
63. Beeck, O., *Advances in Catalysis 2* **1950**, 155.
64. Kokes, R.; Emmett, P., Chemisorption of Nitrogen on Nickel Catalysts. *J. Am. Chem. Soc.* **1958**, *80*, 2082-2086.
65. Parks, E.; Zhu, L.; Ho, J.; Riley, S., The Structure of Small Nickel Clusters. I. Ni_3–Ni_{15}. *J. Chem. Phys.* **1994**, *100*, 7206-7222.
66. Parks, E.; Zhu, L.; Ho, J.; Riley, S., The Structure of Small Nickel Clusters. II. Ni_{16}–Ni_{28}. *J. Chem. Phys.* **1995**, *102*, 7377-7389.
67. Langevin, M. In *Une Formule Fondamentale De Théorie Cinétique*, Annales de chimie et de physique, Series, **1905**; 245-288.
68. Su, T.; Bowers, M. T., Theory of Ion-Polar Molecule Collisions. Comparison with Experimental Charge Transfer Reactions of Rare Gas Ions to Geometric Isomers of Difluorobenzene and Dichloroethylene. *J. Chem. Phys.* **1973**, *58*, 3027-3037.
69. Su, T.; Bowers, M. T., Ion-Polar Molecule Collisions. Proton Transfer Reactions of H_3^+ and CH_5^+ to the Geometric Isomers of Difluoroethylene, Dichloroethylene, and Difluorobenzene. *J. Am. Chem. Soc.* **1973**, *95*, 1370-1373.
70. Berg, C.; Schindler, T.; Niedner-Schatteburg, G.; Bondybey, V. E., Reactions of Simple Hydrocarbons with Nb_n^+: Chemisorption and Physisorption on Ionized Niobium Clusters. *J. Chem. Phys.* **1995**, *102*, 4870-4884.
71. Balteanu, I.; Balaj, O. P.; Fox-Beyer, B. S.; Rodrigues, P.; Barros, M. T.; Moutinho, A. M. C.; Costa, M. L.; Beyer, M. K.; Bondybey, V. E., Size- and Charge-State-Dependent Reactivity of Azidoacetonitrile with Anionic and Cationic Rhodium Clusters $Rh_n^\pm$. *Organometallics* **2004**, *23*, 1978-1985.
72. Anderson, M. L.; Ford, M. S.; Derrick, P. J.; Drewello, T.; Woodruff, D. P.; Mackenzie, S. R., Nitric Oxide Decomposition on Small Rhodium Clusters, Rh_n^+. *J. Phys. Chem. A* **2006**, *110*, 10992-11000.
73. Kummerlöwe, G.; Beyer, M. K., Rate Estimates for Collisions of Ionic Clusters with Neutral Reactant Molecules. *Int. J. Mass spectrom.* **2005**, *244*, 84-90.
74. Eischens, R. P.; Jacknow, J., *in: Proc. 3rd Intern. Congress on Catalysis (NorthHolland, Amsterdam)* **1965**, 627-643.
75. van Hardeveld, R.; van Montfoort, A., The Influence of Crystallite Size on the Adsorption of Molecular Nitrogen on Nickel, Palladium and Platinum. *Surf. Sci.* **1966**, *4*, 396-430.
76. Huber, H.; Kuendig, E. P.; Moskovits, M.; Ozin, G. A., Binary Transition Metal Dinitrogen Complexes. I. Matrix Infrared and Raman Spectra, Structure and Bonding of $Ni(N_2)_n$ and $Pd(N_2)_m$(n = 1-4 and m = 1-3). *J. Am. Chem. Soc.* **1973**, *95*, 332-344.

77. Tsay, C.; Peters, J. C., Thermally Stable N_2 and H_2 Adducts of Cationic Nickel (II). *Chemical Science* **2012**, *3*, 1313-1318.
78. Bridgeman, A. J.; Wilkin, O. M.; Young, N. A., Dinitrogen Bonding Modes to Molecular Nickel(II) Halides: A Matrix Isolation Ir and Dft Study. *Inorg. Chem. Commun.* **2000**, *3*, 681-684.
79. Craig, S. M.; Menges, F. S.; Johnson, M. A., Application of Gas Phase Cryogenic Vibrational Spectroscopy to Characterize the CO_2, CO, N_2 and N_2O Interactions with the Open Coordination Site on a Ni(I) Macrocycle Using Dual Cryogenic Ion Traps. *J. Mol. Spectrosc.* **2016***, in press,* DOI: 10.1016/j.jms.2016.11.015.
80. Peredkov, S.; Neeb, M.; Eberhardt, W.; Meyer, J.; Tombers, M.; Kampschulte, H.; Niedner-Schatteburg, G., Spin and Orbital Magnetic Moments of Free Nanoparticles. *Phys. Rev. Lett.* **2011**, *107*, .233401/1-233401/5.
81. Nosenko, Y.; Menges, F.; Riehn, C.; Niedner-Schatteburg, G., Investigation by Two-Color IR Dissociation Spectroscopy of Hoogsteen-Type Binding in a Metalated Nucleobase Pair Mimic. *PCCP* **2013**, *15*, 8171-8178.
82. Lang, J.; Gaffga, M.; Menges, F.; Niedner-Schatteburg, G., Two-Color Delay Dependent Ir Probing of Torsional Isomerization in a $[AgL1L2]^+$ Complex. *PCCP* **2014**, *16*, 17417-17421.
83. Gaffga, M.; Munstein, I.; Muller, P.; Lang, J.; Thiel, W. R.; Niedner-Schatteburg, G., Multistate-Mediated Rearrangements and $FeCl_2$ Elimination in Dinuclear FePd Complexes. *J. Phys. Chem. A* **2015**, *119*, 12587-12598.
84. Mohrbach, J.; Lang, J.; Dillinger, S.; Prosenc, M. A.; Braunstein, P.; Niedner-Schatteburg, G., Vibrational Fingerprints of a Tetranuclear Cobalt Carbonyl Cluster within an Ion Trap. *J. Mol. Spectrosc.* **2016**, *in press*, DOI: 10.1016/j.jms.2016.11.008.
85. Dillinger, S.; Mohrbach, J.; Hewer, J.; Gaffga, M.; Niedner-Schatteburg, G., Infrared Spectroscopy of N_2 Adsorption on Size Selected Cobalt Cluster Cations in Isolation. *PCCP* **2015**, *17*, 10358-10362.
86. Lang, J.; Mohrbach, J.; Dillinger, S.; Hewer, J. M.; Niedner-Schatteburg, G., Vibrational Blue Shift of Coordinated N_2 in $[Fe_3O(OAc)_6(N_2)_n]^+$: "non-classical" Dinitrogen Complexes. *Chem. Commun.* **2017,** *in press*, DOI: 10.1039/C6CC07481B.
87. Maruyama, S.; Anderson, L. R.; Smalley, R. E., Direct Injection Supersonic Cluster Beam Source for Ft-Icr Studies of Clusters. *Rev. Sci. Instrum.* **1990**, *61*, 3686-3693.
88. Proch, D.; Trickl, T., A High-Intensity Multi-Purpose Piezoelectric Pulsed Molecular Beam Source. *Rev. Sci. Instrum.* **1989**, *60*, 713-716.
89. Caravatti, P.; Allemann, M., The 'Infinity Cell': A New Trapped-Ion Cell with Radiofrequency Covered Trapping Electrodes for Fourier Transform Ion Cyclotron Resonance Mass Spectrometry. *Org. Mass Spectrom.* **1991**, *26*, 514-518.
90. Graf, M., Entwicklung eines auf Evolutionsstrategien basierenden Computerprogrammes zum optimierten Anpassen kinetischer Daten aus FT-ICR-Massenspektrometrie-Messungen*,* Diploma Thesis, TU Kaiserslautern, September **2006**.

91. Adamo, C.; Barone, V., Toward Reliable Density Functional Methods without Adjustable Parameters: The PBE0 Model. *J. Chem. Phys.* **1999**, *110*, 6158-6170.
92. Dunning Jr, T. H., Gaussian Basis Sets for Use in Correlated Molecular Calculations. I. The Atoms Boron through Neon and Hydrogen. *J. Chem. Phys.* **1989**, *90*, 1007-1023.
93. Dolg, M.; Stoll, H.; Preuss, H.; Pitzer, R. M., Relativistic and Correlation Effects for Element 105 (Hahnium, Ha): A Comparative Study of M and Mo (M= Nb, Ta, Ha) Using Energy-Adjusted Ab Initio Pseudopotentials. *J. Phys. Chem.* **1993**, *97*, 5852-5859.
94. Frisch, M. J.; Trucks, G.; Schlegel, H.; Scuseria, G.; Robb, M.; Cheeseman, J.; Scalmani, G.; Barone, V.; Mennucci, B.; Petersson, G.; et al., Gaussian 09, Revision A. 1. *Gaussian Inc., Wallingford, CT* **2009**.
95. Grunze, M. J.; Fühler, J.; Neumann, M.; Brundle, C. R.; Auerbach, D. J.; Behm, J., A Search for Precursor States to Molecular Nitrogen Chemisorption on Ni(100), Re(0001) and W(100) Surfaces at ~ 20 K. *Surf. Sci.* **1984**, *139*, 109-120.
96. Grunze, M.; Driscoll, R. K.; Burland, G. N.; Cornish, J. C. L.; Pritchard, J., Molecular and Dissociative Chemisorption of N_2 on Ni(110). *Surf. Sci.* **1979**, *89*, 381-390.
97. Rapps, T.; Ahlrichs, R.; Waldt, E.; Kappes, M. M.; Schooss, D., On the Structures of 55-Atom Transition-Metal Clusters and Their Relationship to the Crystalline Bulk. *Angew. Chem. Int. Ed.* **2013**, *52*, 6102-6105.
98. For low adsoption numbers DFT modelling suggests the first N_2 coordination to a threefold coordinated Ni atom, most likely to the inner capping Ni atom. This is in conjunction with the observed single absorption band for (9,1) at 2238 cm^{-1}, whereas the (9,2) species shows an additional band at 2250 cm^{-1}. For more information please see supplement.
99. Parks and Riley argue that the metal cluster stability is enhanced by minimizing the number of atoms with low metal coordination, which would make the tricapped octahedron less stable than the bicapped pentagonal bipyramid. It is conceivable, that nitrogen adsorption on the three-coordinate atoms might reverse the relative stabilities, in particular when the adsorption reaches saturation. Our findings agree in principle. However, we propose opposite stabilities: A tricapped octahedron is more stable when covered by a few N_2 adsorbates, and it becomes a bicapped pentagonal bipyramid when covered with nitrogen up to saturation.
100. Grimme, S.; Antony, J.; Ehrlich, S.; Krieg, H., A Consistent and Accurate Ab Initio Parametrization of Density Functional Dispersion Correction (DFT-D) for the 94 Elements H-Pu. *J. Chem. Phys.* **2010**, *132*, 154104/1-154104/19.
101. Niemeyer, M.; Hirsch, K.; Zamudio-Bayer, V.; Langenberg, A.; Vogel, M.; Kossick, M.; Ebrecht, C.; Egashira, K.; Terasaki, A.; Möller, T.; et al., Spin Coupling and Orbital Angular Momentum Quenching in Free Iron Clusters. *Phys. Rev. Lett.* **2012**, *108*, 057201/1- 057201/5.

4.2.8 Supplementary Information

Cryo Kinetics and Spectroscopy of Cationic Nickel Clusters: Rough and Smooth Surfaces

Jennifer Mohrbach, Sebastian Dillinger, and Gereon Niedner-Schatteburg

Fachbereich Chemie and Forschungszentrum OPTIMAS,
Technische Universität Kaiserslautern,
67663 Kaiserslautern, Germany

Table of content

1. Energy differences including zero-point-energy corrections for several $[Ni_9(N_2)_1]^+$ isomers 111

Table S1. Relative stabilities including zero-point-correction (in kJ/mol) for the computed tricapped octahedral Ni_9^+ cluster core upon the first N_2 adsorption for decet spin states at several adsorption positions. 111

2. Detailed information on all observed reaction steps of the N_2 adsorption/desorption 112

Table S2. Pseudo-first-order rate constants for the N_2 adsorption/desorption on Ni_9^+ clusters ($k_{(9,m)}$ and $k_{-(9,m+1)}$), related absolute rate constants ($k(9,m)abs$ and $k-(9,m+1)abs$) calculated collision rates (k_L and k_{SCC}). 112

Table S3. Pseudo-first-order rate constants for the N_2 adsorption/desorption on Ni_{13}^+ clusters ($k_{(13,m)}$ and $k_{-(13,m+1)}$), related absolute rate constants ($k(13,m)abs$ and $k-(13,m+1)abs$) and calculated collision rates (k_L and k_{SCC}). 113

3. Spectrum of the (9,13) species in an extended frequency range 114

Figure S1. IR-MPD spectrum of the (9,13) species in an extended frequency range of 1010 - 2340 cm^{-1}. Note, that this spectrum has been recorded with increased laser power. 114

4. Computed geometries and relative energies for multiple local minimum structures for the naked Ni_9^+ cluster and relative stabilities for icosahedral Ni_{13}^+ clusters considereing several spin states. 115

Figure S2: Computed geometries for Ni_9^+ and their relative stabilities. Note, that the stated values are given for the favoured spin multiplicity, respectively. 115

Table S4. Relative stabilities for computed icosahedral Ni_{13}^+ with variation of the spin multiplicity, 2S + 1 = 10-18. 116

5. Possible adsorption positions on the tricapped octahedral Ni_9^+ cluster core and relative stabilities with variation of the spin multiplicity 117

Figure S3: Tricapped octahedron with numbered adsorption positions. Note, that each number reflects the Ni-Ni coordination, respectively. 117

Table S5. Relative stabilities for the computed tricapped octahedral Ni_9^+ cluster core upon the first N_2 adsorption with variation of the spin multiplicity and adsorption position. 118

6. Comparison of the experimental IR-PD spectrum of (9,2) and calculated IR absorption spectra for the assumed tricapped octahedral and bicapped pentagonal bipyramidal Ni_9^+ motifs 119

Figure S4. IR-PD spectrum of (9,2) (blue) and the calculated IR absorption spectra for the tricapped octahedral and bicapped pentagonal bipyramidal motifs with variation in the adsorbing Ni atoms (black; PBE0/ECP(Ni), cc-pVTZ(N), 2S + 1 = 10). The calculated spectra are scaled by 0.93 and simulated using the gaussian profile of fwhm = 5 cm^{-1}. 119

7. Comparison of the experimental IR-PD spectra of (9,m) (m = 3,4,6,7, and 10-13) and calculated IR absorption spectra for the assumed tricapped octahedral and bicapped pentagonal bipyramidal Ni_9^+ motifs 120

Figure S5. IR-PD spectrum of (9,3) (blue) and the calculated IR absorption spectra for the tricapped octahedral and bicapped pentagonal bipyramidal motifs with variation in the adsorbing Ni atoms (black; PBE0/ECP(Ni), cc-pVTZ(N), 2S + 1 = 10). The calculated spectra are scaled by 0.93 and simulated using the gaussian profile of fwhm = 5 cm^{-1}. 120

Figure S6. IR-PD spectrum of (9,4) (blue) and the calculated IR absorption spectra for the tricapped octahedral and bicapped pentagonal bipyramidal motifs with variation in the adsorbing Ni atoms (black; PBE0/ECP(Ni), cc-pVTZ(N), 2S + 1 = 10). The calculated spectra are scaled by 0.93 and simulated using the gaussian profile of fwhm = 5 cm^{-1}. 121

Figure S7. IR-PD spectrum of (9,6) (blue) and the calculated IR absorption spectra for the tricapped octahedral and bicapped pentagonal bipyramidal motifs with variation in the adsorbing Ni atoms (black; PBE0/ECP(Ni), cc-pVTZ(N), 2S + 1 = 10). The calculated spectra are scaled by 0.93 and simulated using the gaussian profile of fwhm = 5 cm^{-1}. 122

Figure S8. IR-PD spectrum of (9,7) (blue) and the calculated IR absorption spectra for the tricapped octahedral and bicapped pentagonal bipyramidal motifs with variation in the adsorbing Ni atoms (black; PBE0/ECP(Ni), cc-pVTZ(N), 2S + 1 = 10). The calculated spectra are scaled by 0.93 and simulated using the gaussian profile of fwhm = 5 cm^{-1}. 123

Figure S9. IR-PD spectrum of (9,10) (blue) and the calculated IR absorption spectra for the tricapped octahedral and bicapped pentagonal bipyramidal motifs with variation in the adsorbing Ni atoms and in spin multiplicities (black; PBE0/ECP(Ni), cc-pVTZ(N)). The calculated spectra are scaled by 0.93 and simulated using the gaussian profile of fwhm = 5 cm^{-1}. 124

Figure S10. IR-PD spectrum of (9,11) (blue) and the calculated IR absorption spectra for the tricapped octahedral and bicapped pentagonal bipyramidal motifs with variation in the adsorbing Ni atoms and in spin multiplicities (black; PBE0/ECP(Ni), cc-pVTZ(N)). The calculated spectra are scaled by 0.93 and simulated using the gaussian profile of fwhm = 5 cm^{-1}. 125

Figure S11. IR-PD spectrum of (9,12) (blue) and the calculated IR absorption spectra for the tricapped octahedral and bicapped pentagonal bipyramidal motifs with variation in the sole vacant Ni atom and in spin multiplicities (black; PBE0/ECP(Ni), cc-pVTZ(N)). The calculated spectra are scaled by 0.93 and simulated using the gaussian profile of fwhm = 5 cm^{-1}. 126

Figure S12. IR-PD spectrum of (9,13) (blue) and the calculated IR absorption spectra for the tricapped octahedral and bicapped pentagonal bipyramidal motifs with maximum N_2 adsorption as shown in Fig. 5 (black; PBE0/ECP(Ni), cc-pVTZ(N)). The calculated spectra are scaled by 0.93 and simulated using the gaussian profile of fwhm = 5 cm^{-1}. 127

8. Calculated IR absorption spectra including the Grimme correction for dispersion with the original D3 damping function (GD3) 128

Figure S13. Calculated IR absorption spectra for the tricapped octahedral motif (top lanes) in comparison with calculated IR absorption spectra including the Grimme correction for dispersion with the original D3 damping function (bottom lanes) for (9,8) for the octet spin state (left) and the decet spin state (right). The calculated spectra are scaled by 0.93 and simulated using the gaussian profile of fwhm = 5 cm^{-1}. 128

Figure S14. Calculated IR absorption spectra for the tricapped octahedral motif (top lanes) in comparison with calculated IR absorption spectra including the Grimme correction for dispersion with the original D3 damping function (bottom lanes) for (9,9) for the octet spin state (left) and the decet spin state (right). The calculated spectra are scaled by 0.93 and simulated using the gaussian profile of fwhm = 5 cm^{-1}. 129

1. Energy differences including zero-point-energy corrections for several $[Ni_9(N_2)_1]^+$ isomers

Table S1. Relative stabilities including zero-point-correction (in kJ/mol) for the computed tricapped octahedral Ni_9^+ cluster core upon the first N_2 adsorption for decet spin states at several adsorption positions.

position	$\Delta_f U_{0\,K}$	$\Delta_f U_{0\,K}^{ZPE}$	$\Delta_f U_{300\,K}$	$\Delta_f H_{300\,K}$	$\Delta_f G_{300\,K}$
3,1	4.5	5.5	9.5	9.5	0
3,2	0	0	0	0	0.8
4	15.9	16.1	18.3	18.3	13.7
5	10.8	10.8	12.8	12.8	9.2

2. Detailed information on all observed reaction steps of the N_2 adsorption/desorption

Table S2. Pseudo-first-order rate constants for the N_2 adsorption/desorption on Ni_9^+ clusters ($k_{(9,m)}$ and $k_{-(9,m+1)}$), related absolute rate constants ($k_{(9,m)}^{abs}$ and $k_{-(9,m+1)}^{abs}$) calculated collision rates (k_L and k_{SCC}).

m	$k_{(9,m)}$ s^{-1}	$k_{-(9,m+1)}$ s^{-1}	$k_{(9,m)}^{abs}$ 10^{-10} cm³ s⁻¹	$k_{-(9,m+1)}^{abs}$ 10^{-13} cm³ s⁻¹	k_L 10^{-10} cm³ s⁻¹	k_{SCC} 10^{-10} cm³ s⁻¹
0	3.6(3)	<0.001	6.37	<1.77	6.05	12.66
1	4.2(3)	<0.001	7.43	<1.77	6.04	12.78
2	3.9(3)	<0.001	6.90	<1.77	6.03	12.91
3	3.9(3)	<0.001	6.90	<1.77	6.02	13.02
4	3.6(4)	<0.001	6.37	<1.77	6.02	13.13
5	3.5(4)	<0.001	6.19	<1.77	6.01	13.24
6	3.1(3)	<0.001	5.48	<1.77	6.01	13.36
7	2.4(2)	<0.001	4.25	<1.77	6.00	13.46
8	1.5(2)	<0.001	2.65	<1.77	6.00	13.57
9	2.1(2)	<0.001	3.72	<1.77	5.99	13.68
10	3.8(4)	<0.001	6.72	<1.77	5.99	13.78
11	1.1(1)	<0.001	1.94	<1.77	5.99	13.88
12	0.7(1)	0.07(1)	1.24	123	5.98	13.98

Table S3. Pseudo-first-order rate constants for the N_2 adsorption/desorption on Ni_{13}^+ clusters ($k_{(13,m)}$ and $k_{-(13,m+1)}$), related absolute rate constants ($k^{abs}_{(13,m)}$ and $k^{abs}_{-(13,m+1)}$) and calculated collision rates (k_L and k_{SCC}).

m	$k_{(13,m)}$ s^{-1}	$k_{-(13,m+1)}$ s^{-1}	$k^{abs}_{(13,m)}$ 10^{-10} cm^3 s^{-1}	$k^{abs}_{-(13,m+1)}$ 10^{-13} cm^3 s^{-1}	k_L 10^{-10} cm^3 s^{-1}	k_{SCC} 10^{-10} cm^3 s^{-1}
0	4.2(2)	<0.001	7.43	<1.77	6.00	13.60
1	4.2(2)	<0.001	7.43	<1.77	5.99	13.71
2	4.2(2)	<0.001	7.43	<1.77	5.99	13.81
3	4.4(2)	<0.001	7.78	<1.77	5.99	13.91
4	4.4(2)	<0.001	7.78	<1.77	5.98	14.01
5	4.5(2)	<0.001	7.96	<1.77	5.98	14.11
6	4.6(3)	<0.001	8.14	<1.77	5.98	14.20
7	4.6(3)	<0.001	8.14	<1.77	5.97	14.30
8	4.6(3)	<0.001	8.14	<1.77	5.97	14.39
9	4.3(2)	<0.001	7.61	<1.77	5.97	14.48
10	4.2(2)	<0.001	7.43	<1.77	5.97	14.57
11	4.4(2)	<0.001	7.78	<1.77	5.96	14.66

3. Spectrum of the (9,13) species in an extended frequency range

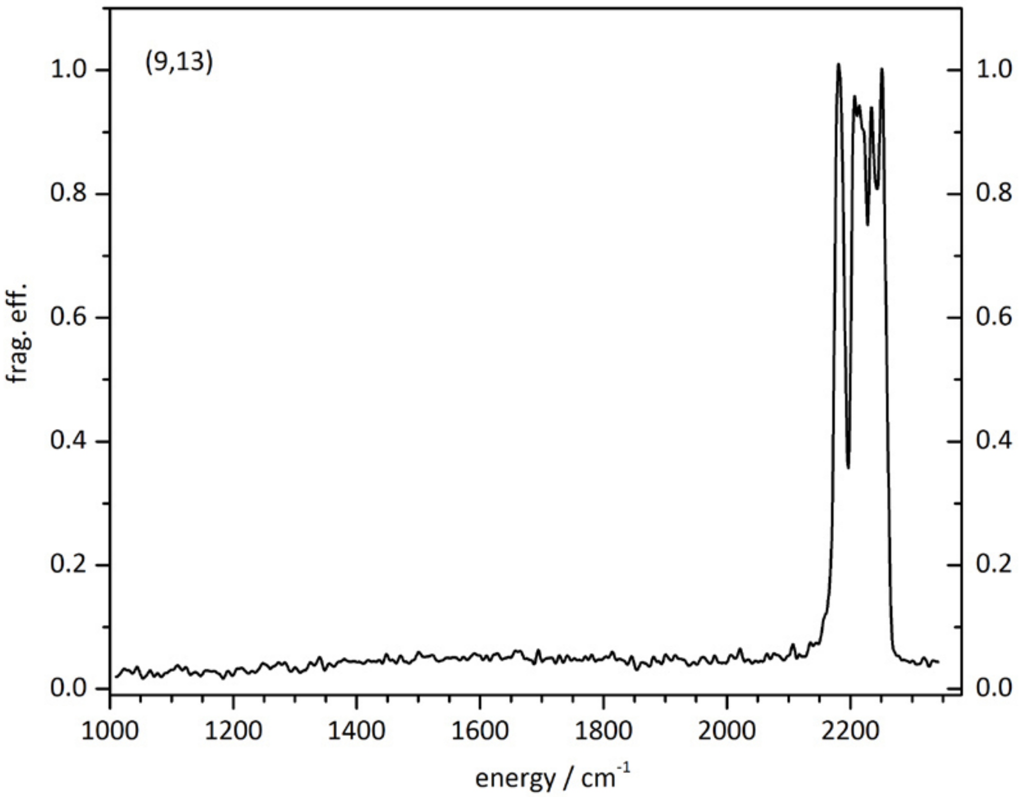

Figure S1. IR-MPD spectrum of the (9,13) species in an extended frequency range of 1010 - 2340 cm^{-1}. Note, that this spectrum has been recorded with increased laser power.

4. Computed geometries and relative energies for multiple local minimum structures for the naked Ni_9^+ cluster and relative stabilities for icosahedral Ni_{13}^+ clusters considereing several spin states.

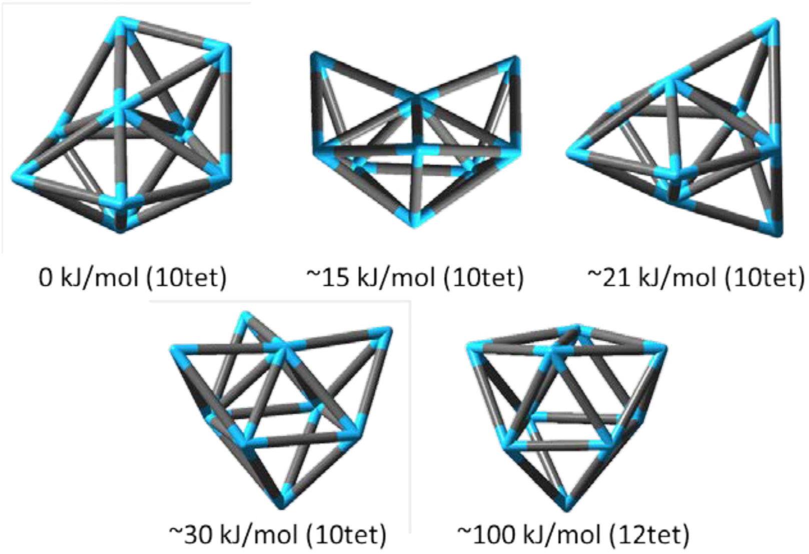

0 kJ/mol (10tet)

~15 kJ/mol (10tet)

~21 kJ/mol (10tet)

~30 kJ/mol (10tet)

~100 kJ/mol (12tet)

Figure S2: Computed geometries for Ni_9^+ and their relative stabilities. Note, that the stated values are given for the favoured spin multiplicity, respectively.

Table S4. Relative stabilities for computed icosahedral Ni_{13}^+ with variation of the spin multiplicity, 2S + 1 = 10-18.

2S+1	rel. energy / kJ/mol
10	56
12	50
14	31
16	0
18	89

5. Possible adsorption positions on the tricapped octahedral Ni_9^+ cluster core and relative stabilities with variation of the spin multiplicity

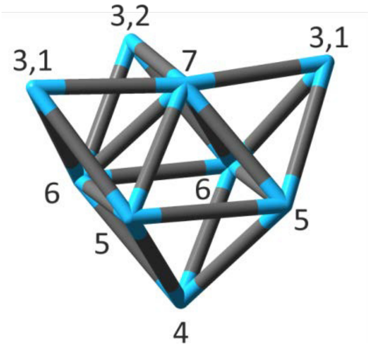

Figure S3: Tricapped octahedron with numbered adsorption positions. Note, that each number reflects the Ni-Ni coordination, respectively.

Table S5. Relative stabilities for the computed tricapped octahedral Ni_9^+ cluster core upon the first N_2 adsorption with variation of the spin multiplicity and adsorption position.

position	2S+1	rel. energy / kJ/mol
3,1	6	23
	8	67
	10	**5**
	12	103
	14	168
3,2	6	75
	8	82
	10	**0**
	12	97
	14	139
4	6	22
	8	74
	10	16
	12	94
	14	205
5	6	22
	8	17
	10	10
	14	154
6	6	24
	8	57
	10	15
	12	74
	14	189
7	6	138
	8	33
	10	22
	12	111
	14	187

For low adsoption numbers DFT modelling suggests the first N_2 coordination to a threefold (3,1 and 3,2) coordinated Ni atom, most likely to the middle capping atom (3,2,).

6. Comparison of the experimental IR-PD spectrum of (9,2) and calculated IR absorption spectra for the assumed tricapped octahedral and bicapped pentagonal bipyramidal Ni_9^+ motifs

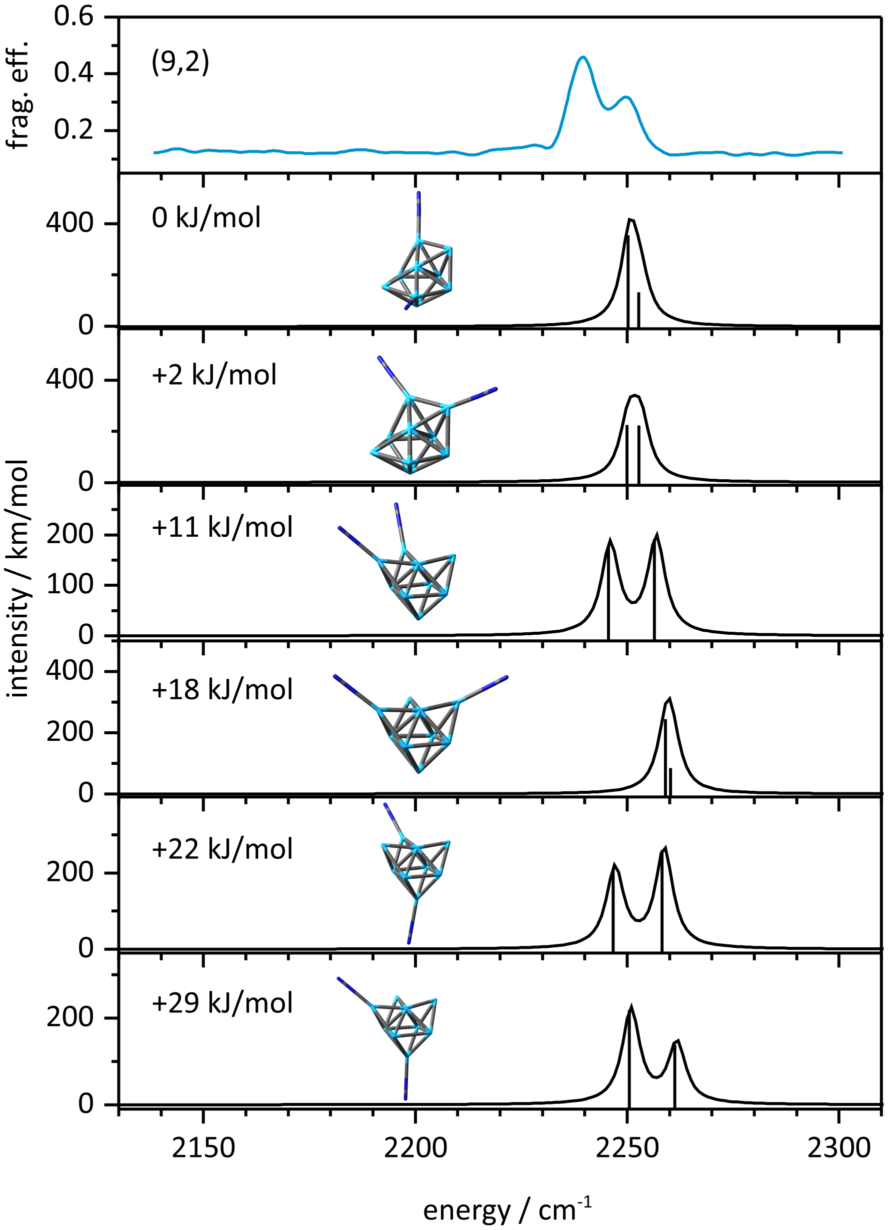

Figure S4. IR-PD spectrum of (9,2) (blue) and the calculated IR absorption spectra for the tricapped octahedral and bicapped pentagonal bipyramidal motifs with variation in the adsorbing Ni atoms (black; PBE0/ECP(Ni), cc-pVTZ(N), 2S + 1 = 10). The calculated spectra are scaled by 0.93 and simulated using the gaussian profile of fwhm = 5 cm^{-1}.

7. Comparison of the experimental IR-PD spectra of (9,m) (m = 3,4,6,7, and 10-13) and calculated IR absorption spectra for the assumed tricapped octahedral and bicapped pentagonal bipyramidal Ni_9^+ motifs

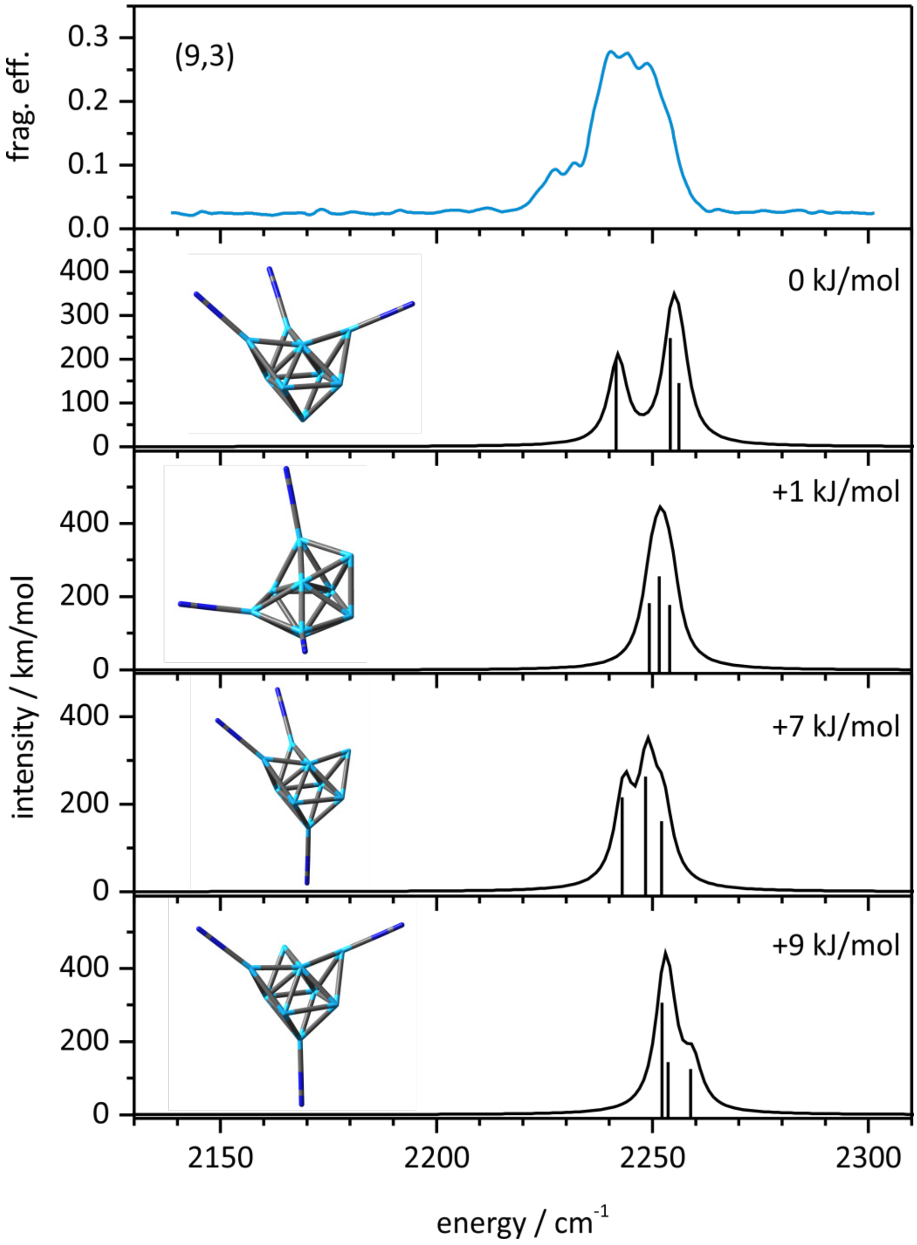

Figure S5. IR-PD spectrum of (9,3) (blue) and the calculated IR absorption spectra for the tricapped octahedral and bicapped pentagonal bipyramidal motifs with variation in the adsorbing Ni atoms (black; PBE0/ECP(Ni), cc-pVTZ(N), 2S + 1 = 10). The calculated spectra are scaled by 0.93 and simulated using the gaussian profile of fwhm = 5 cm^{-1}.

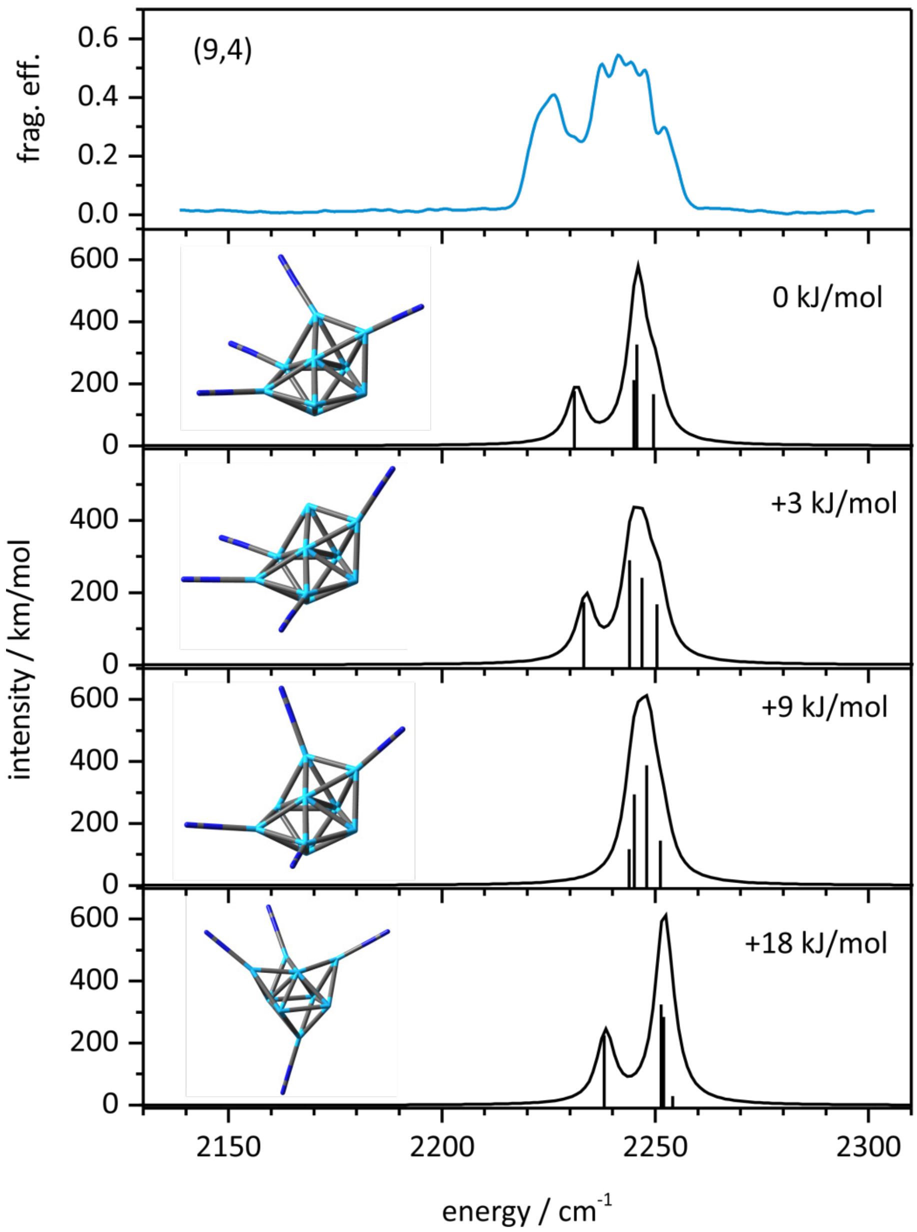

Figure S6. IR-PD spectrum of (9,4) (blue) and the calculated IR absorption spectra for the tricapped octahedral and bicapped pentagonal bipyramidal motifs with variation in the adsorbing Ni atoms (black; PBE0/ECP(Ni), cc-pVTZ(N), 2S + 1 = 10). The calculated spectra are scaled by 0.93 and simulated using the gaussian profile of fwhm = 5 cm^{-1}.

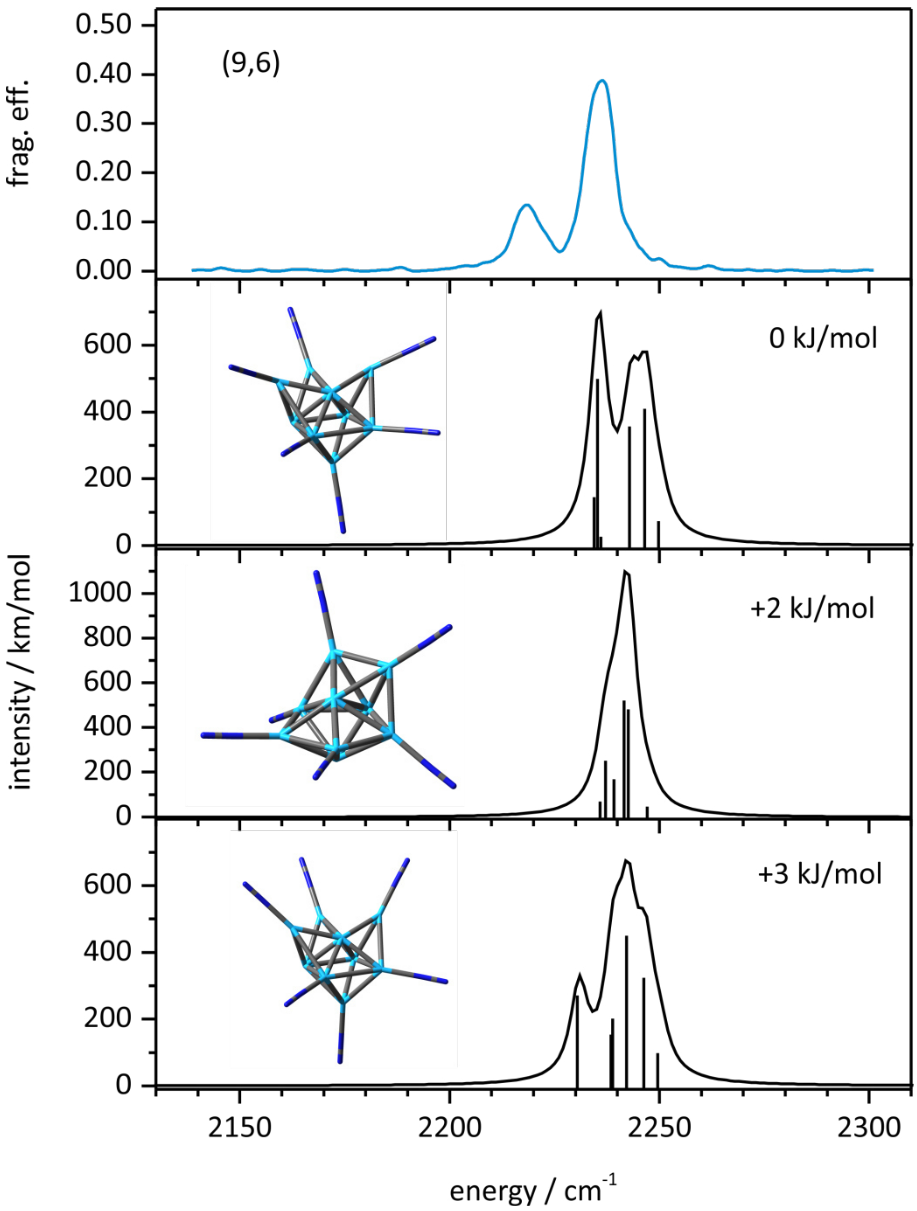

Figure S7. IR-PD spectrum of (9,6) (blue) and the calculated IR absorption spectra for the tricapped octahedral and bicapped pentagonal bipyramidal motifs with variation in the adsorbing Ni atoms (black; PBE0/ECP(Ni), cc-pVTZ(N), 2S + 1 = 10). The calculated spectra are scaled by 0.93 and simulated using the gaussian profile of fwhm = 5 cm^{-1}.

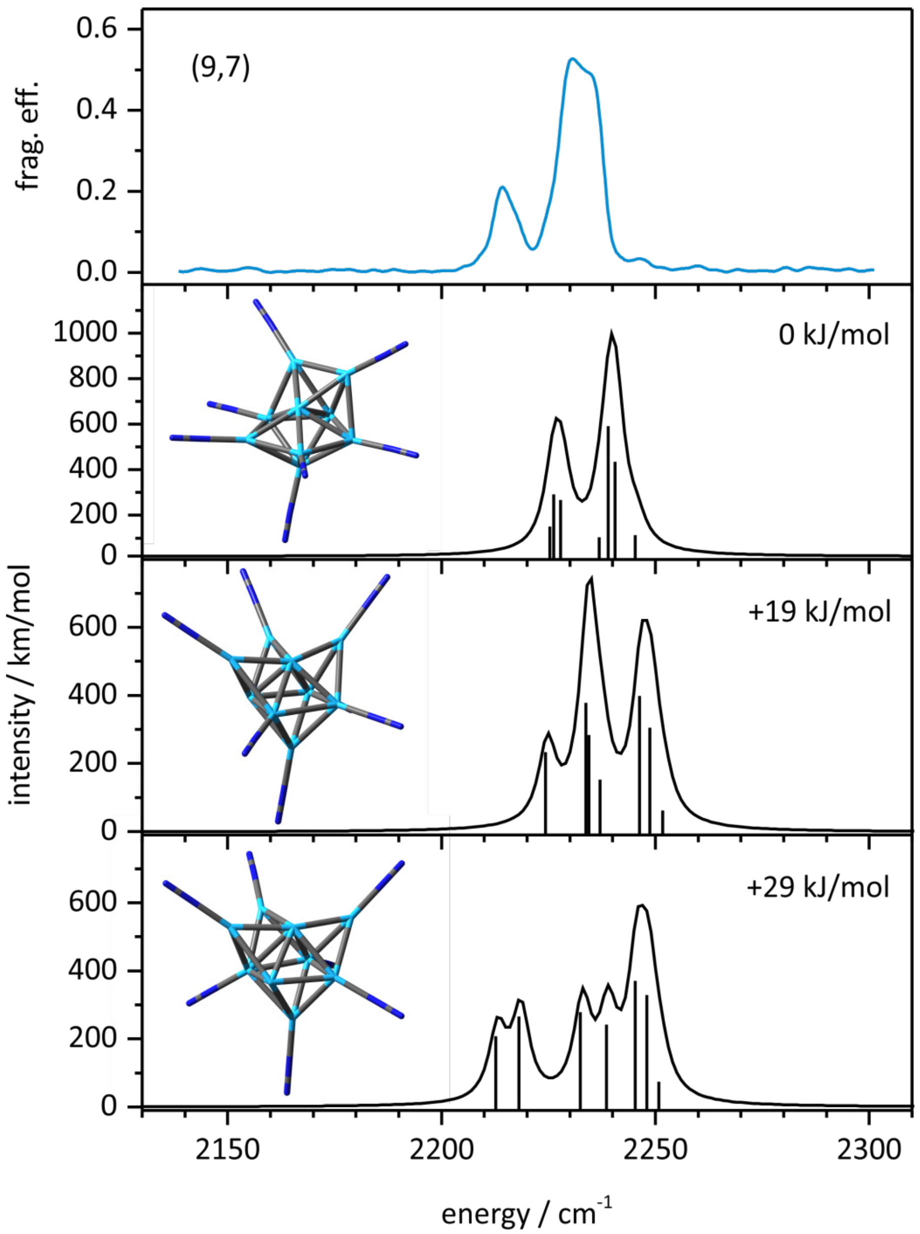

Figure S8. IR-PD spectrum of (9,7) (blue) and the calculated IR absorption spectra for the tricapped octahedral and bicapped pentagonal bipyramidal motifs with variation in the adsorbing Ni atoms (black; PBE0/ECP(Ni), cc-pVTZ(N), $2S + 1 = 10$). The calculated spectra are scaled by 0.93 and simulated using the gaussian profile of fwhm = 5 cm^{-1}.

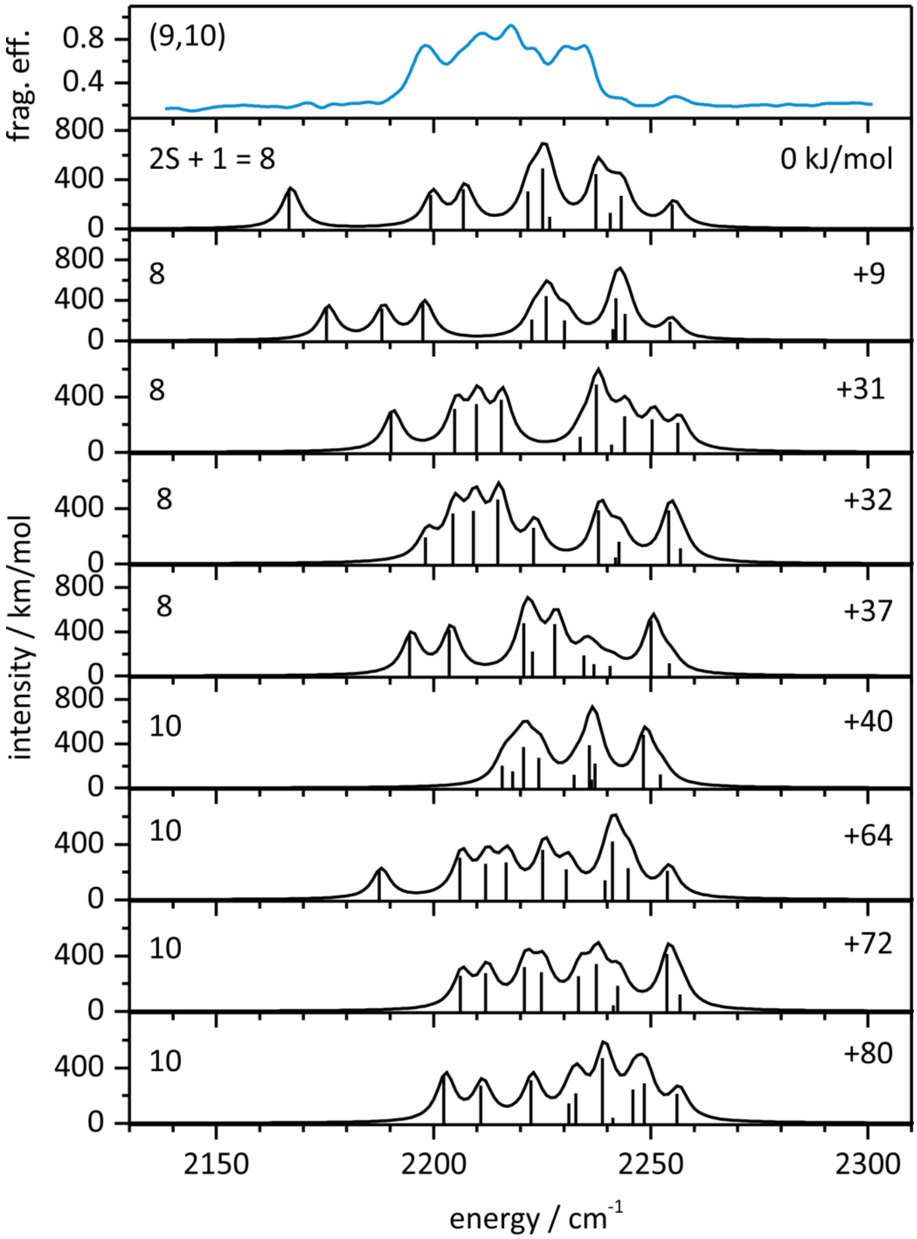

Figure S9. IR-PD spectrum of (9,10) (blue) and the calculated IR absorption spectra for the tricapped octahedral and bicapped pentagonal bipyramidal motifs with variation in the adsorbing Ni atoms and in spin multiplicities (black; PBE0/ECP(Ni), cc-pVTZ(N)). The calculated spectra are scaled by 0.93 and simulated using the gaussian profile of fwhm = 5 cm^{-1}.

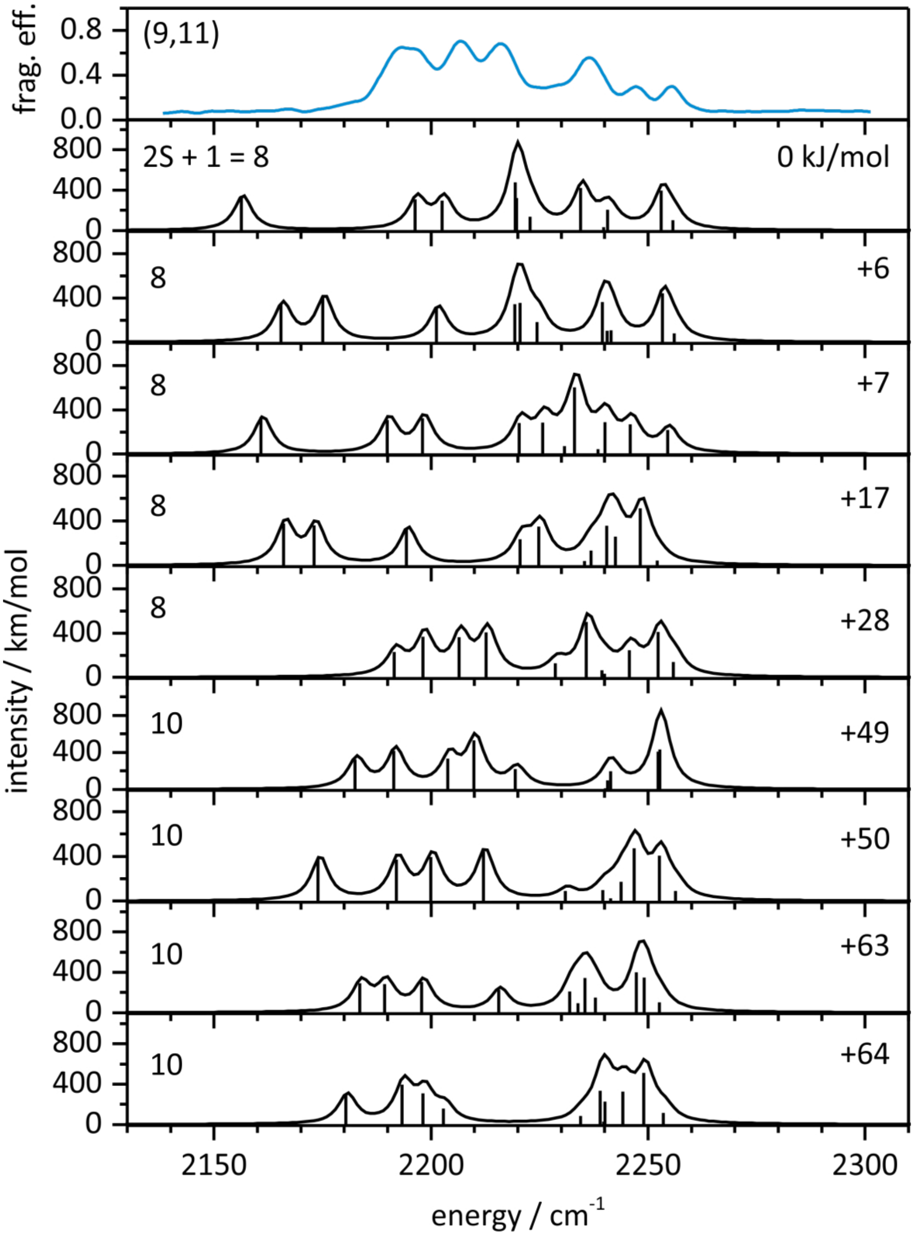

Figure S10. IR-PD spectrum of (9,11) (blue) and the calculated IR absorption spectra for the tricapped octahedral and bicapped pentagonal bipyramidal motifs with variation in the adsorbing Ni atoms and in spin multiplicities (black; PBE0/ECP(Ni), cc-pVTZ(N)). The calculated spectra are scaled by 0.93 and simulated using the gaussian profile of fwhm = 5 cm^{-1}.

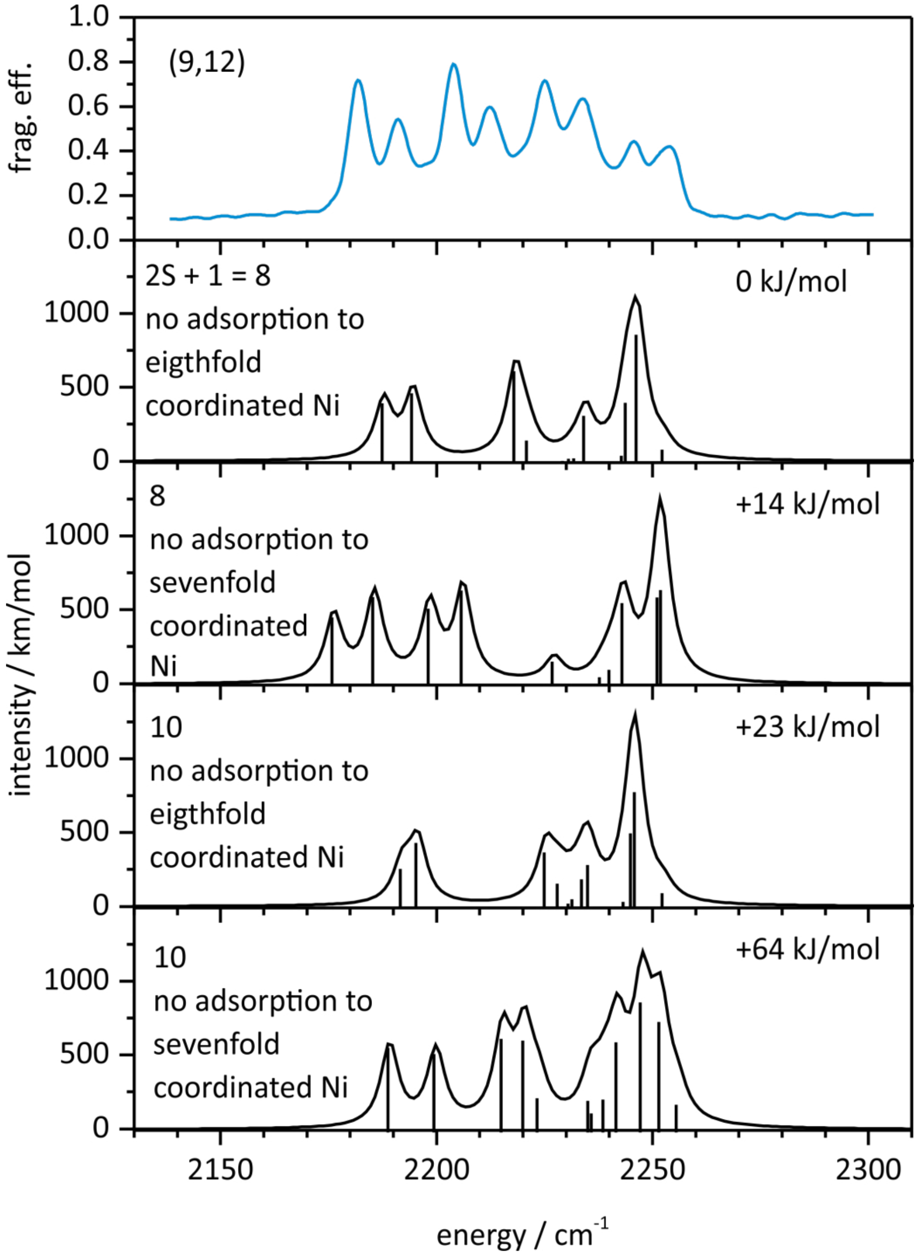

Figure S11. IR-PD spectrum of (9,12) (blue) and the calculated IR absorption spectra for the tricapped octahedral and bicapped pentagonal bipyramidal motifs with variation in the sole vacant Ni atom and in spin multiplicities (black; PBE0/ECP(Ni), cc-pVTZ(N)). The calculated spectra are scaled by 0.93 and simulated using the gaussian profile of fwhm = 5 cm^{-1}.

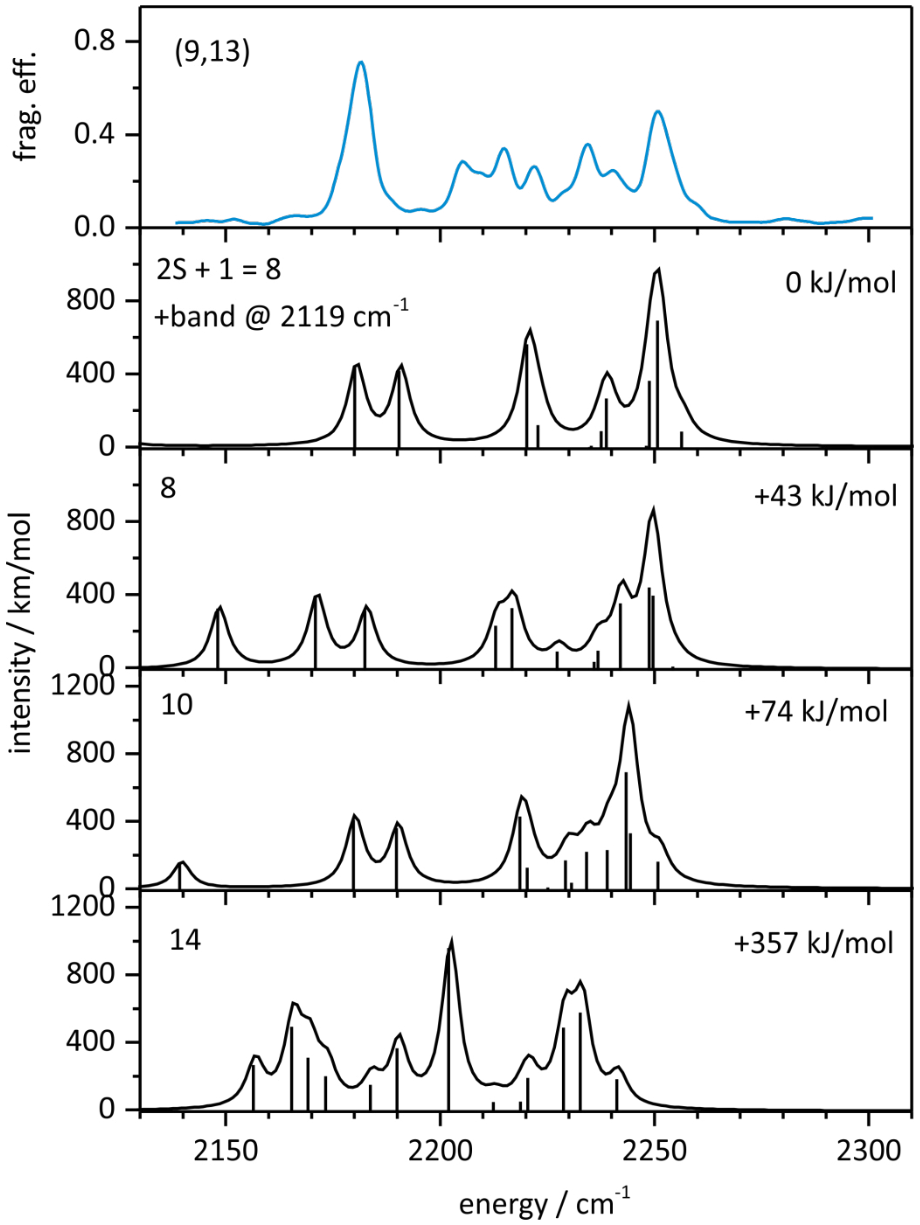

Figure S12. IR-PD spectrum of (9,13) (blue) and the calculated IR absorption spectra for the tricapped octahedral and bicapped pentagonal bipyramidal motifs with maximum N_2 adsorption as shown in Fig. 5 (black; PBE0/ECP(Ni), cc-pVTZ(N)). The calculated spectra are scaled by 0.93 and simulated using the gaussian profile of fwhm = 5 cm^{-1}.

8. Calculated IR absorption spectra including the Grimme correction for dispersion with the original D3 damping function (GD3)

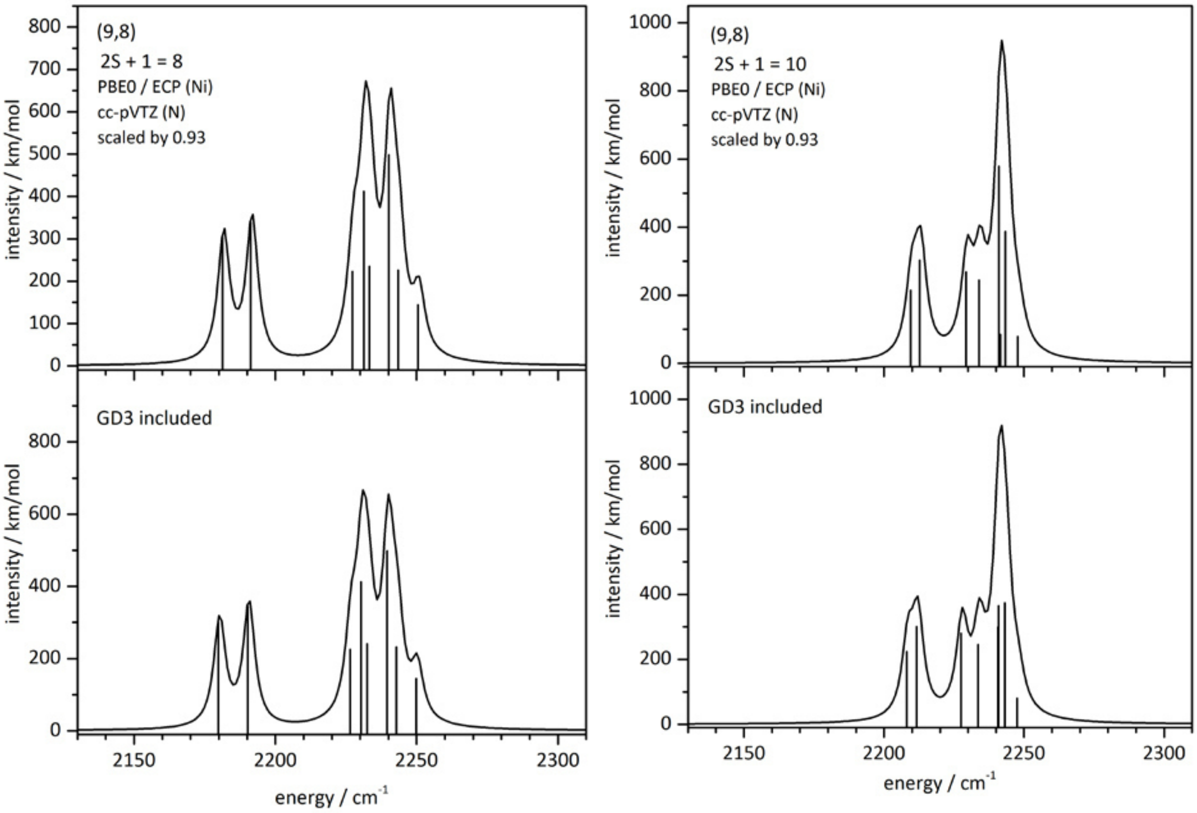

Figure S13. Calculated IR absorption spectra for the tricapped octahedral motif (top lanes) in comparison with calculated IR absorption spectra including the Grimme correction for dispersion with the original D3 damping function (bottom lanes) for (9,8) for the octet spin state (left) and the decet spin state (right). The calculated spectra are scaled by 0.93 and simulated using the gaussian profile of fwhm = 5 cm^{-1}.

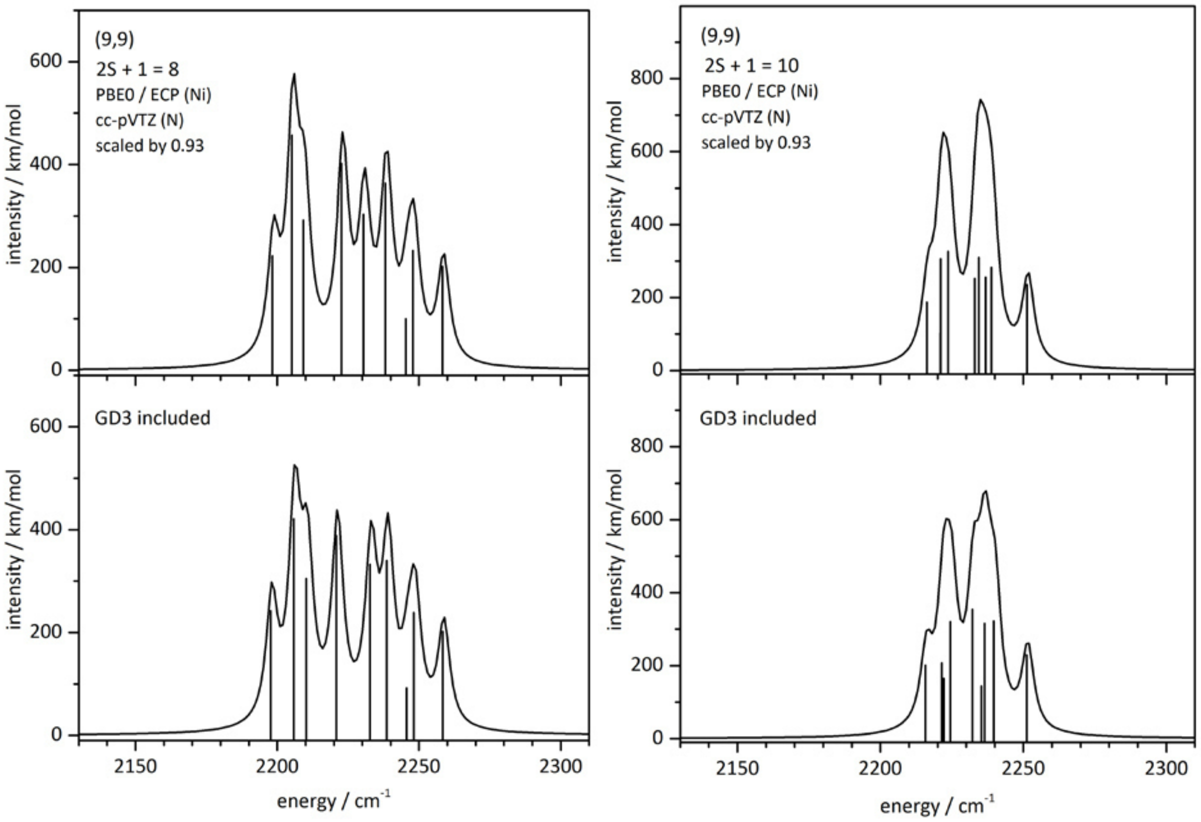

Figure S14. Calculated IR absorption spectra for the tricapped octahedral motif (top lanes) in comparison with calculated IR absorption spectra including the Grimme correction for dispersion with the original D3 damping function (bottom lanes) for (9,9) for the octet spin state (left) and the decet spin state (right). The calculated spectra are scaled by 0.93 and simulated using the gaussian profile of fwhm = 5 cm^{-1}.

4.3 Paper draft: “Isothermal Cryo Kinetics of Cationic Nickel Clusters”

The following paper draft named “Isothermal Cryo Kinetics of Cationic Nickel Clusters” was prepared to be published in a slightly shorter version. The experiments were performed by Sebastian Dillinger and myself. The data evaluation was done by myself. The initial paper draft was put together by myself. G. Niedner-Schatteburg was involved in the revision of the manuscript.

Isothermal Cryo Kinetics of Cationic Nickel Clusters

Jennifer Mohrbach, Sebastian Dillinger, and Gereon Niedner-Schatteburg

Fachbereich Chemie and Forschungszentrum OPTIMAS,
Technische Universität Kaiserslautern,
67663 Kaiserslautern, Germany

4.3.1 Abstract

The stepwise N_2 adsorption on size selected Ni_n^+ (n =5-20) clusters at 26 K is studied in a hybrid tandem ion trap instrument in order to predict geometrical cluster structures. Isothermal adsorption kinetics of these clusters allow for the elucidation of N_2 coverage and cluster size dependent effects, which are related to the respective cluster surface morphologies. Pseudo-first-order kinetic fits confirm consecutive adsorption steps by single exponentially decays exclusively. N_2 desorption, if any, only occurs at high levels of N_2 coverage. In all investigated cases, stepwise N_2 uptake reaches a strict adsorption limit m_{max}, which shows no evidence for further increase and scales with cluster size. The reaction rates for the initial N_2 adsorption increase smoothly with cluster size. There is no significant size-dependent variation in the reaction rates. Recorded Infrared Photon Dissociation (IR-PD) spectra of the $[Ni_n(N_2)_{1,2}]^-$ cluster adsorbate complexes reveal IR active bands in the head-on bound N_2 stretching vibrational region. The observed overall redshift with cluster size is understood in terms of the charge dilution model.

4.3.2 Introduction

The determination of the geometrical structure of transition metal (TM) clusters is of great interest, e.g. for the elucidation of active sites on the respective clusters in catalytic processes. Yet, it remains extremely difficult, both theoretically and experimentally. Reactivity studies of naked metal clusters provide a suitable experimental technique for cluster structure determination. The adsorption of weakly bound molecules to clusters can be used to probe the arrangement of the clusters' surface atoms. From the knowledge of the cluster surface it is often possible to infer the overall cluster structure. In the context of CO adsorption to metal clusters and of related carbonyl complexes it showed that adsorbates may well serve to titrate available surface sites up to saturation for the elucidation of underlying structural motifs.[1-2] Beyond mere adsorption it warrants to study and understand the activation of this and other diatomic molecules such as e.g. NO, N_2, and H_2, driven by perspectives and challenges in heterogeneous catalysis.[3-5]

The N_2 adsorption to Fe surfaces has been elucidated by angle resolved LEED studies in conjunction with potential surface modelling, concluding in α-N_2 and γ-N_2 motifs[6] which resemble η^2 side-on and η^1 end-on coordination of N_2 to multiple and single metal centers, respectively. Early adsorption studies of CO on Ni_n^- (n=3-10) clusters determined saturation limits,[7] and the results on those cluster reactions with N_2, O_2, CO_2 and N_2O were interpreted in terms of cluster structures by empirical many-body potential and by subsequent mol. dynamics (MD) simulations.[8] Collision induced dissoociation (CID) studies of Ni_n^+ (n=2-18) determined bond strengths and cohesion energies.[9] Butadiene dehydrogenation by Ni_n^+ (n≤10) was found to be less efficient than by Pd_n^+ or Pt_n^+.[10] Kinetic studies of nickel cluster reactions with NO_2 revealed complex reaction mechanisms.[11] Hot kinetics of C_{60} adsorption to Ni_n (n=2-72) revealed a size dependence consistent with C_{60} adsorption on essentially spherical Ni_n clusters without any evidence for C_{60} decomposition.[12] Methanol undergoes chemisorption, demethanation, and carbide formation by Ni_n^+ (n=3-11), which was found to change dramatically with cluster size,[13] and the total reactivity to anti-correlate to the HOMO-LUMO gap.[14] Exposure of isolated Ni_n^+ (n=3-11) cluster cations to benzene revealed vivid acetylene formation.[13] Multistep reactions of Ni_n^+ (n=2-29) with O_2 revealed a selective formation of the nickel suboxides $Ni_{13}O_8^+$ and $Ni_{16}O_{10}^+$.[15] Structural, magnetic and adsorption properties of Ni_n (n=2-16, 21, 55) by DFT calculations with the Perdew-Burke-Ernzerhof (PBE) functional elucidated the most stable isomers and their CH_4 adsorption into "on top" sites to be understood in terms of the electronic stability and localization of the frontier MO's.[16] Chemical probe experiments helped to elucidate structural motifs of Ni_n and Co_n clusters (n = 50-200), using ammonia and water as chemical probe molecules.[17-18] The uptake of molecular nitrogen to small Ni_n clusters (n = 3-28, 49-71) helped to propose structures for bare clusters as well as for fully nitrogenated clusters.[19-21]

The dissociation of ions and mass detection of the resulting fragments helps in gathering structural information of molecules. The study of the vibrational modes of adsorbates on TM clusters and in TM coordination complexes as isolated ions by Infrared Multiple Photon Dissociation (IR-MPD) is prevalent.[22-25] The IR-MPD method has been extended by the introduction of tunable free electron lasers (FEL).[26-28] Nowadays, cryo IR-action spectroscopy in combination with the so called tagging or messenger techniques achieves significant advantages. The weakly bound messenger provides for a preferred fragmentation channel, often driven by the adsorption of a single photon.[29-30] The influence of net charge and the oxidation state of TM clusters onto CO adsorption in terms of a charge dilution model.[31-33]

We have performed kinetic studies of hydrocarbon activation on charged TM clusters,[34] and we have introduced X-ray studies by cryo ion trapping for the investigation of spin and orbital contributions to the magnetic moments of TM clusters.[35-36] By utilizing table top IR lasers we have been investigating dark IR-MPD bands in oligonuclear TM complexes,[37] torsional isomerizations,[38] and multistate-mediated rearrangements.[39] Our tandem cryo ion trap instrument[40] enabled us to focus on the vibrational spectroscopy of N_2 adsorbates on size selected TM clusters under isothermal cryo conditions, first results on $[Co_n(N_2)_1]^+$ (n = 8 - 17) clusters, $[Ni_n(N_2)_m]^+$ (n = 9, 13; m = 0 - 13) clusters and on "non classical" Fe dinitrogen complexes being published.[41-43]

This study aims to elucidate N_2 adsorption onto cationic nickel clusters $[Ni_n(N_2)_m]^+$ (n = 5-20) by kinetic investigations, supported by IR-PD . We aim to gain insight into the metal-adsorbate bonding and to unravel structure-reactivity relationships. All of the present findings from our current kinetics and spectroscopic studies shall receive swift comparison to/with appropriate further extended spectroscopic investigations and with large scale DFT modelling – both of which are in the making.

4.3.3 Experimental and computational methods

A customized Fourier Transform-Ion Cyclotron Resonance (FT-ICR) mass spectrometer (Apex Ultra Bruker Daltonics) served to perform the cluster production, isolation, N_2 condensation and mass analysis. A detailed description has been given before.[42] In brief: The nickel clusters were generated using a home-built laser vaporization cluster ion source as described before.[44-45] Nickel atoms are evaporated from a rotating 0.4 mm thick isotopically enriched Ni foil (99,61%, Oak Ridge National Laboratories) by the second harmonic of a pulsed Nd:YAG laser (Innolas *Spitlight 300*, 20 Hz). The hot plasma is captured by a He gas pulse (40 µs, 15 bar) created by a homebuilt piezoelectric valve[46] and expanded into vacuum (10^{-7} mbar). The mass selected clusters injected into a cryogenic hexapole ion trap. The ion trap is cooled to 26 K by a closed cycle He cryostat. Buffer and reaction gas are introduced continuously. Sufficient nitrogen attachment is achieved by increasing the pressure in the ion trap from 1 x 10^{-7} mbar up to 4.5 x 10^{-7} mbar. Additional He is introduced to accomplish an efficient trapping and cooling of the ions (~ 5 x 10^{-6} mbar). After storing the mass-selected ions for a variable time (0-30 s), the manipulated ions of the form $[Ni_n(N_2)_m]^+$ = (n,m) are guided by electrostatic lenses into the FT-ICR cell of the so-called “infinity” type.[47] The ICR cell is held at temperatures below 10 K with a closed cycle He cryostat to prevent heating of the clusters by black body radiation prior to ion detection.

The ICR cell serves for the detection of the formed $[Ni_n(N_2)_m]^+$ = (n,m) cluster adsorbate complexes. The kinetic curves of cationic nickel clusters and their nitrogen adducts originate from reaction delay scans and subsequent evaluation of the recorded mass spectra. Fits to pseudo-first-order-kinetics occur through the “evofit” program.[48] Our thus determined rate constants for the (n,m) species (recorded at various pressures $p(N_2)$ = 1.1 - 3.5 x 10^{-7} mbar) are normalized to the experimental conditions for the (13,m) species (recorded at $p(N_2)$ = 1.3 x 10^{-7} mbar). Fitting the experimental kinetics implies the quantitative determination of relative rate constants for N_2 adsorption $k_{(n,m)}$ for each step m → m+1, and for N_2 desorption $k_{-(n,m+1)}$ for each step m+1 → m alike:

$$[Ni_n(N_2)_m]^+ + N_2 \underset{k_{-(n,m+1)}}{\overset{k_{(n,m)}}{\rightleftarrows}} [Ni_n(N_2)_{m+1}]^+$$

The relative rate constants $k_{(n,m)}$ determine the absolute rate constants $k_{(n,m)}^{abs}$, the absolute collision gas number densities $\rho_{N2}(T)$ serving as the conversion factor:

$$k_{(n,m)}^{abs} = k_{(n,m)}/\rho_{N2}(T)$$

We obtain approximate values for $\rho_{N2}(T)$ indirectly from the pressure in the surrounding chamber $p_c^{(300\,K)}$ and an effective geometry factor c_{app}:

$$\rho_{N2}(26\,K) = \frac{c_{app} p_c^{300\,K}}{k_B T_{300\,K}}$$

The geometry factor c_{app} shows to bear a significant dependence on the temperature of the hexapole ion trap. By numerous kinetic studies of transition metal cluster cations with neutral reactants at cryogenic temperatures we evaluated this factor c_{app} to 1.8 ± 0.4 at 26 K with a net uncertainty of ± 50%.

The classical Langevin collision rate of ions with neutrals[49] is conveniently extended towards polar molecules by the average dipole orientation theory (ADO).[50-51] The ADO theory gives the theoretical limit of the absolute rate constants, the collision rate k^{ADO}, based on a classical trajectory of a linear dipole in the field of a point charge:

$$k^{ADO} = \frac{q}{2\varepsilon_0\sqrt{\mu}}\left(\sqrt{\alpha} + c\mu_D\sqrt{\frac{2}{\pi k_B T}}\right)$$

μ is the reduced mass (of the cluster adsorbate complex), α is the polarizability and μ_D is the dipole moment (in Debye). The parameter c lies between 0 and 1, and can be expressed by the polarizability volume $\alpha'$and μ_D.[52]

This ADO theory is frequently used to calculate the reaction rates of charged clusters with small molecules, knowingly underestimating the reaction rates for charged metal clusters significantly.[53-54] Kummerlöwe and Beyer introduced two models for calculating the collision rates of ionic clusters with neutral molecules, the HSA model (hard sphere average dipole orientation) and the surface charge capture (SCC) model.[55] In both models, the cluster and the neutral reaction partner are treated as hard speres, and the charge is treated as point charge. For the HSA collision rate k^{HSA}, the charge is located in the center of the cluster, while in the SCC model (k^{SCC}), the charge is drawn to the cluster surface by the attractive interaction with the neutral collision partner.

4.3.4 Results and Discussion

We investigated the stored $[Ni_n(N_2)_m]^+$ = (n,m) clusters for their N_2 adsorption in the cryogenic hexapole under isothermal conditions at 26 K. In general, we observe two different adsorption behaviors – reminiscent of the two show cases Ni_9^+ and Ni_{13}^+ that we have discussed before.[43] The mass spectra of all detected Ni_n^+ clusters reveal a successive gain of 28 m/z, which does indicate the stepwise adsorption of molecular nitrogen in consecutive chains of individual adsorption processes (see Fig. S1 within the supplementary information). In all investigated cases (n = 5,..,20) stepwise N_2 uptake reaches a strict adsorption limit m_{max} within $t < 12$ sec, and this does not increase further up to $t < 30$ sec. In some cases we observe the N_2 adsorption limit preceded by one or more additional intermittent adsorption limits, which do not suppress further adsorption but cause some retardation. In the other cases we observe a sole N_2 adsorption limit without any intermittent adsorption limit or retardation. This behavior is representative for rough and smooth cluster surfaces, respectively.

The intermittent adsorption limits (green stars in Fig. 1) and the adsorption limits (filled circles in Fig. 1) serve as guidelines for some elucidation of cluster geometries. It shows, that Ni_n^+ clusters tend to adsorb nitrogen close to an equal atom-N_2-ratio (n = m), which correlates with single N_2 head-on adsorption to each cluster surface atom. Small clusters ($n < 13$) exceed this 1:1 ratio preferably by geminal adsorption to low coordinated surface atoms (1:2 ratio for four or less coordinate Ni atoms). An exception is given by n = 6, which smoothly adsorbs six N_2 molecules. Clusters of the size $13 \leq n \leq 16$ and n = 19 do not form pronounced intermittent adsorption limits either, indicative for smooth cluster surfaces. An intermittent adsorption limit close to the adsorption limit is observed for n = 17, 18 and 20. This is most likely due to one or two exposed surface atoms, e.g. capping atoms, which accept a second N_2 adsorbate, but reluctantly.

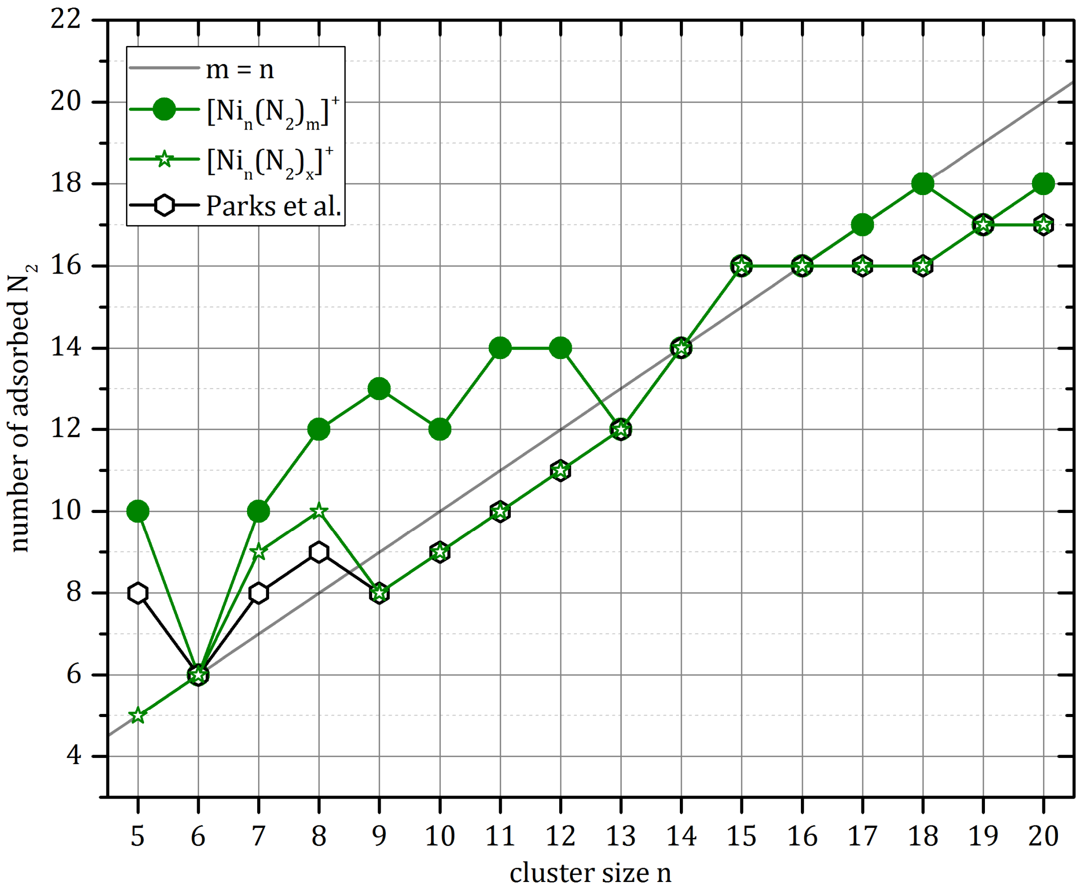

Figure 1. Recorded adsorption limits m_{max} (filled circles) and most intense intermittent adsorption limits (stars) of N_2 adsorption to cationic nickel clusters Ni_n^+, n = 5–20 in comparison to N_2 uptake "plateaus" of neutral nickel clusters[19-20] (black hexagons). Each mass-selected Ni_n^+ cluster was stored for up to 30 s – typically reaching equilibrium within less than half of that time.

We further investigated in more detail the stepwise N_2 adsorption on Ni_n^+ clusters by recording their reaction kinetics in more detail, and we performed pseudo-first-order kinetic fits by our genetic algorithm routine. The obtained fits confirm consecutive adsorption steps (Fig.s 2-5). All Ni_n^+ clusters decay mono exponentially without any indication of a second component. This, and the overall superior quality of all fits, entitles us to fit each consecutive step by a single rate constant throughout. Some fits require significant backward reaction in cases of high N_2 coverages, which indicates swift N_2 desorption (see the supplementary information for details on the corresponding rate constants $k_{(n,m)}$ for all cluster kinetics).

Ni_5^+ – Ni_{12}^+:

Small nickel clusters Ni_n^+ in the range of n = 5–12 exhibit a large deviation in the observed adsorption limits and the intermittent adsorption limits. This finding is characteristic for rough cluster morphologies. Such clusters provide a variety of unique surface atoms, likely by low Ni-Ni coordination. There is no significant backward reaction for the adsorption steps of n = 5-8. All clusters reveal a strict adsorption limit at n ≥ m (*cf.* Fig. 2).

In the case of (5,m) we observe an intermittent adsorption limit at (5,5) and the adsorption limit at (5,10). A structure with only fourfold or less coordinated Ni atoms would explain the intermittent adsorption limit by single N_2 adsorption on each Ni atom as well as the adsorption limit (of m = 2n) by the adsorption of a second N_2 molecule, respectively. The trigonal bipyramid – only having three- and fourfold coordinated Ni atoms – would represent the most likely structure for Ni_5^+.

The (6,m) case represents an exception. The smooth N_2 adsorption on (6,m) clusters is indicative for a highly symmetrical structure of six equally coordinated surface atoms. The Ni_6^+ cluster has most likely an octahedral structure. By merely adsorbing a single N_2 molecule on each Ni atom, the cluster adsorbate complex would retain its symmetry. This finding is also corroborated by our spectroscopic studies, to discuss later.

In the case of (7,m) we observe two intermittent adsorption limits at (7,1) and (7,7), and the adsorption limit at (7,10). A structure with a single unique atom of low coordination could cause an intermittent limit at (7,1). Single binding to all Ni atoms and the adsorption of a second N_2 molecule by three Ni atoms would result in dominat (7,7) and (7,10) species. The capped octahedron would be the most likely structure for Ni_7^+, having a single threefold coordinated Ni capping atom. We cannot exclude, however, a structural change of the cluster geometry upon N_2 adsorption.

In the case of (8,m) we observe several intermittent adsorption limits at (8,4), (8,7) and (8,10), and the adsorption limit at (8,12). A structure with four atoms of low coordination could cause a first intermittent limit at (8,4).In addition this cluster is the first to show an intermittent limit at m = n-1. This indicates the presence of highly coordinated Ni atom which adsorbs N_2 less swiftly than a low coordinated Ni site accepting ist second N_2 adsorbate. Single binding to all Ni atoms but the highest coordinated Ni atom and the adsorption of a second N_2 molecule by four Ni atoms would result in dominat (8,7) and (8,12) species. The capped pentagonal bipyramid would be the most likely structure for Ni_8^+, having one threefold, three fourfold, two fivefold, one sixfold and one sevenfold coordinated Ni atom.

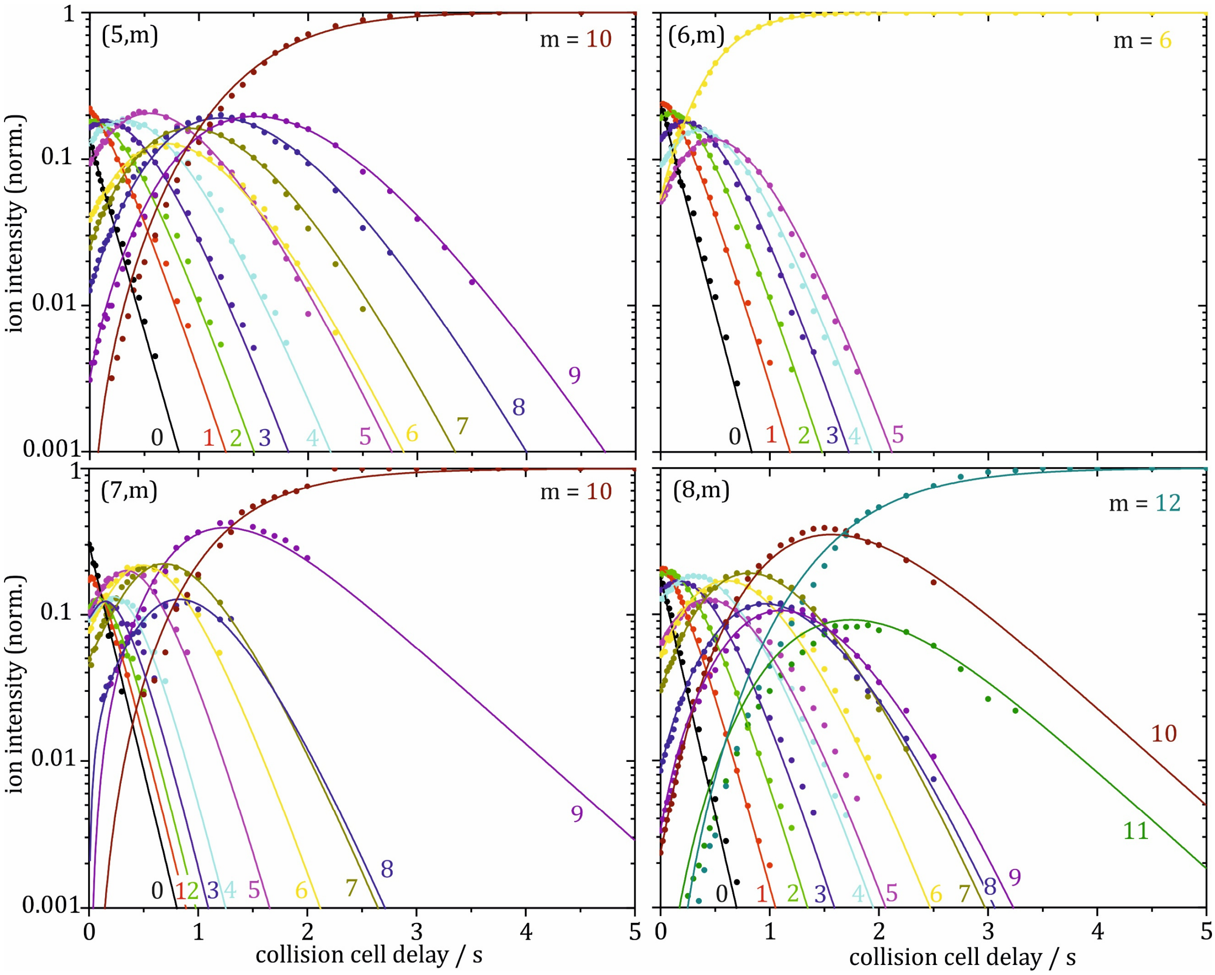

Figure 2. Isothermal kinetics of the stepwise N_2 adsorption by isolated Ni_n^+ clusters (n = 5–8) within 26 Kelvin He buffer gas and 3.0×10^{-7} mbar of N_2. The fits (shown as lines) assume pseudo-first-order kinetics in a reaction chain of up to 12 consecutive steps.

Clusters with more than eight Ni atoms (n = 9–12) reveal significant backward reactions for the last adsorption steps, suggesting one or more weakly bound N_2 molecules when reaching cluster saturation (*cf.* Fig. 3).

The cases of (9,m) and (13,m) have been discussed *in extenso* earlier.[42] We observe an intermittent adsorption limit at (9,8) and the adsorption limit at (9,13). In conjunction with our spectroscopic investigation and DFT computations, we have concluded a possible isomerization with low N_2 coverage, most likely from a tricapped octahedron to a bicapped pentagonal bipyramid, and geminal binding of N_2 setting in at m = 9. In the case of Ni_{13}^+ we assume an icosahedral structure which coincides with all experimental findings and theory.

In the cases of (10,m), (11,m) and (12,m) we observe dominant intermittent adsorption limits at m = n-1. This might indicate structures based on successive packing of surface atoms to the pentagonal bipyramid leading to the icosahedral Ni_{13}^{+} cluster. However, the observed adsorption limits at (10,12), (11,14) and (12,14) are not in line with this suggestion. There might be some cluster distortion upon increasing N_2 coverage.

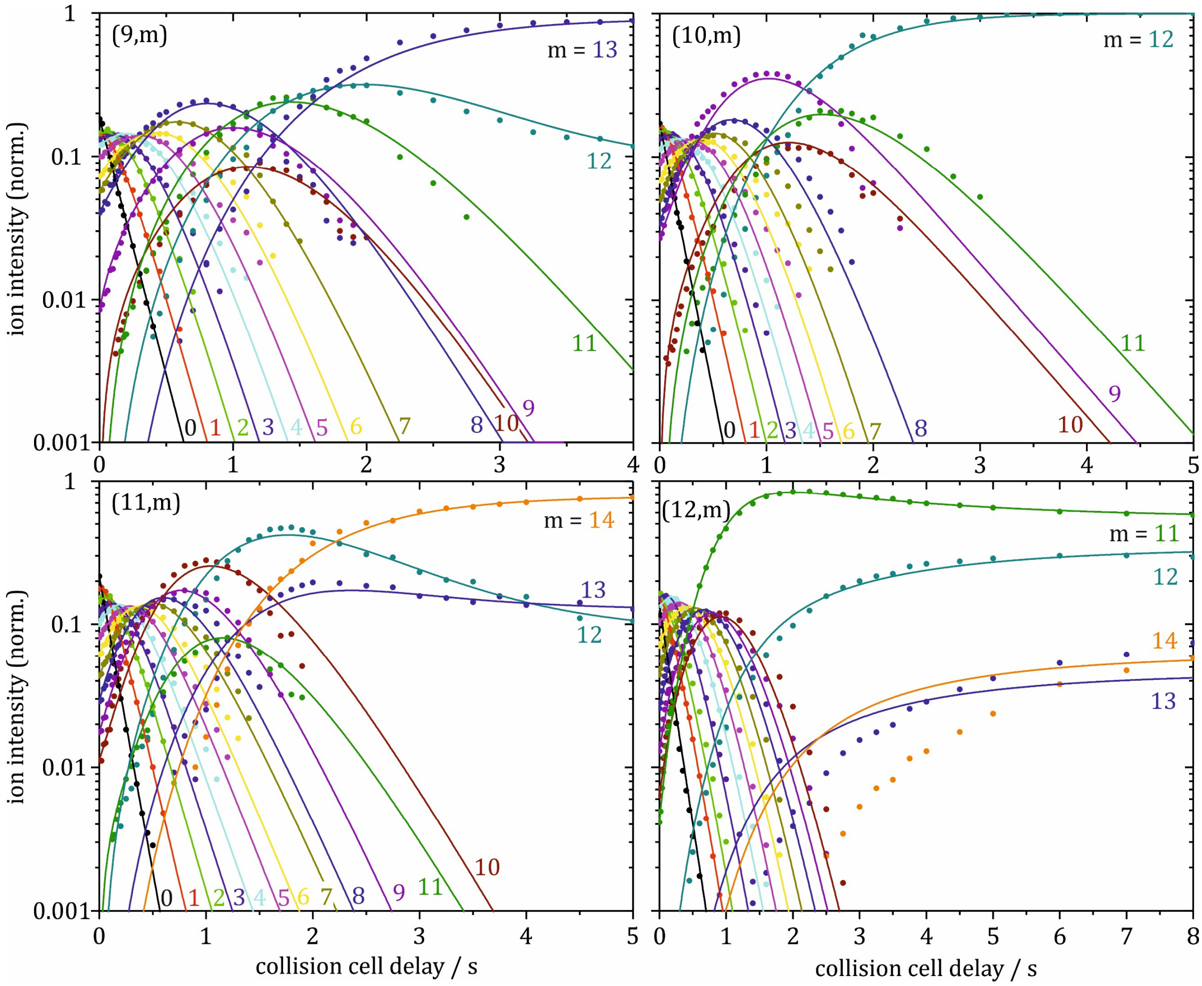

Figure 3. Isothermal kinetics of the stepwise N_2 adsorption by isolated Ni_n^{+} clusters (n = 9–12) within 26 Kelvin He buffer gas and 3.0 x 10^{-7} mbar of N_2 (n = 12: $p(N_2) = 3.2 \times 10^{-7}$ mbar). The fits (shown as lines) assume pseudo-first-order kinetics in a reaction chain of up to 14 consecutive steps.

Ni_{13}^+ – Ni_{16}^+:

Clusters of the size $13 \leq n \leq 16$ do not form pronounced intermittent adsorption limits. However, we observe little retardation in the adsorption steps (15,13) → (15,14) and (16,14) → (16,15) (*cf*. Fig. 4). A perfect icosahedron of Ni_{13}^+ provides for a single bulk atom and for 12 surface atoms of equal coordination to six nearest neighbors. It shows a smooth surface, coinciding with the found constant reaction rates up to the adsorption limit at (13,12).

In the case of (14,m) we observe the adsorption limit at (14,14). This could be easily explained by a capped icosahedron, where the capping atom binds two N_2 molecules. However, one would expect the second N_2 molecule to bind significantly weaker and thus to form an intermittent adsorption limit at (14,13) – other than observed.

In the case of (15,m) we observe the adsorption limit at (15,16) preceded by a weak intermittent adsorption limit at (15,13). This finding is not in line with the expected bicapped icosahedron, which would form an intermittent adsorption limit at (15,12) due to its two eightfold coordinated Ni surface atoms. The observed intermittent adsorption limit at (15,13) – admittedly weak – rather indicates a truncated octahedron with two fourfold, four fivefold and eight sixfold coordinated Ni atoms.

In the case of (16,m) we also observe a weak intermittent adsorption limit at (16,14) and the adsorption limit at (16,16). Again a structure with two unique atoms of low coordination would explain the intermittent limit. It is most likey, to describe the Ni_{16}^+ cluster as a tricapped icosahedral structure, providing for two fourfold coordinated atoms and a ninefold coordinated atom. The later one unlikely binds any N_2. One might label this Ni^{9coord} site as “semi internal”, marking the very onset of bulk formation.

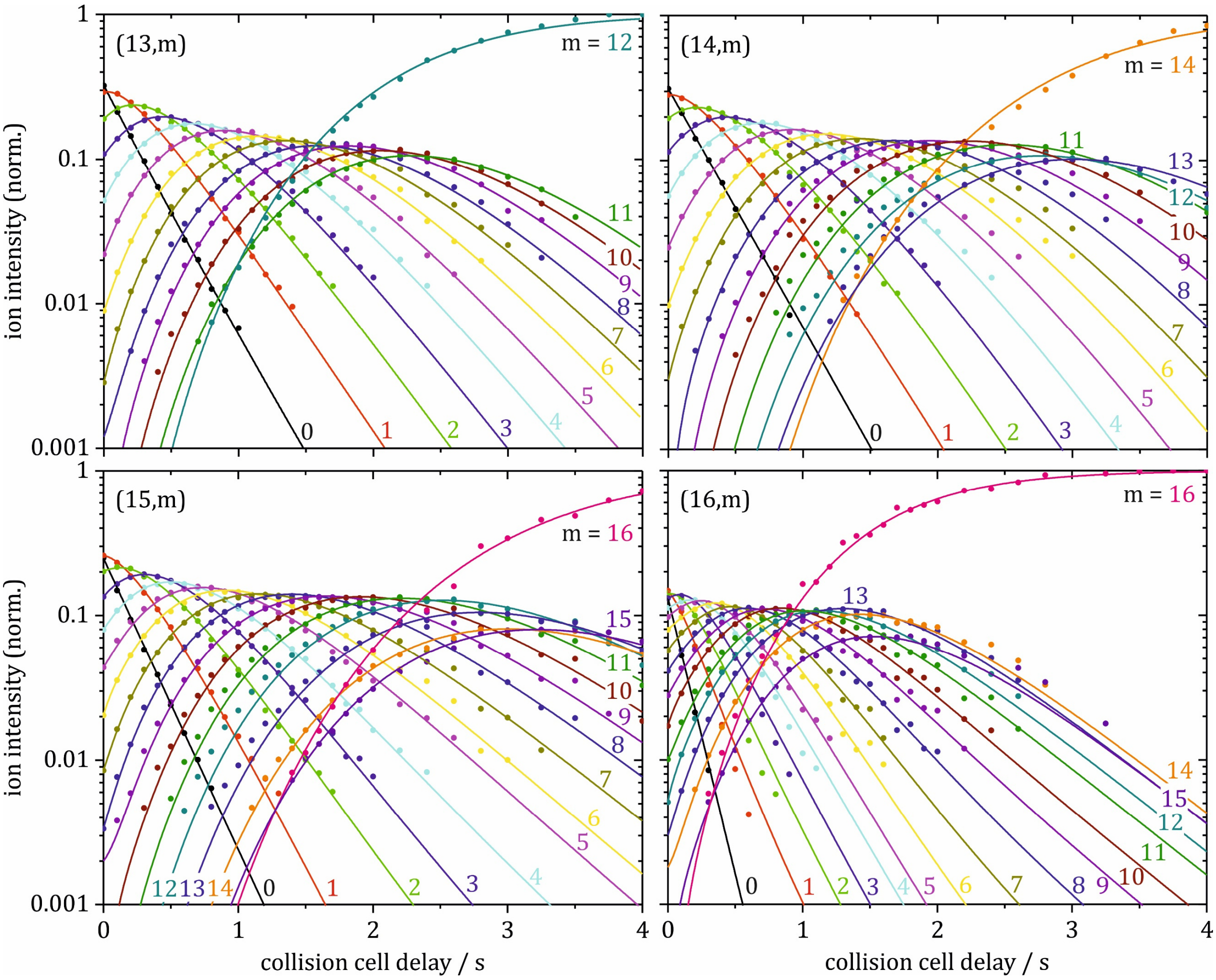

Figure 4. Isothermal kinetics of the stepwise N_2 adsorption by isolated Ni_n^+ clusters ($n = 13–16$) within 26 Kelvin He buffer gas and 1.3×10^{-7} mbar of N_2. The fits (shown as lines) assume pseudo-first-order kinetics in a smooth reaction chain of up to 16 consecutive steps.

Ni_{17}^+ – Ni_{20}^+:

Clusters of the size $17 \leq n \leq 20$ form intermittent adsorption limits close to their adsorption limits. Their overall adsorption behavior is very similar, which indicates uniform cluster structures.

In the case of (17,m) we observe an intermittent adsorption limit at (17,16) and the adsorption limit at (17,17). Adding another Ni atom to the icosahedral Ni_{16}^+ cluster would form an intermittent adsorption limit at (17,15) and an adsorption limit at (17,17).

In the case of (19,m) we observe the adsorption limit at (19,17) which is in line with a double icosahedral structure. This structure provides for twelve sixfold coordinated atoms, five eightfold coordinated atoms and for two internal atoms.

In the case of (18,m) we observe an intermittent adsorption limit at (18,16) and the adsorption limit at m = 18 (*cf.* Fig.s S1 and S2 of the SI). Adding another Ni atom to the icosahedral structure would result in a double icosahedral structure minus one sixfold coordinated atom. An adsorption limit at (18,16) would form when removing one of the atoms located at either end of the double icosahdron. The observed additional adsorption of two N_2 molecules might indicate a slightly different arrangement of the clusters' surface atoms.

In the case of (20,m) we observe a strong intermittent adsorption limit at (20,17) and further adsorption to (20,18). This could be explained by an additional atom added to the double icosahedral Ni_{19}^+, most likely around its waist.

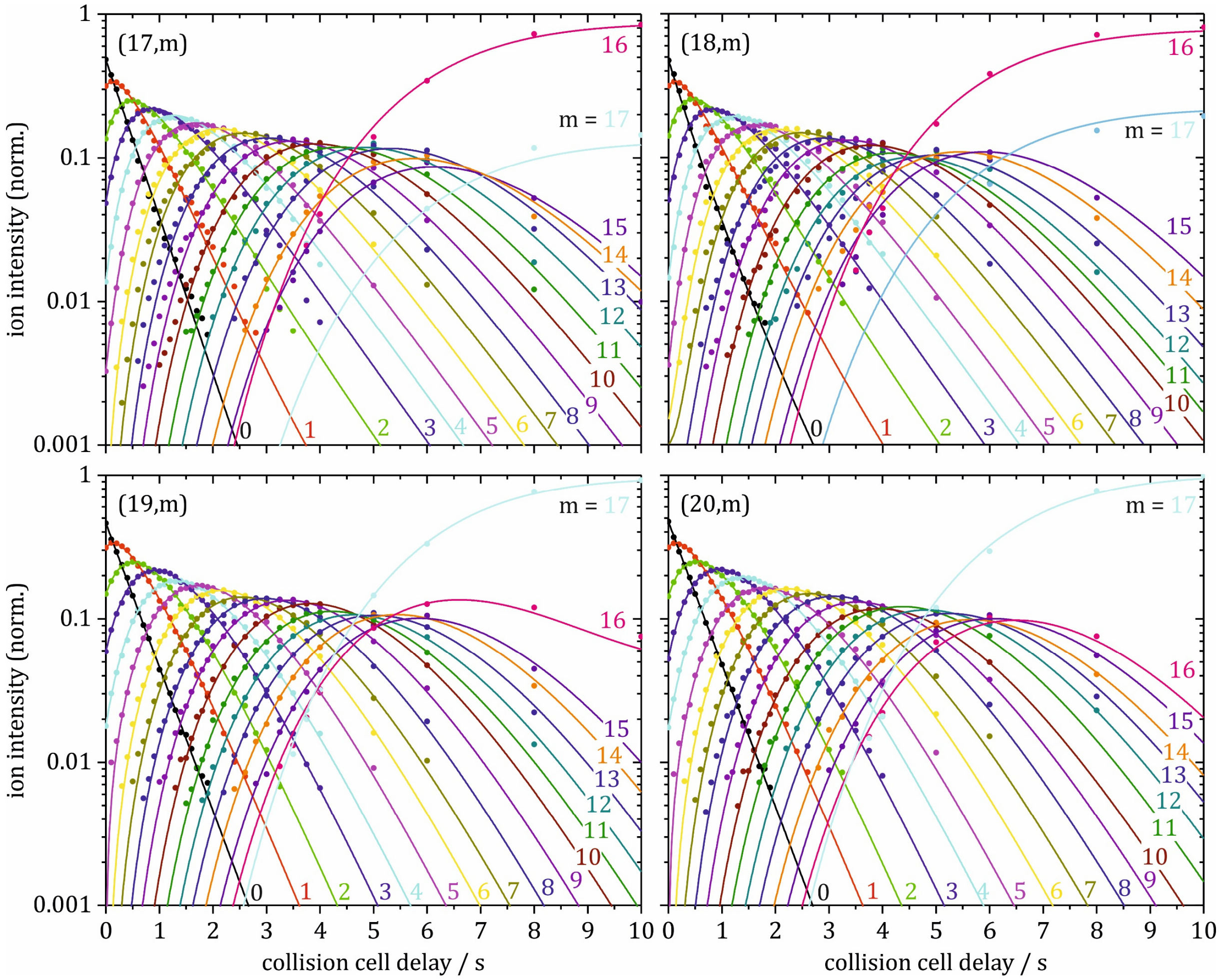

Figure 5. Isothermal kinetics of the stepwise N_2 adsorption by isolated Ni_n^+ clusters (n = 17–20) within 26 Kelvin He buffer gas and 1.1 x 10^{-7} mbar of N_2. The fits (shown as lines) assume pseudo-first-order kinetics in a reaction chain of up to 17 consecutive steps. Note, that Ni_{18}^+ and Ni_{20}^+ reach their adsorption limit with m = 18, which did not form with sufficient intensity. Please see the supplementary information for the fit of $[Ni_{18}(N_2)_m]^+$ species when recorded at $p(N_2)$ = 3.2 x 10^{-7} mbar.

Absolute rate constants of the initial N_2 adsorption

The absolute rate constants $k_{(n,m)}^{abs}$ are obtained from the pseudo-first-order rate constants. These are shown for the initial N_2 adsorption $k_{(n,0)}^{abs}$ as a function of cluster size in Figur 6 (green circles). Also shown are the collision rate constants calculated on the basis of classical ADO theory, as well as on the HSA and SCC models.

We observe an overall increase in the absolute rate constants with cluster size (~ 120 % increase from n = 5 to n = 20). There is no evidence for tremendous size-dependent effect. Clusters in the range from n = 12 to 15 show a slight decrease in reactivity towards N_2 adsorption as compared to the observed increase with cluster size. The absolute rate constants for clusters with n > 8 exceed those calculated by classical ADO theory. They are predicted more reliably by the hard sphere average dipole orientation model where the charge is located in the center of the cluster.

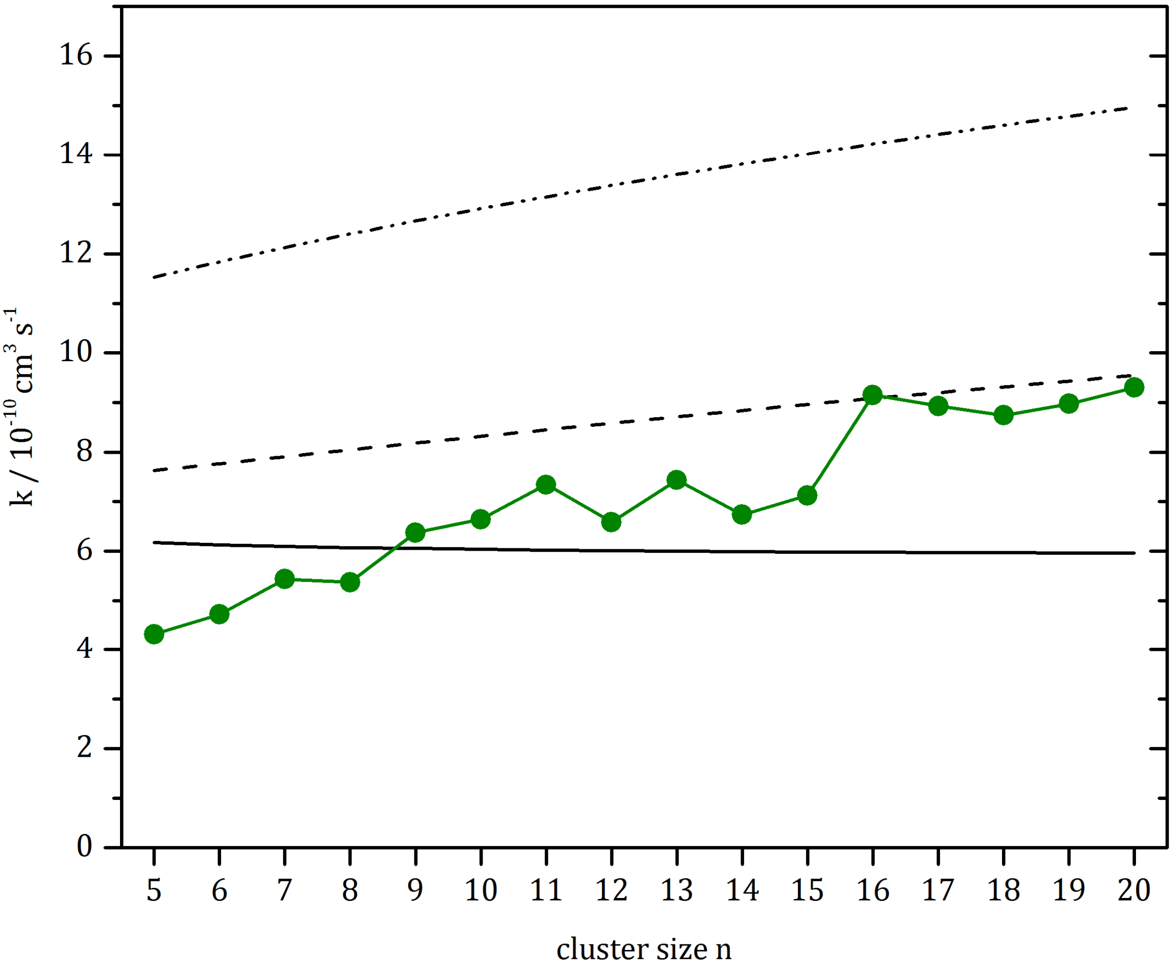

Figure 6. Rate constants $k_{(n,0)}^{abs}$ of the initial N_2 adsorption to Ni_n^+ clusters by experiment (green), according to the ADO theory (black line), to the HSA model (dashed line), and to the SCC model (dot-dashed line).

Table 1. Pseudo-first-order rate constants $k_{(n,0)}$ and absolute rate constants $k_{(n,0)}^{abs}$ for the initial N_2 adsorption on Ni_n^+ (n = 5–20) clusters in comparison to collision rates determined by ADO theory, by the HSA model and by the SCC model.

n	$k_{(n,0)}$ s^{-1}	$k_{(n,0)}^{abs}$ 10^{-10} cm^3 s^{-1}	$k_{(n,0)}^{ADO}$ 10^{-10} cm^3 s^{-1}	$k_{(n,0)}^{HSA}$ 10^{-10} cm^3 s^{-1}	$k_{(n,0)}^{SCC}$ 10^{-10} cm^3 s^{-1}
5	2.4	4.32	6.17	7.63	11.53
6	2.7	4.72	6.12	7.77	11.84
7	3.1	5.43	6.09	7.91	12.13
8	3.0	5.37	6.06	8.05	12.40
9	3.6	6.37	6.05	8.18	12.66
10	3.8	6.64	6.03	8.32	12.91
11	4.2	7.34	6.02	8.45	13.15
12	3.7	6.58	6.01	8.58	13.38
13	4.2	7.43	6.00	8.71	13.60
14	3.8	6.73	5.99	8.84	13.82
15	4.0	7.12	5.98	8.96	14.02
16	5.2	9.15	5.98	9.08	14.22
17	5.1	8.93	5.97	9.20	14.42
18	4.9	8.74	5.97	9.32	14.60
19	5.1	8.97	5.96	9.43	14.79
20	5.3	9.30	5.96	9.54	14.97

IR spectroscopic characterization of the initial N_2 adsorption steps

The IR(M)PD spectra of the (n,1) and (n,2) species show IR active bands in the region from 2210 cm^{-1} to 2280 cm^{-1} (*cf.* Fig. 7). There is an overall redshift with cluster size of ~ 50 cm^{-1} within the range of n = 5–20 (*cf.* Fig. 8).

Most (n,1) species reveal a single band in the N-N stretching region of head-on bound N_2. There are two exceptions: The n = 10 and n = 18 species. Both cluster adsorbate complexes show one additional weaker band in the respective IR(M)PD spectrum. In the case of (10,1) we observe this additional band, blueshifted by about 10 cm^{-1}. For (18,1) the second band appears to be redshifted by about 10 cm^{-1}. In the cases of (5,1) and (7,1), we observe the N_2 stretching vibrational band less redshifted (~ 10 cm^{-1}) than expected from the overall redshift with cluster size. The adsorption of a second N_2 molecule in these two cases, causes the surmised redshift, respectively.

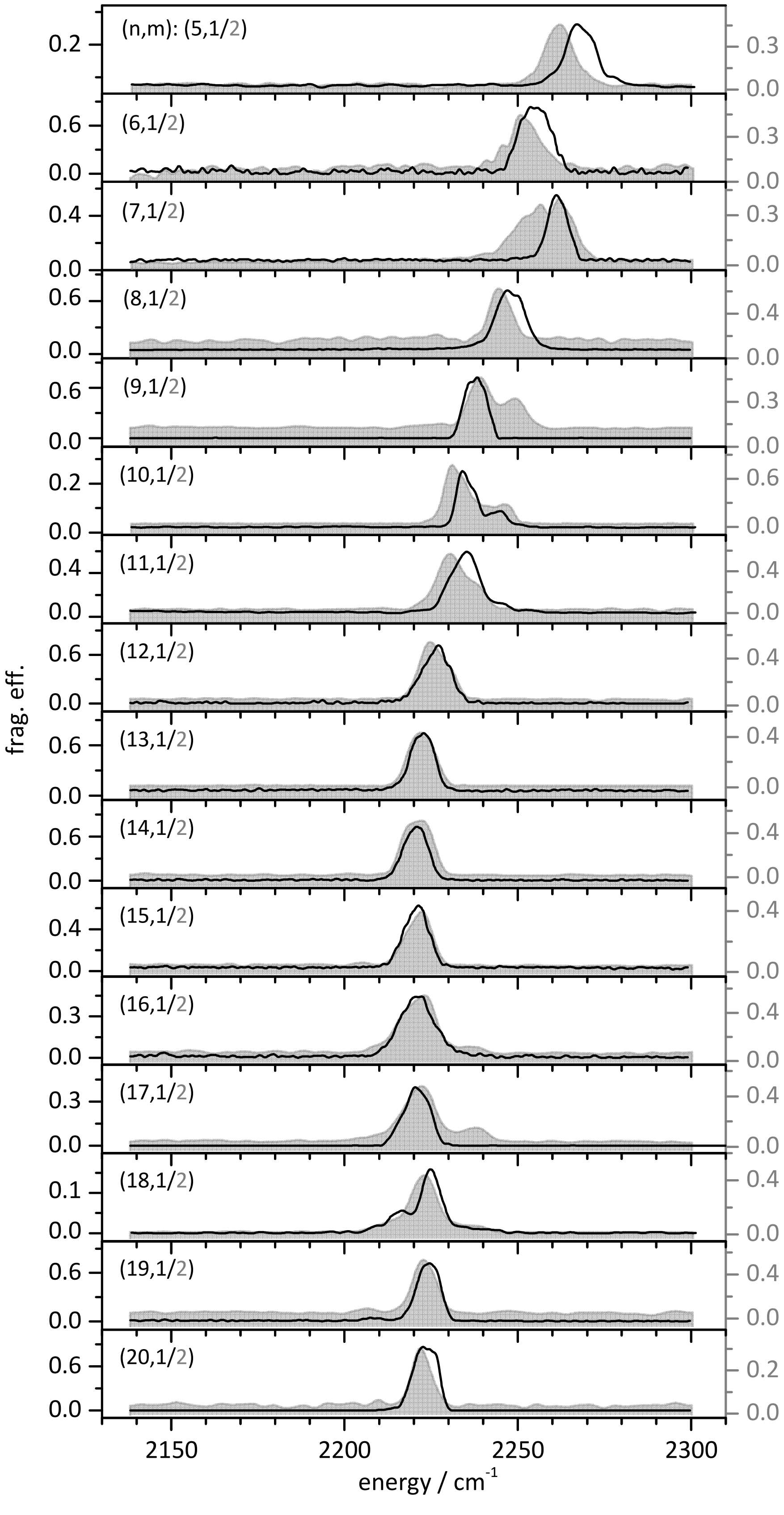

Figure 7. IR(M)PD spectra of $[Ni_n(N_2)_1]^+ = (n,1)$ (solid lines) and $[Ni_n(N_2)_2]^+ = (n,2)$ (gray shaded areas) for n = 5–20. There are subtle differences in the IR(M)PD spectra induced by the adsorption of a second N_2 molecule. See text for details.

The direct comparison of all (n,1) and (n,2) species provides for subtle differences in the recorded spectra. We observe distinct shifts in the N_2 stretching frequency for $n < 12$ cluster adsorbate complexes and an additional second band for n = 7, 9, 11, and 17 with the adsorption of a second N_2 molecule. In the case of (9,m) cluster adsorbate complexes, it has been shown that the head-on N_2 adsorption to individual sites on the cluster surface strongly influences the stretching frequency of the adsorbed N_2.[42] The presence of additional bands at low N_2 coverages strenghthens the assumption of unique, preferrably low coordinated Ni sites on the respective clusters, e.g. capping atoms.

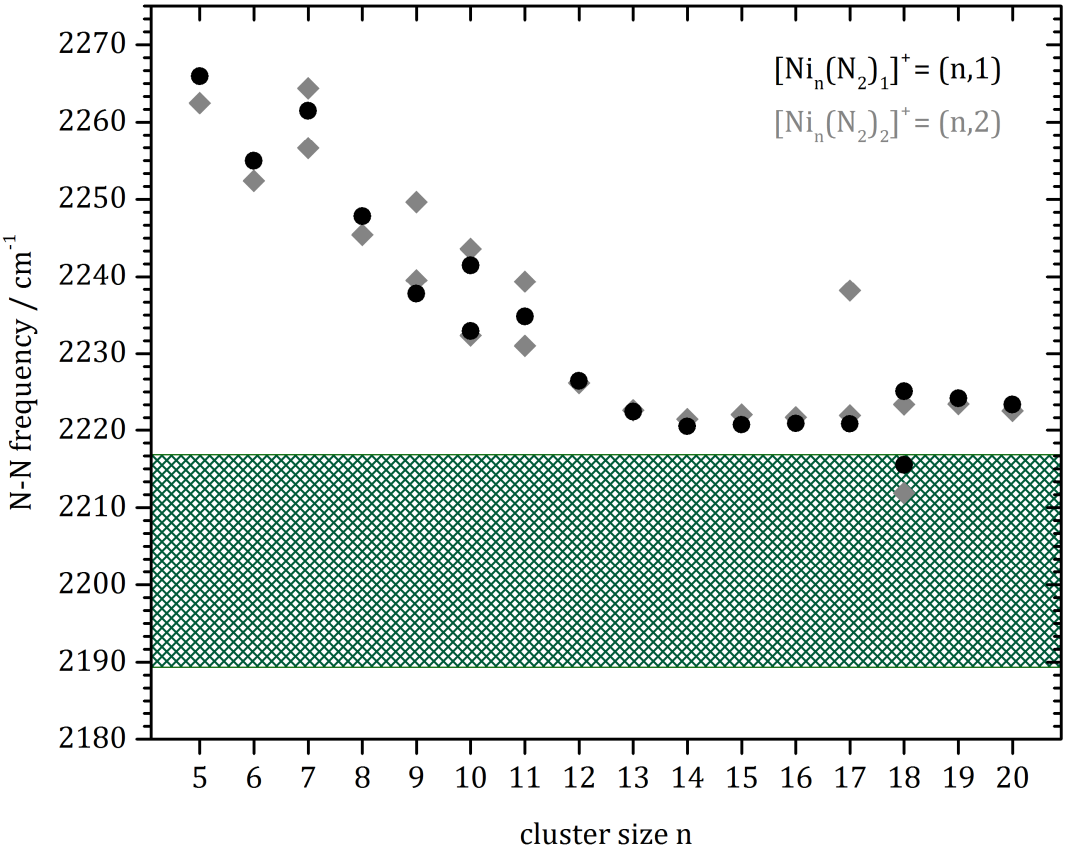

Figure 8. Frequency of the vibration of head-on bound N_2 in cationic $[Ni_nN_2]^+$ = (n,1) and $[Ni_n(N_2)_2]^+$ = (n,2) cluster adsorbate complexes (black dots and grey diamonds) as a function of cluster size. The shaded area indicates the range of the N-N stretching frequencies on various Ni surfaces.[56-57] Note the slight increase of the N_2 stretching frequency with clusters sizes of $n > 15$.

The pronounced overall redshift within the range of n = 5–20 reflects the observed cluster size dependent redshifts of the CO stretching frequency when adsorbed on cationic Ni clusters.[32] IR photodepletion spectra of cationic Ni_nCO^+ (n = 4–23) complexes revealed a singl band attributed to head-on bound CO which shifts to the red with cluster size. The magnitude of the observed red shifts is identical in both case – CO and N_2.

4.3.5 Conclusions

We have investigated the stepwise N_2 adsorption on size selected Ni_n^+ (n = 5–20) clusters by recording their reaction kinetics at 26 K in a hexapole ion trap. We performed pseudo-first-order kinetic fits, which confirm consecutive adsorption steps by single exponentially decays exclusively. N_2 desorption, if any, only occurs at high levels of N_2 coverage. In all investigated cases stepwise N_2 uptake reaches a strict adsorption limit m_{max}, which showe no evidence for further increase and scale with cluster size. In some cases we observe the N_2 adsorption limit preceded by one or more additional intermittent adsorption limits, which do not suppress further adsorption but cause some retardation. In the other cases we observe a sole N_2 adsorption limit without any intermittent adsorption limit or retardation. This behavior is representative for rough and smooth cluster surfaces, respectively. Observed stoichiometries are understood in terms of initial single adsorbate occupation of available binding sites, followed by further adsorption through solvent shell re-organization towards double (geminal) occupation of low coordinated Ni surface sites, as proposed by Parks and Riley for neutral Ni clusters.

Small nickel Ni_n^+ clusters (n < 13) exhibit a large deviation in the observed adsorption limits and the intermittent adsorption limits. This finding is characteristic for rough cluster morphologies by a variety of unique surface atoms. All clusters reveal a strict adsorption limit at $n \geq m$. Clusters with more than eight Ni atoms (n = 9–12) reveal significant backward reactions for the last adsorption steps, suggesting one or more weakly bound N_2 molecules when reaching cluster saturation. The most likely preferred structures for small nickel clusters are based on bipyramidal (trigonal and pentagonal) and octahedral motifs. Clusters of the size $13 \leq n \leq 16$ neither form pronounced intermittent adsorption limits nor reveal N_2 desorption. Their respective cluster structures presumably form by adding capping atoms to the smooth icosahedral Ni_{13}^+ cluster. Larger clusters with $17 \leq n \leq 20$ disclose backward reactions at highest N_2 coverages. Their overall adsorption behavior is very similar and stepwise N_2 adsorption takes place at equal rates and close to collision rate, characteristic for smooth cluster morphologies.

We observe an overall increase in the absolute rate constants with cluster size without huge size-dependent effect. Clusters in the range from n = 12 to 15 show a slight decrease in reactivity towards N_2 adsorption as compared to the observed increase with cluster size. The absolute rate constants of the initial N_2 adsorption are predicted quite reliably by the hard sphere average dipole orientation model.

The recorded IR(M)PD spectra of all $[Ni_n(N_2)_{1,2}]^-$ cluster adsorbate complexes show IR active bands in the N_2 stretching vibrational region from head-on bound N_2 (~ 2250 cm^{-1}). We observe an overall redshift (~ 50 cm^{-1}) with cluster size, which confirms the charge dilution model by Fielicke et al.

4.3.6 Acknowledgements

The ^{58}Ni isotopic sample used in this research was supplied by the United States Department of Energy Office of Science by the Isotope Program in the Office of Nuclear Physics. This work was supported by the German research foundation DFG within the transregional collaborative research center SFB/TRR 88 “Cooperative effects in homo and heterometallic complexes” (3MET.de) and by the state research center OPTIMAS.

4.3.7 References

1. Ervin, K. M., Metal-Ligand Interactions: Gas-Phase Transition Metal Cluster Carbonyls. *Int. Rev. Phys. Chem.* **2001**, *20*, 127-164.
2. Ganteför, G.; Icking-Konert, G. S.; Handschuh, H.; Eberhardt, W., Co Chemisorption on Ni N, Pd N and Pt N Clusters. *Int. J. Mass Spectrom. Ion Processes* **1996**, *159*, 81-109.
3. Zambelli, T.; Wintterlin, J.; Trost, J.; Ertl, G., Identification of the" Active Sites" of a Surface-Catalyzed Reaction. *Science* **1996**, *273*, 1688.
4. Nørskov, J. K.; Bligaard, T.; Logadottir, A.; Bahn, S.; Hansen, L. B.; Bollinger, M.; Bengaard, H.; Hammer, B.; Sljivancanin, Z.; Mavrikakis, M., Universality in Heterogeneous Catalysis. *J. Catal.* **2002**, *209*, 275-278.
5. Honkala, K.; Hellman, A.; Remediakis, I.; Logadottir, A.; Carlsson, A.; Dahl, S.; Christensen, C. H.; Nørskov, J. K., Ammonia Synthesis from First-Principles Calculations. *Science* **2005**, *307*, 555-558.
6. Freund, H. J.; Bartos, B.; Messmer, R. P.; Grunze, M.; Kuhlenbeck, H.; Neumann, M., The Adsorption of N2 on Fe(111) - Angle Resolved Photoemission and Theoretical-Model Studies. *Surf. Sci.* **1987**, *185*, 187-202.
7. Hintz, P. A.; Ervin, K. M., Chemisorption and Oxidation Reactions of Nickel Group Cluster Anions with N2, O2, Co2, and N2o. *J. Chem. Phys.* **1995**, *103*, 7897-906.
8. Nayak, S. K.; Khanna, S. N.; Rao, B. K.; Jena, P., Physics of Nickel Clusters: Energetics and Equilibrium Geometries. *J. Phys. Chem. A* **1997**, *101*, 1072-1080.
9. Lian, L.; Su, C. X.; Armentrout, P. B., Collision-Induced Dissociation of Nickel(Ni_n^+) (n = 2=18) with Xenon: Bond Energies, Geometrical Structures, and Dissociation Pathways. *J. Chem. Phys.* **1992**, *96*, 7542-54.

10. Magnera, T. F.; David, D. E.; Michl, J., Dehydrogenation and Cracking of N-Butane with Gas-Phase Nickel (Nin+), Palladium (Pdn+), and Platinum (Ptn+), Cluster Ions. *J. Am. Chem. Soc.* **1987**, *109*, 936-8.
11. Vann, W. D.; Bell, R. C.; Castleman, A. W., Jr., Gas-Phase Reactions of Nickel and Nickel Oxide Clusters with Nitrogen Oxides. 3. Reactions of Cations with Nitric Oxide. *J. Phys. Chem. A* **1999**, *103*, 10846-10850.
12. Parks, E. K.; Kerns, K. P.; Riley, S. J.; Winter, B. J., Adsorption of C60 on Nickel Clusters at High Temperature. *Phys. Rev. B: Condens. Matter Mater. Phys.* **1999**, *59*, 13431-13445.
13. Hanmura, T.; Ichihashi, M.; Kondow, T., Reaction of Benzene Molecule on Size-Selected Nickel Cluster Ions. *J. Phys. Chem. A* **2002**, *106*, 4525-4528.
14. Yadav, R. T.; Ichihashi, M.; Kondow, T., Origin of Size-Dependent Reactivity of Nickel Cluster Ions with Methanol. *J. Phys. Chem. A* **2004**, *108*, 7188-7192.
15. Sugawara, K.-i.; Koga, K., Selective Formation of Ni13o8+ and Ni16o10+ by the Reactions of Nickel Cluster Cations with Oxygen. *Chem. Phys. Lett.* **2005**, *409*, 197-202.
16. Rodriguez-Kessler, P. L.; Rodriguez-Dominguez, A. R., Stability of Ni Clusters and the Adsorption of Ch4: First-Principles Calculations. *J. Phys. Chem. C* **2015**, *119*, 12378-12384.
17. Klots, T.; Winter, B.; Parks, E.; Riley, S. t. J., Icosahedral Structure in Hydrogenated Cobalt and Nickel Clusters. *The Journal of chemical physics* **1991**, *95*, 8919-8930.
18. Parks, E.; Winter, B.; Klots, T.; Riley, S., The Structure of Nickel Clusters. *The Journal of chemical physics* **1991**, *94*, 1882-1902.
19. Parks, E.; Zhu, L.; Ho, J.; Riley, S., The Structure of Small Nickel Clusters. I. Ni3–Ni15. *The Journal of chemical physics* **1994**, *100*, 7206-7222.
20. Parks, E.; Zhu, L.; Ho, J.; Riley, S., The Structure of Small Nickel Clusters. Ii. Ni16–Ni28. *The Journal of chemical physics* **1995**, *102*, 7377-7389.
21. Parks, E.; Riley, S., Nickel Cluster Structure Determined from the Adsorption of Molecular Nitrogen: Ni49-Ni71. *Zeitschrift für Physik D Atoms, Molecules and Clusters* **1995**, *33*, 59-70.
22. Duncan, M. A., Spectroscopy of Metal Ion Complexes: Gas-Phase Models for Solvation. *Annual Review of Physical Chemistry* **1997**, *48*, 69-93.
23. Duncan, M. A., Infrared Spectroscopy to Probe Structure and Dynamics in Metal Ion-Molecule Complexes. *International Reviews in Physical Chemistry* **2003**, *22*, 407-435.
24. Walker, N. R.; Walters, R. S.; Duncan, M. A., Frontiers in the Infrared Spectroscopy of Gas Phase Metal Ion Complexes. *New Journal of Chemistry* **2005**, *29*, 1495-1503.
25. Roithova, J., Characterization of Reaction Intermediates by Ion Spectroscopy. *Chemical Society Reviews* **2012**, *41*, 547-559.
26. Oomens, J.; Sartakov, B. G.; Meijer, G.; von Helden, G., Gas-Phase Infrared Multiple Photon Dissociation Spectroscopy of Mass-Selected Molecular Ions. *International Journal of Mass Spectrometry* **2006**, *254*, 1-19.
27. MacAleese, L.; Maitre, P., Infrared Spectroscopy of Organometallic Ions in the Gas Phase: From Model to Real World Complexes. *Mass Spectrometry Reviews* **2007**, *26*, 583-605.
28. Schöllkopf, W.; Gewinner, S.; Junkes, H.; Paarmann, A.; von Helden, G.; Bluem, H.; Todd, A. M. M. In *The New Ir and Thz Fel Facility at the Fritz Haber Institute in Berlin*, 2015; pp 95121L-95121L-13.

29. Kamrath, M. Z.; Garand, E.; Jordan, P. A.; Leavitt, C. M.; Wolk, A. B.; Van Stipdonk, M. J.; Miller, S. J.; Johnson, M. A., Vibrational Characterization of Simple Peptides Using Cryogenic Infrared Photodissociation of H-2-Tagged, Mass-Selected Ions. *Journal of the American Chemical Society* **2011**, *133*, 6440-6448.
30. Wolk, A. B.; Leavitt, C. M.; Garand, E.; Johnson, M. A., Cryogenic Ion Chemistry and Spectroscopy. *Accounts of Chemical Research* **2014**, *47*, 202-210.
31. Gruene, P.; Fielicke, A.; Meijer, G.; Rayner, D. M., The Adsorption of Co on Group 10 (Ni, Pd, Pt) Transition-Metal Clusters. *Physical Chemistry Chemical Physics* **2008**, *10*, 6144-6149.
32. Fielicke, A.; von Helden, G.; Meijer, G.; Pedersen, D. B.; Simard, B.; Rayner, D. M., Size and Charge Effects on the Binding of Co to Late Transition Metal Clusters. *Journal of Chemical Physics* **2006**, *124*, 194305-194305.
33. Harding, D. J.; Fielicke, A., Platinum Group Metal Clusters: From Gas-Phase Structures and Reactivities Towards Model Catalysts. *Chemistry – A European Journal* **2014**, *20*, 3258-3267.
34. Pfeffer, B.; Jaberg, S.; Niedner-Schatteburg, G., Reactions of Simple Aromatic Heterocycles with Niobium Cluster Ions (N < 30). *Journal of Chemical Physics* **2009**, *131*, 194305.
35. Peredkov, S.; Neeb, M.; Eberhardt, W.; Meyer, J.; Tombers, M.; Kampschulte, H.; Niedner-Schatteburg, G., Spin and Orbital Magnetic Moments of Free Nanoparticles. *Physical Review Letters* **2011**, *107*.
36. Meyer, J.; Tombers, M.; van Wüllen, C.; Niedner-Schatteburg, G.; Peredkov, S.; Eberhardt, W.; Neeb, M.; Palutke, S.; Martins, M.; Wurth, W., The Spin and Orbital Contributions to the Total Magnetic Moments of Free Fe, Co, and Ni Clusters. *The Journal of Chemical Physics* **2015**, *143*, 104302.
37. Nosenko, Y.; Menges, F.; Riehn, C.; Niedner-Schatteburg, G., Investigation by Two-Color Ir Dissociation Spectroscopy of Hoogsteen-Type Binding in a Metalated Nucleobase Pair Mimic. *Physical Chemistry Chemical Physics* **2013**, *15*, 8171-8178.
38. Lang, J.; Gaffga, M.; Menges, F.; Niedner-Schatteburg, G., Two-Color Delay Dependent Ir Probing of Torsional Isomerization in a Agl1l2 (+) Complex. *Physical Chemistry Chemical Physics* **2014**, *16*, 17417-17421.
39. Gaffga, M.; Munstein, I.; Muller, P.; Lang, J.; Thiel, W. R.; Niedner-Schatteburg, G., Multistate-Mediated Rearrangements and Fecl2 Elimination in Dinuclear Fepd Complexes. *Journal of Physical Chemistry A* **2015**, *119*, 12587-12598.
40. Mohrbach, J.; Lang, J.; Dillinger, S.; Prosenc, M. A.; Braunstein, P.; Niedner-Schatteburg, G., Vibrational Fingerprints of a Tetranuclear Cobalt Carbonyl Cluster within an Cryo Tandem Ion Trap. *Journal of Molecular Spectroscopy* **2016**, accepted 21.11.2016.
41. Dillinger, S.; Mohrbach, J.; Hewer, J.; Gaffga, M.; Niedner-Schatteburg, G., Infrared Spectroscopy of N2 Adsorption on Size Selected Cobalt Cluster Cations in Isolation. *Physical Chemistry Chemical Physics* **2015**, *17*, 10358-10362.
42. Mohrbach, J.; Dillinger, S.; Niedner-Schatteburg, G., Cryo Kinetics and Spectroscopy of Cationic Nickel Clusters: Rough and Smooth Surfaces. *The Journal of Physical Chemistry C* **2016**.
43. Lang, J.; Mohrbach, J.; Dillinger, S.; Hewer, J.; Niedner-Schatteburg, G., Vibrational Blue Shift of Coordinated N2 in [Fe3o(Oac)6(N2)N]+:“Non Classical” Dinitrogen Complexes. *Chemical Communications (London)* **2016**, accepted 2.12.2016
44. Berg, C.; Schindler, T.; Niedner-Schatteburg, G.; Bondybey, V. E., Reactions of Simple Hydrocarbons with Nb+ N: Chemisorption and Physisorption on Ionized Niobium Clusters. *The Journal of chemical physics* **1995**, *102*, 4870-4884.

45. Maruyama, S.; Anderson, L. R.; Smalley, R. E., Direct Injection Supersonic Cluster Beam Source for Ft-Icr Studies of Clusters. *Review of scientific instruments* **1990**, *61*, 3686-3693.
46. Proch, D.; Trickl, T., A High-Intensity Multi-Purpose Piezoelectric Pulsed Molecular Beam Source. *Review of Scientific Instruments* **1989**, *60*, 713-716.
47. Caravatti, P.; Allemann, M., The 'Infinity Cell': A New Trapped-Ion Cell with Radiofrequency Covered Trapping Electrodes for Fourier Transform Ion Cyclotron Resonance Mass Spectrometry. *Organic Mass Spectrometry* **1991**, *26*, 514-518.
48. Graf, M., *Diploma Thesis, TU Kaiserslautern* **2006**, *(unpublished)*.
49. Langevin, M. In *Une Formule Fondamentale De Théorie Cinétique*, Annales de chimie et de physique, Series, 1905; pp 245-288.
50. Su, T.; Bowers, M. T., Theory of Ion-Polar Molecule Collisions. Comparison with Experimental Charge Transfer Reactions of Rare Gas Ions to Geometric Isomers of Difluorobenzene and Dichloroethylene. *The Journal of Chemical Physics* **1973**, *58*, 3027-3037.
51. Su, T.; Bowers, M. T., Ion-Polar Molecule Collisions. Proton Transfer Reactions of H3+ and Ch5+ to the Geometric Isomers of Difluoroethylene, Dichloroethylene, and Difluorobenzene. *Journal of the American Chemical Society* **1973**, *95*, 1370-1373.
52. Su, T.; Bowers, M. T., Ion-Polar Molecule Collisions: The Effect of Ion Size on Ion-Polar Molecule Rate Constants; the Parameterization of the Average-Dipole-Orientation Theory. *International Journal of Mass Spectrometry and Ion Physics* **1973**, *12*, 347-356.
53. Anderson, M. L.; Ford, M. S.; Derrick, P. J.; Drewello, T.; Woodruff, D. P.; Mackenzie, S. R., Nitric Oxide Decomposition on Small Rhodium Clusters, Rh N+. *The Journal of Physical Chemistry A* **2006**, *110*, 10992-11000.
54. Balteanu, I.; Balaj, O. P.; Fox-Beyer, B. S.; Rodrigues, P.; Barros, M. T.; Moutinho, A. M. C.; Costa, M. L.; Beyer, M. K.; Bondybey, V. E., Size- and Charge-State-Dependent Reactivity of Azidoacetonitrile with Anionic and Cationic Rhodium Clusters Rhn±. *Organometallics* **2004**, *23*, 1978-1985.
55. Kummerlöwe, G.; Beyer, M. K., Rate Estimates for Collisions of Ionic Clusters with Neutral Reactant Molecules. *International Journal of Mass Spectrometry* **2005**, *244*, 84-90.
56. Grunze, M.; Driscoll, R. K.; Burland, G. N.; Cornish, J. C. L.; Pritchard, J., Molecular and Dissociative Chemisorption of N2 on Ni(110). *Surface Science* **1979**, *89*, 381-390.
57. Yoshinobu, J.; Zenobi, R.; Xu, J.; Xu, Z.; Yates Jr, J. T., N2 Chemisorption on Ni (111). An Infrared Investigation under Steady-State Conditions. *The Journal of chemical physics* **1991**, *95*, 9393-9400.

4.3.8 Supplementary Information

Isothermal Cryo Kinetics of Cationic Nickel Clusters

Jennifer Mohrbach, Sebastian Dillinger, and Gereon Niedner-Schatteburg

Fachbereich Chemie and Forschungszentrum OPTIMAS,
Technische Universität Kaiserslautern,
67663 Kaiserslautern, Germany

Table of content

Figure S1. Temporal evolution of the mass spectra of mass-selected Ni_6^+, Ni_{18}^+ clusters at 26 K.

Figure S2. Isothermal kinetics of the stepwise N_2 adsorption by isolated Ni_{18}^+ clusters at $p(N_2) = 1.1 \times 10^{-7}$ mbar (top) and $p(N_2) = 3.2 \times 10^{-7}$ mbar (bottom) within 26 Kelvin He buffer gas. The fits (shown as lines) assume pseudo-first-order kinetics in a reaction chain of up to 18 consecutive steps.

Figure S3. Observed rate constants of the (n,m) species n = 5-8 as a function of N_2 coverage. Filled circles show the rate of adsorption and open circles indicate single N_2 desorption.

Table S1. Pseudo-first-order rate constants for the N_2 adsorption/desorption $k_{(n,m)}$ / $k_{-(n,m+1)}$ on Ni_n^+ (n = 5-8) clusters.

Figure S4. Observed rate constants of the (n,m) species n = 9-12 as a function of N_2 coverage. Filled circles show the rate of adsorption and open circles indicate single N_2 desorption.

Table S2. Pseudo-first-order rate constants for the N_2 adsorption/desorption $k_{(n,m)}$ / $k_{-(n,m+1)}$ on Ni_n^+ (n = 9-12) clusters.

Figure S5. Observed rate constants of the (n,m) species n = 13-16 as a function of N_2 coverage. Filled circles show the rate of adsorption and open circles indicate single N_2 desorption.

Table S3. Pseudo-first-order rate constants for the N_2 adsorption/desorption $k_{(n,m)}$ / $k_{-(n,m+1)}$ on Ni_n^+ (n = 13-16) clusters.

Figure S6. Observed rate constants of the (n,m) species n = 17-20 as a function of N_2 coverage. Filled circles show the rate of adsorption and open circles indicate single N_2 desorption.

Table S4. Pseudo-first-order rate constants for the N_2 adsorption/desorption $k_{(n,m)}$ / $k_{-(n,m+1)}$ on Ni_n^+ (n = 17-20) clusters.

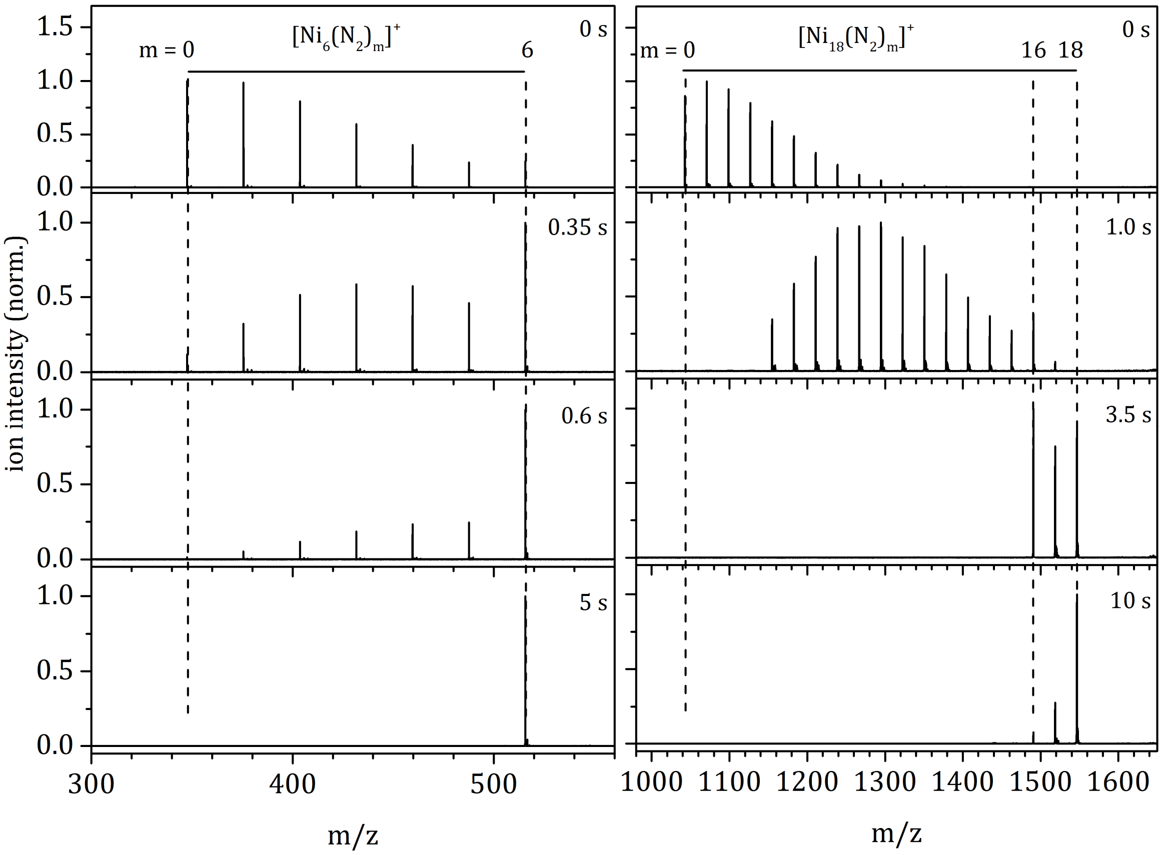

Figure S1. Temporal evolution of the mass spectra of mass-selected Ni_6^+, Ni_{18}^+ clusters at 26 K.

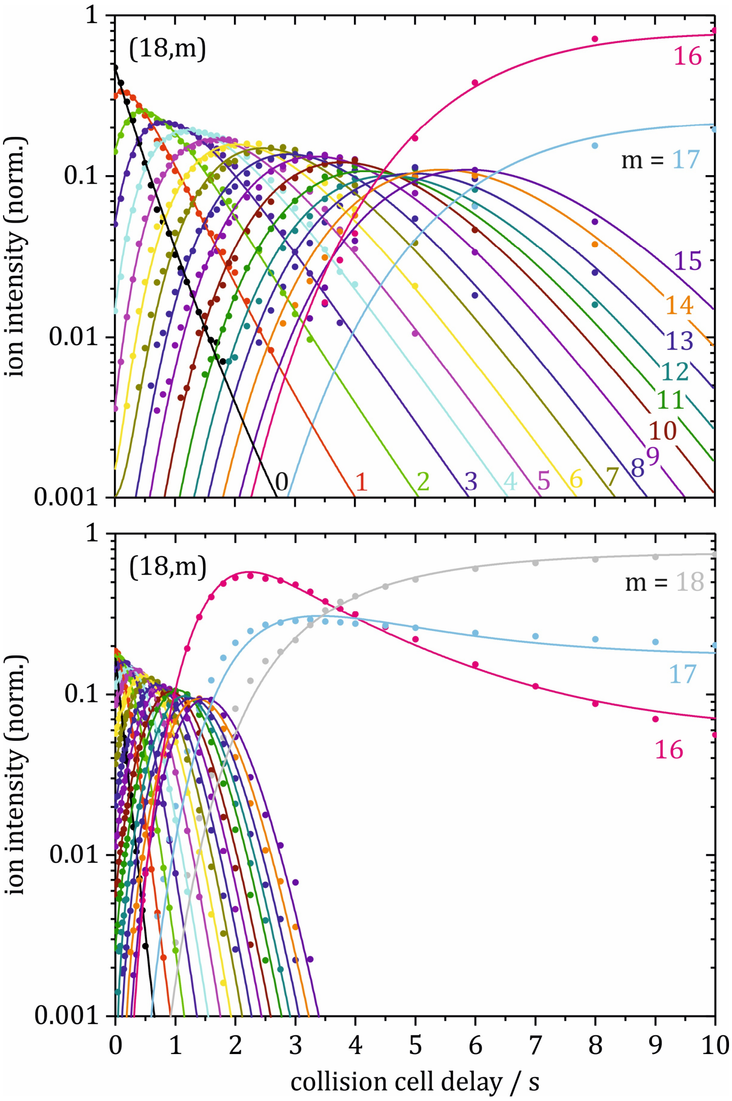

Figure S2. Isothermal kinetics of the stepwise N_2 adsorption by isolated Ni_{18}^+ clusters at $p(N_2) = 1.1 \times 10^{-7}$ mbar (top) and $p(N_2) = 3.2 \times 10^{-7}$ mbar (bottom) within 26 Kelvin He buffer gas. The fits (shown as lines) assume pseudo-first-order kinetics in a reaction chain of up to 18 consecutive steps.

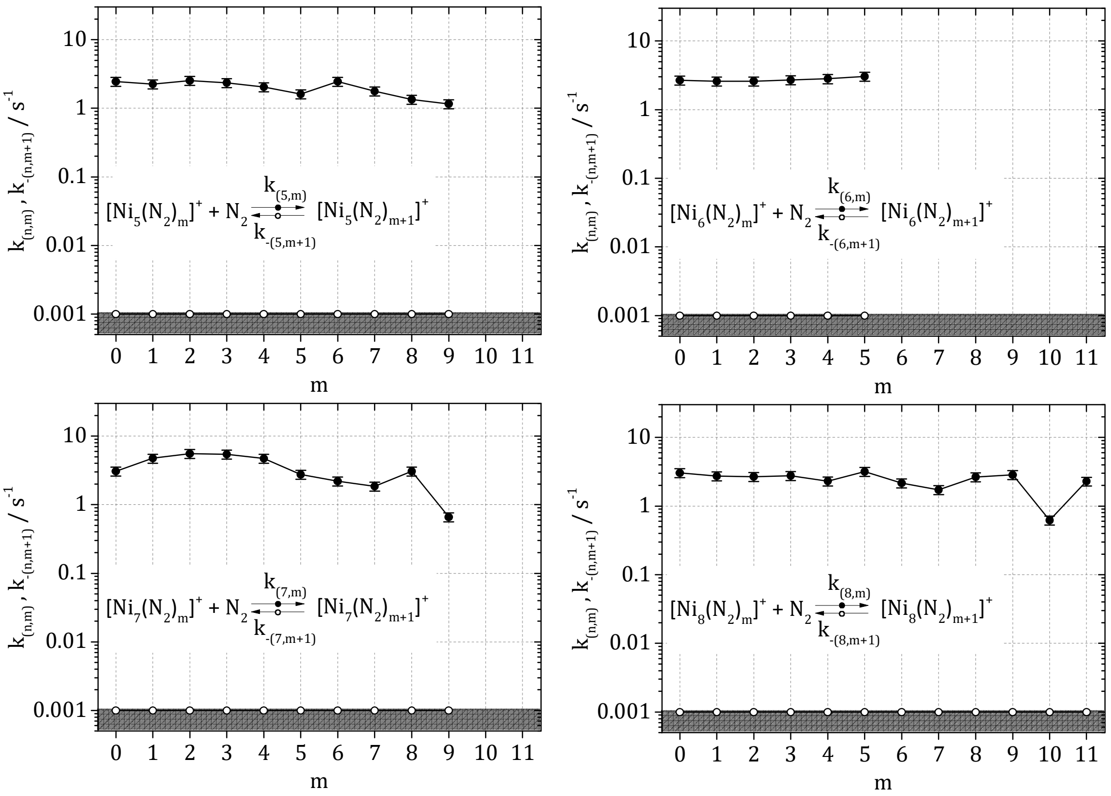

Figure S3. Observed rate constants of the (n,m) species n = 5–8 as a function of N_2 coverage. Filled circles show the rate of adsorption and open circles indicate single N_2 desorption.

Table S1. Pseudo-first-order rate constants for the N_2 adsorption/desorption $k_{(n,m)}$ / $k_{-(n,m+1)}$ on Ni_n^+ (n = 5–8) clusters.

m	$k_{(5,m)}$ s^{-1}	$k_{-(5,m+1)}$ s^{-1}	$k_{(6,m)}$ s^{-1}	$k_{-(6,m+1)}$ s^{-1}	$k_{(7,m)}$ s^{-1}	$k_{-(7,m+1)}$ s^{-1}	$k_{(8,m)}$ s^{-1}	$k_{-(8,m+1)}$ s^{-1}
0	2.4	<0.001	2.7	<0.001	3.1	<0.001	3.0	<0.001
1	2.2	<0.001	2.6	<0.001	4.7	<0.001	2.7	<0.001
2	2.5	<0.001	2.6	<0.001	5.5	<0.001	2.7	<0.001
3	2.3	<0.001	2.7	<0.001	5.4	<0.001	2.8	<0.001
4	2.0	<0.001	2.8	<0.001	4.7	<0.001	2.3	<0.001
5	1.6	<0.001	3.0	<0.001	2.8	<0.001	3.2	<0.001
6	2.5	<0.001			2.2	<0.001	2.2	<0.001
7	1.8	<0.001			1.9	<0.001	1.7	<0.001
8	1.3	<0.001			3.1	<0.001	2.7	<0.001
9	1.2	<0.001			0.7	<0.001	2.8	<0.001
10							0.6	<0.001
11							2.3	<0.001

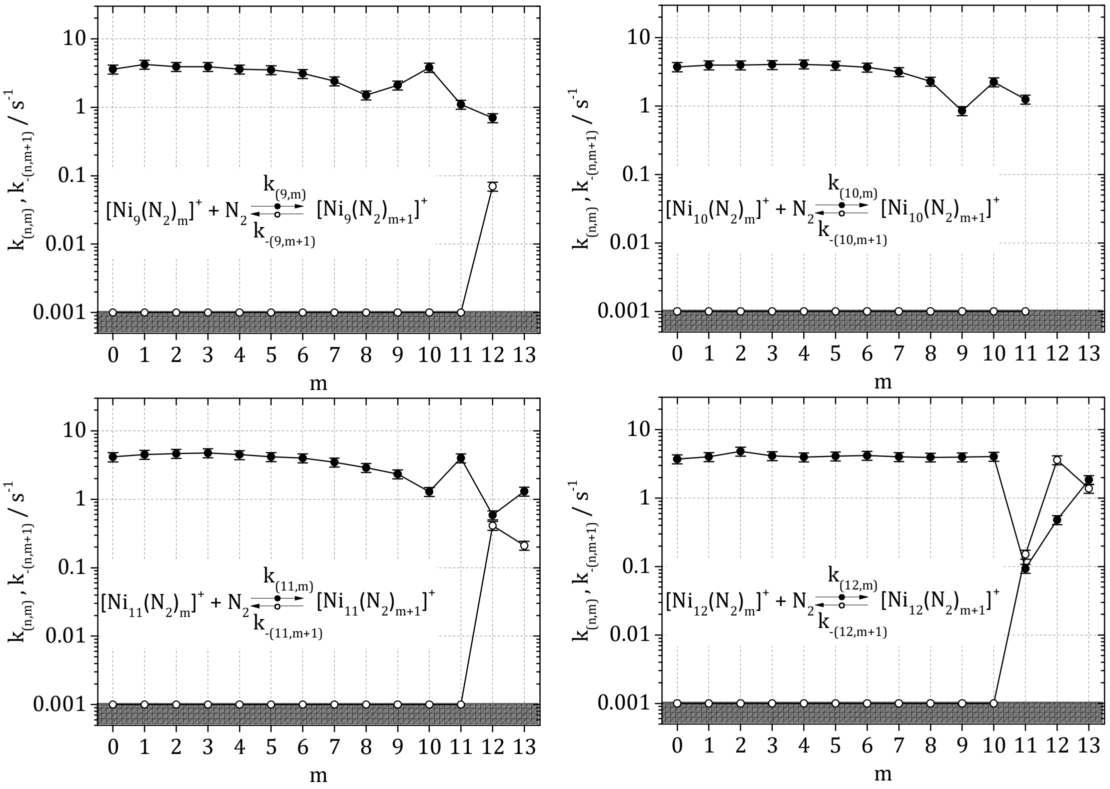

Figure S4. Observed rate constants of the (n,m) species n = 9–12 as a function of N_2 coverage. Filled circles show the rate of adsorption and open circles indicate single N_2 desorption.

Table S2. Pseudo-first-order rate constants for the N_2 adsorption/desorption $k_{(n,m)}$ / $k_{-(n,m+1)}$ on Ni_n^+ (n = 9–12) clusters.

m	$k_{(9,m)}$ s^{-1}	$k_{-(9,m+1)}$ s^{-1}	$k_{(10,m)}$ s^{-1}	$k_{-(10,m+1)}$ s^{-1}	$k_{(11,m)}$ s^{-1}	$k_{-(11,m+1)}$ s^{-1}	$k_{(12,m)}$ s^{-1}	$k_{-(12,m+1)}$ s^{-1}
0	3.6	<0.001	3.8	<0.001	4.2	<0.001	3.7	<0.001
1	4.2	<0.001	4.0	<0.001	4.5	<0.001	4.0	<0.001
2	3.9	<0.001	4.0	<0.001	4.6	<0.001	4.8	<0.001
3	3.9	<0.001	4.1	<0.001	4.7	<0.001	4.2	<0.001
4	3.6	<0.001	4.1	<0.001	4.5	<0.001	4.0	<0.001
5	3.5	<0.001	3.9	<0.001	4.2	<0.001	4.1	<0.001
6	3.1	<0.001	3.7	<0.001	4.0	<0.001	4.2	<0.001
7	2.4	<0.001	3.2	<0.001	3.5	<0.001	4.0	<0.001
8	1.5	<0.001	2.3	<0.001	2.9	<0.001	4.0	<0.001
9	2.1	<0.001	0.9	<0.001	2.3	<0.001	4.0	<0.001
10	3.8	<0.001	2.2	<0.001	1.3	<0.001	4.1	<0.001
11	1.1	<0.001	1.3	<0.001	4.0	<0.001	0.1	0.15
12	0.7	0.07			0.6	0.41	0.5	3.62
13					1.3	0.21	1.9	1.38

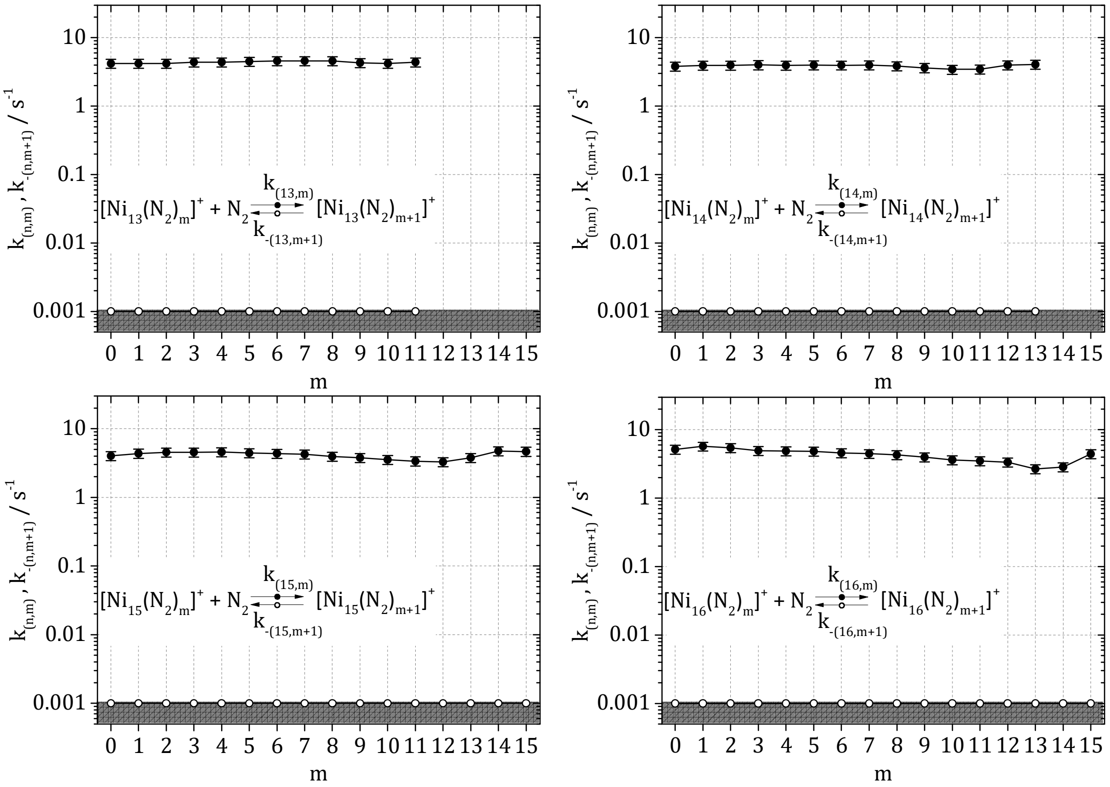

Figure S5. Observed rate constants of the (n,m) species n = 13–16 as a function of N_2 coverage. Filled circles show the rate of adsorption and open circles indicate single N_2 desorption.

Table S3. Pseudo-first-order rate constants for the N_2 adsorption/desorption $k_{(n,m)}$ / $k_{-(n,m+1)}$ on Ni_n^+ (n = 13–16) clusters.

m	$k_{(13,m)}$ s^{-1}	$k_{-(13,m+1)}$ s^{-1}	$k_{(14,m)}$ s^{-1}	$k_{-(14,m+1)}$ s^{-1}	$k_{(15,m)}$ s^{-1}	$k_{-(15,m+1)}$ s^{-1}	$k_{(16,m)}$ s^{-1}	$k_{-(16,m+1)}$ s^{-1}
0	4.2	<0.001	3.8	<0.001	4.0	<0.001	5.2	<0.001
1	4.2	<0.001	3.9	<0.001	4.4	<0.001	5.7	<0.001
2	4.2	<0.001	4.0	<0.001	4.6	<0.001	5.4	<0.001
3	4.4	<0.001	4.0	<0.001	4.6	<0.001	5.0	<0.001
4	4.4	<0.001	3.9	<0.001	4.6	<0.001	4.9	<0.001
5	4.5	<0.001	4.0	<0.001	4.4	<0.001	4.8	<0.001
6	4.6	<0.001	4.0	<0.001	4.4	<0.001	4.6	<0.001
7	4.6	<0.001	4.0	<0.001	4.2	<0.001	4.5	<0.001
8	4.6	<0.001	3.9	<0.001	3.9	<0.001	4.3	<0.001
9	4.3	<0.001	3.6	<0.001	3.8	<0.001	4.0	<0.001
10	4.2	<0.001	3.4	<0.001	3.5	<0.001	3.6	<0.001
11	4.4	<0.001	3.5	<0.001	3.4	<0.001	3.5	<0.001
12			4.0	<0.001	3.3	<0.001	3.3	<0.001
13			4.1	<0.001	3.8	<0.001	2.7	<0.001
14					4.8	<0.001	2.9	<0.001
15					4.7	<0.001	4.4	<0.001

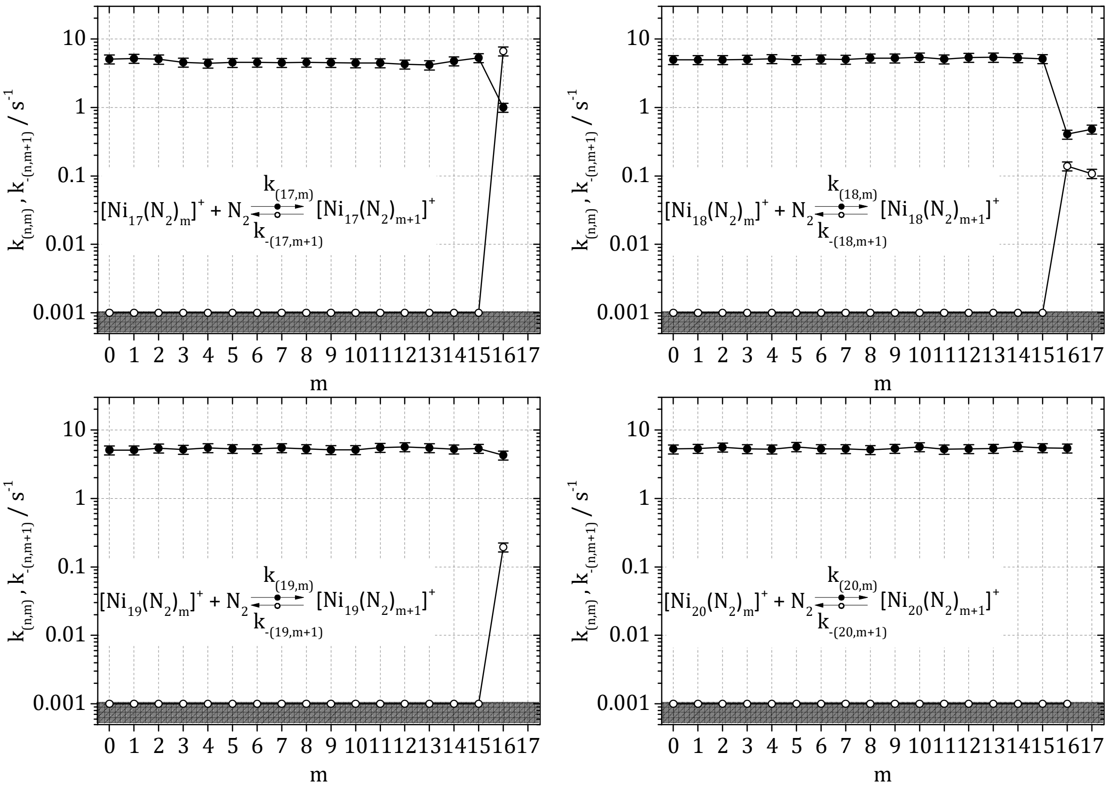

Figure S6. Observed rate constants of the (n,m) species n = 17–20 as a function of N_2 coverage. Filled circles show the rate of adsorption and open circles indicate single N_2 desorption.

Table S4. Pseudo-first-order rate constants for the N_2 adsorption/desorption $k_{(n,m)}$ / $k_{-(n,m+1)}$ on Ni_n^+ (n = 17–20) clusters.

m	$k_{(17,m)}$ s^{-1}	$k_{-(17,m+1)}$ s^{-1}	$k_{(18,m)}$ s^{-1}	$k_{-(18,m+1)}$ s^{-1}	$k_{(19,m)}$ s^{-1}	$k_{-(19,m+1)}$ s^{-1}	$k_{(20,m)}$ s^{-1}	$k_{-(20,m+1)}$ s^{-1}
0	5.1	<0.001	4.9	<0.001	5.1	<0.001	5.3	<0.001
1	5.2	<0.001	4.9	<0.001	5.1	<0.001	5.3	<0.001
2	5.0	<0.001	4.9	<0.001	5.4	<0.001	5.6	<0.001
3	4.5	<0.001	5.0	<0.001	5.2	<0.001	5.3	<0.001
4	4.4	<0.001	5.1	<0.001	5.5	<0.001	5.2	<0.001
5	4.5	<0.001	4.9	<0.001	5.3	<0.001	5.7	<0.001
6	4.5	<0.001	5.1	<0.001	5.3	<0.001	5.3	<0.001
7	4.5	<0.001	5.0	<0.001	5.5	<0.001	5.3	<0.001
8	4.5	<0.001	5.2	<0.001	5.3	<0.001	5.1	<0.001
9	4.5	<0.001	5.2	<0.001	5.1	<0.001	5.3	<0.001
10	4.4	<0.001	5.4	<0.001	5.1	<0.001	5.7	<0.001
11	4.5	<0.001	5.1	<0.001	5.5	<0.001	5.2	<0.001
12	4.3	<0.001	5.4	<0.001	5.6	<0.001	5.3	<0.001
13	4.2	<0.001	5.4	<0.001	5.5	<0.001	5.4	<0.001
14	4.7	<0.001	5.3	<0.001	5.2	<0.001	5.7	<0.001
15	5.3	<0.001	5.1	<0.001	5.3	<0.001	5.4	<0.001
	1.0	6.63	0.4	0.14	4.3	0.19	5.4	<0.001
			0.5	0.11				

4.4 Paper draft: “Isothermal Cryo Kinetics of Cationic Iron Clusters”

The following paper draft named “Isothermal Cryo Kinetics of Cationic Iron Clusters” was prepared to be published in a slightly shorter version. The experiments were performed by Sebastian Dillinger and myself. The data evaluation was done by myself. The initial paper draft was put together by myself. G. Niedner-Schatteburg was involved in the revision of the manuscript.

Isothermal Cryo Kinetics of Cationic Iron Clusters

Jennifer Mohrbach, Sebastian Dillinger, and Gereon Niedner-Schatteburg

Fachbereich Chemie and Forschungszentrum OPTIMAS,
Technische Universität Kaiserslautern,
67663 Kaiserslautern, Germany

4.4.1 Abstract

The stepwise N_2 adsorption on size selected Fe_n^+ (n = 8–20) clusters at 26 K is studied in a hybrid tandem ion trap instrument. Pseudo-first-order kinetic fits confirm consecutive adsorption steps by single exponentially decays and by a biexponentially decay in one case. N_2 desorption occurs for small clusters at high levels of N_2 coverage. In all investigated cases, stepwise N_2 uptake reaches a strict adsorption limit m_{max}, which shows no evidence for further increase. The adsorption limit does not scale with cluster size and the variation in reaction rates for the initial N_2 adsorption corroborates the unique adsorption behavior of Fe_n^+ clusters. We find evidence for N_2 head-on adsorption which might change to side-on adsorption at high N_2 coverages.

4.4.2 Introduction

The ligation of transition metal (TM) clusters exhibits physical and chemical properties that are highly dependent on the geometrical cluster structure. Many studies of such metal-ligand clusters are largely motivated by their potential applications in catalysis.[1-5] Early research on the chemical reactivity of transition metal clusters reveals a strong size effect.[6-8] Iron clusters, in particular, show a strong variation in their reaction rates with small molecules as the cluster size increases. Several experimental and theoretical studies on the gas phase reactivity of Fe_n clusters with different ligands, such as the adsorption of hydrogen,[7, 9-11], ammonia,[7] carbon[12], water,[7, 13] and benzene[14-16] have been carried out. These studies demonstrated the high reactivity exhibited especially for small iron clusters. Time-of-flight (TOF) mass spectra reveal an unusual sequence of magic numbers $n = 7$, 13, 15, 19 and 23 for Fe_n clusters,[17] which can be explained neither by electronic shell closure[18] nor by packing of hard spheres.[19] Because of the unique ferromagnetic properties of bulk iron, studies on the magnetic properties of small iron clusters have drawn considerable interests. Iron clusters are found to be magnetic with higher moments than those found in the bulk.[20-23] The intimate relationship between structure, magnetic properties and stability poses an uncommon challenge that motivated many theoretical studies of Fe_n clusters.[24-33] Still, important controversies remain unresolved among the reported results, including the ground-state atomic arrangements, magnetic moments, noncollinear magnetism, and finally the stability spectrum of small Fe aggregates.

The physisorption and chemisorption of N_2 on metal surfaces have been studied extensively[34] due to their importance in many catalytic processes. For example, the rate-determining step in the industrial synthesis of ammonia is the dissociation of N_2, using iron as a catalyst.[35] The fixation of nitrogen by the nitrogenase enzyme is the equivalent process in biological systems.[36] The behavior of N_2 reacting with iron clusters of different nuclearity is therefore particularly relevant to industrial and biological processes involving N-N bond breaking. Experimentally, it has been shown that N_2 adsorption to Fe(111) surfaces takes place in α-N_2 and γ-N_2 motifs, elucidated by angle resolved LEED studies in conjunction with potential surface modelling.[37] This resembles η^2 side-on and η^1 end-on coordination of N_2 to multiple and single metal centers, respectively. Spectroscopic and kinetic studies of N_2 adsorbed on Fe(111) revealed that there are three characteristic α-, δ- and γ-states, which refer to side-on, and head-on adsorption to highly and to less coordinated metal surface atoms.[34, 38-39] Early density functional theory (DFT) calculations revealed strong preference for end-on coordination of N_2 to single Fe centers with some evidence for rather exceptional η^2 side-on coordination of at most two N_2 to otherwise naked Fe atoms.[40-41] Surprisingly, little is known about how N_2 reacts with iron clusters, irrespective of their charge state.

Our tandem cryo ion trap instrument allows for the study of adsorption and reaction kinetics of clusters under single collision conditions at temperature as low as 11 K and for Infrared Photon Dissociation (IR-PD) spectroscopy –initially focusing on the one and two colour investigations of metal organic complexes.[42] We have started a systematic study of N_2 and H_2 cryo adsorption on size selected Fe, Co, and Ni clusters, first results being published.[43-44] X-ray studies by cryo ion trapping help for the investigation of spin and orbital contributions to the magnetic moments of these TM clusters.[45-46]

Here, we present detailed isothermal cryo kinetics of the N_2 adsorption onto cationic iron clusters Fe_n^+ (n = 8 – 20). This study aims to enable insight into the metal-adsorbate bonding and into the reactivity of individual iron clusters towards N_2 adsorption. All of the present findings from our current kinetics shall receive swift comparison to appropriate further spectroscopic investigations of the cluster adsorbate complexes and with DFT modelling – both of which are in the making.[47]

4.4.3 Experimental and computational methods

A customized Fourier Transform Ion Cyclotron Resonance (FT-ICR) mass spectrometer (Apex Ultra Bruker Daltonics) served to perform the cluster production, isolation, N_2 condensation and mass analysis. The iron clusters were generated using a home-built laser vaporization cluster ion source as described before.[48-49] In brief, iron atoms are evaporated from a rotating 0.4 mm thick isotopically enriched ^{56}Fe foil (99,93%, Oak Ridge National Laboratories) by the second harmonic of a pulsed Nd:YAG laser (Innolas *Spitlight 300*, 20 Hz). The hot plasma is captured by a He gas pulse (40 µs, 15 bar) created by a homebuilt piezoelectric valve.[50] The atoms and ions are cooled and aggregate to clusters in the subsequent jet expansion through a 50 mm long channel (Ø 2 mm) into vacuum (10^{-7} mbar). The clusters are skimmed, mass selected and injected into a cryogenic hexapole ion trap. The ion trap is cooled to 26 K by a closed cycle He cryostat. Buffer and reaction gas are introduced continuously. Sufficient nitrogen attachment is achieved by increasing the pressure in the ion trap from 1.1 x 10^{-7} mbar to 1.6 x 10^{-7} mbar. Additional He is introduced to increase the pressure up to 3.5 x 10^{-6} mbar to accomplish an efficient trapping and cooling of the ions. After storing the mass-selected ions for a variable time (0-10 s), the manipulated ions of the form $[Fe_n(N_2)_m]^+$ = (n,m) are guided by electrostatic lenses into the FT-ICR cell of the so-called "infinity" type.[51] The ICR cell is held at temperatures below 10 K with a closed cycle He cryostat to prevent heating of the clusters by black body radiation prior to ion detection. The ICR cell serves for the detection of the formed $[Fe_n(N_2)_m]^+$ = (n,m) cluster adsorbate complexes. The kinetic curves of cationic iron clusters and their nitrogen adducts originate from reaction delay scans and subsequent evaluation of the recorded mass spectra. Each of these mass spectra originates from an average of 20 mass spectra for the fixed collision cell delay. Fits to pseudo-first-order-kinetics occur through the "evofit" program.[52] The relative rate constants $k_{(n,m)}$ determine the absolute rate constants $k_{(n,m)}^{abs}$, the absolute collision gas number densities $\rho_{N2}(T)$ serving as the conversion factor:

$$k_{(n,m)}^{abs} = k_{(n,m)}/\rho_{N2}(T)$$

We obtain approximate values for $\rho_{N2}(T)$ indirectly from the pressure in the surrounding chamber $p_c^{(300\,K)}$ and an effective geometry factor c_{app}:

$$\rho_{N2}(26\,K) = \frac{c_{app}p_c^{300\,K}}{k_B T_{300\,K}}$$

The geometry factor c_{app} shows to bear a significant dependence on the temperature of the hexapole ion trap. By numerous kinetic studies of transition metal cluster cations with neutral reactants at cryogenic temperatures we evaluated this factor c_{app} to 1.8 ± 0.4 at 26 K with a net uncertainty of ± 50%.

The classical Langevin collision rate of ions with neutrals[53] is conveniently extended towards polar molecules by the average dipole orientation theory (ADO).[54-55] The ADO theory gives the theoretical limit of the absolute rate constants, the collision rate k^{ADO}, based on a classical trajectory of a linear dipole in the field of a point charge:

$$k^{ADO} = \frac{q}{2\varepsilon_0\sqrt{\mu}}\left(\sqrt{\alpha} + c\mu_D\sqrt{\frac{2}{\pi k_B T}}\right)$$

μ is the reduced mass (of the cluster adsorbate complex), α is the polarizability and μ_D is the dipole moment (in Debye). The parameter c lies between 0 and 1, and can be expressed by the polarizability volume $\alpha'$and μ_D.[56]

This ADO theory is frequently used to calculate the reaction rates of charged clusters with small molecules, knowingly underestimating the reaction rates for charged metal clusters significantly.[57-58] Kummerlöwe and Beyer introduced two models for calculating the collision rates of ionic clusters with neutral molecules, the HSA model (hard sphere average dipole orientation) and the surface charge capture (SCC) model.[59] In both models, the cluster and the neutral reaction partner are treated as hard speres, and the charge is treated as point charge. For the HSA collision rate k^{HSA}, the charge is located in the center of the cluster, while in the SCC model (k^{SCC}), the charge is drawn to the cluster surface by the attractive interaction with the neutral collision partner.

4.4.4 Results and Discussion

Molecular nitrogen adsorption on iron cluster cations: Trends and limits of adsorption

We investigated the stored $[Fe_n(N_2)_m]^+$ = (n,m) clusters for their N_2 adsorption in the cryogenic hexapole under isothermal conditions at 26 K. The mass spectra of all detected Fe_n^+ clusters - except for Fe_{17}^+ - reveal a successive gain of 28 m/z, which does indicate the stepwise adsorption of molecular nitrogen in consecutive chains of individual adsorption processes (*cf.* Fig. 1).

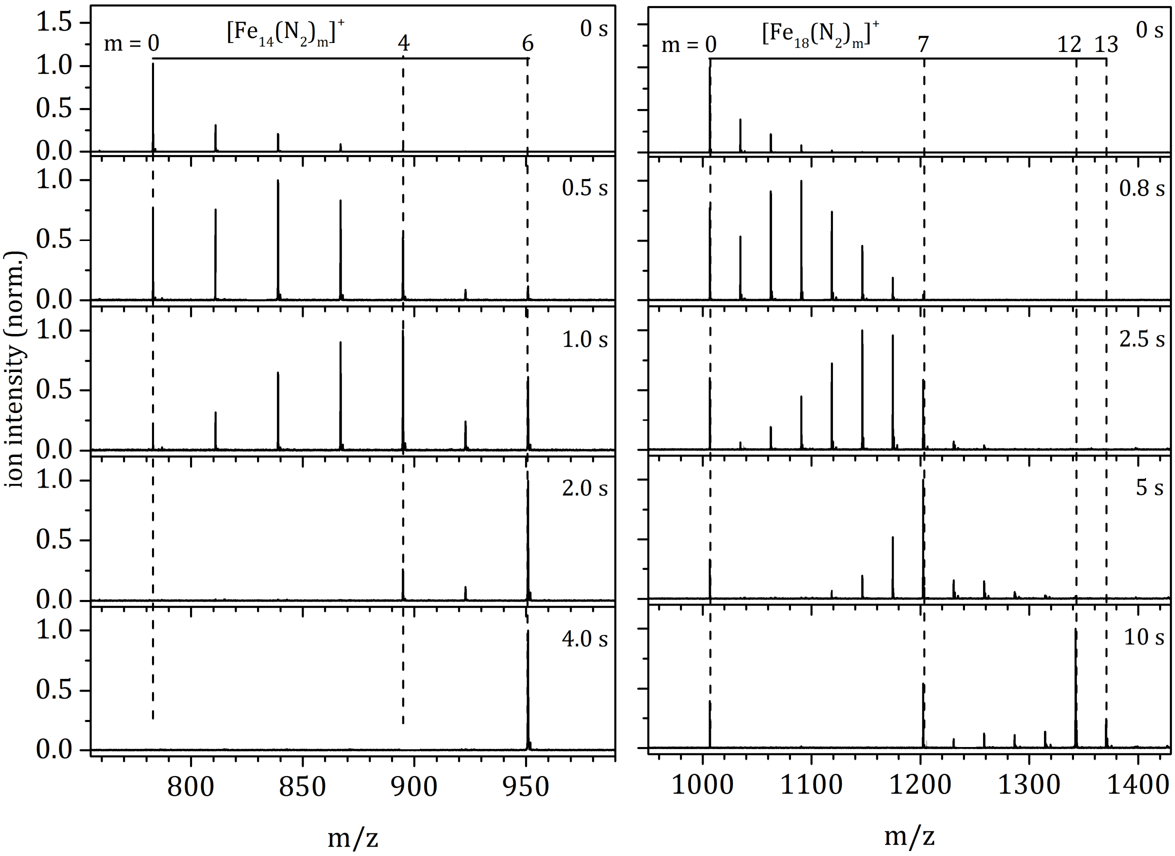

Figure 1. Temporal evolution of the mass spectra of mass-selected Fe_{13}^+ = (13,0) clusters up to 4 s (left) and of mass-selected Fe_{18}^+ = (18,0) clusters up to 10 s (right), exposed to 1.6 x 10^{-7} mbar N_2 within 26 K He buffer gas (3.5 x 10^{-6} mbar).

In all investigated cases (n = 8,..,20) stepwise N_2 uptake reaches a strict adsorption limit m_{max} within t < 12 sec, and this does not increase further up to t < 30 sec. In most cases we observe the N_2 adsorption limit preceded by one or more additional intermittent adsorption limits, which do not suppress further adsorption but cause some retardation.

The intermittent adsorption limits (blue stars in Fig. 2) and the adsorption limits (filled blue circles in Fig. 2) serve as guidelines for some elucidation of adsorbate bonding and cluster geometries. It shows, that the n:m stoichiometry is > 1 in all investigated cases n = 8–20, when reaching the respective N_2 adsorption limit. Yet, there is a trend in N_2 adsorption limits towards a molar ratio of $n{:}m_{max}$ = 1:1 for small clusters (n ≤ 12). The overall adsorption behavior cannot be explained by single N_2 head-on adsorption to each cluster surface atom, as shown for Ni_n^+ clusters.[60] For clusters with less than 18 Fe atoms the observed intermittent adsorption limits are close to the recorded adsorption limits. Note the pronounced dip in the adsorption limits for 13 ≤ n ≤ 16 and the absence of N_2 adsorption to Fe_{17}^+ clusters. Clusters with n > 17 exhibit an increase in reactivity towards N_2 adsorption. Preliminary infrared photon dissociation experiments indicate μ_1 head-on adsorption of the initial adsorbed N_2 for all investigated (n,1) cluster adsorbate complexes.[47]

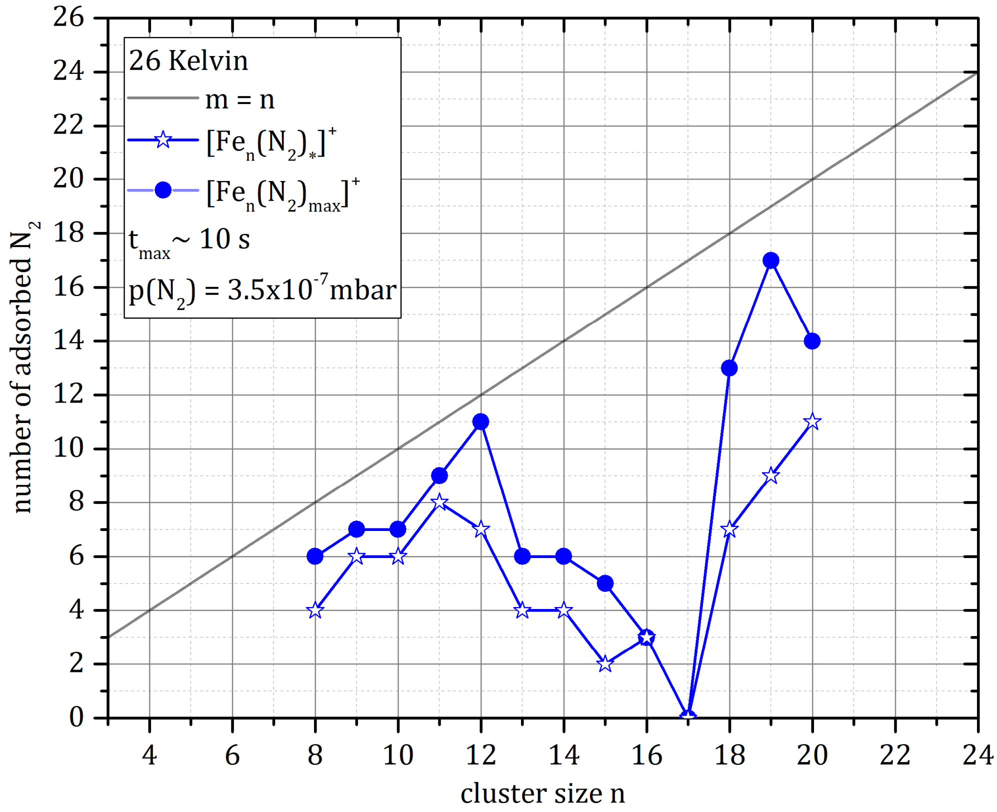

Figure 2. Recorded adsorption limits (filled circles) and intermittent limits (stars) of nitrogen adsorbed on a cationic iron clusters. The limits are displayed as a function of cluster size for n = 8 – 20.

We further investigated the stepwise N_2 adsorption on Fe_n^+ clusters by recording their reaction kinetics in more detail, and we performed pseudo-first-order kinetic fits by our genetic algorithm routine. The obtained fits confirm consecutive adsorption steps

(Fig.s 2-4). Most Fe_n^+ clusters decay mono exponentially without any indication of a second component. This, and the overall superior quality of all fits, entitles us to fit each consecutive step by a single rate constant. Some fits require significant backward reaction in cases of high N_2 coverages, which indicates swift N_2 desorption (see the supplementary information for details on the corresponding rate constants $k_{(n,m)}$ for all cluster kinetics). There is one exception: The N_2 adsorption to Fe_{18}^+ exhibits a biexponentially decay in the initial adsorption step.

Fe_8^+ – Fe_{11}^+:

Small iron clusters Fe_n^+ in the range of n = 8–11 exhibit little deviation in the observed adsorption limits and the intermittent adsorption limits. All clusters reveal a strict adsorption limit at $n \geq m$. There are significant backward reactions for the last adsorption steps, suggesting one or more weakly bound N_2 molecules when reaching cluster saturation (*cf.* Fig. 3).

In the case of (8,m) we observe an intermittent adsorption limit at (8,4) and the adsorption limit at (8,6). The predicted most stable structures for Fe_8 clusters correspond to a capped pentagonal bipyramid,[29-30, 61-62] or a bisdisphenoid structure.[29-33] The capped pentagonal bipyramid consists of one threefold, three fourfold, two fivefold, one sixfold and one sevenfold coordinated Fe atom. Assuming the same N_2 adsorption 'rules' as stated for Ni_n^+ clusters,[44] the adsorption limits should be observed at (8,7) and (8,12). In contrast, initial binding to the three- and fourfold coordinated Fe sites and additional adsorption to the fivefold atoms would result in limits at (8,4) and (8,6), as obseved. The bisdisphenoid structure consists of four fourfold and four fivefold coordinated Fe atoms, which would result in limits at (8,8) and (8,12) or at (8,4) and (8,8), other than observed.

In the cases of (9,m) and (10,m) we observe an intermittent adsorption limit at n = 6 and the adsorption limit at n = 7. The reported most stable structures for Fe_9 and Fe_{10} clusters correspond to capped square antiprisms, capped pentagonal bipyramidal motifs or a capped trigonal bipyramidal motifs. These geometries are possible growth models leading to the icosahedral structure predicted for Fe_{13}.[29-30, 61-62] The (11,m) cluster adsorbate complex exhibits an intermittent adsorption limit at (11,6) and the adsorption limit at (11,9), in equilibrium with its precursor. The preferred structure for this cluster is found to be a tetra-capped pentagonal bipyramid.

Unfortunately, there is no universally applicable adsorption rule, which would explain the observed adsorption limits. Without further knowledge of the exact N_2 adsorption site, no comprehensive structural interpretation can be drawn out of the adsorption limits in this study. We tentatively assume μ_1 head-on adsorption up to the adsorption limit, based on the shape of the kinetic curves in conjunction with those obtained for Ni_n^+ clusters. In addition, preliminary infrared spectroscopic investigations of the (n,1) cluster adsorbate complexes point towards μ_1 head-on N_2 adsorption.

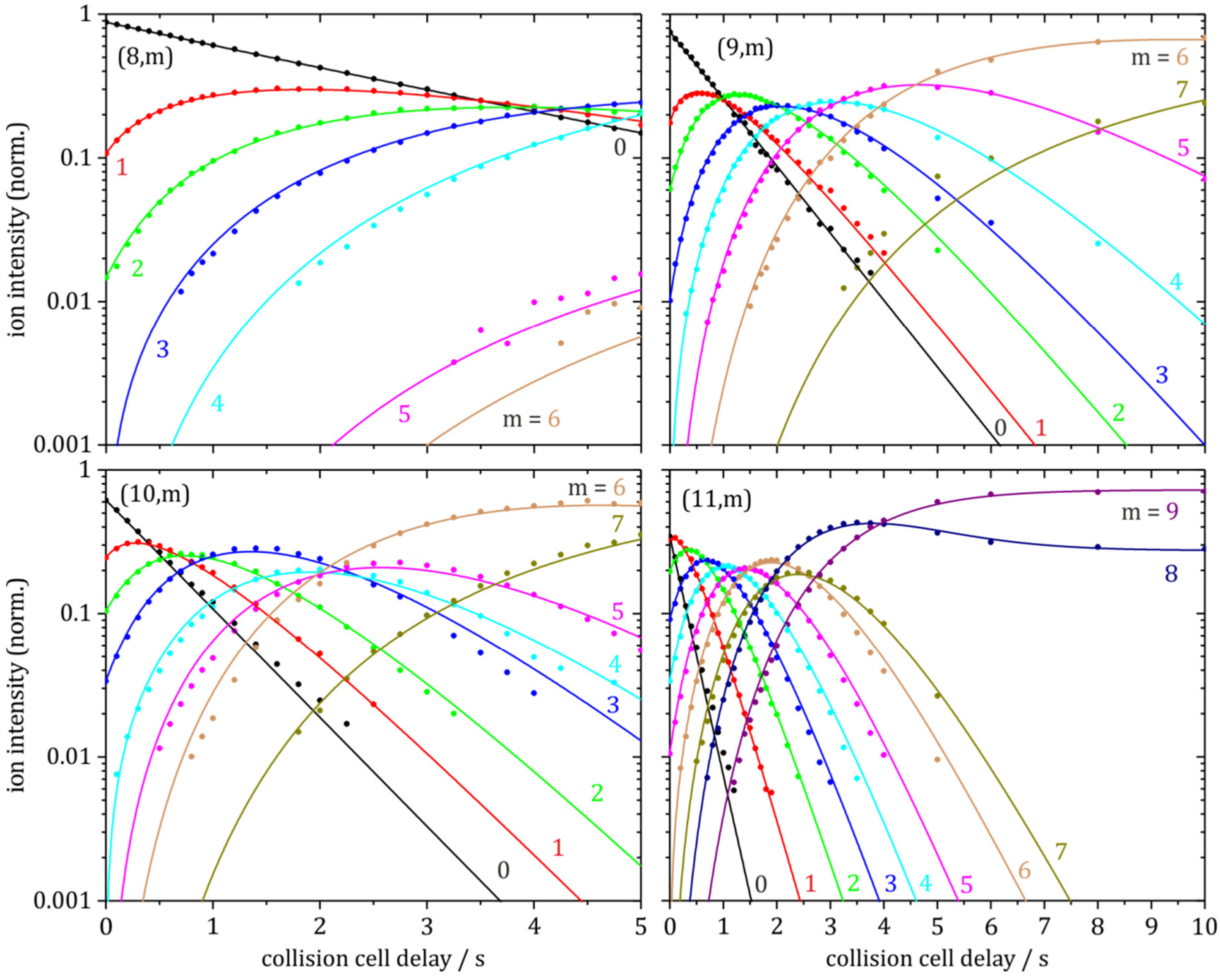

Figure 3. Isothermal kinetics of the stepwise N_2 adsorption by isolated Fe_n^+ clusters (n = 8–11). The fits (shown as lines) assume pseudo-first-order kinetics in a reaction chain of up to 9 consecutive steps.

Fe_{12}^+ – Fe_{15}^+:

In the range of n = 12–15 the N_2 adsorption behavior to Fe_n^+ clusters changes dramatically (*cf*. Fig. 4). We observe a significant decrease in N_2 adsorption with cluster size for n > 12.

In the case of (12,m) we observe an intermittent adsorption limit at (12,7) and the adsorption limit at (12,11). In the cases of (13,m) and (14,m) we observe intermittent adsorption limits at m = 4 and the adsorption limit at m = 6. The (15,m) cluster adsorbate complex exhibits only five consecutive steps. The terminal four adsorbate species (m = 2 – 5) are in equilibrium in favor of m = 2. Note, that the intensities of the minor adsorption limits (m = 3 – 5) are close to our detection limit, resulting in a reduction of the fit quality.

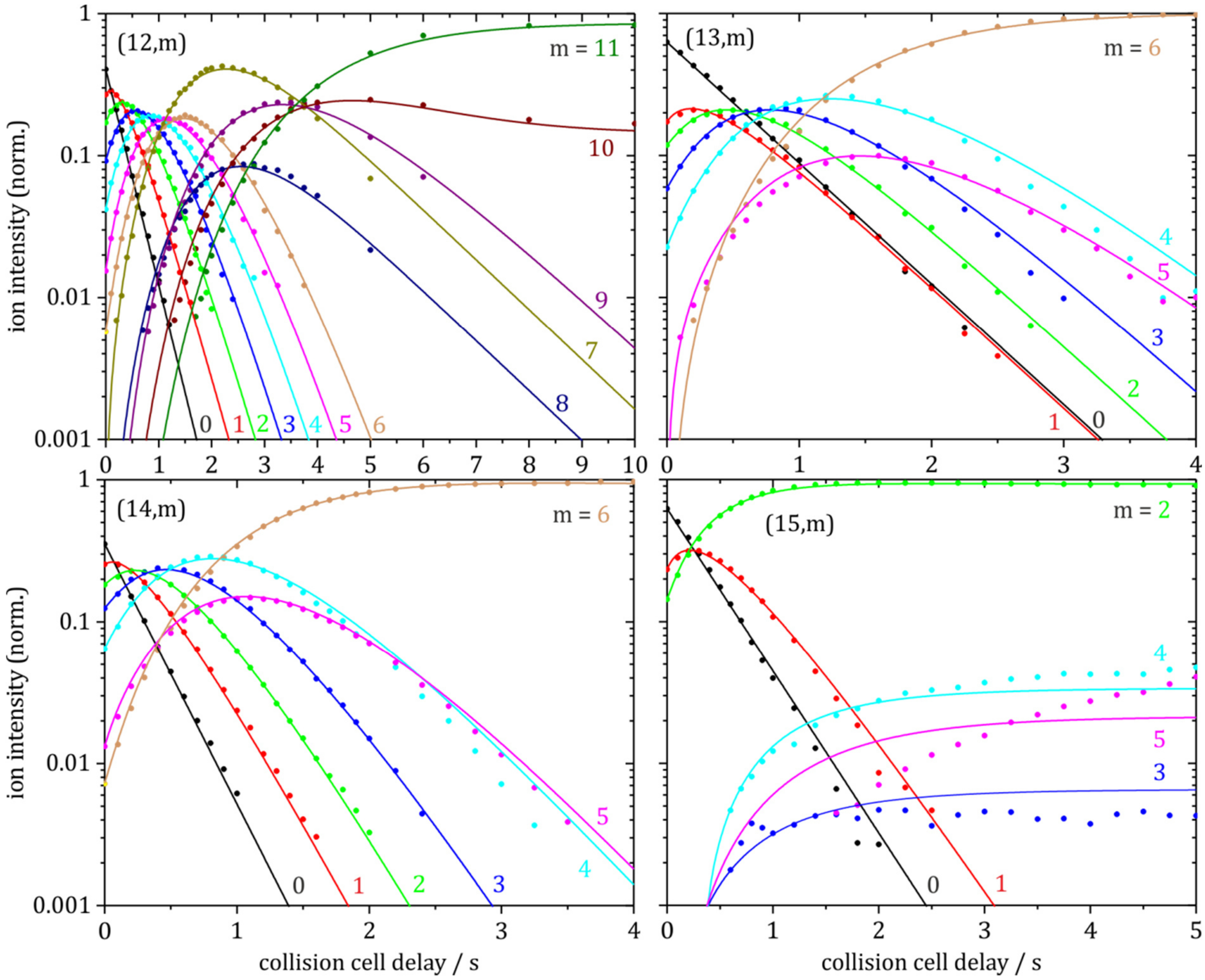

Figure 4. Isothermal kinetics of the stepwise N_2 adsorption by isolated Fe_n^+ clusters (n = 12–15). The fits (shown as lines) assume pseudo-first-order kinetics in a reaction chain of up to 11 consecutive steps.

Fe_{16}^+ – Fe_{20}^+:

In the range of n = 16–20 a significant change in reactivity towards N_2 adsorption is observed (*cf*. Fig. 4). Note, that in the case of Fe_{17}^+ no N_2 adsorption could be detected within the described experimental conditions.

In the case of (16,m) we observe a sole adsorption limit at (16,3). Clusters of the sizes n = 18, 19 and 20 exhibit dominant intermittent adsorption limits. Note the observed irregularity in intensity with further N_2 adsorption beyond these limits, which can still be fitted as consecutive reaction steps with mono-exponentially decays in good quality. This finding might indicate a change in e.g. adsorption site, likely from head-on to side-on coordination by tilting the adsorbed N_2.

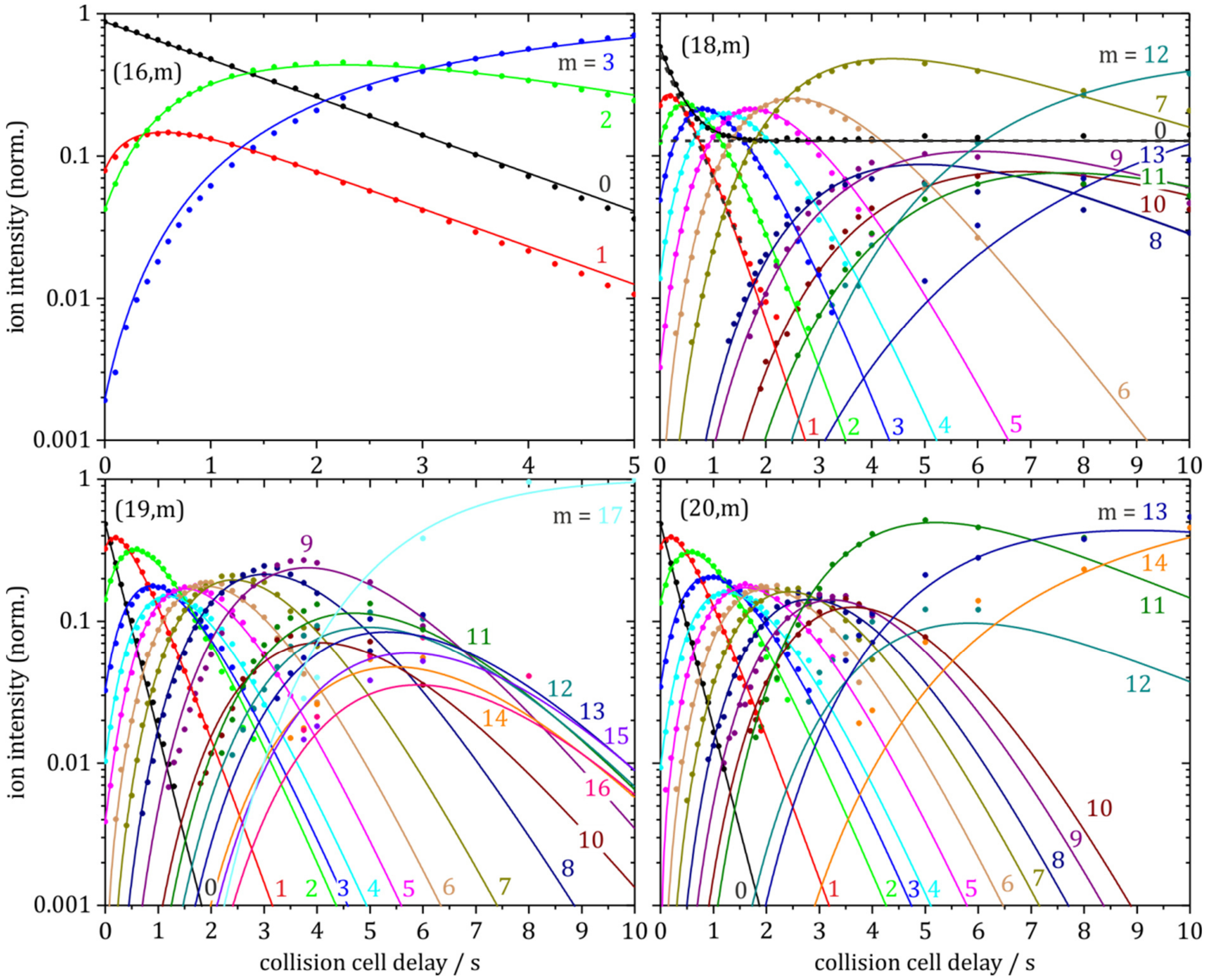

Figure 5. Isothermal kinetics of the stepwise N_2 adsorption by isolated Fe_n^+ clusters (n = 16, 18–20). The fits (shown as lines) assume pseudo-first-order kinetics in a reaction chain of up to 17 consecutive steps.

In the case of (18,m) we assume the presence of a second isomer which does not adsorb N_2 (~ 13 %, cf. Tab. 1) – presumably analogous to Fe_{17}^+. We observe a distinct intermittent adsorption limit at (18,7) and the adsorption limit at (18,13). In the cases of (19,m) and (20,m) we observe a first intermittent adsorption limit at m = 2 followed by intermittent adsorption limits at (19,9) and (20,11). The respective adsorption limits are observed at (19,17) and (20,14).

Table 1. Pseudo-first-order rate constants for the initial N_2 adsorption to Fe_{18}^+ in 1.6×10^{-7} mbar of N_2 and 26 K He buffer gas.

	$[Fe_{18}(N_2)_m]^+$	
	isomer I	isomer II
%	87	13
$k_{(18,0)}$ / s^{-1}	2.91	0.00

Absolute rate constants of the initial N_2 adsorption

The absolute rate constants $k_{(n,m)}^{abs}$ are obtained from the pseudo-first-order rate constants as a function of cluster size (Fig. 6, blue circles). Collision rate constants are calculated on the basis of classical ADO theory, as well as on the HSA and SCC models.

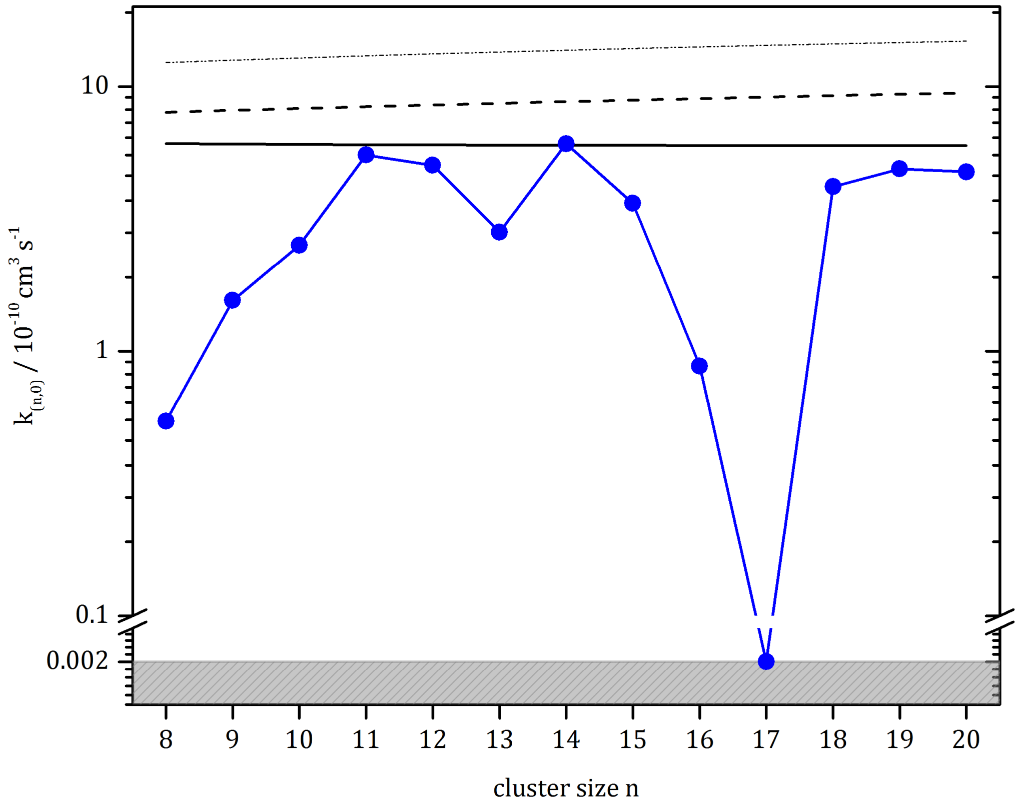

Figure 6. Absolute rate constant $k_{(n,0)}^{abs}$ of the initial N_2 adsorption to Fe_n^+ clusters by experiment (blue), according to classical average dipole orientation theory (black line), to the hard-sphere average dipole orientation model (dashed line), and to the surface charge capture model (dot-dashed line). See text for details.

We observe an overall increase in the absolute rate constants with cluster size towards collision rates predicted by ADO theory. The absolute rate constants for clusters up to n = 11 increase rapidly. Clusters with n = 13 and 15 – 17 show a decrease in reactivity towards N_2 adsorption as compared to the stated increase with cluster size. Larger clusters with n ≥ 18 reveal equal rates for the initial N_2 adsorption (*cf.* Tab. 2).

Table 2. Relative and calculated absolute rate constants for the initial N_2 adsorption to Fe_n^+ clusters in comparison to the calculated rate constants assuming classical ADO theory, the HSA model, and the SCC model.

n	$k_{(n,0)}$ s^{-1}	$k_{(n,0)}^{abs}$ 10^{-10} cm^3 s^{-1}	$k_{(n,0)}^{ADO}$ 10^{-10} cm^3 s^{-1}	$k_{(n,0)}^{HSA}$ 10^{-10} cm^3 s^{-1}	$k_{(n,0)}^{SCC}$ 10^{-10} cm^3 s^{-1}
8	0.4	0.54	6.07	8.01	12.33
9	1.1	1.55	6.05	8.14	12.58
10	1.7	2.51	6.04	8.27	12.83
11	3.8	5.50	6.02	8.40	13.06
12	3.5	5.03	6.01	8.53	13.29
13	2.0	2.82	6.00	8.65	13.50
14	4.2	6.07	5.99	8.77	13.71
15	2.5	3.61	5.99	8.89	13.91
16	0.6	0.88	5.98	9.01	14.11
17	<0.001	<0.002	5.98	9.13	14.30
18	2.9	4.18	5.97	9.24	14.48
19	3.4	4.88	5.97	9.35	14.66
20	3.3	4.78	5.96	9.46	14.84

In view of the lack of contemporary structure calculations, we reach limits when trying to interpret the subtle details of the current kinetic findings. Most noticeable, the seeming inertness of the Fe_{17}^+ cluster bears elements of a miracle – as of now.

It seems highly speculative to associate antiferromagnetic couplings with observed reluctance for N_2 adsorption to iron clusters. We do not see a convincing chain of arguments that might point towards such an interpretation. It is worth pointing out, however, that the drop in adsorption limit at n = 13 sets in at the very same cluster size that is confirmed for its antiferromagnetic coupling.[63-64] Inevitably, N_2 activation and nitride formation come to mind when dealing with the [Fe,N] system. While this is conceivable, in general such processes would not explain an almost complete absence of any adsorption in the case of n = 17. Reaction products would be detected by MS. However, there are none. Fission or loss of charge when storing the clusters in the traps is negligible (see Fig. S5 in the supplementary information for more details).

4.4.5 Conclusions and Outlook

We have investigated the stepwise N_2 adsorption on size selected Fe_n^+ (n = 8–20) clusters by recording their reaction kinetics at 26 K in a hexapole ion trap. We performed pseudo-first-order kinetic fits, which confirm consecutive adsorption steps by single exponentially decays and by a biexponential decay in the case of Fe_{18}^+. There is little N_2 adsorption to Fe_{13}^+ - Fe_{16}^+ and no N_2 adsorption to Fe_{17}^+ clusters.

We observe intermittent adsorption limits and adsorption limits which stay below a molar ratio of n:m = 1:1 in all investigated cases n = 8–20. As of now, we fail to understand the observed stoichiometries in terms of evolving overall applicable adsorption rules for the N_2 adsorption on Fe clusters. The drop in the adsorption limit from n = 13 – 17 remains unexplored. The adsorption behavior revealed in this study cannot be explained by single N_2 head-on adsorption to each cluster surface atom. We tentatively interpret the change in the kinetic curves for $n \geq 18$ at high coverages as a change in e.g. adsorption site from head-on to side-on coordination. As a result, the Fe_{18}^+ cluster would represent the minimum cluster size for tiltet N_2 adsorption, likely to highly coordinated Fe sites.

Future experiments shall help to unravel the unique adsorption behavior of Fe clusters. Various temperature controlled adsorption schemes can be performed within our tandem cryo trap instrument, e.g. N_2 adsorption kinetics under single collision conditions in the ICR cell. By focusing on the observed backward reactions, experiments using $^{15}N_2$ as adsorbate in combination with decay kinetics or infrared spectroscopy, we might gain insight into the underlying adsorption sites.

4.4.6 Acknowledgements

The ^{56}Fe isotopic sample used in this research was supplied by the United States Department of Energy Office of Science by the Isotope Program in the Office of Nuclear Physics. This work was supported by the German research foundation DFG within the transregional collaborative research center SFB/TRR 88 “Cooperative effects in homo and heterometallic complexes” (3MET.de) and by the state research center OPTIMAS.

4.4.7 References

1. Boissel, P., Organometallic Chemistry and the Interstellar Medium: Experimental Evidence of Coordination between Metal Cations and Polycyclic Hydrocarbons in the Gas Phase. *Astronomy and Astrophysics* **1994**, *285*.
2. Böhme, D. K.; Schwarz, H., Gas-Phase Catalysis by Atomic and Cluster Metal Ions: The Ultimate Single-Site Catalysts. *Angewandte Chemie International Edition* **2005**, *44*, 2336-2354.
3. Kubas, G. J., Fundamentals of H-2 Binding and Reactivity on Transition Metals Underlying Hydrogenase Function and H-2 Production and Storage. *Chem. Rev.* **2007**, *107*, 4152-4205.
4. Armentrout, P. B., Gas-Phase Perspective on the Thermodynamics and Kinetics of Heterogeneous Catalysis. *Catalysis Science & Technology* **2014**, *4*, 2741-2755.
5. Russo, N.; Salahub, D. R., *Metal-Ligand Interactions: Structure and Reactivity*; Springer Science & Business Media, 2012; Vol. 474.
6. Morse, M. D.; Geusic, M.; Heath, J.; Smalley, R., Surface Reactions of Metal Clusters. Ii. Reactivity Surveys with D2, N2, and Co. *The Journal of chemical physics* **1985**, *83*, 2293-2304.
7. Parks, E.; Weiller, B.; Bechthold, P.; Hoffman, W.; Nieman, G.; Pobo, L.; Riley, S., Chemical Probes of Metal Cluster Structure: Reactions of Iron Clusters with Hydrogen, Ammonia, and Water. *The Journal of Chemical Physics* **1988**, *88*, 1622-1632.
8. Whetten, R.; Cox, D.; Trevor, D.; Kaldor, A., Correspondence between Electron Binding Energy and Chemisorption Reactivity of Iron Clusters. *Physical review letters* **1985**, *54*, 1494.
9. Richtsmeier, S.; Parks, E.; Liu, K.; Pobo, L.; Riley, S., Gas Phase Reactions of Iron Clusters with Hydrogen. I. Kinetics. *The Journal of chemical physics* **1985**, *82*, 3659-3665.
10. Parks, E.; Liu, K.; Richtsmeier, S.; Pobo, L.; Riley, S., Reactions of Iron Clusters with Hydrogen. Ii. Composition of the Fully Hydrogenated Products. *The Journal of chemical physics* **1985**, *82*, 5470-5474.
11. Jones, N.; Beltran, M.; Khanna, S. N.; Baruah, T.; Pederson, M., Hydrogen Adsorption and Magnetic Behavior of Fe N and Co N Clusters: Controlling the Magnetic Moment and Anisotropy One Atom at a Time. *Physical Review B* **2004**, *70*, 165406.
12. Gutsev, G. L.; Bauschlicher, C. W., Interaction of Carbon Atoms with Fe N, Fe N−, and Fe N+ Clusters (N= 1–6). *Chemical physics* **2003**, *291*, 27-40.
13. Gutsev, G.; Mochena, M.; Bauschlicher, C., Interaction of Water with Small Fe N Clusters. *Chemical physics* **2005**, *314*, 291-298.
14. Gehret, O.; Irion, M. P., Reactions of Fe+ N Clusters (N= 2–11) with C6h6 and C6d6. Ligand Isomerization in the Benzene Precursor Ion Fe4 (C2h2)+ 3. *Chemical physics letters* **1996**, *254*, 379-383.
15. Valencia, I., On the Structure and Reactivity of Small Iron Clusters with Benzene, [Fen–C6h6]0,+,−, N ⩽ 7: A Theoretical Study. *Chemical Physics* **2016**, *476*, 46-60.
16. Zheng, W.; Eustis, S. N.; Li, X.; Nilles, J. M.; Thomas, O. C.; Bowen, K. H.; Kandalam, A. K., Photoelectron Spectroscopic Study of Iron–Benzene Cluster Anions. *Chemical Physics Letters* **2008**, *462*, 35-39.
17. Sakurai, M.; Watanabe, K.; Sumiyama, K.; Suzuki, K., Magic Numbers in Transition Metal (Fe, Ti, Zr, Nb, and Ta) Clusters Observed by Time-of-Flight Mass Spectrometry. *The Journal of chemical physics* **1999**, *111*, 235-238.

18. Knight, W.-D.; Clemenger, K.; de Heer, W. A.; Saunders, W. A.; Chou, M.; Cohen, M. L., Electronic Shell Structure and Abundances of Sodium Clusters. *Physical review letters* **1984**, *52*, 2141.
19. Miehle, W.; Kandler, O.; Leisner, T.; Echt, O., Mass Spectrometric Evidence for Icosahedral Structure in Large Rare Gas Clusters: Ar, Kr, Xe. *The Journal of chemical physics* **1989**, *91*, 5940-5952.
20. Billas, I. M.; Chatelain, A.; de Heer, W. A., Magnetism from the Atom to the Bulk in Iron, Cobalt, and Nickel Clusters. *Science* **1994**, *265*, 1682-1684.
21. Bucher, J.; Douglass, D.; Bloomfield, L., Magnetic Properties of Free Cobalt Clusters. *Physical review letters* **1991**, *66*, 3052.
22. Cox, D.; Trevor, D.; Whetten, R.; Rohlfing, E.; Kaldor, A., Magnetic Behavior of Free-Iron and Iron Oxide Clusters. *Physical Review B* **1985**, *32*, 7290.
23. de Heer, W. A.; Milani, P.; Chtelain, A., Spin Relaxation in Small Free Iron Clusters. *Physical review letters* **1990**, *65*, 488.
24. Chen, J.; Wang, C.; Jackson, K. A.; Pederson, M. R., Theory of Magnetic and Structural Ordering in Iron Clusters. *Physical Review B* **1991**, *44*, 6558.
25. Castro, M.; Salahub, D. R., Density-Functional Calculations for Small Iron Clusters: Fe N, Fe N+, and Fe N− for N≤ 5. *Physical Review B* **1994**, *49*, 11842.
26. Ballone, P.; Jones, R., Structure and Spin in Small Iron Clusters. *Chemical physics letters* **1995**, *233*, 632-638.
27. Oda, T.; Pasquarello, A.; Car, R., Fully Unconstrained Approach to Noncollinear Magnetism: Application to Small Fe Clusters. *Physical review letters* **1998**, *80*, 3622.
28. Hobbs, D.; Kresse, G.; Hafner, J., Fully Unconstrained Noncollinear Magnetism within the Projector Augmented-Wave Method. *Physical Review B* **2000**, *62*, 11556.
29. Diéguez, O.; Alemany, M.; Rey, C.; Ordejón, P.; Gallego, L., Density-Functional Calculations of the Structures, Binding Energies, and Magnetic Moments of Fe Clusters with 2 to 17 Atoms. *Physical Review B* **2001**, *63*, 205407.
30. Rollmann, G.; Entel, P.; Sahoo, S., Competing Structural and Magnetic Effects in Small Iron Clusters. *Computational materials science* **2006**, *35*, 275-278.
31. Yu, S.; Chen, S.; Zhang, W.; Yu, L.; Yin, Y., Theoretical Study of Electronic Structures and Magnetic Properties in Iron Clusters (N⩽ 8). *Chemical Physics Letters* **2007**, *446*, 217-222.
32. Ma, Q.-M.; Xie, Z.; Wang, J.; Liu, Y.; Li, Y.-C., Structures, Binding Energies and Magnetic Moments of Small Iron Clusters: A Study Based on All-Electron Dft. *Solid state communications* **2007**, *142*, 114-119.
33. Gutsev, G.; Weatherford, C.; Jena, P.; Johnson, E.; Ramachandran, B., Structure and Properties of Fe N, Fe N–, and Fe N+ Clusters, N= 7–20. *The Journal of Physical Chemistry A* **2012**, *116*, 10218-10228.
34. Rao, C. N. R.; Rao, G. R., Nature of Nitrogen Adsorbed on Transition-Metal Surfaces as Revealed by Electron-Spectroscopy and Cognate Techniques. *Surface Science Reports* **1991**, *13*, 221-263.
35. Ertl, G., Reactions at Surfaces: From Atoms to Complexity (Nobel Lecture). *Angew. Chem. Int. Ed.* **2008**, *47*, 3524-3535.
36. Bottomley, F.; Burns, R., Treatise on Nitrogen Fixation. Wiley Interscience, New York: 1979.
37. Freund, H. J.; Bartos, B.; Messmer, R. P.; Grunze, M.; Kuhlenbeck, H.; Neumann, M., The Adsorption of N2 on Fe(111) - Angle Resolved Photoemission and Theoretical-Model Studies. *Surf. Sci.* **1987**, *185*, 187-202.

38. Tsai, M. C.; Ship, U.; Bassignana, I. C.; Küppers, J.; Ertl, G., A Vibrational Spectroscopy Study on the Interaction of N2 with Clean and K-Promoted Fe(111) Surfaces: Π-Bonded Dinitrogen as Precursor for Dissociation. *Surface Science* **1985**, *155*, 387-399.
39. de Paola, R. A.; Hoffmann, F. M.; Heskett, D.; Plummer, E. W., Adsorption of Molecular Nitrogen on Clean and Modified Ru(001) Surfaces: The Role of <I>Σ</I> Bonding. *Physical Review B* **1987**, *35*, 4236-4249.
40. Duarte, H. A.; Salahub, D. R.; Haslett, T.; Moskovits, M., Fe (N2) N (N= 1-5): Structure, Bonding, and Vibrations from Density Functional Theory. *Inorg. Chem.* **1999**, *38*, 3895-3903.
41. Haslett, T.; Fedrigo, S.; Bosnick, K.; Moskovits, M.; Duarte, H.; Salahub, D., Binary Iron-Dinitrogen Compounds Synthesized by Co-Deposition of Mass-Selected Fe, Fe2, and Fe3 with N2. *J. Am. Chem. Soc.* **2000**, *122*, 6039-6044.
42. Lang, J.; Gaffga, M.; Menges, F.; Niedner-Schatteburg, G., Two-Color Delay Dependent Ir Probing of Torsional Isomerization in a Agl1l2 (+) Complex. *PCCP* **2014**, *16*, 17417-17421.
43. Dillinger, S.; Mohrbach, J.; Hewer, J.; Gaffga, M.; Niedner-Schatteburg, G., Infrared Spectroscopy of N2 Adsorption on Size Selected Cobalt Cluster Cations in Isolation. *PCCP* **2015**, *17*, 10358-10362.
44. Mohrbach, J.; Dillinger, S.; Niedner-Schatteburg, G., Cryo Kinetics and Spectroscopy of Cationic Nickel Clusters: Rough and Smooth Surfaces. *The Journal of Physical Chemistry C* **2017**, *in press*.
45. Peredkov, S.; Neeb, M.; Eberhardt, W.; Meyer, J.; Tombers, M.; Kampschulte, H.; Niedner-Schatteburg, G., Spin and Orbital Magnetic Moments of Free Nanoparticles. *Phys. Rev. Lett.* **2011**, *107*.
46. Meyer, J.; Tombers, M.; van Wüllen, C.; Niedner-Schatteburg, G.; Peredkov, S.; Eberhardt, W.; Neeb, M.; Palutke, S.; Martins, M.; Wurth, W., The Spin and Orbital Contributions to the Total Magnetic Moments of Free Fe, Co, and Ni Clusters. *The Journal of Chemical Physics* **2015**, *143*, 104302.
47. Das, N. K.; Shoji, T., Geometry, Orbital Interaction, and Oxygen Chemisorption Properties of Chromium-Doped Nickel Clusters. *J. Phys. Chem. C* **2012**, *116*, 13353-13367.
48. Berg, C.; Schindler, T.; Niedner-Schatteburg, G.; Bondybey, V. E., Reactions of Simple Hydrocarbons with Nb+ N: Chemisorption and Physisorption on Ionized Niobium Clusters. *The Journal of chemical physics* **1995**, *102*, 4870-4884.
49. Maruyama, S.; Anderson, L. R.; Smalley, R. E., Direct Injection Supersonic Cluster Beam Source for Ft-Icr Studies of Clusters. *Rev. Sci. Instrum.* **1990**, *61*, 3686-3693.
50. Proch, D.; Trickl, T., A High-Intensity Multi-Purpose Piezoelectric Pulsed Molecular Beam Source. *Rev. Sci. Instrum.* **1989**, *60*, 713-716.
51. Caravatti, P.; Allemann, M., The 'Infinity Cell': A New Trapped-Ion Cell with Radiofrequency Covered Trapping Electrodes for Fourier Transform Ion Cyclotron Resonance Mass Spectrometry. *Org. Mass Spectrom.* **1991**, *26*, 514-518.
52. Graf, M., *Diploma Thesis, TU Kaiserslautern* **2006**, *(unpublished)*.
53. Langevin, M. In *Une Formule Fondamentale De Théorie Cinétique*, Annales de chimie et de physique, Series, 1905; pp 245-288.
54. Su, T.; Bowers, M. T., Theory of Ion-Polar Molecule Collisions. Comparison with Experimental Charge Transfer Reactions of Rare Gas Ions to Geometric Isomers of Difluorobenzene and Dichloroethylene. *The Journal of Chemical Physics* **1973**, *58*, 3027-3037.

55. Su, T.; Bowers, M. T., Ion-Polar Molecule Collisions. Proton Transfer Reactions of H3+ and Ch5+ to the Geometric Isomers of Difluoroethylene, Dichloroethylene, and Difluorobenzene. *J. Am. Chem. Soc.* **1973**, *95*, 1370-1373.
56. Su, T.; Bowers, M. T., Ion-Polar Molecule Collisions: The Effect of Ion Size on Ion-Polar Molecule Rate Constants; the Parameterization of the Average-Dipole-Orientation Theory. *International Journal of Mass Spectrometry and Ion Physics* **1973**, *12*, 347-356.
57. Anderson, M. L.; Ford, M. S.; Derrick, P. J.; Drewello, T.; Woodruff, D. P.; Mackenzie, S. R., Nitric Oxide Decomposition on Small Rhodium Clusters, Rh N+. *The Journal of Physical Chemistry A* **2006**, *110*, 10992-11000.
58. Balteanu, I.; Balaj, O. P.; Fox-Beyer, B. S.; Rodrigues, P.; Barros, M. T.; Moutinho, A. M. C.; Costa, M. L.; Beyer, M. K.; Bondybey, V. E., Size- and Charge-State-Dependent Reactivity of Azidoacetonitrile with Anionic and Cationic Rhodium Clusters Rhn±. *Organometallics* **2004**, *23*, 1978-1985.
59. Kummerlöwe, G.; Beyer, M. K., Rate Estimates for Collisions of Ionic Clusters with Neutral Reactant Molecules. *Int. J. Mass spectrom.* **2005**, *244*, 84-90.
60. Mohrbach, J.; Dillinger, S.; Niedner-Schatteburg, G., Cryo Kinetics and Spectroscopy of Cationic Nickel Clusters: Rough and Smooth Surfaces. *The Journal of Physical Chemistry C* **2016**.
61. Jedidi, A.; Markovits, A.; Minot, C.; Abderrabba, M.; Van Hove, M. A., Co Dissociation on Magnetic Fen Clusters. *Physical Chemistry Chemical Physics* **2014**, *16*, 20703-20713.
62. Roy, D.; Robles, R.; Khanna, S., Magnetic Moment and Local Moment Alignment in Anionic and/or Oxidized Fen Clusters. *The Journal of chemical physics* **2010**, *132*.
63. Niemeyer, M.; Hirsch, K.; Zamudio-Bayer, V.; Langenberg, A.; Vogel, M.; Kossick, M.; Ebrecht, C.; Egashira, K.; Terasaki, A.; Möller, T., Spin Coupling and Orbital Angular Momentum Quenching in Free Iron Clusters. *Phys. Rev. Lett.* **2012**, *108*, 057201.
64. Meyer, J.; Tombers, M.; van Wüllen, C.; Niedner-Schatteburg, G.; Peredkov, S.; Eberhardt, W.; Neeb, M.; Palutke, S.; Martins, M.; Wurth, W., The Spin and Orbital Contributions to the Total Magnetic Moments of Free Fe, Co, and Ni Clusters. *J. Chem. Phys.* **2015**, *143*, 104302.

4.4.8 Supplementary Information

Isothermal Cryo Kinetics of Cationic Iron Clusters

Jennifer Mohrbach, Sebastian Dillinger, and Gereon Niedner-Schatteburg

Fachbereich Chemie and Forschungszentrum OPTIMAS,
Technische Universität Kaiserslautern,
67663 Kaiserslautern, Germany

Table of content

Figure S1. Observed rate constants of the (n,m) species n = 8-11 as a function of N_2 coverage. Filled circles show the rate of adsorption and open circles indicate single N_2 desorption.

Table S1. Relative rate constants for the N_2 adsorption $k_{(n,m)}$ to Fe_n^+ clusters (n = 8-11) and for the respective N_2 desorption $k_{-(n,m+1)}$ from $[Fe_n(N_2)_m]^+$ clusters.

Figure S2. Observed rate constants of the (n,m) species n = 12-15 as a function of N_2 coverage. Filled circles show the rate of adsorption and open circles indicate single N_2 desorption.

Table S2. Relative rate constants for the N_2 adsorption $k_{(n,m)}$ to Fe_n^+ clusters (n = 12-15) and for the respective N_2 desorption $k_{-(n,m+1)}$ from $[Fe_n(N_2)_m]^+$ clusters.

Figure S3. Observed rate constants of the (n,m) species n = 16, 18-20 as a function of N_2 coverage. Filled circles show the rate of adsorption and open circles indicate single N_2 desorption.

Table S3. Relative rate constants for the N_2 adsorption $k_{(n,m)}$ to Fe_n^+ clusters (n = 16, 18-12) and for the respective N_2 desorption $k_{-(n,m+1)}$ from $[Fe_n(N_2)_m]^+$ clusters.

Figure S4. Relative rate constant $k_{(n,0)}$ of the initial N_2 adsorption to Fe_n^+ clusters recorded at 26 K (filled circles), and recorded at 25 K (open circles). Note, that the measurements at 25 K have been performed at a lower N_2 pressure, which causes the offset in relative rate constants.

Figure S5. Temporal intensity decrease of isolated Fe_n^+ (n = 17 – 19) clusters at 26 K in the presence of 1.6×10^{-7} mbar of N_2. The grey shaded area indicates the loss of trapped ions.

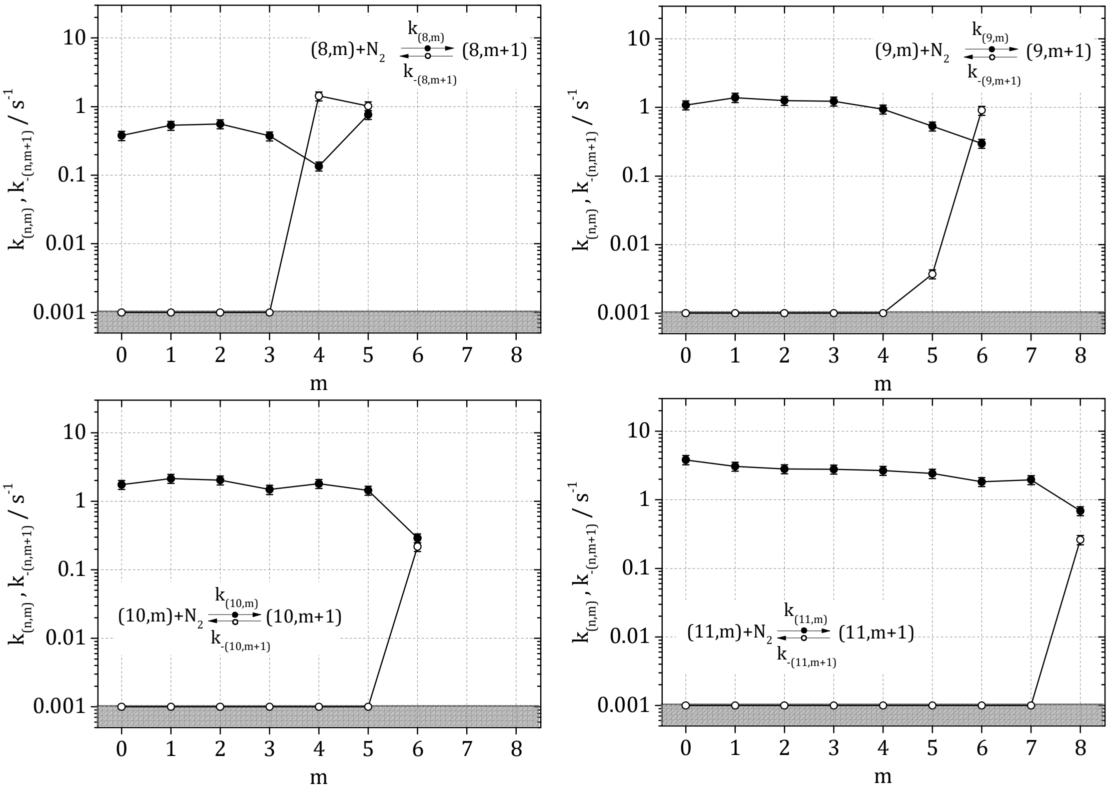

Figure S1. Observed rate constants of the (n,m) species n = 8–11 as a function of N2 coverage. Filled circles show the rate of adsorption and open circles indicate single N2 desorption.

Table S1. Relative rate constants for the N_2 adsorption $k_{(n,m)}$ to Fe_n^+ clusters (n = 8–11) and for the respective N_2 desorption $k_{-(n,m+1)}$ from $[Fe_n(N_2)_m]^+$ clusters.

m	$k_{(8,m)}$ s^{-1}	$k_{-(8,m+1)}$ s^{-1}	$k_{(9,m)}$ s^{-1}	$k_{-(9,m+1)}$ s^{-1}	$k_{(10,m)}$ s^{-1}	$k_{-(10,m+1)}$ s^{-1}	$k_{(11,m)}$ s^{-1}	$k_{-(11,m+1)}$ s^{-1}
0	0.4	<0.001	1.1	<0.001	1.7	<0.001	3.8	<0.001
1	0.5	<0.001	1.4	<0.001	2.1	<0.001	3.1	<0.001
2	0.6	<0.001	1.3	<0.001	2.0	<0.001	2.8	<0.001
3	0.4	<0.001	1.2	<0.001	1.5	<0.001	2.8	<0.001
4	0.1	1.43	0.9	<0.001	1.8	<0.001	2.7	<0.001
5	0.8	1.02	0.5	0.004	1.4	<0.001	2.4	<0.001
6			0.3	0.907	0.3	0.218	1.8	<0.001
7							2.0	<0.001
8							0.7	0.261

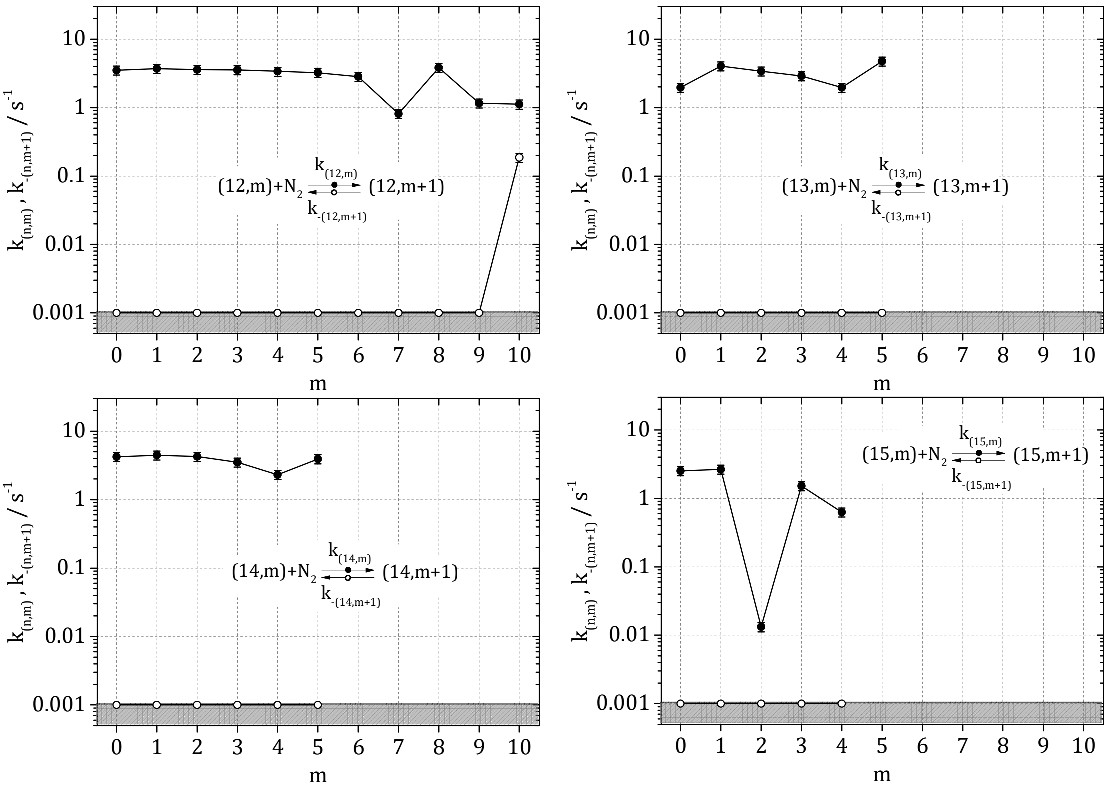

Figure S2. Observed rate constants of the (n,m) species n = 12–15 as a function of N_2 coverage. Filled circles show the rate of adsorption and open circles indicate single N_2 desorption.

Table S2. Relative rate constants for the N_2 adsorption $k_{(n,m)}$ to Fe_n^+ clusters (n = 12–15) and for the respective N_2 desorption $k_{-(n,m+1)}$ from $[Fe_n(N_2)_m]^+$ clusters.

m	$k_{(12,m)}$ s^{-1}	$k_{-(12,m+1)}$ s^{-1}	$k_{(13,m)}$ s^{-1}	$k_{-(13,m+1)}$ s^{-1}	$k_{(14,m)}$ s^{-1}	$k_{-(14,m+1)}$ s^{-1}	$k_{(15,m)}$ s^{-1}	$k_{-(15,m+1)}$ s^{-1}
0	3.5	<0.001	2.0	<0.001	4.2	<0.001	2.5	<0.001
1	3.7	<0.001	4.0	<0.001	4.5	<0.001	2.6	<0.001
2	3.6	<0.001	3.4	<0.001	4.2	<0.001	0.0	<0.001
3	3.5	<0.001	2.9	<0.001	3.5	<0.001	1.5	<0.001
4	3.4	<0.001	2.0	<0.001	2.3	<0.001	0.6	<0.001
5	3.2	<0.001	4.8	<0.001	3.9	<0.001		
6	2.8	<0.001						
7	0.8	<0.001						
8	3.8	<0.001						
9	1.2	<0.001						
10	1.1	0.186						

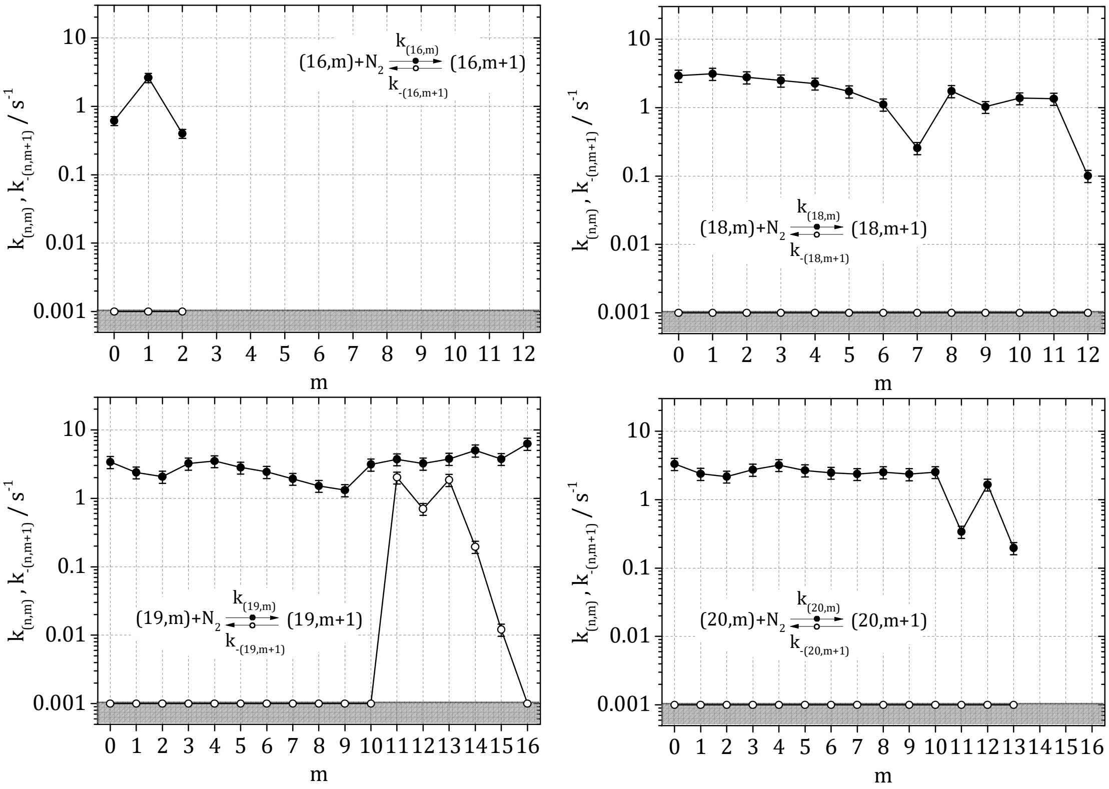

Figure S3. Observed rate constants of the (n,m) species n = 16, 18–20 as a function of N_2 coverage. Filled circles show the rate of adsorption and open circles indicate single N_2 desorption.

Table S3. Relative rate constants for the N_2 adsorption $k_{(n,m)}$ to Fe_n^+ clusters (n = 16, 18–12) and for the respective N_2 desorption $k_{-(n,m+1)}$ from $[Fe_n(N_2)_m]^+$ clusters.

m	$k_{(16,m)}$ s^{-1}	$k_{-(16,m+1)}$ s^{-1}	$k_{(18,m)}$ s^{-1}	$k_{-(18,m+1)}$ s^{-1}	$k_{(19,m)}$ s^{-1}	$k_{-(19,m+1)}$ s^{-1}	$k_{(20,m)}$ s^{-1}	$k_{-(20,m+1)}$ s^{-1}
0	0.6	<0.001	2.9	<0.001	3.40	<0.001	3.31	<0.001
1	2.6	<0.001	3.1	<0.001	2.39	<0.001	2.39	<0.001
2	0.4	<0.001	2.8	<0.001	2.06	<0.001	2.17	<0.001
3			2.5	<0.001	3.23	<0.001	2.73	<0.001
4			2.2	<0.001	3.49	<0.001	3.20	<0.001
5			1.7	<0.001	2.81	<0.001	2.67	<0.001
6			1.1	<0.001	2.43	<0.001	2.47	<0.001
7			0.3	<0.001	1.93	<0.001	2.37	<0.001
8			1.7	<0.001	1.52	<0.001	2.50	<0.001
9			1.0	<0.001	1.31	<0.001	2.36	<0.001
10			1.4	<0.001	3.13	<0.001	2.52	<0.001
11			1.3	<0.001	3.71	2.019	0.34	<0.001
12			0.1	<0.001	3.23	0.702	1.66	<0.001
13					3.77	1.859	0.20	<0.001
14					5.00	0.196		
15					3.76	0.012		
16					6.28	0.001		

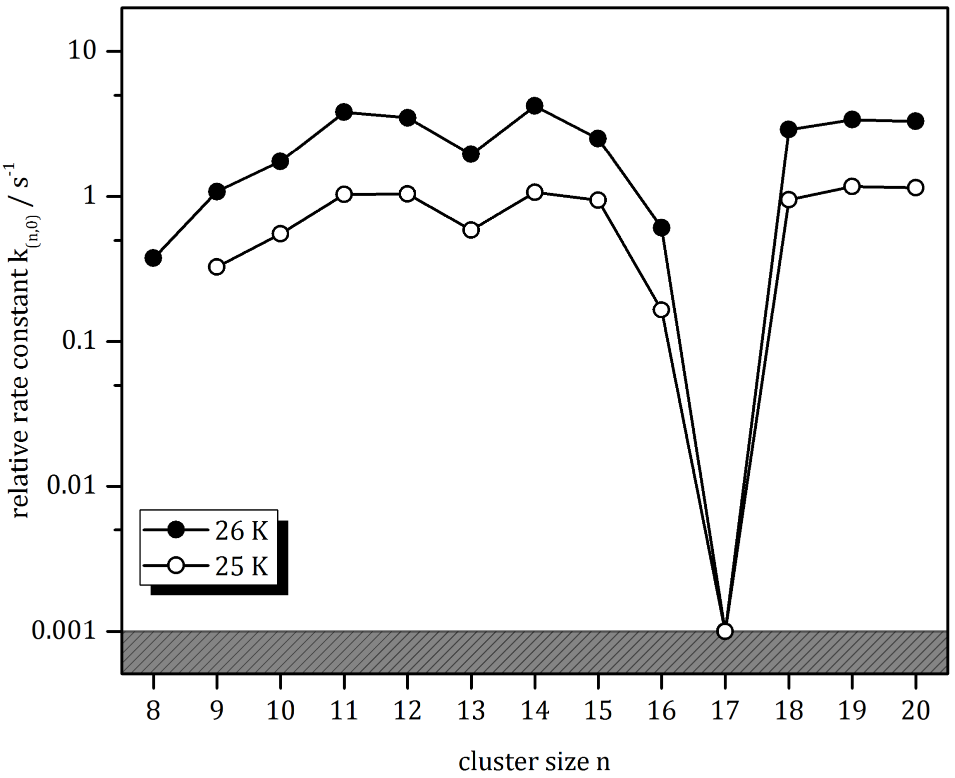

Figure S4. Relative rate constant $k_{(n,0)}$ of the initial N_2 adsorption to Fe_n^+ clusters recorded at 26 K (filled circles), and recorded at 25 K (open circles). Note, that the measurements at 25 K have been performed at a lower N_2 pressure, which causes the offset in relative rate constants.

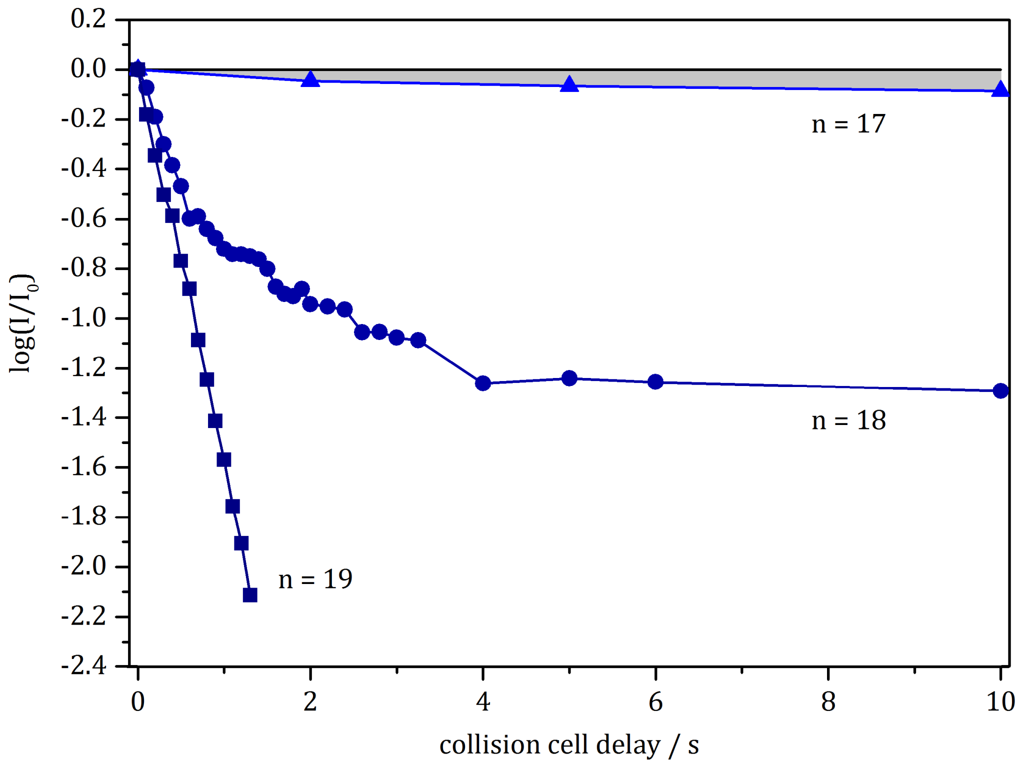

Figure S5. Temporal intensity decrease of isolated Fe_n^+ (n = 17 – 19) clusters at 26 K in the presence of 1.6×10^{-7} mbar of N_2. The grey shaded area indicates the loss of trapped ions.

5. SUMMARY AND OUTLOOK

In the present work, the adsorption behavior and adsorbate influences on transition metal containing complexes and naked transition metal clusters were investigated. A tandem cryo trap instrument has been equipped with two separately operable ion sources. This setup (FRITZ) was used for the kinetic and spectroscopic investigation of neutral adsorbates on size selected transition metal clusters under isothermal cryo conditions. Gas phase infrared multiple photon dissociation (IR-MPD) experiments in conjunction with density functional theory (DFT) computations enabled the analysis of adsorbate induced changes on the structure and spin multiplicity of transition metal cores. The investigation of the given complexes as isolated species in the gas phase enabled insight into the metal-adsorbate bonding and unraveled structure-reactivity relationships.

It became possible to record well resolved IR spectra of $[Co_4(CO)_n(dppa\text{-}H^+)]^-$ (n = 3 - 10, dppa = $NH(PPh_2)_2$) complexes in the range of CO_{term} and μ_2-CO vibrations when isolating these species at low temperatures (26 K and below). A successive loss of CO ligands was achieved by in source collision induced dissociation. Several bands were found which shift upon reduction of CO coverage, indicating a variation of coordination motifs. In conjunction with DFT modelling, we found a conclusive interpretation of all recorded IR features in the case of the saturated n = 10 compound. We found evidence for spin switching into higher multiplet states (from singlet into triplet/quintet or even higher) upon stepwise decarbonylation.

We further recorded IR-MPD spectra of Co_4 species with a mixed N_2 – CO coverage $[Co_4(CO)_n(N_2)_1L]^-$ (n = 6, 8, L = dppa-H$^+$), induced by the loss of either two or four CO ligands. The spectra revealed N_2 stretching frequencies of head-on bound N_2. We found strong evidence for CO rearrangements on the Co_4 core, triggered by the adsorption of a single N_2 molecule. The spectra of the $[Co_4(CO)_6L]^-$ and $[Co_4(CO)_6(N_2)_1L]^-$ complexes showed partially resolved CO features, which we attributed to the presence of $[Co_4(CO)_6L]^-$ and $[Co_4(CO)_6(N_2)_1L]^-$ isomers.

Next to the investigation of electro-sprayed transition metal containing complexes, the present work focuses on the N_2 adsorption on size selected Fe_n^+ ($8 \leq n \leq 20$), Co_n^+ ($8 \leq n \leq 17$), and Ni_n^+ ($5 \leq n \leq 20$) clusters. The presented cryo IR-PD spectra reveal head-on bound N_2 on all investigated cluster adsorbate complexes. We recorded isothermal cryo kinetics to gain insight into the specific adsorption trends and limits.

We investigated the N_2 adsorption on size selected Co_n^+ ($8 \leq n \leq 17$) clusters via IR-PD spectroscopy. The recorded spectra revealed remarkable cluster size dependent features. All species exhibited bands according to head-on μ_1 coordination of the N_2 molecule on the respective cluster surfaces. DFT calculations revealed a possible icosahedral Co_{13}^+ core. Nevertheless, the calculations did not allow for a final assignment of the observed spectral features (e.g. the "jump" from $n = 9$ to $n = 10$ or the presence of multiple bands).

We investigated the stepwise N_2 adsorption on size selected Ni_n^+ ($n = 5\text{-}20$) and Fe_n^+ ($n = 8\text{-}20$) clusters by recording their reaction kinetics at 26 K in the cryo hexapole ion trap. We performed pseudo-first-order kinetic fits, which confirmed consecutive adsorption steps by single exponentially decays almost exclusively. We have chosen to discuss the archetypical cases of Ni_9^+ and Ni_{13}^+ in more detail. These two clusters revealed remarkable differences in the N_2 adsorption trends and in the adsorption limits of saturation: N_2 adsorption on Ni_9^+ was observed at individual rates up to the adsorption limit and showed retardation at an additional intermittent adsorption limit. The fit of the very last adsorption step revealed a significant backward reaction, indicative for swift N_2 desorption. In contrast, the stepwise N_2 adsorption on Ni_{13}^+ occurred at equal rates up to the adsorption limit. This led to the assumption of a rough cluster surface of Ni_9^+ with inequivalent adsorption sites and a smooth cluster surface of Ni_{13}^+ with equivalent adsorption sites. The recorded IR-PD spectra of $[Ni_9(N_2)_m]^+$ and of $[Ni_{13}(N_2)_m]^+$ ($m = 1 - m_{max}$) corroborated the kinetic findings of the stated cluster morphologies. The issue of possible changes in the cluster geometry and adsorption site was addressed by DFT calculations. Possible explanations for the observed variation in relative rate constants in Ni_9^+ and its absence in Ni_{13}^+ and their feasibility were discussed such as an isomerization with low N_2 coverage in the case of Ni_9^+. In the case of Ni_{13}^+ we concluded an icosahedral structure which coincided with all experimental findings and theory.

The large-scale kinetic investigation of N_2 adsorption on size selected Ni_n^+ (n = 5-20) Fe_n^+ (n = 8-20) clusters revealed strong size- and TM-dependent stoichiometries. The found stoichiometries for Ni_n^+ clusters were interpreted in terms of initial single adsorbate occupation of available binding sites, followed by further adsorption through solvent shell re-organization towards double (geminal) occupation of low coordinated Ni surface sites. The N_2 adsorption studies on Ni_n^+ clusters allowed for comprehensive structure predictions. In contrast, we failed to understand the observed stoichiometries for the N_2 adsorption on Fe_n^+ clusters. In view of the lack of contemporary structure calculations, we reached limits when trying to interpret the subtle details of our kinetic findings. Most noticeable, the seeming inertness of the Fe_{17}^+ cluster bears elements of a miracle – as of now.

The present work shows that the combination of isothermal cryo kinetics with the IR spectroscopic investigation of the adsorbates is a powerful tool to investigate metal-adsorbate bonding and to unravel structure-reactivity relationships.

The next step in the investigation of TM adsorbate complexes by our group will be the expansion of the presented investigations to other TM clusters and alloys, first experiments on the adsorption of N_2 on Rh_n^+ and Rh-doped Fe_n^+ clusters being performed.[1-2] Furthermore, we have started a systematic study on the cryo adsorption of H_2 on various TM clusters. In future experiments, next to the adsorption of either nitrogen or hydrogen, the investigation of co-adsorption of these or other diatomic molecules on TM clusters is of great interest.

References

1. Klein, M., Diploma Thesis, TU Kaiserslautern. **2016**.
2. Ehrhard, A., Diploma Thesis, TU Kaiserslautern. **2016**.

5.1 ZUSAMMENFASSUNG UND AUSBLICK

In der vorliegenden Arbeit wurden das Adsorptionsverhalten und die Adsorbateinflüsse auf übergangsmetallhaltige Komplexe und nackte Übergangsmetallcluster (TM Cluster) untersucht. Ein Tandem-Kryo-Fallen-Instrument wurde mit zwei separat betreibbaren Ionenquellen ausgestattet. Dieser Aufbau (FRITZ) wurde für die kinetischen und spektroskopischen Untersuchungen von neutralen Adsorbaten auf größenselektierten Übergangsmetallclustern unter isothermen kryo-Bedingungen verwendet. Gasphasen Infrarote Multiphotonen Dissoziation (IR-MPD) in Verbindung mit Dichtefunktionaltheorie (DFT) Berechnungen ermöglichten die Analyse von adsorbatinduzierten Veränderungen der Struktur und der Spinmultiplizität von Übergangsmetallkernen. Die Untersuchung der gegebenen Komplexe als isolierte Spezies in der Gasphase ermöglichte Einblicke in die Metall-Adsorbat Bindung und Struktur-Reaktivitäts-Beziehungen.

Es wurde möglich, hoch aufgelöste IR-Spektren von $[Co_4(CO)_n(dppa\text{-}H^+)]^-$ (n = 3-10, dppa = $NH(PPh_2)_2$) Komplexen im Bereich der CO_{term} und μ_2-CO Schwingungen aufzuzeichnen, wenn diese Spezies bei tiefen Temperaturen (26 K und darunter) isoliert wurden. Ein sukzessiver Verlust von CO-Liganden wurde durch eine stoßinduzierte Dissoziation in der Ionenquelle erreicht. Es wurden mehrere Banden gefunden, die sich mit Reduktion des CO-Bedeckungsgrades verschieben, was auf eine Variation von Koordinationsmotiven hinweist. In Verbindung mit DFT-Modellierungen fanden wir bei der gesättigten Verbindung (n = 10) eine schlüssige Interpretation aller aufgezeichneten IR-Merkmale. Wir fanden Beweise für Spin-Switching in höhere Multiplettzustände (von Singlet zu Triplet / Quintett oder sogar höher) durch schrittweise Decarbonylierung.

Weiterhin wurden IR-MPD-Spektren von Co_4-Spezies mit gemischtem N_2-CO-Bedeckungsgrad $[Co_4(CO)_n(N_2)_1L]^-$ (n = 6, 8, L = dppa-H^+) aufgenommen, welche durch den Verlust von zwei oder vier CO-Liganden erhalten wurden. Die Spektren weisen N_2-Streckschwingungsfrequenzen von *head-on* gebundenem N_2 auf. Wir fanden starke Hinweise für CO-Umlagerungen auf dem Co_4-Kern, die durch die Adsorption eines einzelnen N_2-Moleküls ausgelöst wurde. Die Spektren der $[Co_4(CO)_6L]^-$ und

$[Co_4(CO)_6(N_2)_1L]^-$ Komplexe zeigten partiell aufgelöste CO Eigenschaften, die wir auf die Anwesenheit von $[Co_4(CO)_6L]^-$ und $[Co_4(CO)_6(N_2)_1L]^-$ Isomere zurückfuhren.

Neben der Untersuchung von elektrogesprühten übergangsmetallhaltigen Komplexen, konzentriert sich die vorliegende Arbeit auf die N_2-Adsorption an größenselektierte Fe_n^+ ($8 \leq n \leq 20$), Co_n^+ ($8 \leq n \leq 17$) und Ni_n^+ ($5 \leq n \leq 20$) Cluster. Die dargestellten kryo-IR-PD-Spektren zeigen ausschließlich *head-on* gebundenen molekularen Stickstoff auf allen untersuchten Cluster-Adsorbat-Komplexen. Wir haben isotherme Kryokinetiken aufgenommen, um Einblicke in die spezifischen Adsorptionstrends und Adsorptionsgrenzen zu gewinnen.

Die Untersuchung der N_2-Adsorption an größenselektierten Co_n^+ ($8 \leq n \leq 17$) Clustern erfolgte mittels IR-PD-Spektroskopie. Die aufgezeichneten Spektren zeigten bemerkenswerte clustergrößenabhängige Merkmale. Alle Spezies wiesen Banden des μ_1-koordinierten N_2-Moleküls auf. DFT-Rechnungen zeigten einen möglichen ikosaedrischen Co_{13}^+ Kern. Trotzdem erlaubten die Berechnungen keine endgültige Zuordnung der beobachteten spektralen Merkmale (z. B. den Sprung von $n = 9$ zu $n = 10$ oder die Anwesenheit mehrerer Banden).

Die Untersuchung der schrittweisen N_2-Adsorption an größenselektierten Ni_n^+ ($n = 5$-20) und Fe_n^+ ($n = 8$-20) Clustern gelang durch die Aufzeichnung ihrer Reaktionskinetik bei 26 K in der Hexapol-Ionenfalle. Wir führten kinetische Fits pseudo-erster-Ordnung durch, die aufeinanderfolgende Adsorptionsschritte durch einzelne exponentielle Zerfälle bestätigten. Wir haben beschlossen, die archetypischen Fälle von Ni_9^+ und Ni_{13}^+ genauer zu erörtern. Diese beiden Cluster zeigten bemerkenswerte Unterschiede in den N_2-Adsorptionstrends und in den Adsorptionsgrenzen bei Sättigung: Die N_2-Adsorption an Ni_9^+ wurde mit individuellen Raten bis zum Adsorptionsmaximum beobachtet und zeigte eine Verzögerung bei einer zusätzlichen intermittierenden Adsorptionsgrenze. Die Anpassung des letzten Adsorptionsschrittes ergab einen signifikanten Anteil einer Rückreaktion, der auf eine schnelle N_2-Desorption hinweist. Im Gegensatz dazu trat die schrittweise N_2-Adsorption an Ni_{13}^+ bis zum Adsorptionsmaximum mit gleichbleibender Geschwindigkeit auf. Dies führte zu der Annahme einer rauen Clusteroberfläche von Ni_9^+ mit ungleichen Adsorptionsstellen und einer glatten Clusteroberfläche von Ni_{13}^+ mit äquivalenten Adsorptionsstellen. Die aufgezeichneten IR-PD-Spektren von $[Ni_9(N_2)_m]^+$ und $[Ni_{13}(N_2)_m]^+$ ($m = 1 - m_{max}$)

bestätigten die kinetischen Befunde der angegebenen Clustermorphologien. Die Frage nach möglichen Änderungen in der Clustergeometrie und der Adsorptionsstelle wurde durch DFT-Rechnungen behandelt. Mögliche Erklärungen für die beobachtete Variation der relativen Geschwindigkeitskonstanten im Falle von Ni_9^+ und deren Abwesenheit bei Ni_{13}^+ sowie deren Durchführbarkeit wurden diskutiert. So wurde eine Isomerisierung bei niedrigem N_2-Bedeckungsgrad im Falle von Ni_9^+ erläutert. Im Falle von Ni_{13}^+ lies sich auf eine ikosaedrische Struktur schließen, die mit allen experimentellen und theoretischen Befunden übereinstimmte.

Die großflächige kinetische Untersuchung der N_2-Adsorption an größenselektierten Ni_n^+ ($n = 5$-20) und Fe_n^+ ($n = 8$-20) Cluster zeigte starke größenabhängige und übergangsmetallabhängige Stöchiometrien. Die gefundenen Stöchiometrien für Ni_n^+ Cluster wurden im Hinblick auf eine vorerst einzelne Adsorbatbesetzung der verfügbaren Bindungsstellen interpretiert, gefolgt von einer weiteren Adsorption zur doppelten (geminalen) Besetzung niederkoordinierter Ni-Oberflächenstellen. Die N_2-Adsorptionsstudien an Ni_n^+ Clustern erlaubten umfassende Strukturvorhersagen. Im Gegensatz dazu, waren wir noch nicht in der Lage die beobachteten Stöchiometrien für die N_2-Adsorption an Fe_n^+ Clustern zu erklären. Angesichts des Mangels an aussagekräftigen Strukturberechnungen erreichten wir unsere Grenzen bei der vollständigen Interpretation aller Details unserer kinetischen Ergebnisse. Am deutlichsten wirft die scheinbar absolute Unreaktivität des Fe_{17}^+ Clusters Fragen auf.

Die vorliegende Arbeit zeigt, dass die Kombination der isothermen Kryokinetik mit IR-spektroskopischen Untersuchungen der Adsorbate ein mächtiges Werkzeug ist, um die Metall-Adsorbat-Bindung zu untersuchen und Struktur-Reaktivitäts-Beziehungen zu entwirren.

Der nächste Schritt bei der Untersuchung von Übergangsmetall-Adsorbat-Komplexen durch unsere Gruppe ist die Aufweitung der präsentierten Untersuchungen auf andere Übergangsmetallcluster und –Legierungen. Erste Experimente zur Adsorption von N_2 an Rh_n^+ und Rh-dotierten Fe_n^+ Clustern wurden bereits durchgeführt.[1-2] Des Weiteren haben wir eine systematische Studie zur Kryoadsorption von H_2 an verschiedenen Übergangsmetallclustern begonnen. In künftigen Experimenten ist neben der Adsorption von Stickstoff oder Wasserstoff auch die Untersuchung der Co-Adsorption dieser oder anderer zweiatomiger Moleküle auf Übergangsmetallclustern von großem Interesse.

Referenzen

1. Klein, M., Diploma Thesis, TU Kaiserslautern. **2016**.
2. Ehrhard, A., Diploma Thesis, TU Kaiserslautern. **2016**.

6. APPENDIX

6.1 Publication: “Vibrational Blue Shift of coordinated N_2 in $[Fe_3O(OAc)_6(N_2)_n]^+$: “Non Classical” Dinitrogen Complexes”

The presented manuscript named “Vibrational Blue Shift of coordinated N_2 in $[Fe_3O(OAc)_6(N_2)_n]^+$: “Non Classical” Dinitrogen Complexes” was put together by Johannes Lang. It has been published at Chemical Communications. The presented results are also part of the doctoral thesis of J. Lang.

The contributions of myself to the presented manuscript consist in being part of the experimental team which acquired the presented data, being involved in parts of the data evaluation and revision of the manuscript.

Full reference to the publication:

JOHANNES LANG, JENNIFER MOHRBACH, SEBASTIAN DILLINGER, JOACHIM M. HEWER AND GEREON NIEDNER-SCHATTEBURG, *Vibrational Blue Shift of coordinated N_2 in $[Fe_3O(OAc)_6(N_2)_n]^+$: “Non Classical” Dinitrogen Complexes,* Chem. Commun., **2017**, *53,* 420-423.

DOI: 10.1039/C6CC07481B

The paper is reproduced from the above reference with permission from The Royal Society of Chemistry (RSC).

ChemComm

COMMUNICATION

View Article Online
View Journal | View Issue

Cite this: *Chem. Commun.*, 2017, **53**, 420

Received 14th September 2016, Accepted 2nd December 2016

DOI: 10.1039/c6cc07481b

www.rsc.org/chemcomm

Vibrational blue shift of coordinated N_2 in $[Fe_3O(OAc)_6(N_2)_n]^+$: "non-classical" dinitrogen complexes†

Johannes Lang,* Jennifer Mohrbach, Sebastian Dillinger, Joachim M. Hewer and Gereon Niedner-Schatteburg

We present "non-classical" dinitrogen Fe(III) oxo acetate complexes *in vacuo* utilizing Infrared Photodissociation (IR-PD) at cryo temperatures. The IR-PD spectra reveal a blue shift of the N_2 stretching vibration frequencies in the complexes. Density Functional Theory (DFT) calculations confirm the experiments and indicate strengthened N–N bonds due to pronounced σ bonding and a lack of π back donation.

The discovery of transition metal dinitrogen complexes in 1965[1] launched the ever growing research field of N_2 coordination chemistry.[2,3] One of the main goals is the conversion of N_2 to ammonia under mild conditions[4] by homogenous catalysis.[5,6] The basic idea is to weaken N–N bonds upon coordination to enable subsequent functionalization. Precursors to N_2 activation manifest by elongated N–N distances and by red shifting of stretching frequencies[7,8] with respect to the vibration of the free N_2 molecule. Such bond activation and vibrational red shifts have been interpreted before, *e.g.* in terms of the Dewar–Chatt–Duncanson (DCD) model,[9] and the Blyholder surface coordination (BSC)[10] model. Theoretical as well as spectroscopic investigations confirmed these interpretations.[11] However, FT-IR studies on N_2 coordinated to Lewis acid centers in zeolites[12] and alumina[13] revealed blue shifted vibrational N_2 stretching frequencies (up to 24 cm^{-1}). This indicates N–N bond strengthening rather than weakening – much beyond these established models. A similar effect has been observed in the case of isoelectronic carbon monoxide: so called "non-classical" metal carbonyl complexes[14,15] exhibit blue shifted vibrational CO stretching frequencies (up to 138 cm^{-1}).[16] Gas phase studies of isolated non-classical metal carbonyl clusters[17,18] proved the intrinsic molecular origin of this effect. The cause for the CO blue shift was a topic of debate[19] and is now understood in terms of an interplay between π back donation and electrostatic effects.[20] It is paramount to characterize the geometrical and electronic structures of such complexes in order to acquire a fundamental insight into the prevailing interactions leading to such non-classical behaviour.

The combination of Electrospray Ionization Mass Spectrometry[21] (ESI-MS) and infrared (IR) laser spectroscopy is suitable for the characterization of isolated coordination complexes with defined stoichiometry. Infrared (Multiple) Photon Dissociation (IR-(M)PD) provides direct access to structural and vibrational information, both under cryogenic conditions[22,23] and at room temperature.[24] The experimental results and dedicated *ab initio* calculations are combined in order to obtain detailed insight into the geometrical structure and intrinsic properties of the isolated molecular ions.

In this work we investigate isolated dinitrogen complexes $[Fe_3O(OAc)_6(N_2)_n]^+$ (n = 1–3, OAc = $CH_3CO_2^-$, *cf.* Scheme 1), which exhibit a significant blue shift (17 cm^{-1}) of N_2 vibrations in the complex with respect to the free N_2 molecule. We examine the N_2 coordination in detail to rationalize the blue shift and N–N bond strengthening. This is, to the best of our knowledge, the first report on the "non-classical" behaviour of isolated N_2 complexes.

We utilize a customized Fourier Transform-Ion Cyclotron Resonance (FT-ICR)-mass spectrometer (Apex Ultra, Bruker Daltonics) equipped with an ESI ion source (Apollo 2, Bruker).

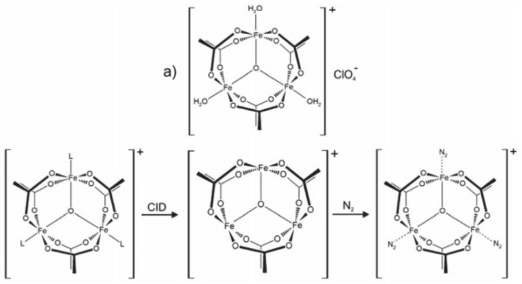

Scheme 1 (a) Molecular structure of the precursor $[Fe_3O(OAc)_6(H_2O)_3](ClO_4)$ salt. In solution the water molecules exchange with solvent molecules (L = *e.g.* acetonitrile). (b) ESI-MS reveals the formation of $[Fe_3O(OAc)_6(L)_n]^+$ (n = 0, 1, 2, 3). Collision induced dissociation (CID) of L yields the under-coordinated $[Fe_3O(OAc)_6]^+$ complex, which binds 1–3 N_2 molecules at 26 K.

Fachbereich Chemie and Forschungszentrum OPTIMAS, Technische Universität Kaiserslautern, 67663 Kaiserslautern, Germany. E-mail: jlang@chemie.uni-kl.de

† Electronic supplementary information (ESI) available. See DOI: 10.1039/c6cc07481b

This journal is © The Royal Society of Chemistry 2017

We coupled the ICR cell with a KTP/KTA optical parametric oscillator/amplifier (OPO/A) IR laser system (LaserVision). Optimized minimum energy structures and linear IR absorption spectra were calculated at the B3LYP[25] level of theory using cc-pVTZ basis sets[26] and Stuttgart RSC 1997[27] effective core potential basis sets (Gaussian 09[28]). We present calculations with 15 unpaired alpha electrons yielding a spin multiplicity of 16 with other multiplicities (2–18) found to be significantly less stable (*cf.* Fig. S12, ESI†). We scale the calculated frequencies with two different scaling factors: one scaling factor (0.951) is specifically designed to elucidate N_2 stretching bands in $[Fe_3O(OAc)_6(N_2)_n]^+$. It scales the calculated N_2 stretching frequencies such that a calculated free N_2 stretching vibration frequency matches the experimental value[29] of 2330 cm^{-1}. This approach conveniently reveals any effects of Fe–N_2 coordination on N_2 stretching frequencies. A second unspecific scaling factor (0.986) is applied for all other bands below 1800 cm^{-1}. It scales the calculated asymmetric carboxylate stretching vibration frequencies of $[Fe_3O(OAc)_6(N_2)_1]^+$ to match our own experimental value of 1587 cm^{-1}. Unscaled spectra are provided in the ESI† (*cf.* Fig. S4).

Upon spraying the sample solution and recording mass spectra in the ICR-cell, we observe a series of isotopic peaks matching convincingly with simulated isotopic patterns (*cf.* Fig. S1, ESI†). We assign those peaks to $[Fe_3O(OAc)_6(L)_n]^+$ (L = H_2O, acetonitrile, acetic acid; n = 0, 1, 2, 3). Elimination of L by Collision Induced Dissociation (CID) and subsequent coordination of N_2 in the hexapole at cryo temperatures (26 K) leads to the formation of $[Fe_3O(OAc)_6(N_2)_n]^+$ (*cf.* Scheme 1b and Fig. S2, ESI†). Note that we observe n_{max} = 3, thus "titrating" the three available Fe coordination sites. The calculated Gibbs energies at various temperatures reveal N_2 binding energies of 11, 9, and 8 kJ mol^{-1} for the first, second, and third N_2 (26 K; BSSE corrected, *cf.* Fig. S3, ESI†). The N_2 binding Gibbs energies diminish with increasing temperature, vanishing above 80 K.

We recorded IR-PD spectra of cryocooled $[Fe_3O(OAc)_6(N_2)_n]^+$ (n = 1, 2, 3, Fig. 1, black traces) and conducted DFT simulations to obtain their linear IR absorption spectra (Fig. 1, green traces). The DFT calculations reveal optimized minimum structures as depicted in the insets of Fig. 1. We observe several bands between 1300 cm^{-1} and 1500 cm^{-1}, coinciding with the predicted CH_3 bending modes of the acetate ligands. While the calculated band frequencies around 1423 cm^{-1} and 1467 cm^{-1} agree well with the IR-PD spectrum, the calculated intensities differ significantly. Switching the DFT functional from B3LYP to PBE0 yields a much better match of IR intensities but significant deviations of calculated and observed vibrational frequencies (*cf.* Fig. S5, ESI†). Neither of these empirical functionals predicts both entities correctly. In the following we utilize the B3LYP results for further discussion.

The amount of N_2 coordination (n = 1, 2, 3) has no significant influence on the frequency and intensity of the CH_3 bending bands (neither in the IR-PD experiments nor in the DFT calculations). This finding likely originates from the spatial separation of the affected methyl groups from the Fe–N_2 coordination sites.

We find a strong IR-PD band at 1587, 1590, and 1591 cm^{-1} in the cases of n = 1, 2, 3. We assign this band to carboxylic CO stretching bands of the six coordinated acetate ligands. The n = 1 CO stretching band is red shifted by ≈3–4 cm^{-1} with

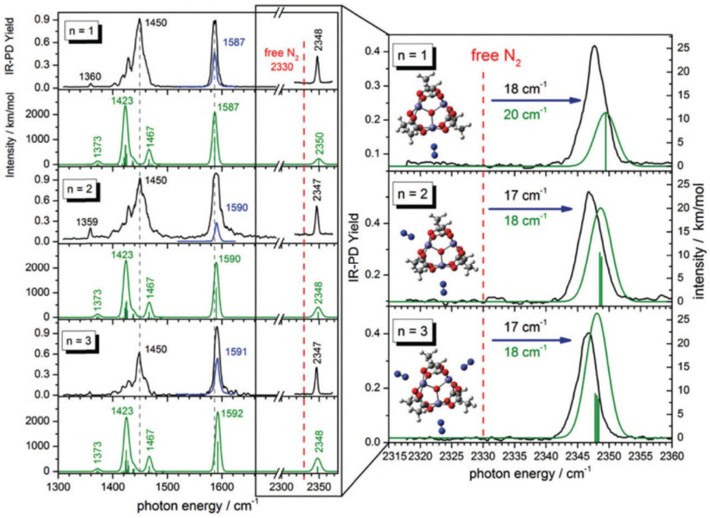

Fig. 1 Left: IR-PD spectra of $[Fe_3O(OAc)_6(N_2)_n]^+$ (n = 1, 2, 3) at 26 K (black and blue curves) and calculated IR absorption spectra of optimized $[Fe_3O(OAc)_6(N_2)_n]^+$ (n = 1–3) (green curves) in the range of 1300–2400 cm^{-1}. The blue IR-PD spectrum shows the CO stretching band (recorded with highly attenuated laser power to avoid saturation effects). The calculations were performed at the B3LYP/cc-pVTZ (H,C,N,O) and Stuttgart 1997 ECP (Fe) level of theory. The multiplicity is 16 and frequencies are scaled with 0.951 (0.986) above 2300 cm^{-1} (below 2300 cm^{-1}). Calculated stick spectra were convoluted with a Gaussian envelope of FWHM = 7 cm^{-1}. Right: A zoom into the N_2 stretching vibration region. Calculated lines were convoluted with a Gaussian envelope of FWHM = 3.5 cm^{-1}. Insets show associated geometry optimized structures.

respect to the $n = 2, 3$ bands, and with respect to the corresponding band of the free acetate anion[30] at 1591 cm^{-1}. The DFT calculated asymmetric carboxylate stretching frequencies – scaled to match the experiment at $n = 1$ – reproduce well the reduced redshift of the experiments on $n = 2, 3$. The coordinated carboxylate groups thus sense N_2 coordination through their common Fe centers. We provide an illustrative visualization of the calculated displacement vectors of these modes in Fig. S6 of the ESI.† Note that the $n = 1$ and 2 coordinations lift the sixfold degeneracy of these asymmetric stretching bands of the six coordinated acetate ligands. The recorded bands (slightly broadened to FWHM $\approx$ 7 cm^{-1}) may well contain the predicted splittings of $\approx$0.5 cm^{-1} – yet unresolved (*cf.* Fig. S7, ESI†).

We observe sharp bands (FWHM $\approx$ 3.5 cm^{-1}) above 2300 cm^{-1} revealing the IR active N_2 stretching vibrations of $[Fe_3O(OAc)_6(N_2)_n]^+$ (*cf.* the displacement vector visualization of these modes in Fig. S8, ESI†). Isotope labeling of the N_2 molecule confirms our assignment of these IR-PD bands to the N_2 stretching frequencies. We observe a red shift of the $^{15}N–^{15}N$ vibration band relative to the $^{14}N–^{14}N$ vibration band (79 cm^{-1}; *cf.* Fig. S17, ESI†) and the same blue shift with respect to the free N_2 in both isotopomers.

In all cases ($n = 1, 2, 3$) the solitary $^{14}N_2$ stretching bands of the experimental IR-PD spectra shift to the blue (17–18 cm^{-1}) with respect to the (IR inactive) stretching frequency of the free $^{14}N_2$ molecule (2330 cm^{-1}).[29] These blue shifts indicate N–N bond strengthening upon coordination. Our DFT calculations predict this blue shift remarkably well (18–20 cm^{-1}). Multiple coordinated N_2 molecules have almost identical stretching frequencies. There seems to be no coupling between the N_2 molecules adsorbing at distinct, equivalent Fe sites. In contrast to the carboxylate asymmetric stretching bands the N_2 stretching bands shift slightly to lower frequencies with increasing n (IR-PD spectrum: 1 cm^{-1}; DFT: 1.5 cm^{-1}). However, in all three cases ($n = 1–3$) the N_2 stretching band is blue shifted with respect to the free N_2.

The DFT calculations reveal subtle distortions of the triangular Fe_3O-core upon coordination of N_2 (*cf.* Scheme 2 and Table S2, ESI†). Each N_2 molecule binds end on to the respective Fe atom. In general, the coordination of N_2 enlarges Fe–Fe distances and Fe–$O_{central}$ bond lengths (by 0.03 Å resp. 0.01 Å) of those bonds which involve the N_2 coordinating Fe-center. All the other Fe–Fe distances and Fe–$O_{central}$ bond lengths shorten by approx. 0.03 Å or 0.01 Å. Natural Population Analysis (NPA) of $[Fe_3O(OAc)_6(N_2)_n]^+$ ($n = 0, 1, 2, 3$) reveals the dependence upon n of local charge densities within the triangular Fe_3O-core (*cf.* Scheme 2). The Fe centers gain 0.058–0.064 e electron density per coordinating N_2. The non-coordinated N atoms donate 0.121–0.134 e electron density in about equal parts to the coordinating N and Fe atoms. Free, non-polar N_2 molecules thus polarize and oxidize significantly upon Fe coordination, both magnitudes decreasing with n – as does the blue shift of the N_2 stretching bands. Note that the N–N bond length contracts slightly upon coordination (−0.002 Å). The high positive charge on the Fe centers (1.862–1.922 e) diminishes their electron donating capability and thus inhibits the π back donation. Such charge effects seem to increase the "non-classical" effect in metal carbonyl complexes.[31]

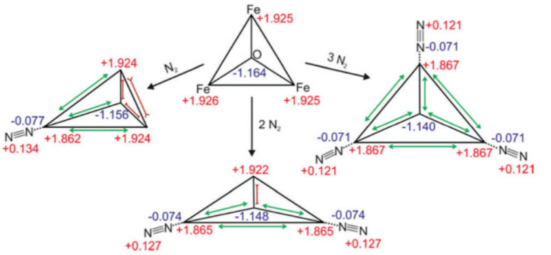

Scheme 2 Calculated geometries and natural charge distributions of the Fe_3O-core and the coordinated N_2 in $[Fe_3O(OAc)_6(N_2)_n]^+$ ($n = 0, 1, 2, 3$).

Non covalent interaction (*cf.* Fig. 2 for $n = 1$ and Fig. S11 for $n = 2, 3$, ESI†) analysis reveals a rather strong attractive, but non covalent interaction between the Fe atoms and the coordinated N atoms at rather long Fe–N coordination distances of 2.451–2.501 Å ($n = 1–3$). At such distances the π back donation is doomed to weakness due to scant π orbital overlap. Instead, it stands to reason that σ-donation of the N_2 molecule constitutes the driving force of attraction in the Fe–N_2 coordination in $[Fe_3O(OAc)_6(N_2)_n]^+$. Besides the obvious attractive Fe–N interaction, we identify repulsive interactions between the carboxylate O atoms and the coordinated N atoms.

Simple considerations as *e.g.* by the DCD and BSC models do not explain the observed blue shift of the N_2 stretching vibrations upon coordination. To rationalize this effect in a fairly perspicuous way we refer to the molecular orbital (MO) diagram of N_2 (*cf.* Scheme S1, ESI†): all bonding MOs are populated. When ruling out short range π back donation into empty anti-bonding MOs (inhibited by the net positive charge of the coordinating complex), there is a way to increase the formal N–N bond order (and thus strengthen the N–N bond and increase the stretching frequency): this is a depopulation of the antibonding 4σ* orbital into appropriate Fe centered acceptor orbitals. We have elucidated the prevailing coordination and bonding by inspection of computed molecular orbitals in $[Fe_3O(OAc)_6(N_2)_n]^+$. Indeed, we found that the 4σ* MO of the N_2 unit overlaps efficiently with MOs located at the Fe centers and at the carboxylate oxygen atoms of the $[Fe_3O(OAc)_6]^+$ subunit (*cf.* Fig. 3 for $n = 1$ and

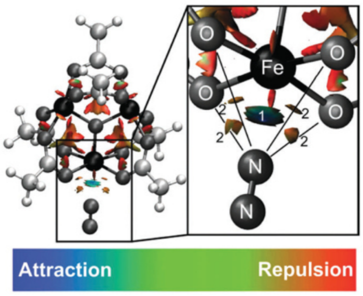

Fig. 2 NCI plot of geometry optimized $[Fe_3O(OAc)_6(N_2)_1]^+$ (*cf.* Fig. S10 for $n = 2, 3$, ESI†). The NCI plot reveals attractive interaction between the Fe center and the coordinated N atom (1) and repulsive interaction between of the O atoms and the N atom (2).

This journal is © The Royal Society of Chemistry 2017

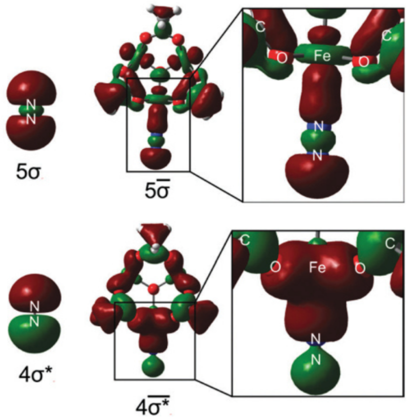

Fig. 3 Left: $4\sigma^*/5\sigma$ molecular orbitals of free N_2. Right: Selected molecular orbitals of $[Fe_3O(OAc)_6(N_2)_1]^+$ involving the former $4\sigma^*(N_2)$ and $5\sigma(N_2)$ orbitals. $4\sigma^*(N_2)$ electron density delocalizes into the whole complex, thus strengthening the N–N bond.

Fig. S13 for $n = 2, 3$, ESI†). The electrons of the anti-bonding $4\sigma^*(N_2)$ orbital delocalize into a $4\bar{\sigma}^*$ MO of the whole complex, whereby the $4\sigma^*(N_2)$ orbital polarizes towards the Fe center. Note that the node plane of $4\sigma^*(N_2)$ (between the N atoms) shifts somewhat towards the Fe center. The depletion of the anti-bonding electron density along the N–N bond increases the net bond order of N_2 and blue shifts the N_2 stretching vibration. The bonding $5\sigma(N_2)$ contributes to a $5\bar{\sigma}$ MO of the complex. This is expected to result in N–N bond weakening counteracting the effect of $4\sigma^*(N_2)$ delocalization. However, $5\sigma(N_2)$ receives a partial $4\sigma^*(N_2)$ character to form the $5\bar{\sigma}$ MO *via* hybridization. The strengthening effect of $4\sigma^*(N_2)$ electron density delocalization thus seems to be the critical factor for the "non-classical" behavior of $[Fe_3O(OAc)_6(N_2)_n]^+$. The involvement of the $4\sigma^*(N_2)$ orbital in the M–N_2 bonding scheme as well as $4\sigma^*/5\sigma$ hybridization has been suggested in the context of X-ray absorption studies of N_2 adsorbed on metal surfaces.[32] Inspection of all other delocalized MOs in the $[Fe_3O(OAc)_6(N_2)_1]^+$ complex reveals a total lack of π back donation from the $[Fe_3O(OAc)_6]^+$ unit to empty $\pi^*(N_2)$ orbitals. Considering the high charge on the Fe center and the long Fe–N_2 distance (see above) this seems reasonable. The N_2 coordination and thus the "non-classical" behavior of $[Fe_3O(OAc)_6(N_2)_n]^+$ originate from σ bonding effects.

Our fundamental insight into the class of "non-classical" N_2–Fe complexes is remarkable in view of the industrial use of bulk iron for N_2 activation and hydrogenation. It might help to advance a general understanding of dinitrogen chemistry beyond established coordination models.

This work was supported by the German Research Foundation DFG within the Transregional Collaborative Research Center SFB/TRR 88 "Cooperative effects in homo and heterometallic complexes" (3MET).

Notes and references

1 M. D. Fryzuk, *Chem. Commun.*, 2013, **49**, 4866–4868.
2 J. L. Crossland and D. R. Tyler, *Coord. Chem. Rev.*, 2010, **254**, 1883–1894.
3 N. Khoenkhoen, B. de Bruin, J. N. H. Reek and W. I. Dzik, *Eur. J. Inorg. Chem.*, 2015, 567–598.
4 S. F. McWilliams and P. L. Holland, *Acc. Chem. Res.*, 2015, **48**, 2059–2065.
5 D. V. Yandulov and R. R. Schrock, *Science*, 2003, **301**, 76–78.
6 H. Tanaka, K. Arashiba, S. Kuriyama, A. Sasada, K. Nakajima, K. Yoshizawa and Y. Nishibayashi, *Nat. Commun.*, 2014, **5**, 1–11.
7 N. Lehnert and F. Tuczek, *Inorg. Chem.*, 1999, **38**, 1659–1670.
8 N. Lehnert and F. Tuczek, *Inorg. Chem.*, 1999, **38**, 1671–1682.
9 J. Chatt and L. A. Duncanson, *J. Chem. Soc.*, 1953, 2939–2947.
10 G. Blyholder, *J. Phys. Chem.*, 1964, **68**, 2772–2777.
11 F. Studt and F. Tuczek, *J. Comput. Chem.*, 2006, **27**, 1278–1291.
12 K. Hadjiivanov and H. Knözinger, *Catal. Lett.*, 1999, **58**, 21–26.
13 R. Wischert, C. Coperet, F. Delbecq and P. Sautet, *Chem. Commun.*, 2011, **47**, 4890–4892.
14 H. Willner and F. Aubke, *Angew. Chem., Int. Ed.*, 1997, **36**, 2402–2425.
15 A. J. Lupinetti, G. Frenking and S. H. Strauss, *Angew. Chem., Int. Ed.*, 1998, **37**, 2113–2116.
16 P. K. Hurlburt, J. J. Rack, J. S. Luck, S. F. Dec, J. D. Webb, O. P. Anderson and S. H. Strauss, *J. Am. Chem. Soc.*, 1994, **116**, 10003–10014.
17 J. Velasquez, B. Njegic, M. S. Gordon and M. A. Duncan, *J. Phys. Chem. A*, 2008, **112**, 1907–1913.
18 A. Fielicke, G. von Helden, G. Meijer, B. Simard and D. M. Rayner, *J. Phys. Chem. B*, 2005, **109**, 23935–23940.
19 A. S. Goldman and K. Krogh-Jespersen, *J. Am. Chem. Soc.*, 1996, **118**, 12159–12166.
20 G. Bistoni, S. Rampino, N. Scafuri, G. Ciancaleoni, D. Zuccaccia, L. Belpassi and F. Tarantelli, *Chem. Sci.*, 2016, **7**, 1174–1184.
21 J. B. Fenn, *Angew. Chem., Int. Ed.*, 2003, **42**, 3871–3894.
22 N. Heine and K. R. Asmis, *Int. Rev. Phys. Chem.*, 2014, **34**, 1–34.
23 J. Jašík, J. Žabka, J. Roithová and D. Gerlich, *Int. J. Mass Spectrom.*, 2013, **354–355**, 204–210.
24 J. Lang, M. Gaffga, F. Menges and G. Niedner-Schatteburg, *Phys. Chem. Chem. Phys.*, 2014, **16**, 17417–17421.
25 A. D. Becke, *J. Chem. Phys.*, 1993, **98**, 5648–5652.
26 T. H. Dunning, *J. Chem. Phys.*, 1989, **90**, 1007–1023.
27 M. Dolg, H. Stoll, H. Preuss and R. M. Pitzer, *J. Phys. Chem.*, 1993, **97**, 5852–5859.
28 M. J. Frisch, G. W. Trucks, H. B. Schlegel, G. E. Scuseria, M. A. Robb, J. R. Cheeseman, G. Scalmani, V. Barone, B. Mennucci, G. A. Petersson, H. Nakatsuji, M. Caricato, X. Li, H. P. Hratchian, A. F. Izmaylov, J. Bloino, G. Zheng, J. L. Sonnenberg, M. Hada, M. Ehara, K. Toyota, R. Fukuda, J. Hasegawa, M. Ishida, T. Nakajima, Y. Honda, O. Kitao, H. Nakai, T. Vreven, J. A. Montgomery, Jr., J. E. Peralta, F. Ogliaro, M. Bearpark, J. J. Heyd, E. Brothers, K. N. Kudin, V. N. Staroverov, R. Kobayashi, J. Normand, K. Raghavachari, A. Rendell, J. C. Burant, S. S. Iyengar, J. Tomasi, M. Cossi, N. Rega, J. M. Millam, M. Klene, J. E. Knox, J. B. Cross, V. Bakken, C. Adamo, J. Jaramillo, R. Gomperts, R. E. Stratmann, O. Yazyev, A. J. Austin, R. Cammi, C. Pomelli, J. W. Ochterski, R. L. Martin, K. Morokuma, V. G. Zakrzewski, G. A. Voth, P. Salvador, J. J. Dannenberg, S. Dapprich, A. D. Daniels, Ö. Farkas, J. B. Foresman, J. V. Ortiz, J. Cioslowski and D. J. Fox, *Gaussian 09, Revision E.01*, Gaussian, Inc., Wallingford CT, 2009.
29 K. P. Huber and G. Herzberg, *Constants of Diatomic Molecules*, Van Norstrand, New York, 1979.
30 J. D. Steill and J. Oomens, *J. Phys. Chem. A*, 2009, **113**, 4941–4946.
31 A. M. Ricks, J. M. Bakker, G. E. Douberly and M. A. Duncan, *J. Phys. Chem. A*, 2009, **113**, 4701–4708.
32 A. Nilsson and L. G. M. Pettersson, *Surf. Sci. Rep.*, 2004, **55**, 49–167.

Danken möchte ich:

Prof. G. Niedner-Schatteburg für die wissenschaftliche Betreuung während meiner Promotion, für die gute Zusammenarbeit und für seine beständige Diskussionsbereitschaft. Im Besonderen möchte ich mich für die Freiheit eigene Ideen zu verfolgen und verwirklichen zu können, und für seine Unterstützung in Situationen hohen Zeitdrucks bedanken.

Prof. M. Gerhards für die Übernahme des Zweitgutachtens und Prof. H. Sitzmann für die Übernahme des Prüfungsvorsitzes.

Dr. Thomas Kolling – *Meister Kolling* – für seine Kompetenz, Hilfsbereitschaft und stete Geduld in sämtlichen Belangen, vom allerersten Tag an.

Meinen Arbeitskollegen und Freunden Sebastian Dillinger, Joachim Hewer, Dimitri Imanbaew und Johannes Lang für die großartige Atmosphäre und permanente Unterstützung. Im Besonderen danke ich Sebastian für die hervorragende Zusammenarbeit und Verlässlichkeit. Guter Minion!

Der „alten Garde“ des Arbeitskreises: Lars Barzen, Fabian Menges, Christine Merkert, Jennifer Meyer und Matthias Tombers für die tolle Aufnahme in den Arbeitskreis, die gegenseitige Hilfe bei allen möglichen Problemen und für die Aufrechterhaltung des Kontaktes über die Promotion hinaus.

Mein ganz besonderer Dank gilt Hilde Seelos und Sibylle Heieck für die großartige Unterstützung und das „Alles irgendwie möglich machen“.

Den Mitarbeitern der Chemikalienausgabe für ihre Anteilnahme und moralische Unterstützung; selbstverständlich auch für die unvergleichliche Feuerzangenbowle!

Den Mitarbeitern der Metall- und Elektronikwerkstätten für die vielen beratenden Gespräche und die unkomplizierte Hilfe, wenn's mal wieder schneller gehen musste.

Ein großer Dank gebührt zweifellos Anneken Grün und Patrick Jost. Sie haben dazu beigetragen, mein ernährungstechnisches Wohl nicht zu vernachlässigen und für die erforderliche Aufmunterung und das wesentliche Lachen gesorgt.

Meiner jahrelangen Weggefährtin und guten Freundin Nicole Kiweler für die gemeinsame Zeit im Studium und darüber hinaus. Michael Loch für seine Freundschaft und den Beistand. Vielen Dank für das Gefühl immer zuhause zu sein. Lena Maier für die wunderbare gemeinsame Zeit und ihre Freundschaft weit über Ländergrenzen hinaus.

Mein größter Dank gilt meiner Familie. Ich danke meinen Eltern und meiner Großmutter für die Ermöglichung meines Studiums und für ihr Verständnis in schwierigen Phasen. Ein weiterer Dank gilt besonders Ellen und Joachim, aber auch Michel und Thomas für die herzliche Aufnahme in ihre Familie und ihr stetes Interesse an meiner Arbeit.

Joel für ein Jahrzehnt Freundschaft, Respekt, Rückhalt, Verständnis und Unterstützung. Danke, dass du Teil meines Lebens bist.

Lebenslauf

Jennifer Mohrbach

PROMOTION

10/2013 – 03/2017	Promotion in Physikalischer Chemie, AG Prof. Niedner-Schatteburg, TU Kaiserslautern Titel der Doktorarbeit: „*Cryo tagging infrared spectroscopy and temperature controlled kinetic studies in a tandem trap mass spectrometer*“

STUDIUM

10/2008 – 09/2013	Studienrichtung Chemie Schwerpunkt Physikalische Chemie, TU Kaiserslautern Erreichter Abschluss: Diplom; Titel der Diplomarbeit: „*Charakterisierung ausgewählter Übergangs-metallkomplexe mittels infrarot induzierter Multiphotonendissoziation (IR MPD) bei tiefen Temperaturen*“
10/2006 – 09/2008	Grundstudium Maschinenbau und Verfahrenstechnik an der Technischen Universität Kaiserslautern

SCHULE

09/1997 –06/2006	Allgemeine Hochschulreife: Gymnasium am Krebsberg in Neunkirchen

VERÖFFENTLICHUNGEN

1. *Infrared spectroscopy of N_2 adsorption on size selected cobalt cluster cations in isolation*
   Sebastian Dillinger, **Jennifer Mohrbach**, Joachim Hewer, Maximilian Gaffga, and Gereon Niedner-Schatteburg
   Phys. Chem. Chem. Phys. (2015), 17, 10358.
   http://dx.doi.org/10.1039/c5cp00047e

2. *Laser-induced delayed electron emission of Co_4^- anions*
   Sebastian George, Klaus Blaum, Christian Breitenfeldt, Jürgen Göck, Jonas Karthein, Thomas Kolling, Christian Meyer, **Jennifer Mohrbach**, Gereon Niedner-Schatteburg, Dirk Schwalm, Lutz Schweikhard, Andreas Wolf
   J. Phys.: Conf. Ser. (2015), 635, 112054.
   http://dx.doi.org/10.1088/1742-6596/635/11/112054

3. *An ion source platform of the cryogenic storage ring (CSR)*
   P. M. Mishra, K. Blaum, C. Breitenfeldt, S. George, J. Göck, M. Grieser, R. von Hahn, J. Karthein, T. Kolling, C. Krantz, H. Kreckel, S. Kumar, **J. Mohrbach**, G. Niedner-Schatteburg, C. Meyer, R. Repnow, L. Schweikard, and A. Wolf
   J. Phys.: Conf. Ser. (2015), 635, 112061.
   http://dx.doi.org/10.1088/1742-6596/635/11/112061

4. *Vibrational fingerprints of a tetranuclear cobalt carbonyl cluster within an ion trap*
   Jennifer Mohrbach, Johannes Lang, Sebastian Dillinger, Marc Prosenc, Pierre Braunstein, and Gereon Niedner-Schatteburg
   J. Molec. Spectrosc. (2017), 332, 103–108.
   http://dx.doi.org/10.1016/j.jms.2016.11.008

5. *Cryo Kinetics and Spectroscopy of cationic nickel clusters: Rough and smooth surfaces*
   Jennifer Mohrbach, Sebastian Dillinger, and Gereon Niedner-Schatteburg
   J. Phys. Chem. C (2017), 121 (20), 10907–10918.
   http://dx.doi.org/10.1021/acs.jpcc.6b12167

6. *Vibrational Blue Shift of coordinated N_2 in $[Fe_3O(OAc)_6(N_2)_n]^+$: "Non Classical" Dinitrogen Complexes*
   Johannes Lang, **Jennifer Mohrbach**, Sebastian Dillinger, Joachim M. Hewer and Gereon Niedner-Schatteburg
   Chem. Comm. (2017), 53, 420-423.
   http://dx.doi.org/10.1039/C6CC07481B

7. *Long-term monitoring of the internal energy distribution of isolated cluster systems*
   Christian Breitenfeldt, Klaus Blaum, Sebastian George, Jürgen Göck,1 Gregorio Guzmán-Ramírez, Jonas Karthein, Thomas Kolling, Michael Lange, Sebastian Menk, Christian Meyer, **Jennifer Mohrbach**, Gereon Niedner-Schatteburg, Dirk Schwalm, Lutz Schweikhard, and Andreas Wolf
   Phys. Rev. Lett. (2016, submitted)

VORTRÄGE UND KONFERENZBEITRÄGE

VORTRÄGE

28.02.-04.03.2016	*Surfaces of Clusters: Adsorption, Kinetics and Spectroscopy* S3C, Davos, CH
17-22.01.2016	*Nitrogen Adsorption on Nickel Cluster Cations* GRC: Molecular and ionic clusters, Ventura, CA, USA
17.02.2015	*Recent advances in cryo ion studies* Vortrag im Rahmen des Gruppenseminars JLab, Yale University, New Haven, USA
23-27.03.2015	Cryo kinetics of size selected cobalt clusters Frühjahrstagung der Deutschen Physikalischen Gesellschaft, Heidelberg

POSTERBEITRÄGE

05.-07.10.2016	*Vibrational Blue Shift of coordinated* N_2 *in* $[Fe_3O(OAc)_6(N_2)_n]^+$*: “Non Classical” Dinitrogen Complexes* 3rd International Conference on Bimetallic Complexes, Kaiserslautern
05.-07.10.2016	*Vibrational fingerprints of ligand stabilized tetranuclear transition metal complexes* 3rd International Conference on Bimetallic Complexes, Kaiserslautern
31.08.-02.09.2016	*Surfaces of Clusters: Adsorption, Kinetics and Spectroscopy* The Future of Chemical Physics by JCP, Oxford, UK
17.-22.01.2016	*Cryo kinetics of* N_2 *adsorption on size selected nickel cluster cations* GRC: Molecular and Ionic Clusters, Ventura, CA, USA
22.-27.02.2015	*Kinetic studies and infrared spectroscopy of* N_2 *adsorption to size selected cobalt cluster cations at cryogenic temperatures* GRC: Gaseous Ions, Galveston, USA
14.-16.05.2015	*Cryo kinetics and spectroscopy of size selected cobalt clusters* 114. Bunsentagung für Physikalische Chemie, Bochum
15.-18.06.2015	*Magnetic characterization of Single Molecule Magnets in isolation by X-ray Magnetic Circular Dichroism* 594. Wilhelm and Else Heraeus-Seminar "Spectroscopy and applications of cold molecular ions", Bad Honnef

22.-25.04.2014	*Tandem trapping of cold ions for wide range IR spectroscopy* EFTMS, Paris, Frankreich
09.-11.05.2013	*Benzene activation and H/D isotope effects in reactions of mixed cobalt platinum, cobalt rhodium and cobalt gold cluster ions* 112. Bunsentagung für Physikalische Chemie, Karlsruhe
18.-22.03.2013	*Benzene activation and H/D isotope effects in reactions of size selected iron, cobalt and nickel cluster ions* Frühjahrstagung der Deutschen Physikalischen Gesellschaft, Hannover

Eidesstattliche Erklärung

Hiermit bestätige ich, Jennifer Mohrbach, dass die vorliegende Arbeit gemäß der Promotionsordnung des Fachbereichs Chemie der Technischen Universität Kaiserslautern selbständig und nur unter Verwendung der angegebenen Quellen und Hilfsmittel angefertigt wurde.

Kaiserslautern Jennifer Mohrbach